I. SEISMOLOGICAL STUDY OF THE NINETYEAST AND CHAGOS-LACCADIVE RIDGES, INDIAN OCEAN

II. MODELS FOR ASYMMETRIC AND OBLIQUE SPREADING AT MIDOCEAN RIDGES

III. ATTENUATION STUDIES USING SPLIT NORMAL MODES

Thesis by

Seth Avram Stein

In Partial Fulfillment of the Requirements

for the Degree of

Doctor of Philosophy

California Institute of Technology

Pasadena, California

1978

(Submitted May 22, 1978)

ACKNOWLEDGEMENTS

This research would not have been possible without the generous support of the Fannie and John Hertz Foundation. Additional support was provided by the National Science Foundation under grants EAR 76-14262, EAR 74-22489 and EAR 77-14476.

ABSTRACT

Part I of this work is a study of the seismicity of the Ninetyeast and Chagos-Laccadive Ridges in the Indian Ocean. These two features, in the interior of the oceanic plate, both show unusual seismicity. The mechanisms of these earthquakes were studied using body and surface waves. This analysis shows that the Ninetyeast Ridge is still an active zone of deformation within the plate, along which substantial relative motion is taking place. The Chagos-Laccadive Ridge, though far less active, shows unusual seismicity in its southern portion. The seismicity on both ridges differs substantially from any previously discussed in the ocean basins. Both features should still be regarded as active today, though they do not fit into the classic ridge-transform-trench classifications.

Part II of this work is a study of the mechanics of oblique and asymmetric seafloor spreading. It proposes that asymmetric seafloor spreading occurs as a consequence of the relative motion between ridges and slow moving mantle material below. A mechanical model of asymmetric spreading predicts that the trailing flank of a ridge migrating with respect to the mantle spreads fastest. These predictions are tested against published data and found to be in good agreement in most places. Oblique spreading is said to occur at midocean ridges which spread slowly (half rate less than 3 cm/yr), while the spreading is perpendicular at faster spreading ridges. This relation is explored using the ratio of the power dissipated at ridges to that on transform faults to determine the most energetically favorable ridge-transform geometry. The angle of oblique spreading (θ) is approximately related to the spreading rate

by $\sin \theta \sim V^{-1}$, in good agreement with observations.

Part III of this work is a study of the attenuation of the longest period normal modes of the earth. The rotationally and elliptically split normal modes of the earth are observed for the 1960 Chilean and the 1964 Alaskan earthquakes by analysis in the time domain. Synthetic seismograms are computed using theoretical results which show the dependence of the amplitude and phase of the singlets on source location, depth, mechanism and the position of the receiver. By comparing these synthetics to the filtered record, the Qs of the longest period spheroidal ($_0S_2$ - $_0S_5$) and torsional ($_0T_3$, $_0T_4$) modes can be estimated. In addition, the Q of the fundamental radial mode $_0S_0$ is measured.

TABLE OF CONTENTS

PART I

Chapter		Page
1	Introduction	2
	References	7
2	Seismicity and Tectonics of the Ninetyeast Ridge Area: Evidence for Internal Deformation in the Indian Plate	9
	References	53
3	An Earthquake Swarm on the Chagos-Laccadive Ridge and its Tectonic Implications	58
	References	84

PART II

1	Introduction	88
	References	92
2	Ridge Migration and Asymmetric Seafloor Spreading	94
	References	120
3	A Model for the Relation Between Spreading Rate and Oblique Spreading	124
	References	144

PART III

1	Introduction	149
	References	156
2	Attenuation Studies Using Split Normal Modes for the 1960 Chilean and 1964 Alaskan Earthquakes	157
	References	208

PART I

SEISMOLOGICAL STUDY OF THE NINETYEAST AND CHAGOS-LACCADIVE RIDGES, INDIAN OCEAN

Chapter 1

INTRODUCTION

From a tectonic viewpoint, the Indian Ocean is the most complicated and most puzzling of the major ocean basins. Rather than having a simple spreading ridge down the center with topography decaying away smoothly with distance, the Indian Ocean is divided into a series of isolated basins by a group of topographically elevated features collectively called aseismic ridges [Laughton et al., 1971]. The most dramatic of these are the almost-parallel Ninetyeast Ridge (90°E, 10°N-30°S), and the Chagos-Laccadive Ridge (62°E, 5°N-15°S). Other such ridges include Broken Ridge, the Mascarene Plateau, the Crozet Plateau and the Kerguelen Plateau (Figure 1.1).

The full extent of these features was recognized in the early 1960's during the International Indian Ocean Expedition (1960-1965). Extensive marine geological and geophysical exploration was then carried out, particularly by ships of the Scripps Institute of Oceanography [Fisher et al., 1971; McKenzie and Sclater, 1971; Sclater and Fisher, 1974], and the Deep Sea Drilling Project's D/V GLOMAR CHALLENGER [Fisher et al., 1974; Davies et al., 1974; Von der Borch et al., 1974; Whitmarsh et al., 1974]. A generally accepted synthesis has emerged of the geologic history of the Indian Ocean, although the detailed evolution of this area is still in question [Peirce, 1978; Luyendyk and Rennick, 1977; Ben-Avraham and Bunce, 1977].

The two major aseismic ridges (this phrase will be used throughout this thesis without quotation marks, even in discussing seismicity),

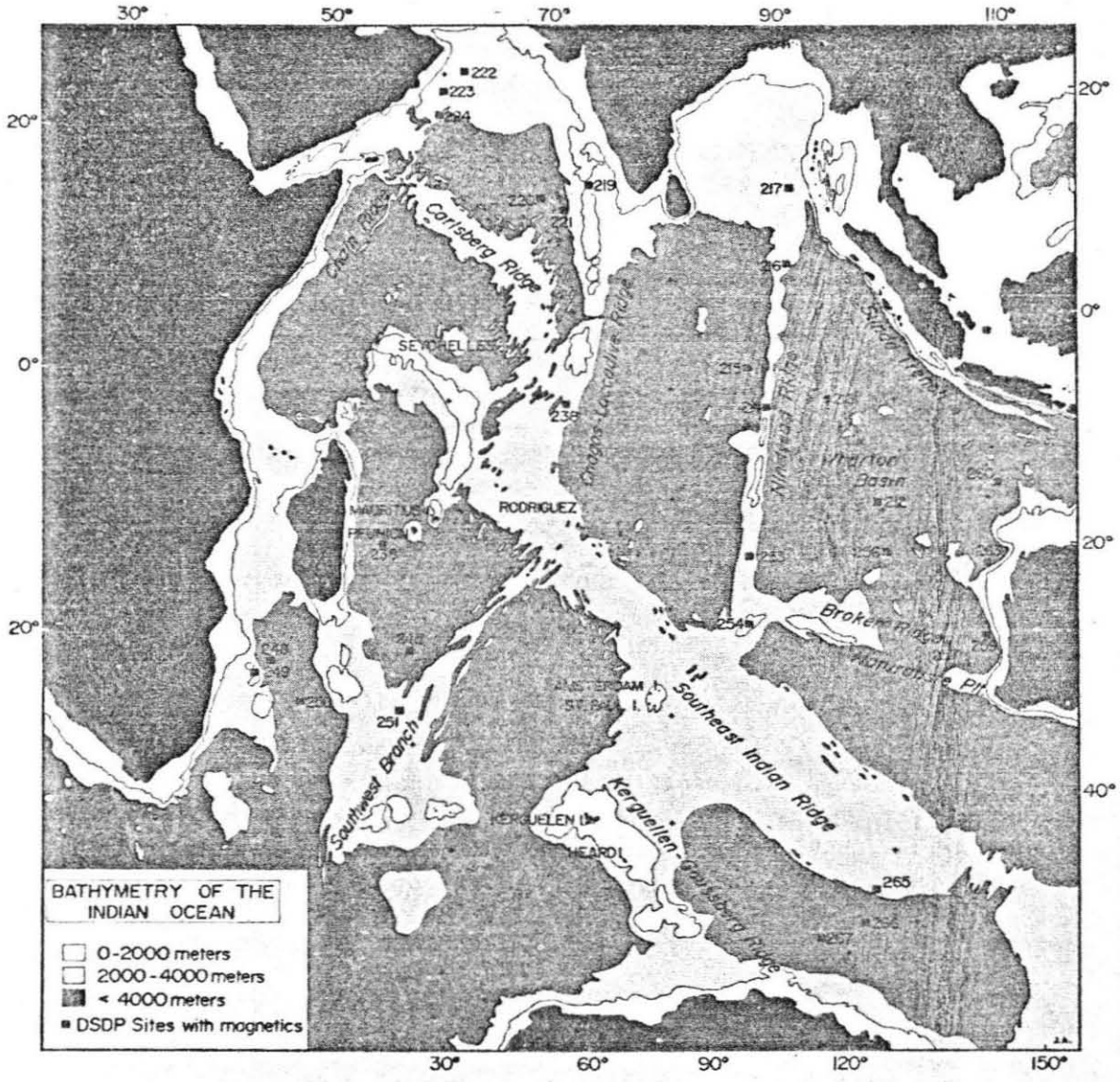

Figure 1.1 Generalized bathymetry of the Indian Ocean, after Peirce [1978]. The Chagos-Laccadive and Ninetyeast Ridges appear as bathymetric highs, as do the other aseismic ridges: the Mascarene Plateau (near the Seychelles), Broken Ridge, and the Kerguelen-Gaussberg Ridge.

the Ninetyeast and Chagos-Laccadive Ridges, played a crucial role in the evolution of the Indian Ocean. Both were associated, in a complex and poorly understood fashion, with gigantic transform faults, thousands of kilometers in length, which divided the Indian Ocean into three plates. The central plate, including the Indian subcontinent, moved north from the time of the breakup of the southern continents [Dietz and Holden, 1970] until its collision with India. The motion along the Ninetyeast transform is described by Sclater and Fisher [1974], and that on the Chagos Fracture Zone by Fisher et al. [1971]. This process was quite unusual in that transform faults, whose length is usually invariant, somehow lengthened themselves.

The association of the two topographically high ridges with these ancestral transform faults is perplexing, and has been the subject of great controversy. It is generally agreed that these ridges are volcanic in origin, although the Chagos Ridge now is coral-topped and appears above the ocean surface in several island groups. Models for the formation of these ridges include extrusion of material at the junction of the ridge and transform [Sclater and Fisher, 1974], hot spot traces [Peirce, 1978; Luyendyk and Rennick, 1977], and extrusion of material along the entire transform fault length (a "leaky" transform).

This work will focus not on the evolution of these features, but instead on their present day tectonics. It has been customary to assume that these ridges are not active features, and play no role in the present day tectonics of the Indian Ocean. Little attention has been paid to the earthquakes associated with these structures.

The World Wide Standardized Seismograph Network provides adequate coverage of even magnitude 5 events in the Indian Ocean. The station configuration used in the study of the Chagos Bank events is shown in Figure 1.2. Coverage, of course, is much worse for the pre-1963 earthquakes, as most useful stations were in Europe or Australia and New Zealand. Nonetheless, it is possible to determine the mechanisms of some of the older events.

This analysis shows that the Ninetyeast Ridge is still an active zone of deformation within the plate, along which substantial relative motion is taking place. The Chagos-Laccadive Ridge, though far less active, shows unusual seismicity in its southern portion. The seismicity on both ridges differs substantially from any previously discussed in ocean basins. Both features should still be regarded as active today, though they do not fit into the classic ridge-transform-trench classifications.

Chapter 2 is in press in the Journal of Geophysical Research [Stein and Okal, 1978]. Chapter 3 is in press in the Geophysical Journal [Stein, 1978].

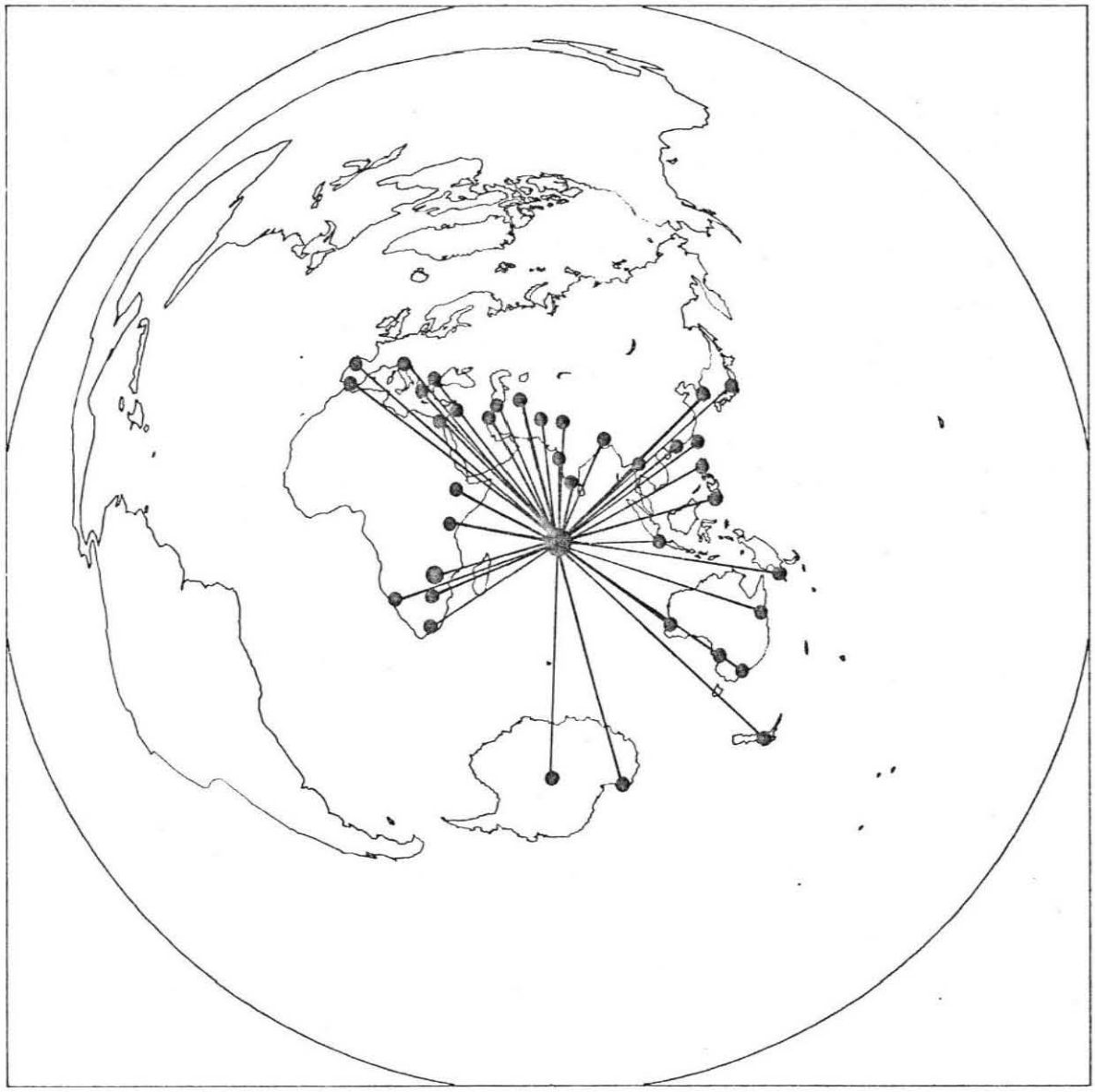

Figure 1.2. Stations used in the study of the Chagos Bank earthquakes. (Not all stations recorded all events, as can be seen by comparison with Figure 3.6.)

REFERENCES

Ben Avraham, Z and E. T. Bunce, Geophysical study of the Chagos-Laccadive Ridge, Indian Ocean, J. Geophys. Res., 82, 1295-1305, 1977.

Davies, T. A. et al., Initial Reports of the Deep Sea Drilling Project, vol. 26, U. S. Government Printing Office, Washington, D.C., 1974.

Dietz, R. S. and J. C. Holden, Reconstruction of Pangea: Breakup and dispersion of continents, Permian through present, J. Geophys. Res., 75, 4939-4956, 1970.

Fisher, R. L., J. G. Sclater and D. P. McKenzie, Evolution of the Central Indian Ridge, Western Indian Ocean, Bull. Geol. Soc. Amer., 82, 553-562, 1971.

Fisher, R. L. et al., Initial Reports of the Deep Sea Drilling Project, vol. 24, U. S. Government Printing Office, Washington, D.C., 1974

Laughton, A. S., D. H. Mathews and R. L. Fisher, The structure of the Indian Ocean, in The Sea, vol. 4, part 2, ed. A. E. Maxwell, Interscience, New York, 543-586, 1971.

Luyendyk, B. P. and W. Rennick, Tectonic history of aseismic ridges in the eastern Indian Ocean, Bull. Geol. Soc. Amer., 88, 1347-1356, 1977.

McKenzie, D. and J. G. Sclater, The evolution of the Indian Ocean since the Late Cretaceous, Geophys. J. Roy. Astr. Soc., 25, 437-528, 1971.

Peirce, J. W., The northward motion of India since the Late Cretaceous, Geophys. J. Roy. Astron. Soc., 52, 277-311, 1978.

Sclater, J. G. and R. L. Fisher, The evolution of the east central Indian Ocean, with emphasis of the tectonic setting of the Ninetyeast Ridge, Bull. Geol. Soc. Amer., 85, 683-702, 1974.

Stein, S., An earthquake swarm on the Chagos-Laccadive Ridge and its tectonic implications, Geophys. J. Roy. Astron. Soc., in press, 1978.

Stein, S. and E. A. Okal, Seismicity and tectonics of the Ninetyeast Ridge area: Evidence for internal deformation of the Indian plate, J. Geophys. Res., in press, 1978.

Von der Borch et al., Initial Reports of the Deep Sea Drilling Project, vol. 22, U. S. Government Printing Office, Washington, D.C., 1974.

Whitmarsh, R. G. et al., Initial Reports of the Deep Sea Drilling Project, vol. 23, U. S. Government Printing Office, Washington, D.C., 1974.

Chapter 2

SEISMICITY AND TECTONICS OF THE NINETYEAST RIDGE AREA: EVIDENCE FOR INTERNAL DEFORMATION OF THE INDIAN PLATE

ABSTRACT

The Ninetyeast Ridge, far from being "aseismic", has historically been a region of substantial seismicity. Since 1913 four magnitude 7 or greater earthquakes (including one with M_S = 7.7) and ten magnitude 6 events have occurred in this general area. The mechanisms of several of these earthquakes suggest that the Ninetyeast Ridge area is presently a complex zone of deformation within the Indian plate. The northern portion (3°N-10°S) of the ridge is the active seismic zone, where both vertical and strike-slip motion occur, while further south the ridge is far less seismic. This transition roughly coincides with a change in the ridge's morphology from irregular *en échelon* blocks to a smooth flat-topped high. The strike-slip motion is left-lateral, which is consistent with the Indian (west) side encountering resistance due to the collision with Asia while the Australian (east) side is subducting smoothly at the Sumatra trench. South of about 9°S the style of deformation differs on the two sides of the ridge. To the east normal faulting occurs, which may be related to the formation of graben-like structures. To the west the topography can be interpreted as the result of NW-SE compression which takes place largely aseismically, but is observed for one large earthquake. This significant intraplate deformation may explain the difficulties that occur in attempts to close the India-Africa-Antarctica triple junction using a rigid Indian plate.

INTRODUCTION

The Ninetyeast Ridge in the eastern Indian Ocean is a long, linear feature extending from about 9°N to about 31°S. Its northern portion separates the thick sediments of the main Bengal fan from its eastern lobe, the Nicobar fan [Curray and Moore, 1974]. In this region (extending to about 7°S) the ridge is broken up into a complex series of *en échelon* blocks, while further south the ridge is straight and flat-topped [Sclater and Fisher, 1974]. The east side of the ridge is bordered by a fracture zone and a complex of ridges and graben-like troughs approximately parallel to the ridge [Bowin, 1973]. West of the ridge (and south of 7°S) a complex terrain composed of north-east trending ridges and deeps appears, along with a broad bathymetric high (15°S, 87°E) named Osborne Knoll by Sclater and Fisher [1974]. An air gun profile across the ridge [Veevers, 1974] showing the ridge, fracture zone and graben is shown in Figure 2.1.

Since the Ninetyeast Ridge's true extent was recognized during the International Indian Ocean expedition (1960-1965), its origin and nature have been subjects of intense discussion. It has been interpreted alternately as a horst [Francis and Raitt, 1967], as the result of over-thrusting [Le Pichon and Heirtzler, 1968], as a hot spot trace [Morgan, 1972], as due to localized emplacement of gabbro [Bowin, 1973] and as a volcanic pile generated at the intersection of a ridge crest and a transform fault [Sclater and Fisher, 1974]. Sclater and Fisher showed that magnetic anomalies to the west of the ridge age to the north, while to the east they age to the south. Their anomaly identifications are shown in Figure 2.2. They also found that the ridge

was attached to the Indian plate and bounded by a transform fault to the east during the Tertiary. The reason for the ridge's elevation above the ocean floor is also in dispute. Sclater and Fisher [1974] and Detrick et al. [1977] show that the ridge is subsiding at the normal rate for oceanic crust and is thus not an actively maintained feature. Paleontological studies of DSDP cores [Luyendyk and Davies, 1974] show that the ridge was formed at or above sea level, and the paleomagnetic data [Cockerham et al., 1975; Peirce, 1978] indicate that the ridge was formed at a high southern latitude. Models involving one [Peirce, 1978] or two [Luyendyk and Rennick, 1977] hot spots have been proposed to fit this data and explain the origin of the ridge. Sclater and Fisher [1974] suggested that motion along the Ninetyeast Ridge ended at least by 40 m.y.b.p. (anomaly 17), and that, since then, the Indian and Australian plates have been acting as a single plate. This chronology is shown in Figure 2.3.

Recently Eguchi et al. [1978] tentatively identified anomalies 12 and 13 nearer to the Sumatra trench, implying that relative motion continued at least until 35 m.y.b.p.

Whatever the way it may have formed, the Ninetyeast Ridge is generally considered to be a dormant, fossil feature in the middle of a quiescent Indian plate. It is frequently cited as a prototype aseismic ridge, where the aseismic ridges are a group of topographically high features which are not spreading ridges. Such features are especially common in the Indian Ocean (Chagos-Laccadive Ridge, Broken Ridge), but occur in the other oceans as well (e.g., Walvis Ridge in the South Atlantic). All are aseismic in the sense

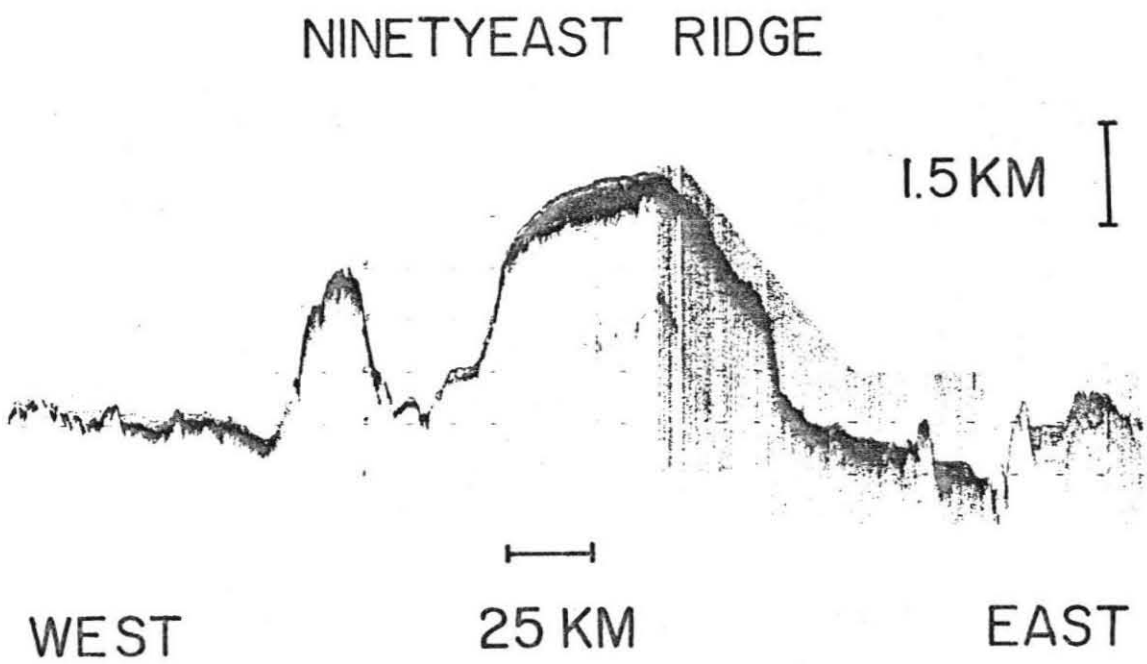

Figure 2.1. Air gun profile across the Ninetyeast Ridge (GLOMAR CHALLENGER, leg 22) from east to west. Note the steep graben with only a hundred meters of sediment fill, the 1200 meter high east scarp of the ridge, and the sediment cap on the ridge. The peak to the west is an isolated seamount.

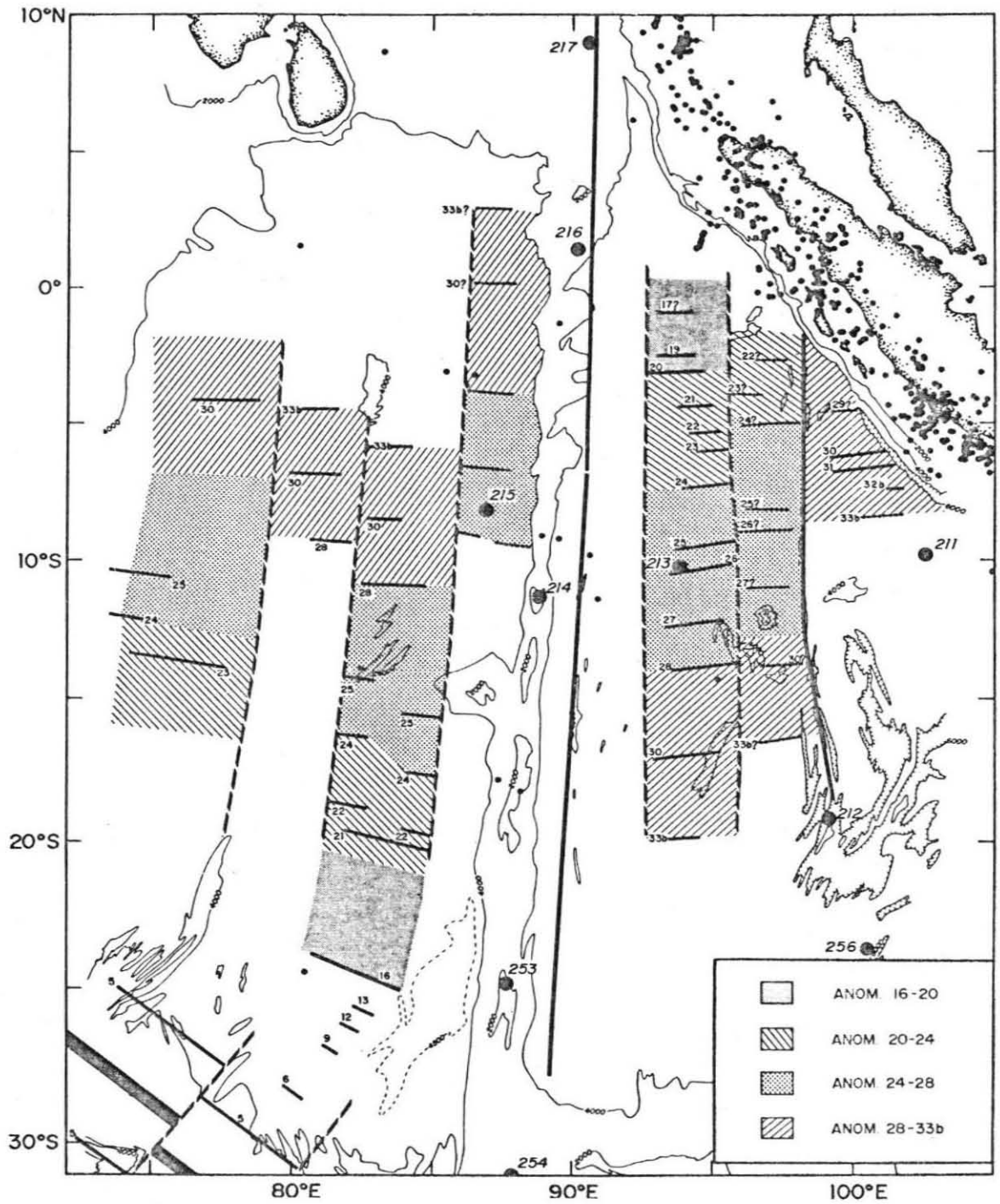

Figure 2.2. Magnetic anomalies in the Ninetyeast Ridge area from Sclater and Fisher [1974]. DSDP drill sites (numbered) are also indicated. Anomaly 32 is about 78 m.y.b.p., anomaly 24 is about 60 m.y.b.p., and anomaly 17 is about 43 m.y.b.p. [Heirtzler et al., 1968]. The proposed Ninetyeast transform fault is marked by the heavy line, separating anomalies which age to the north from those which age to the south.

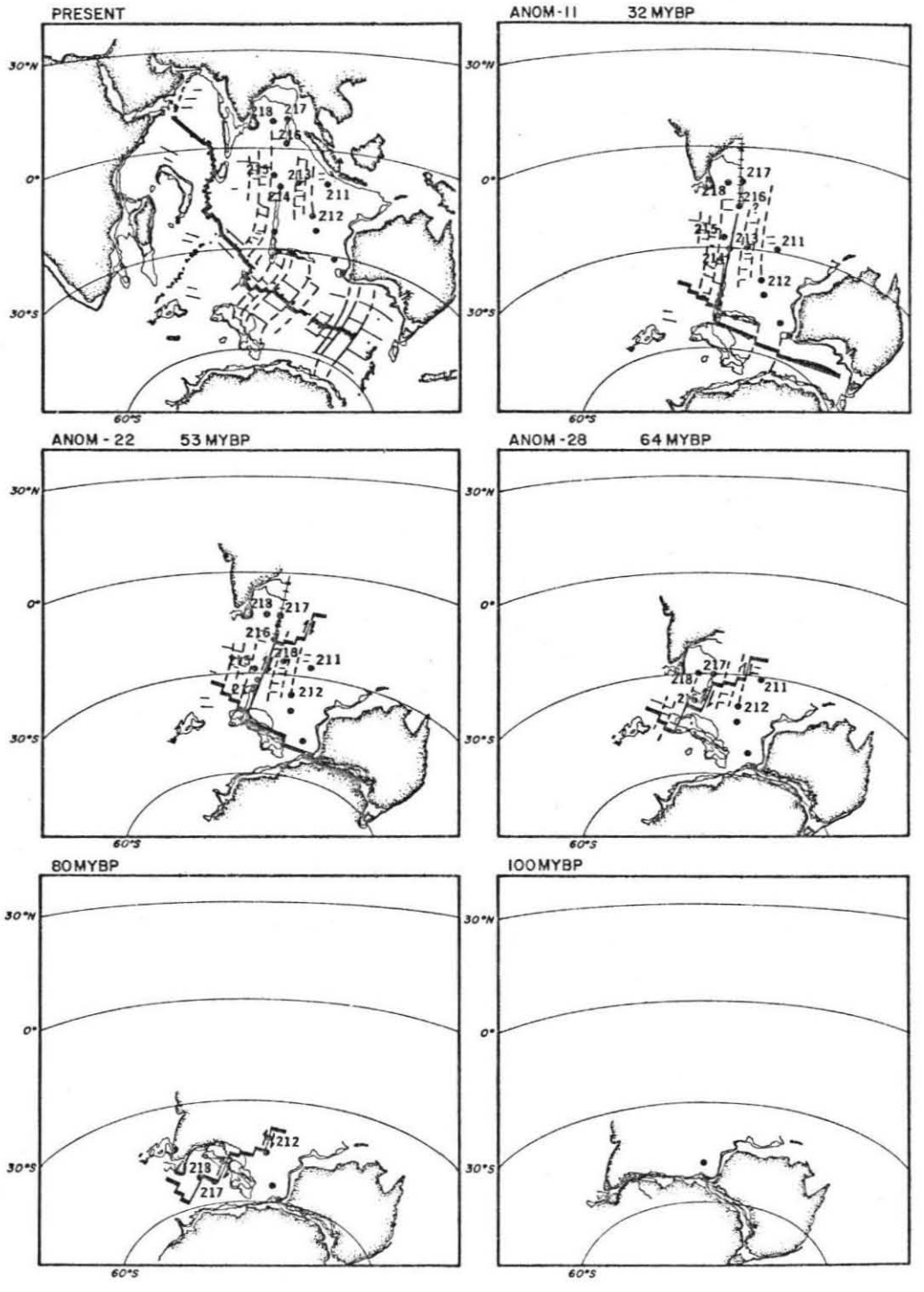

Figure 2.3. Reconstruction [Sclater and Fisher, 1974] of the relative positions of India, Australia and Antarctica from Early Cretaceous (100 m.y.b.p.) to present time. Numbered dots are DSDP drill sites. By 32 m.y.b.p. relative motion along the Ninetyeast transform fault had ended.

that they do not show the many small earthquakes that make spreading ridges stand out on the recent (1974-1970) seismicity maps.

In a broader sense, when large earthquakes over a long period of time are considered, the Ninetyeast ridge is not aseismic, but a rather seismic zone: historically, this area is far more seismic than any spreading ridge, and, in fact, comparable in seismicity to large transform fault systems, such as the San Andreas fault. Only subduction zones are areas of greater total seismic activity, in terms of the number of large earthquakes.

Given this high level of seismicity, the area is either a zone of major intraplate deformation, or an active plate boundary. The tectonics of this area are investigated by studying the mechanisms of three magnitude 7 and three magnitude 6 earthquakes in this area. Although three of these occurred many years ago (1928, 1939, 1955) and are thus difficult to study, it is possible to extract enough information to learn a great deal about the tectonics of the area. The seismological results are discussed in detail in the following three sections.

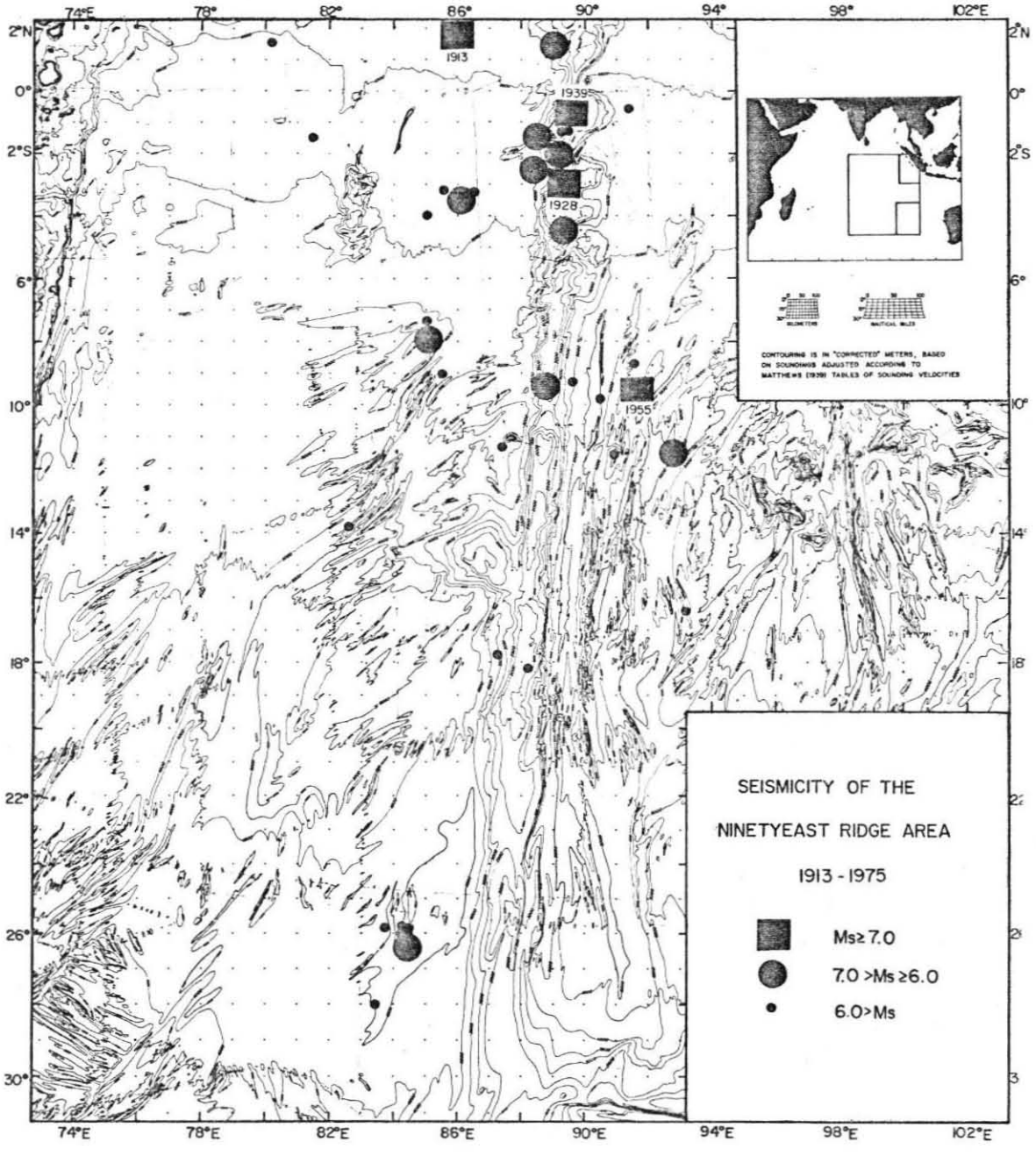

Figure 2.4. Seismicity of the Ninetyeast Ridge area (Table 2.1) plotted on the bathymetric map of Sclater and Fisher [1974]. Earthquakes are divided into three groups based on surface wave magnitude (M_S).

SEISMICITY OF THE NINETYEAST RIDGE AREA

The Ninetyeast Ridge is not "aseismic", as easily demonstrated by the U.S.G.S. World Seismicity map [Tarr, 1974] which includes an event labelled "9 March 1928 (8.1)" at about 3°S, 89°E. Gutenberg and Richter's Seismicity of the Earth [1965], covering earthquakes from 1899 to 1952, shows several large events in this area. They state (p. 78):

> "A peculiarly isolated group of shocks occurs near 2°S, 89°E . . . with other epicenters near 90°E north of the equator, there is suggested a minor seismic belt following imperfectly known rises and ridges roughly north and south."

The seismicity of this area is also discussed by Stover [1966], Rothé [1969], and Sykes [1970].

Using these sources, the worldwide magnetic tape catalogue of epicenters, the "Earthquake Notes" section of the Bulletin of the Seismological Society of America and the International Seismological Summaries (ISS) (1918-1963) the seismicity list in Table 2.1 was compiled. Since 1913, in the region from 80°E to 95°E and 5°N to 30°S (excluding the Sumatra trench) there have been four magnitude (M_S) 7, ten magnitude 6, and at least 26 smaller earthquakes. The epicenter tape often does not include small ($M_S < 6$) events prior to 1950, for example the aftershocks of the 1928 earthquake. In comparison, earthquakes along the midocean ridges almost never exceed surface wave magnitude 7, except infrequently on long transform faults [Gutenberg and Richter, 1965; Burr and Solomon, 1978].

A more useful comparison with Table 2.1 is to consider the entire Southern California fault system north of the Mexican border

Table 2.1

SEISMICITY OF THE NINETYEAST RIDGE AREA

Date	Origin Time	Latitude	Longitude	M_s	m_b	Remarks
$M_s \geq 7.0$						
January 19, 1913	17:05.6	2°N	86°E	7.0		GR
March 9, 1928	18:05:20	2.7°S	88.7°E	7.7		location SO, magnitude GR
March 21, 1939	01:11:12	0.9°S	89.5°E	7.2		location SO, magnitude GR
March 22, 1955	14:05:07	8.8°S	91.7°E	7.0		location SO, magnitude G
M_s = 6.0 to 7.0						
May 9, 1916	14:33:07	1.5°N	89°E	6.3		GR
April 13, 1918	00:51:15	8°N	85°E	6.5		GR
May 28, 1923	01:25:53	1.5°S	88.5°E	6.5		GR
January 18, 1926	21:07:23	2°S	89°E	6.75		GR
February 7, 1928	00:01:43	2.6°S	88.5°E	6.75		location SO, magnitude GR
January 23, 1949	06:31:04	11.6°S	92.8°E	6.75		location SO, magnitude G
September 1, 1950	02:46:55	4.5°S	89.25°E	6.0		GR
May 25, 1964	19:44:07	9.1°S	88.9°E	6.0	5.5	location CGS, magnitude UPS

Table 2.1 (continued)

Date	Origin Time	Latitude	Longitude	M_s	m_b	Remarks
M_s = 6.0 to 7.0 - continued						
October 10, 1970	08:53:05	3.6°S	86.2°E	6.2	5.9	location CGS, magnitude PAS
June 25, 1974	17:22:19	26.1°S	84.3°E	6.6	6.2	GS
M_s < 6.0						
January 13, 1936	18:10:16	4°S	85°E			GR
January 25, 1951	16:35:36	1.5°S	81.5°E			ISS
June 21, 1953	23:58:30	0.5°S	91.4°E			ISS
November 28, 1953	23:11:08	16.6°S	93.1°E			ISS
March 23, 1955	04:54:33	8.7°S	91.6°E			ISS
July 29, 1956	07:13:44	9.0°S	85.5°E			CGS
June 26, 1957	02:47:37	7.3°S	85.0°E			ISS
January 11, 1964	10:23:11	11.4°S	90.9°E			CGS
June 11, 1964	17:51:51	9.2°S	89.5°E			CGS
November 29, 1966	09:21:23	9.8°S	90.6°E		5.0	CGS
April 23, 1967	15:01:06	1.6°N	80.2°E		5.2	CGS
April 26, 1967	13:11:42	1.3°S	89.4°E		5.0	CGS

Table 2.1 (continued)

Date	Origin Time	Latitude	Longitude	M_S	m_b	Remarks
M_S < 6.0 - continued						
February 9, 1968	20:46:44	13.9°S	82.4°E		5.1	CGS
September 14, 1968	01:25:19	24.5°S	80.4°E		5.5	CGS
November 26, 1968	06:08:57	3.2°S	86.5°E			CGS
December 14, 1968	11:43:14	3.1°S	85.5°E		5.1	CGS
January 3, 1969	03:56:59	18.2°S	88.1°E		5.3	CGS
February 14, 1969	06:14:53	17.8°S	87.3°E		5.3	CGS
December 3, 1972	17:58:56	11.3°S	87.5°E		5.3	ERL
December 14, 1972	20:49:35	1.3°S	89.3°E		5.4	ERL
October 29, 1978	07:07:36	28°S	83.4°E			GS
June 25, 1974	18:31:36	25.8°S	84.2°E		5.3	GS
June 26, 1974	05:59:25	26.0°S	84.3°E		4.8	GS
June 26, 1974	09:07:26	26.0°S	84.1°E			GS
June 28, 1974	08:45:44	25.8°S	83.8°E		5.4	GS
August 28, 1975	18:25:44	25.9°S	84.2°E		5.4	GS

Table 2.1 (continued)

KEY

SO	This study	NOS	National Ocean Survey
GR	Gutenberg and Richter	GS	U. S. Geological Survey
G	Gutenberg notepads	ERL	Environmental Research Laboratories
CGS	Coast and Geodetic Survey	ISS	International Seismological Summary

[Allen et al., 1965], including many faults in addition to the San Andreas, since 1912. Adding the Borrego Mountain and San Fernando earthquakes to bring their list up-to-date, there have been eighteen events with $M_S > 6$, and two with $M_S > 7$. Thus, in terms of moderate and large earthquakes, the Ninetyeast Ridge (though a much larger area) is approximately as seismic as Southern California. (Smaller earthquakes in the central Indian Ocean are far less likely to be detected than those on land.)

A number of difficulties are involved in preparing a seismicity list such as Table 2.1. Clearly, the older earthquakes are subject to errors in location. Gutenberg and Richter [1965] state that "location of even large shocks in this area is often difficult" due to the lack of nearby stations. As discussed later, several of the larger events were relocated. This shows (as did Gutenberg and Richter) that these events are definitely not in the Sumatra trench, the only other nearby region of high seismicity. Stover [1966] also relocated many of these events and determined that they were not associated with the trench. The locations in the table are from a variety of sources. Some (including three of the largest events) were relocated for this study. Otherwise, the Gutenberg-Richter location (for events prior to 1952) was used in preference to the ISS location. Since 1952, the locations used are from the appropriate government agency or the International Seismological Center (or Summary).

The magnitude of these events is also a complicated issue, as magnitude is an often quoted but frequently ill-defined number. In

the table we divide the earthquakes by surface wave magnitude into three groups: $M_S \geq 7$, $6 \leq M_S < 7$ and $M_S < 6$. This last group ("garbage earthquakes") also includes those for which no surface wave magnitude was determined as they are almost certainly smaller than 6.

The determination of magnitude for historic earthquakes has been examined in detail by Geller and Kanamori [1977]. They show that the Gutenberg-Richter (GR) magnitudes given in Seismicity of the Earth are essentially equivalent to the modern twenty-second surface wave magnitude, but that the "revised magnitude" frequently used is on the average 0.22 magnitude units higher. For example, the March 9, 1928 earthquake has a GR magnitude of 7.7 and a revised magnitude (shown on the U.S.G.S. map) of 8.1. For earthquakes after 1952 (when Seismicity of the Earth ends), and before 1958, it is sometimes possible to find the GR magnitude by examining Gutenberg and Richter's original worksheets which are still available at Caltech. The March 22, 1955 event, for example, has a GR magnitude of 7.0, although Rothé [1969] quotes the revised magnitude of 7.1.

The earthquakes in Table 2.1 are plotted in Figure 2.4 on the bathymetric map of Sclater and Fisher [1974]. Despite the uncertainty in locations (discussed later) a number of patterns are evident. The seismicity, especially the large events, trends roughly north-south along the ridge. A large number of the earthquakes, including two of the largest, fall on the ridge itself. Many of the others are within a few degrees of the ridge. The large (M_S = 7 and 6) events are especially prone to be near the ridge. (Two of those farthest from the ridge are the poorly located 1913 and 1918 earthquakes.) There is

also a noticeable concentration of events north of 10°S -- all magnitude 7 and eight of ten magnitude 6 events fall there. With the exception of the group of 1974 earthquakes at about 26°S (discussed in detail later) seismicity tends to occur north of 10 to 12°S. As earthquakes of this size further south on the Southeast Indian Ridge are detected (as were the small aftershocks of the 1974 event), it seems that this is not an artifact of the seismic detection capability. There is also a suggestion that, of the events not on the ridge, more occur on the west side than on the east side. A later section attempts to relate these patterns to the bathymetry and tectonics of the area.

EARTHQUAKE RELOCATIONS

Five of the largest earthquakes in the area (three magnitude 7 and two 6) were relocated for several reasons. The primary concern was to show that these events are unlikely to be in the Sumatra trench. This also tests the published GR or ISS locations, which, before the era of computers, were obtained by a graphical technique [Richter, 1958]. In addition this may constrain the depth of these events, as focal depth is important for our surface wave investigations [Tsai and Aki, 1970] as well as for tectonic purposes.

As it was possible to collect only a small fraction of the original records, the arrival times published in the International Seismological Summaries for stations at distances less than 90° were used. The ISS location and origin time were used as starting models. Locations were calculated using a standard location program and a Jeffreys-Bullen travel time table.

The general procedure followed that of Kanamori and Miyamura's [1970] study of the 1923 Kanto earthquake. After the first iteration, all stations with travel time residuals greater than thirty seconds were suppressed. At this point the focal depth was then fixed at a series of depths, and the root mean square residual was calculated for each location. The same procedure was then repeated after deleting all stations with residuals greater than ten seconds.

The results are shown in Figure 2.5. For each of the five events the RMS residual is plotted as a function of focal depth, for locations done after removing residuals greater than thirty and then ten seconds. The figure also shows the number of stations used, and their azimuthal distribution by quadrants. Unfortunately, the southern quadrants have very few stations, even today (see the focal mechanism for the 1974 event, Figure 3).

For all events the RMS residual decreased as the source is placed at shallower depths. The results are much better for the ten-second case. Except for the 1955 event (where the change is too small to be significant) this can be interpreted as evidence of a shallow (less than ten kilometers) focal depth. This is in general accord with Burr and Solomon's [1978] result that transform fault earthquakes tend to occur at shallow depths.

The final locations and origin times for a five-kilometer focal depth are given in Table 2.1. The epicenters were quite stable with respect to changes in focal depth, and in general differed only slightly (usually less than 0.5°) from the ISS (or GR) locations. For example, the March 9, 1928 location is given by the ISS as 2.3°S, 88.5°E;

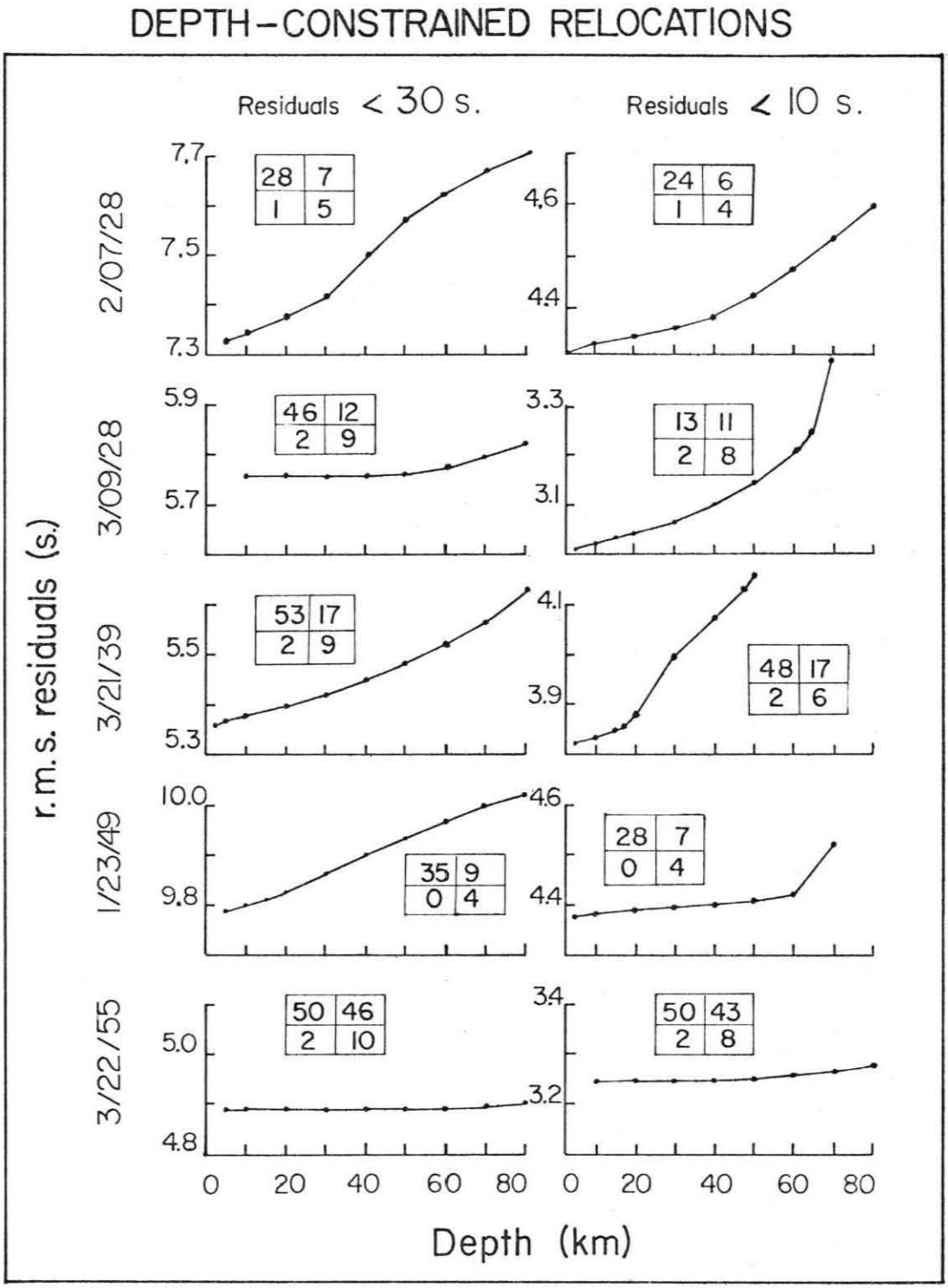

Figure 2.5. Root-mean-square travel-time residuals as a function of constrained depth during relocation of five large earthquakes in the Ninetyeast Ridge area. Left: relocation after deleting all stations with residuals greater than 30 sec. Right: relocation after deleting stations with residuals greater than 10 sec. In each plot, the figures inside the box give the number of stations used in each azimuthal quadrant.

by GR as 2.5°S, 88.5°E, and by relocation as 2.6°S, 88.6°E. Similarly the ISS located the 1955 event at 8.6°S, 91.6°E, the Gutenberg notepads give 9°S, 91.7°E, and the relocation yielded 8.8°S, 91.7°E. For smaller (or older) earthquakes the locations have greater uncertainties due to the small number of stations available. For example the 1918 earthquake was recorded by 40 stations, of which only 26 reported P-times. Gutenberg's location was 8°S, 85°E, in contrast to the ISS's 5°S, 85°E, so the uncertainty is rather large. In contrast, the 1928 main shock was recorded by 121 stations, and the 1939 one by 147. For very old events, such as 1918, when only a small number of stations were available, it appeared that no useful information would result from a relocation.

SOURCE MECHANISM STUDIES

The source mechanisms of two large earthquakes (March 21, 1939, M_S = 7.2; March 22, 1955, M_S = 7.0) and one recent, smaller event (June 25, 1974, M_S = 6.6) were studied. Study of the 1974 event, given the availability of records from many WWSSN stations, followed the general methods of Kanamori [1970a, 1970b]. The older events, for which only small numbers of records could be compiled, were studied using techniques similar to those of Kanamori [1970c] and Okal [1976; 1977].

For two of the older events (1939, 1955) a small fraction of the stations reported first motions, as well as times, to the ISS. Care must be taken in using these pre-WWSSN results, as Wickens and Hodgson [1967] showed that stations were in error a significant portion of the time. In first motion solutions any stations whose travel time

residuals exceeded ten seconds were deleted. In drawing planes heavy weight was given only to groups of stations which were internally consistent. Given these difficulties, and the small number of stations reporting, only one plane could be reliably constrained from the first motions. Surface wave data were used to determine the second plane and ensure the consistency of the plane derived from the first motions. Given the uncertainties in instrument response, only Love-to-Rayleigh wave amplitude ratios at single stations were used. Only for the 1974 event were amplitudes compared between different stations.

Unfortunately, it was not possible to reliably determine the mechanism of the 1928 M_S = 7.7 earthquake, the largest reported in this area. In the absence of recorded first motions, the small set of records available that were usable for surface wave study was not adequate to reliably constrain the solution.

The following sections discuss the mechanism of each event, using the fault parameters: strike (ϕ), dip (δ) and slip angle (λ) defined by Kanamori and Cipar [1974]. The seismic moments of two earthquakes whose mechanisms were discussed previously in the literature are also determined. Table 2.2 presents a summary of the results.

I. June 25, 1974 - M_S = 6.6

First motion readings from 25 WWSSN stations (Figure 2.6) clearly constrain one of the planes near ϕ = 242°, δ = 74°. The compressional readings both in Japan and in Eastern Africa limit the slip angle to the range 25 to 130°, thus restricting the strike-slip component along the constrained plane.

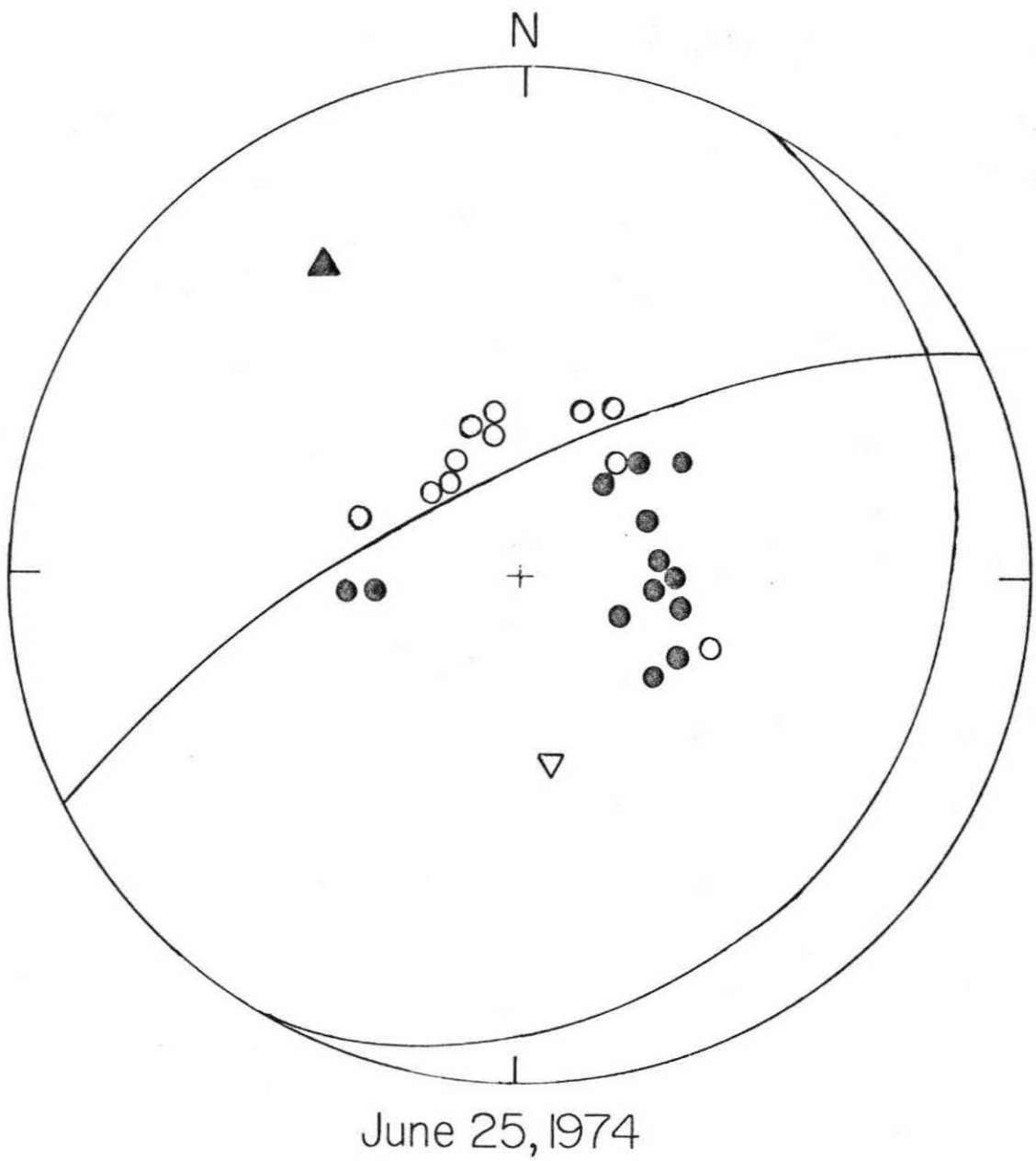

Figure 2.6. Lower focal hemisphere plot of first-motion data for June 25, 1974. Black dots are compressional, open dots dilational. The second plane was constrained from surface-wave data (see Figures 2.7 and 2.8). The black triangle is the compressional axis, the open one the tensional axis.

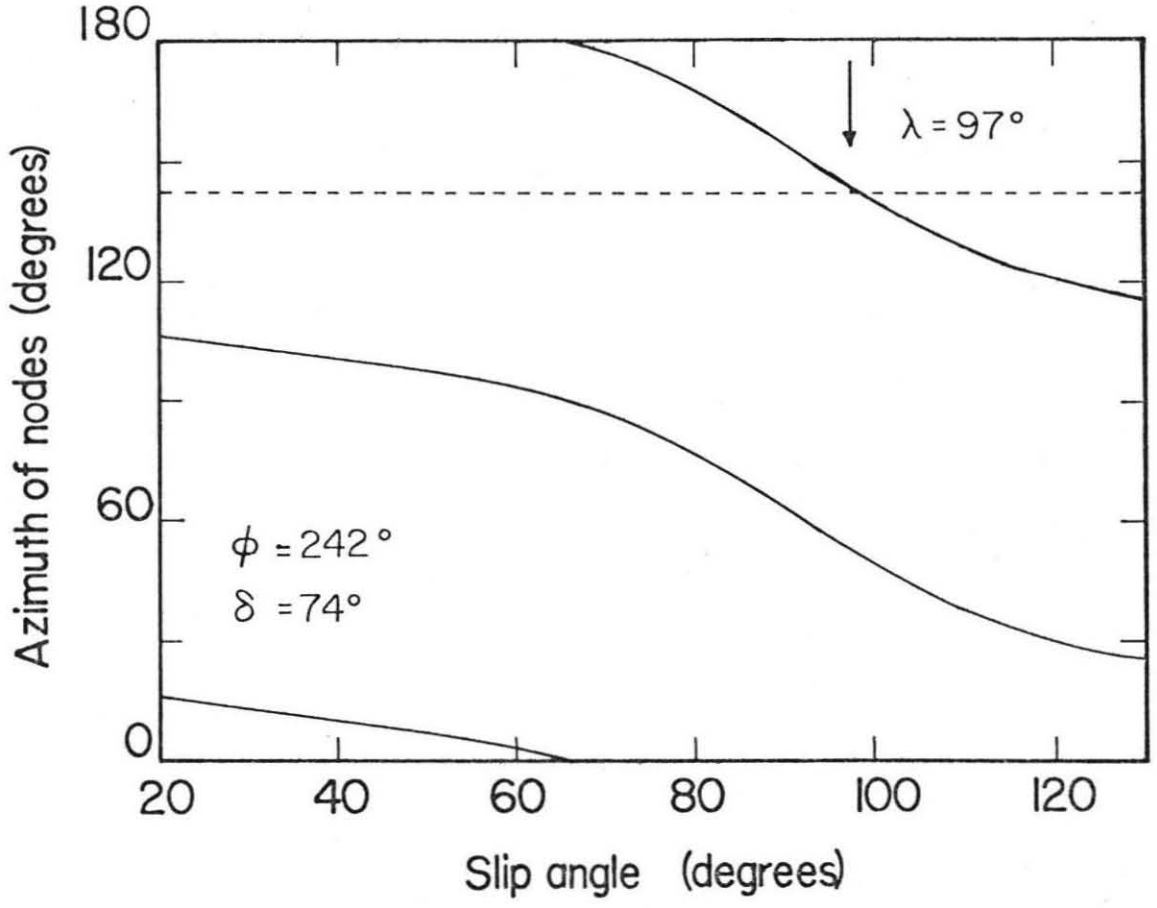

Figure 2.7. Azimuth of nodes in the long period Love wave radiation pattern as a function of slip angle along the fault plane constrained by first-motion data for June 25, 1974 (ϕ = 242°, δ = 74°). The dashed line is the observed node (see Figure 2.8).

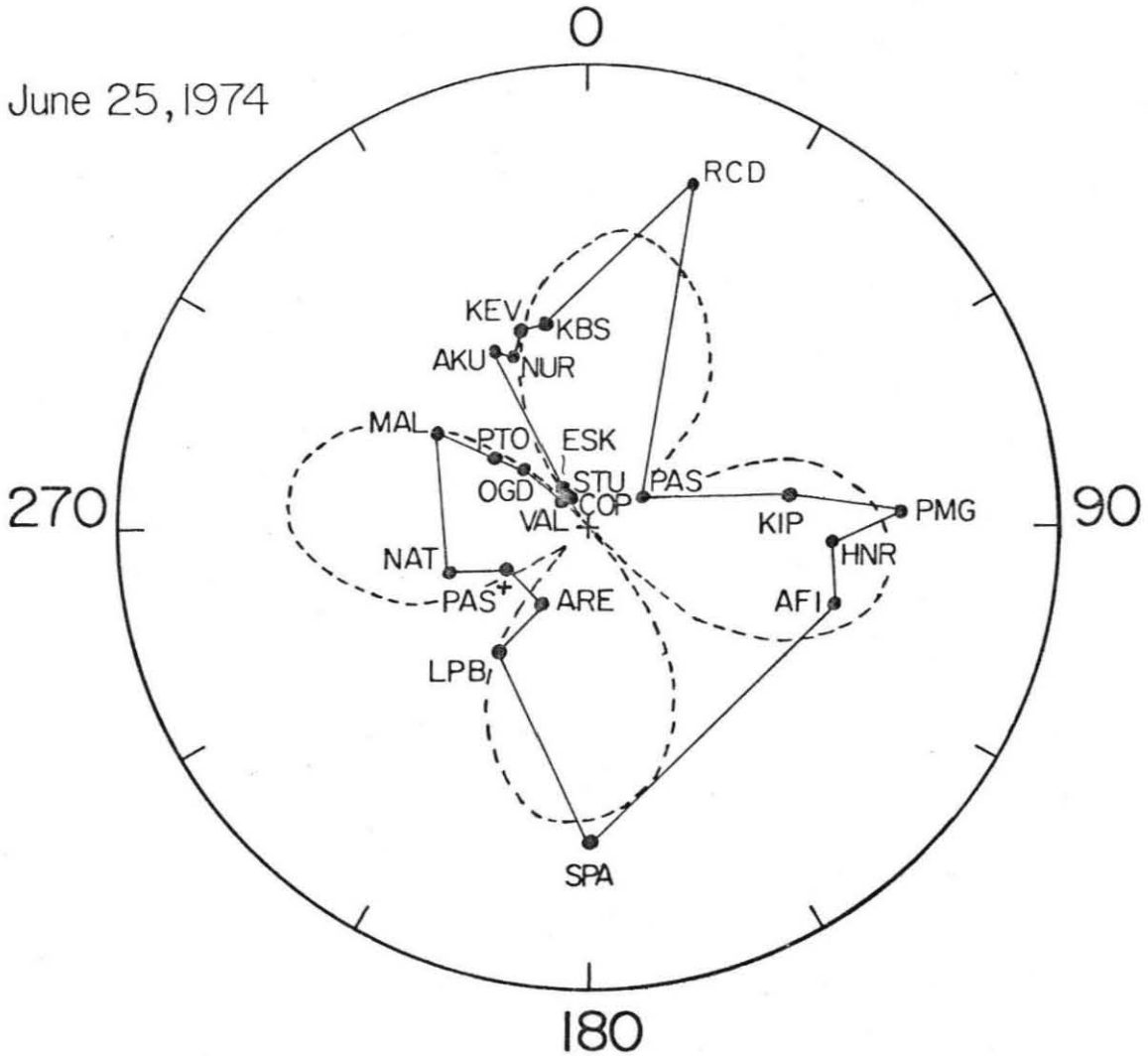

Figure 2.8. Radiation pattern of equalized Love waves (G_1) for June 25, 1974, at 21 stations, using the technique of Kanamori [1970a,b]. PAS^+ denotes G_2 equalized to G_1. This figure yields the azimuth of the main Love wave node as $\phi = 141°$, which constrains the slip angle to $\lambda = 97°$, as shown on Figure 2.7). The resulting theoretical radiation pattern is shown as a dashed line.

For this fault plane, Figure 2.7 shows the azimuthal distribution of the nodes in the Love wave radiation pattern as a function of slip angle. Equalized seismograms from 22 stations (Figure 2.8) exhibit a strong node at the European stations ESK, STU, COP and VAL, constraining the slip angle to 97° ± 3°. The mechanism of the earthquake can then be considered a nearly pure thrust along a steeply dipping NE-SW fault. The seismic moment obtained from the equalized records is 2.5×10^{25} dyne-cm.

II. March 22, 1955 - $M_S = 7.0$

As noted earlier by Sykes [1970], the available first-motion data do not totally constrain the focal mechanism. An additional, compressional reading was obtained from Lwiro, Zaire (LWI). Figure 2.9 shows that one plane has to lie somewhere between 233° ($\delta = 84°$) and 244° ($\delta = 80°$). The number of records suitable for a surface-wave analysis is actually rather small. Love-to-Rayleigh wave amplitude ratios were obtained at two stations: De Bilt, The Netherlands (DBN) and Resolute, Northwest Territories, Canada (RES), after low-pass filtering the records at both 30 seconds and 60 seconds. This considerably reduces the dependence of the Rayleigh wave excitation with depth [Tsai and Aki, 1970]. The resulting values for L/R are 4 at RES (station azimuth 1.9°) and 0.4 at DBN (station azimuth 321.8°). Comparison with the theoretical values shown on Figure 2.10 as a function of slip angle, yields $\lambda = 102°$ (modulo 180°). The solution compatible with first-motion data is then ($\phi = 244°$, $\delta = 80°$, $\lambda = -78°$), a predominantly normal event along a steep NE-SW fault. This solution

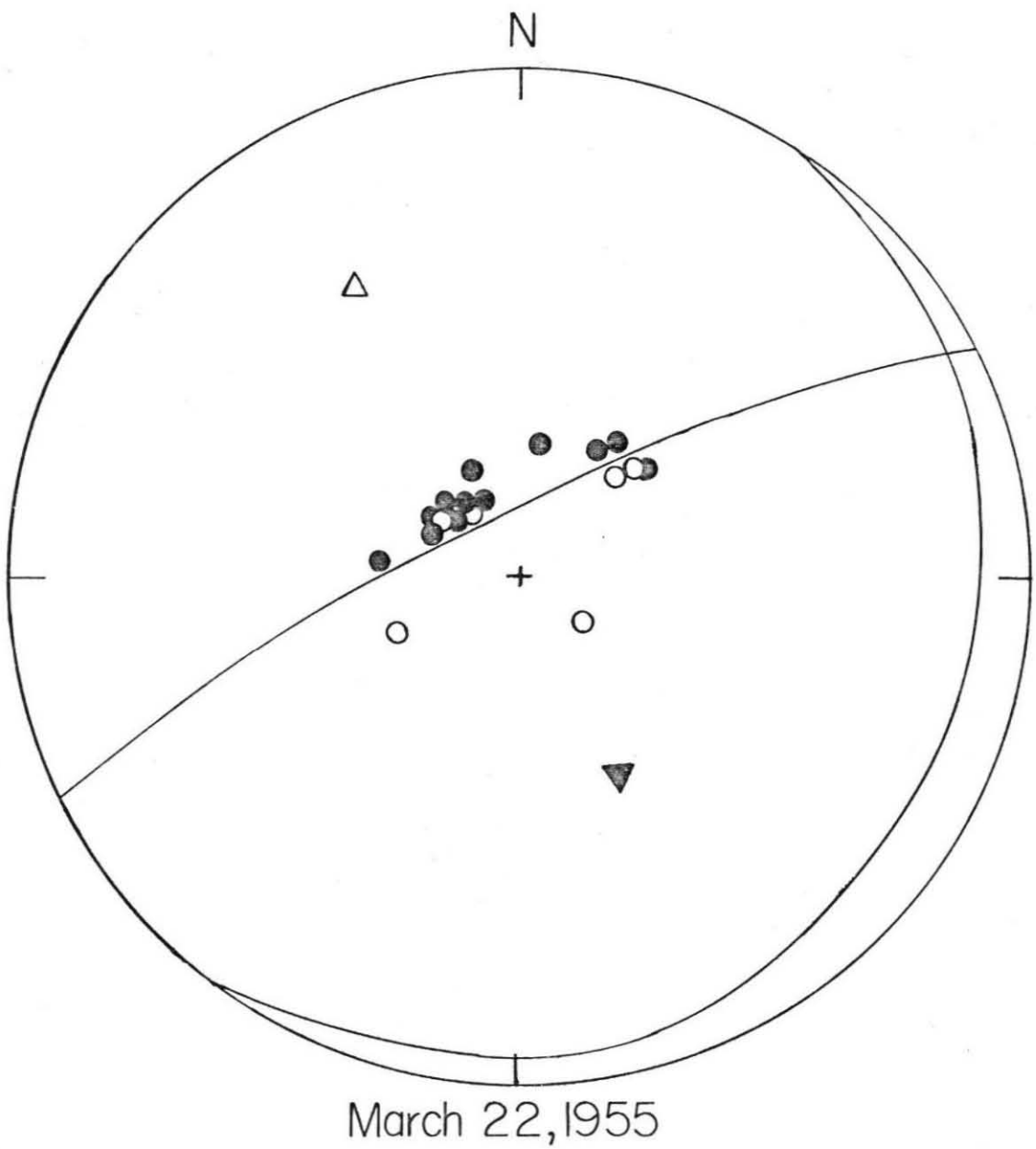

Figure 2.9. Lower focal hemisphere plot of first-motion data for March 22, 1955. Symbols as in Figure 2.6. The second plane was constrained by surface-wave data (see Figure 2.10).

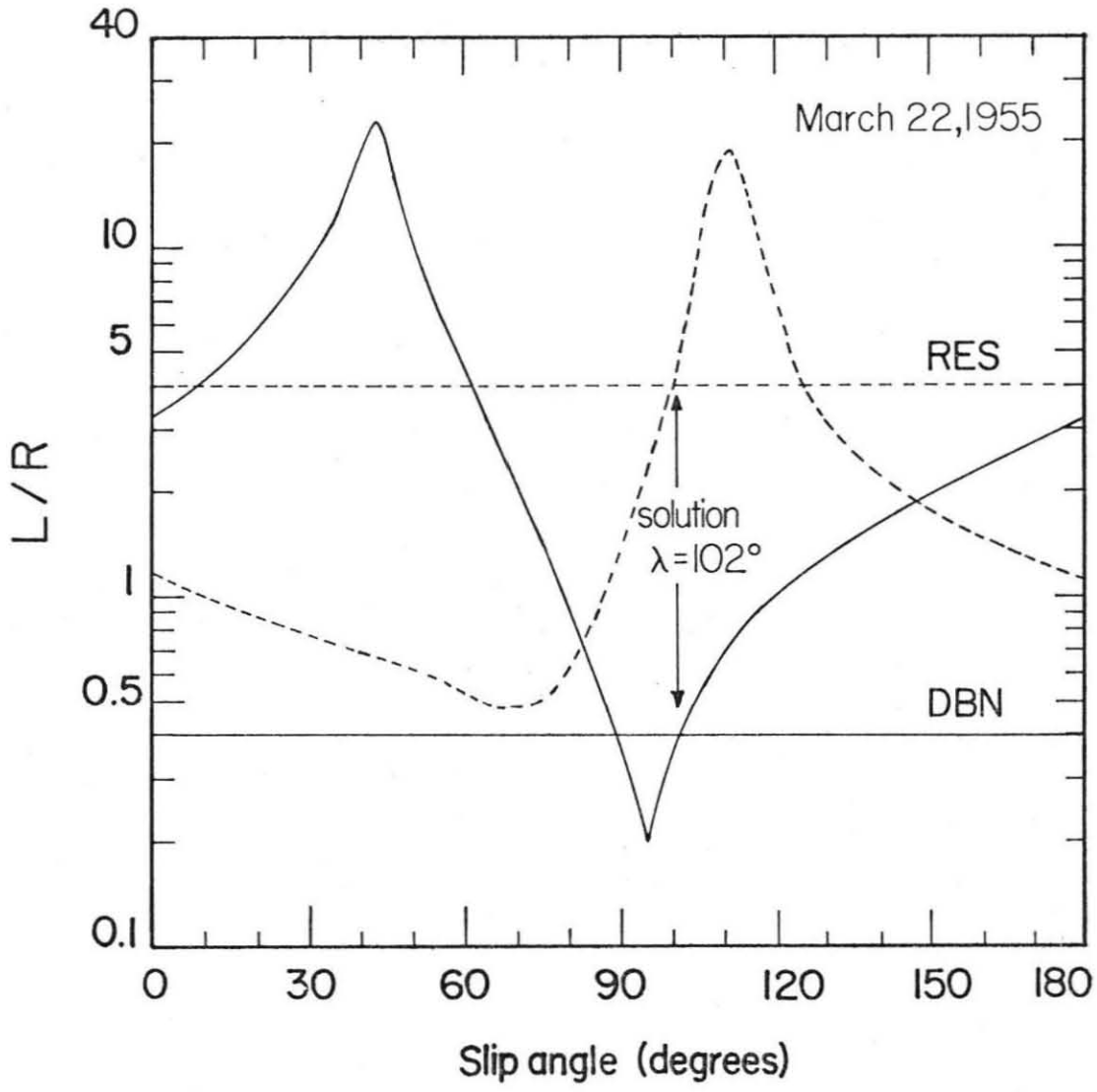

Figure 2.10. Theoretical ratio of long-period Love-to-Rayleigh wave amplitudes as a function of slip angle along the fault plane obtained from first-motion data for March 22, 1955 (ϕ = 244°, δ = 80°). The solid curve is for DBN, the dashed one for RES. Horizontal lines indicate the observed values. The slip angle must satisfy both stations simultaneously.

is also compatible with a strong, although uncalibrated, Rayleigh wave on the vertical Benioff short-period instrument at LWI. Using the instrument responses at DBN and RES, a seismic moment of 4×10^{26} dyne-cm was obtained.

III. March 21, 1939 - $M_S = 7.2$

Only 16 stations at distances less than 90° reported first motions to the ISS (Figure 2.11). The only strong constraint on the focal mechanism results from the clear separation between dilational arrivals in southern Europe (Granada, Rome, Belgrade, Ksara and Helwan) and compressional ones in northern Europe (Cernauti, Bucharest, Zurich, Strasbourg, De Bilt and Paris). On a first-motion diagram, all these stations cluster together and, thus, one fault plane must bisect them.

Excellent surface-wave records at Christchurch, New Zealand (CHR) are shown on Figure 2.12. The Love-to-Rayleigh ratio is 0.8. Records at DBN, unfortunately, did not exhibit clean wave shapes after filtering and as the amplitude ratios were unstable as a function of frequency, we decided against using them.

The Pasadena (PAS) record on the Benioff strainmeter (Figure 2.13) shows distinctive Love and Rayleigh waves, with a L/R ratio of 1.5.

Investigation of a large number of solutions generally consistent with the body wave constraint yielded the mechanism $\phi = 166°$, $\delta = 82°$, $\lambda = 57°$. Superficially, the data might appear insufficient to resolve the focal mechanism. However, given the location and origin time for a point source, it consists of a set of 3 parameters. Given the body wave constraint, two independent Love-to-Rayleigh amplitude ratios can

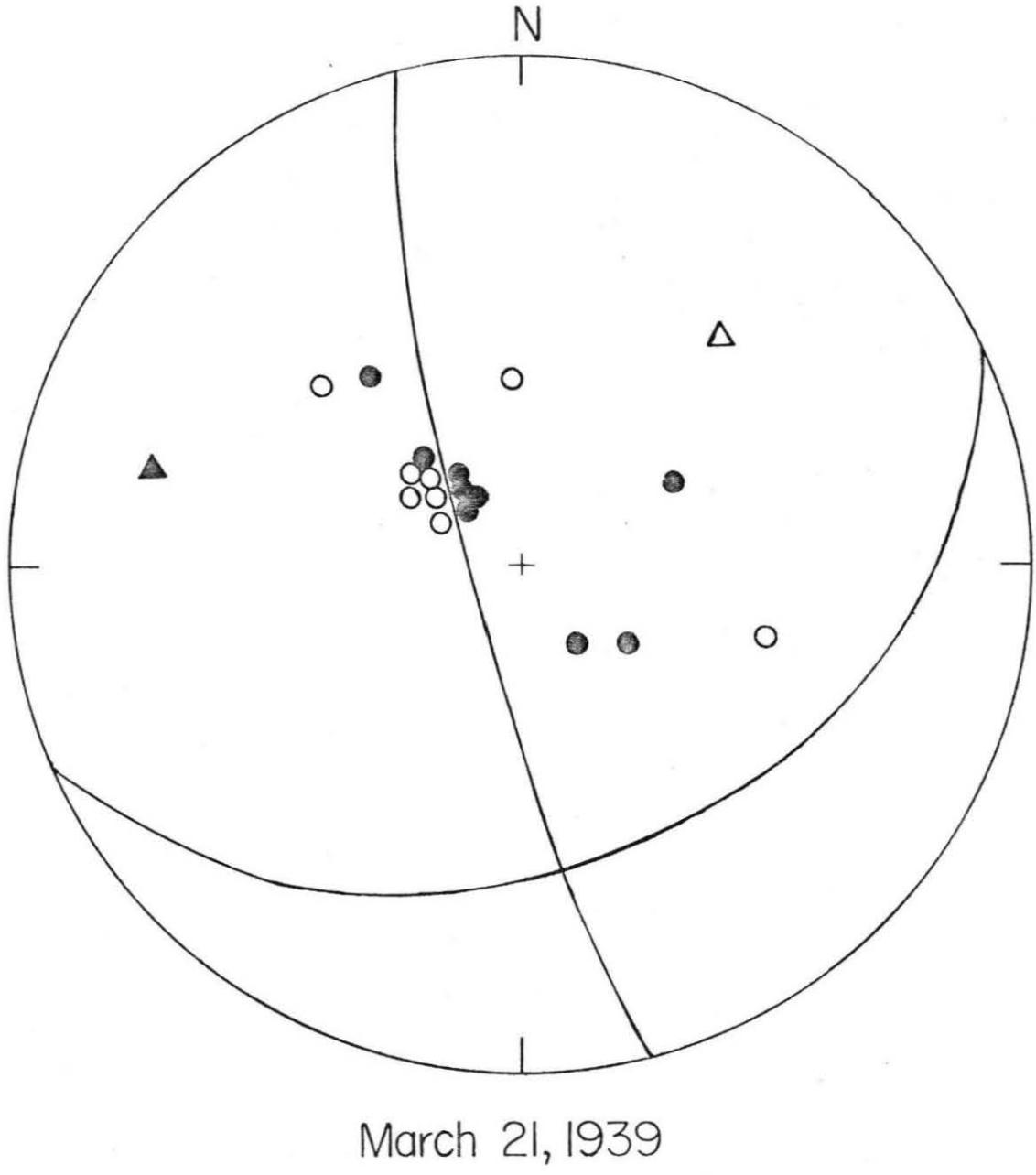

Figure 2.11. Lower focal hemisphere plot of first-motion data for March 21, 1939. Symbols as in Figure 2.6. Both planes were obtained from surface-wave data (see Figure 2.13), subject to the constraint imposed by the first motions.

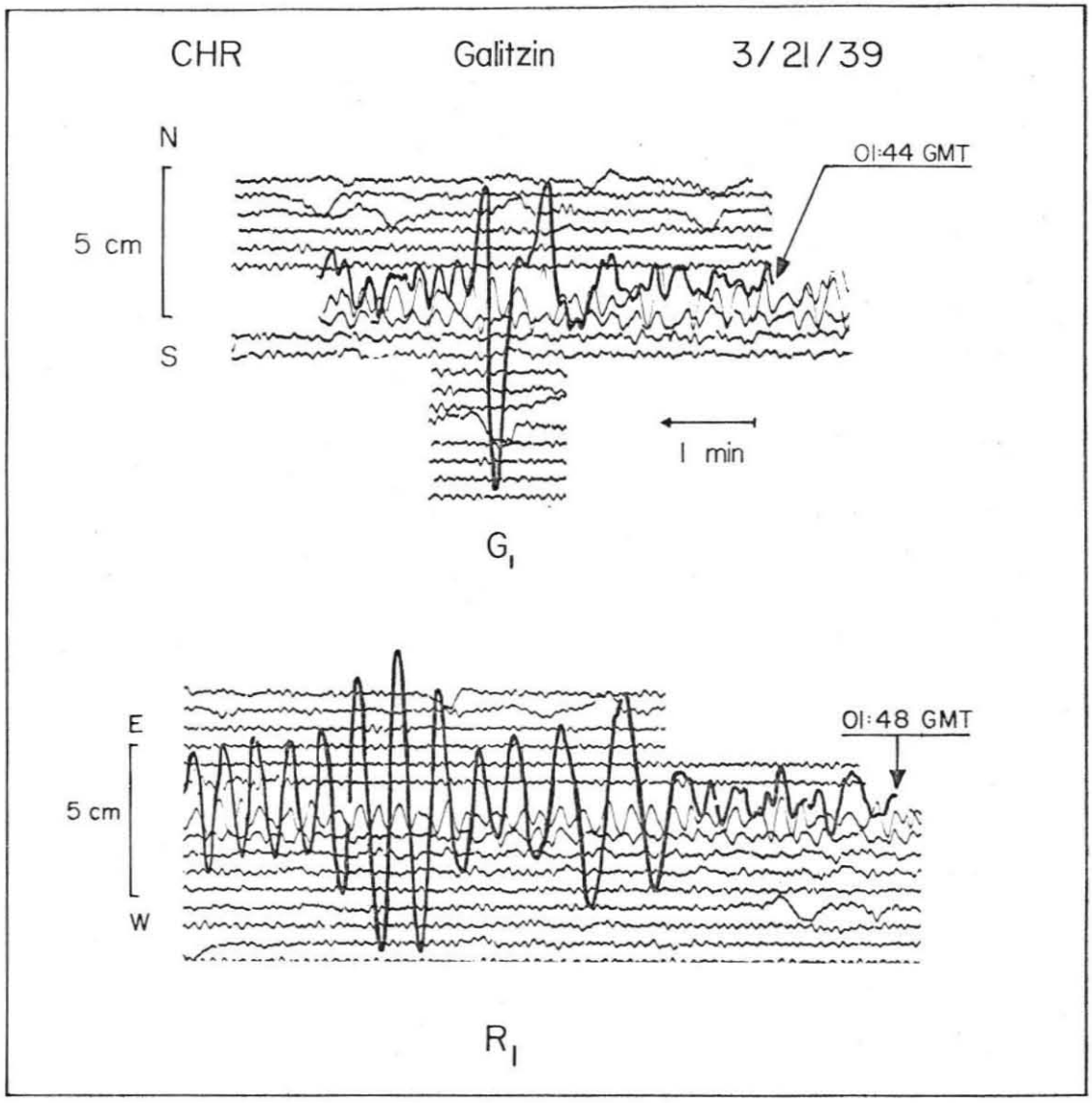

Figure 2.12. Galitzin long-period records for March 21, 1939 at Christchurch, New Zealand.

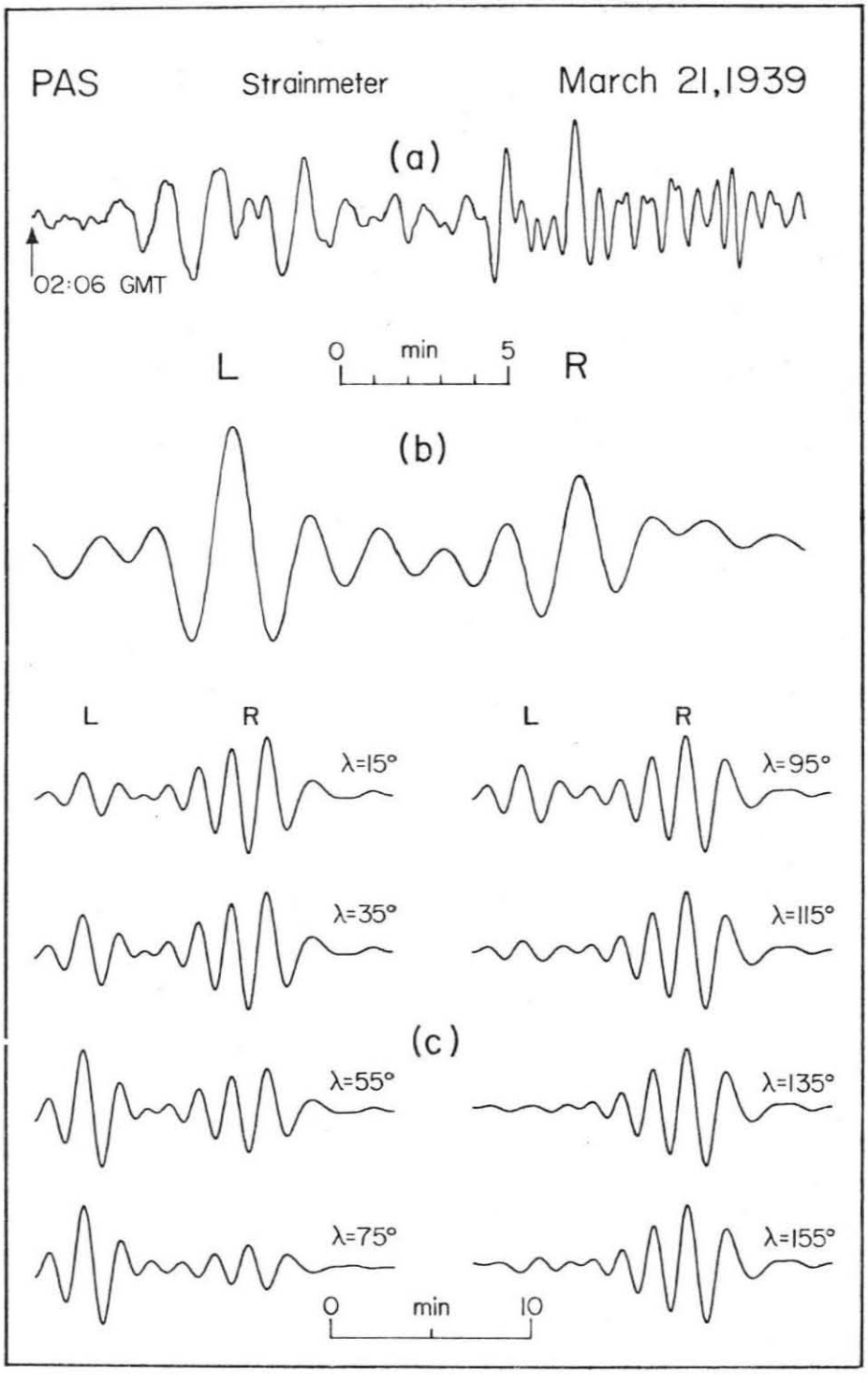

Figure 2.13. (a) Original trace of the Benioff strainmeter at PAS for March 21, 1939.
(b) Observed trace filtered at $T \geq 100$ seconds, showing Love wave (L) and Rayleigh wave (R) contributions to the N-S strain.
(c) Synthetic seismograms obtained for various values of the slip angle λ along a fault plane defined by $\phi = 166°$, $\delta = 82°$. Note the extreme sensitivity to λ of the Love-to-Rayleigh ratio. The best fit is obtained for $\lambda \sim 55°$.

(at least theoretically) yield the mechanism. The Pasadena record shows the dramatic sensitivity of L/R to slip angle, and the excellent fit of the synthetic to the original trace confirms the solution. An acceptable fit could not be obtained if, as the first motions might suggest, the plane were striking slightly farther to the west. The final solution has a roughly N-S plane steeply dipping to the west, on which the motion is about one-half thrust and one-half left-lateral strike-slip.

The seismic moments obtained from CHR (2.6×10^{27} dyne-cm) and PAS (1.5×10^{27} dyne-cm) are in good agreement, especially in view of the problems associated with the strainmeter's calibration [Kanamori, 1976].

IV. March 9, 1928 - $M_S = 7.7$

No first motion data were reported by the ISS in 1928. From the available records, it appeared that WEL (Wellington) was compressional and COP (Copenhagen) and DBN were emergent. The other available records were difficult to interpret, especially as vertical instruments were quite rare in 1928. Love-to-Rayleigh ratios were obtained at WEL (2.5), DBN (0.8) and, despite a very low response at long periods, on the Wood-Anderson EW instrument at RVR (Riverside) (0.4). Love waves are present at La Paz, Bolivia (LPB), but no definite value could be obtained for the L/R ratio. Although several satisfactory focal solutions (generally similar to that for the 1939 event) can be found, the available data are insufficient to yield a unique mechanism. This is especially unfortunate since comparison of the records from 1928 and 1939 at WEL (Figure 2.14) or DBN clearly shows that the 1928 event was much larger

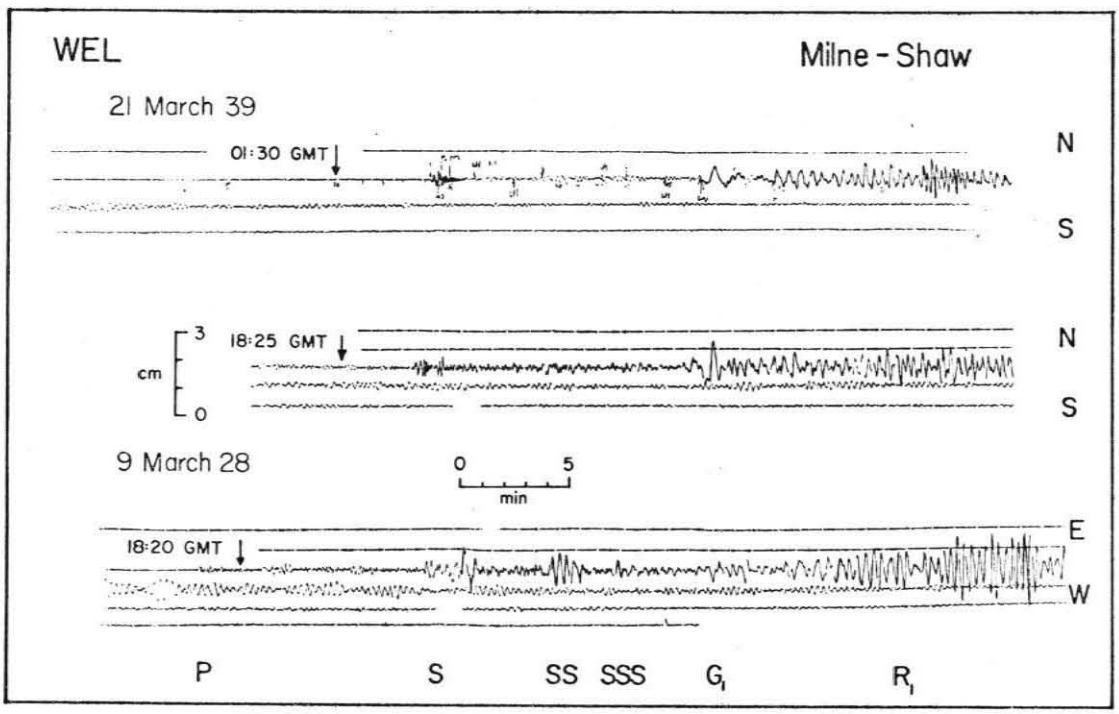

Figure 2.14. A comparison of Milne-Shaw records at WEL for the March 21, 1939 and March 9, 1928 events. Principal seismic phases are identified. This figure illustrates the greater size of the 1928 event and the substantial long-period excitation from both events. The instrument magnification is 150.

than the 1939 one, and contained more long period energy. The large foreshock on February 7, 1928 and the numerous aftershocks (five were detected within a week, but the locations are uncertain) also suggest a very large earthquake. Estimates of the seismic moments computed by comparing a number of plausible mechanisms with the records at WEL or DBN fall in the range 4 to 8 x 10^{27} dyne-cm.

V. May 25, 1964 - M_S = 6.0

The pure strike-slip mechanism of this event, obtained by Sykes [1970] from first motions, agree well with both Rayleigh and Love wave radiation patterns. A sample of high-quality WWSSN records yields a seismic moment of 1.1 x 10^{25} dyne-cm.

VI. October 10, 1970 - M_S = 6.2

The focal solution of this event (almost pure strike-slip) was given by Fitch [1972] using first motions and S-wave polarization angles. Records at PAS are consistent with this solution and yield a seismic moment of 2.9 x 10^{25} dyne-cm. The moment of this event was determined from long period SH wave spectra to be 6.7 x 10^{25} dyne-cm [Richardson and Solomon, 1977].

TECTONIC IMPLICATIONS

This section attempts to describe the present day tectonics of the area using the earthquake mechanisms and bathymetry, and proposes a rather complex tectonic environment which seems generally consistent with the data.

Figure 2.15 shows the three fault mechanisms determined here, and the two others available in the literature for this area: Sykes' [1970] for the May 25, 1964 earthquake, and Fitch's [1972] for the October 10, 1970 event. The figure also shows schematically several major morphological features of the area: the ridge, the zone of ridges and furrows to the west, the graben-like deeps to the east and the deep sea fans.

Along the northern (2°N-10°S) segment of the ridge, the most seismic area roughly corresponds to the area where the ridge is broken up into irregular blocks. The 1939 earthquake mechanism has about equal components of thrust and strike-slip motion. This suggests that the thrusting is related to the irregular blocky nature of the ridge, and thus the southern, aseismic, portion of the ridge is much smoother and undeformed.

This relation between blocky morphology and recent deformation appears to continue to the north to 2°N. The ridge top sediments show evidence of recent faulting [Veevers, 1974]. Historic earthquakes were located in this area [Gutenberg and Richter, 1965], although this northernmost segment was excluded from this study, due to the difficulties in location in an area so close to the trench.

It seems reasonable to interpret the strike-slip motion as left-lateral along a roughly N-S plane. This is consistent with the strike of the ridge and the general N-S alignment of seismicity, and accords with the left-lateral motion found for the 1964 earthquake further south. The alternate interpretation, strike-slip and thrusting on the NE-SW plane seems less plausible, although it would align roughly with the *en échelon* blocks on the ridge. Strike-slip along the ridge's

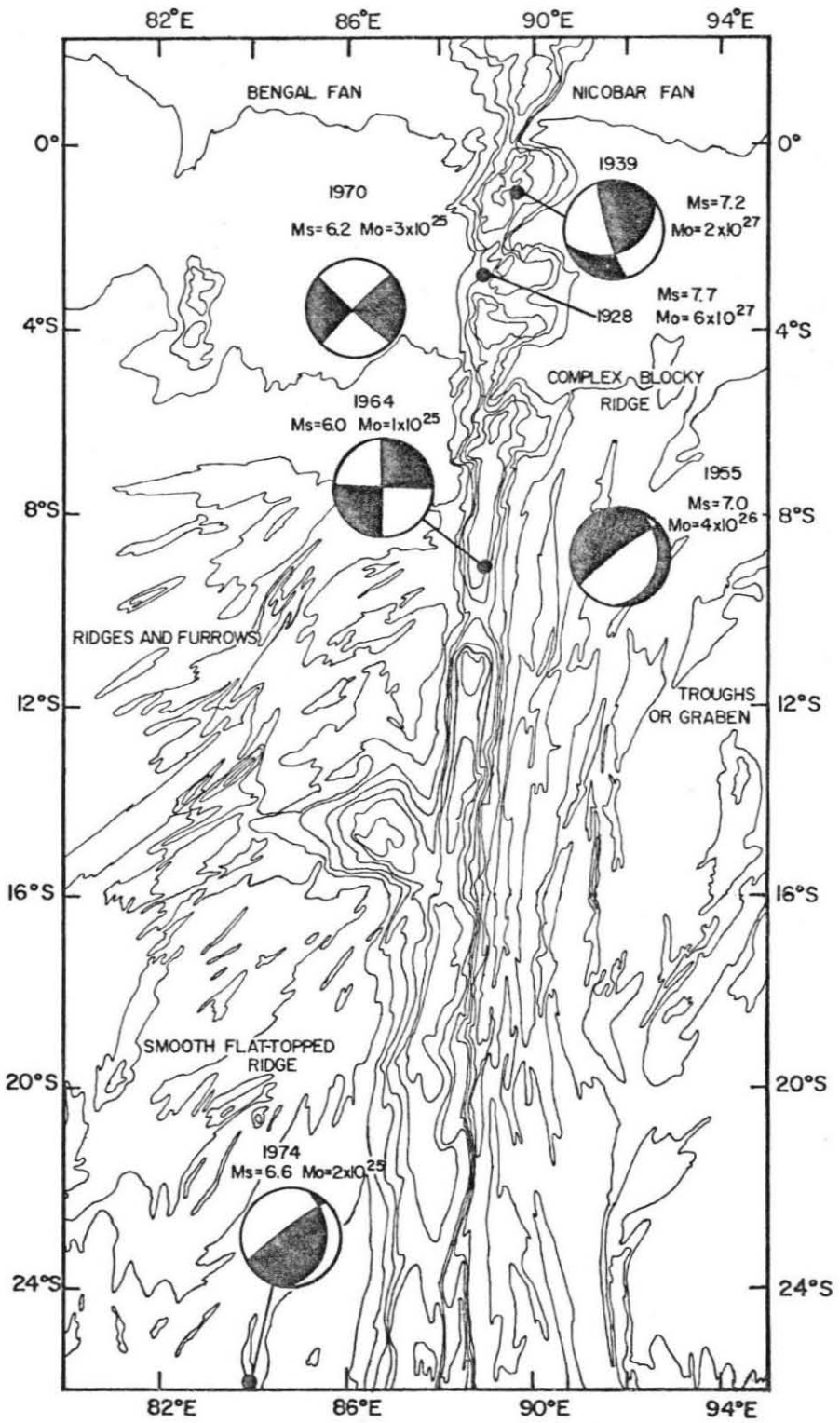

Figure 2.15. Focal mechanisms, magnitudes and moments for major earthquakes near the Ninetyeast Ridge. The mechanism of the 1928 event could not be reliably determined. Note that the 1939 and 1964 events on the ridge show strike-slip motion, the 1955 event is a normal fault, and the 1974 event is a thrust fault. The moments of the 1928 and 1939 earthquakes are much greater than any of the more recent events.

Table 2.2

SOURCE PARAMETERS FOR MAJOR RECENT EARTHQUAKES

IN THE NINETYEAST RIDGE AREA

Date	Origin Time GMT	ϕ deg	δ deg	λ deg	M_S	M_o 10^{25} dyne-cm
March 9, 1928	18:05:20				7.7	400-800
March 21, 1939	01:11:12	166	82	57	7.2	200
March 22, 1955	14:05:07	244	80	-78	7.0	40
May 25, 1964(*)	19:44:07	266	80	0	6.0	1.1
Oct. 10, 1970(†)	08:53:00	126	83	164	6.2	2.9
June 25, 1974	17:22:19	242	74	97	6.6	2.5

(*) Focal mechanism from Sykes [1970].

(†) Focal mechanism from Fitch [1972].

strike suggests that the deformation has some transform fault-like character as well as vertical motion resulting from compression across the ridge. This deformation seems to occur over a broad zone about the Ninetyeast Ridge, rather than on a single sharply defined fault.

South of about 10°S, when the ridge changes in morphology and seismicity, the data suggest that most of the intra-plate deformation takes place off the ridge, leaving the ridge itself undeformed. Although the boundaries between the blocky and smooth ridge segments and the seismic and aseismic portions are not identical, they are close enough to suggest that they may be related. Tectonic structures not on the ridge cannot be seen north of 7°S due to the thick fan sediments, so it is not clear whether a comparable boundary exists off the ridge.

If the NE-SW trending furrows and ridges to the west of the ridge are tectonic in origin, they suggest NW-SE compression. Few earthquakes occur in this region, so this compression appears to be primarily aseismic at present. The only major earthquake off the ridge and south of 10°S is the isolated 1974 shock. The thrust mechanism of this event is also consistent with NW-SE compression, but in the absence of detailed bathymetric data in the epicentral area, it is not possible to relate it to a particular structure. The April 13, 1918 earthquake was also located by Gutenberg and Richter in the furrow and ridge area, but little is known about this event, and due to its date and size, its location may be inaccurate. The seismicity map (Figure 2.4) also suggests that offridge earthquakes occur more frequently in this area than on the ridge's other side, but the total number of events is too small to show this conclusively.

The graben-like troughs that roughly parallel the ridge on its east side (Figure 2.1), south of about 7°S, suggest tensional deformation. The normal fault mechanism of the 1955 earthquake in this area is also tensional, with tension in the NW-SE direction. This is in general accord with the trend of the troughs in the epicentral area, but neither the location accuracy or bathymetry are adequate to assign this event to a specific feature. Presumably the graben formation is continuing today, and some fraction of this deformation occurs seismically.

The remaining portion of the Ninetyeast Ridge area that is covered by the sediment fans is difficult to discuss. The only moderate sized earthquake which can confidently be located in this region is the 1970 event studied by Fitch [1972], who proposed strike-slip motion consistent with N-S compression. (The 1913 earthquake was also located in the fan area but as discussed earlier, the location is quite uncertain.) Deformation of the fan sediments themselves, suggesting N-S compression, was observed to the southeast (7°S, 80°E) by Eittreim and Ewing [1972].

The overall tectonics of the ridge and the ocean basin to the west can be crudely described if the west side is encountering resistance resulting from the Indian collision, and the east side is subducting at the Sumatra trench. Such a situation would give rise to compression and left-lateral motion in the region of the Ninetyeast Ridge, if the ridge is the approximate boundary between the two sides. The situation is more complicated since the compression seems to be occurring over a broad zone, rather than precisely along the ridge. Thus, although the ridge is presently behaving in some sense like a transform fault,

it is not exactly one. It appears plausible that the present-day deformation would be concentrated about the old zone of weakness left by the transform fault.

Again, it may be worth recalling the San Andreas fault system. Although the general plate motion is along the transform fault, an entire complex of associated faults occurs nearby, frequently with senses of motion which differ from that of the San Andreas itself. The San Andreas system occurs in continental lithosphere, while the Ninetyeast Ridge deformation is occurring in old, thick oceanic lithosphere, in contrast to transforms near spreading ridges which are developed in young, thin oceanic lithosphere. These may be the reason why the present deformation near the Ninetyeast Ridge resembles that observed on land more than at spreading ridges.

It is less clear what causes the tensional tectonics which this study suggests occur to the east of the ridge. This may be related to the subduction at the Sumatra trench, as the north-south trending topography extends all the way to the trench [Sclater and Fisher, 1974], but it is difficult to explain the direction of the tension. In addition, closer to the trench, Fitch [1972] noted a strike-slip event (2°N, 94.6°E) which also suggests E-W extension. The Sumatra trench is an extremely complex subduction zone, along which the subduction is oblique and may be coupled to strike-slip motion behind the trench [Fitch, 1972] and the opening of the Andaman Sea [Curray et al., 1978; Eguchi et al., 1978]. The trench is also interacting with the Indian Plate and Ninetyeast Ridge in a very complex way.

Sykes [1970] studied the area of the Ninetyeast Ridge and suggested

that its earthquakes might represent an incipient subduction zone forming between Australia and Ceylon. This study uses additional data (the mechanisms of the 1939, 1955 and 1974 events) and recent bathymetric maps and proposes a different model. The earthquake locations, especially the large ones, appear to be near the Ninety-east Ridge and oriented roughly north-south rather than northwest-southeast. The mechanisms of two (1939, 1964) of the largest events show significant strike-slip components. This is more suggestive of relative motion along the Ninetyeast Ridge than of nascent subduction. The 1974 thrust earthquake is also difficult to reconcile with incipient subduction. Only the 1955 event shows normal faulting, but this seems to be associated with the graben structures. Finally, no bathymetric evidence for an incipient subduction zone has been observed in the area [Sclater and Fisher, 1974].

This model suggests that a significant fraction of the morphology of the Ninetyeast Ridge is due to the present-day tectonics of the area. Alternatively, Sclater and Fisher [1974] suggest that several of these features, including the *en échelon* nature of the northern segment of the ridge, are much older, and may be related to the early history of the ridge. In this work's model, the present seismic deformation is concentrated near the old ridge and transform fault and is modifying these preexisting features. There is no way that this study can determine when this deformation began, and thus the results do not directly bear on the question of the origin of the ridge as a topographic high. It is possible, on the other hand, that the graben are completely the result of the present tectonic environment. A possible difficulty

with this interpretation is the time spanned by the seismic data. The spatial distribution of seismicity we observe may not be representative. Even on a longer time scale, though, this model predicts that the segment south of 9°S would be aseismic, based on its smooth morphology.

This internal deformation of the Indian plate bears directly on the question of determining relative plate motions. The relative motions of all plates can be simultaneously found using plate boundary data by the method of least squares [Chase, 1972; Minster et al., 1974; Chase, 1978; Minster and Jordan, 1978], assuming all the plates are rigid. Minster and Jordan's [1978] solution yields inadequate closure of the triple junction. The failure of the junction closure suggests either inaccurate data or nonrigid plates. Chase [1978] treats this problem using the opening of the African rift, while Minster and Jordan [1978] prefer internal deformation of the Indian plate. They split the Indian plate into West Indian and Australian plates and determine a pole between them which satisfies the relative motion data. No specific boundary is required by this analysis, but if the plate boundary were the Ninetyeast Ridge, NW-SE compression would occur across it. This prediction agrees with the earthquake mechanisms and interpretation of the bathymetry.

A very crude estimate of the relative motion rate across the seismic portion of the ridge area can be obtained using a method suggested by Brune [1968]. Having determined the seismic moment for three earthquakes that appear to have been on the ridge (1928, 1939, 1964), it is possible to derive a rough relation between magnitude (M_S) and moment and estimate the moment of other events from M_S. The

total seismic moment along the ridge can be found by adding the 1923, 1926, 1928 and 1950 magnitude 6 events, which seem to have also been on the ridge (the pre-1923 locations seem too unreliable to justify using these earthquakes). It is worth noting that the total moment is almost completely due to the two largest events (1928, 1939).

This total moment (8.6×10^{27} dyne-cm) can be divided by the rigidity, the length of ridge (10°) over which the earthquakes occurred, and an assumed fault width. The depths were estimated at less than ten kilometers (which is reasonable for transform faults), so a conservative fault width would be twenty kilometers. This yields 144 cm, over 41 years, or about 3.1 cm/year. Assuming that half the motion is dip-slip, division by $\sqrt{2}$ yields 2.2 cm/year of strike-slip motion. Given the assumptions involved, and the range of uncertainty in M_o, this should be regarded as only an order of magnitude estimate. It is approximately consistent with the rate (1 cm/year) inferred from the triple junction misclosure [Minster and Jordan, 1978].

As this area appears to be the most active tectonic area within any of the oceanic plates, further study would be desirable. Ocean bottom seismometer experiments, along the ridge and its flanks, might explain a great deal about the present tectonics of this puzzling region.

CONCLUSION

The Ninetyeast Ridge area is a broad seismic zone considerably more active than the interior of any other oceanic plate. Focal mechanisms of the large earthquakes in the area suggest left-lateral strike-slip motion along the ridge, and compression across it. The

seismicity is concentrated in a zone paralleling the ridge, on its northern segment. To the south the ridge is aseismic, and deformation appears to occur on both sides. The bathymetry on the west side suggests compression, while the east side suggests tension. Mechanisms of earthquakes in these areas are in general agreement with this interpretation. The Indian plate is undergoing substantial internal deformation, with resolvable relative motion (at least in the seismic zone) between the Indian and Australian sides.

REFERENCES

Allen, C. R., P. St. Amand, C. F. Richter and J. N. Nordquist, Relationship between seismicity and geologic structure in the southern California region, Bull. Seism. Soc. Am., 55, 753-797, 1965.

Bowin, C. O., Origin of the Ninetyeast Ridge from studies near the equator, J. Geophys. Res., 78, 6029-6043, 1973.

Brune, J. N., Seismic moment, seismicity and rate of slip along major fault zones, J. Geophys. Res., 73, 777-784, 1968.

Burr, N. C. and S. C. Solomon, The relationship of source parameters of oceanic transform earthquakes to plate velocity and transform length, J. Geophys. Res., 83, 1193-1205, 1978.

Chase, C. G., The N plate problem of plate tectonics, Geophys. J. R. Astr. Soc., 29, 117-122, 1972.

Chase, C. G., Plate kinematics: The Americas, East Africa, and the rest of the world, Earth Planet. Sci. Lett., 37, 355-368, 1978.

Cockerham, R. S., B. P. Luyendyk and R. D. Jarrad, Paleomagnetic study of sediments from site 253 DSDP, Ninetyeast Ridge (abstract), EOS Trans. AGU, 56 (12), 978, 1975.

Curray, J. R. and D. G. Moore, Sedimentary and tectonic processes in the Bengal deep-sea fan geosyncline, in Geology of Continental Margins, ed. C. A. Burk and C. L. Drake, Springer-Verlag, New York, 1974.

Curray, J. R., D. G. Moore, L. Lawver, F. Emmel, R. W. Raith and M. Henry, Tectonics of the Andaman Sea and Burma, Geology, in press, 1978.

Detrick, R. S., J. G. Sclater and J. Thiede, The subsidence of aseismic ridges, Earth Planet. Sci. Lett., 34, 185-196, 1977.

Eguchi, T., S. Uyeda and T. Maki, Seismotectonics and tectonic history of the Andaman Sea, Tectonophysics, in press, 1978.

Eittreim, S. L. and J. Ewing, Mid-plate tectonics in the Indian Ocean, J. Geophys. Res., 77, 6413-6421, 1972.

Fitch, T. J., Plate convergence, transcurrent faults and the internal deformation adjacent to Southeast Asia and the western Pacific, J. Geophys. Res., 77, 4432-4460, 1972.

Francis, T. J. G., and R. W. Raitt, Seismic refraction measurements in the Southern Indian Ocean, J. Geophys. Res., 72, 3015-3041, 1967.

Geller, R. J., and H. Kanamori, Magnitudes of great shallow earthquakes from 1904 to 1952, Bull. Seism. Soc. Am., 67, 587-598, 1977.

Gutenberg, B. and C. F. Richter, Seismicity of the Earth and Associated Phenomena, Hafner, New York, 1965.

Heirtzler, J. R., G. O. Dickson, E. M. Herron, W. C. Pitman, III, and W. LePichon, Marine magnetic anomalies, geomagnetic field reversals and motions of the ocean floors and continents, J. Geophys. Res., 73, 2119-2136, 1968.

Kanamori, H., Synthesis of long-period surface waves and its application to earthquake source studies -- Kurile Islands earthquake of October 13, 1963, J. Geophys. Res., 75, 5011-5025, 1970a.

Kanamori, H., The Alaska earthquake of 1964: Radiation of long-period surface waves and source mechanism, J. Geophys. Res., 75, 5029-5040, 1970b.

Kanamori, H., Seismological evidence for a lithospheric normal faulting -- the Sanriku earthquake of 1933, Phys. Earth Planet. Int., 4, 289-300, 1970c.

Kanamori, H., Reexamination of the earth's free oscillations excited by the Kamchatka earthquake of November 4, 1952, Phys. Earth Planet. Int., 11, 216-226, 1976.

Kanamori, H. and S. Miyamura, Seismometrical reevaluation of the great Kanto earthquake of September 1, 1923, Bull. Earthquake Res. Inst. Tokyo Univ., 48, 115-125, 1970.

Kanamori, H. and J. J. Cipar, Focal process of the great Chilean earthquake, May 22, 1960, Phys. Earth Planet. Int., 9, 128-136, 1974.

Kanamori, H. and D. L. Anderson, Theoretical basis of some empirical relations in seismology, Bull. Seism. Soc. Am., 65, 1073-1095, 1975.

Le Pichon, X. and J. R. Heirtzler, Magnetic anomalies in the Indian Ocean and sea floor spreading, J. Geophys. Res., 73, 2101-2117, 1968.

Luyendyk, B. P. and T. A. Davies, Results of DSDP leg 26 and the geologic history of the southern Indian Ocean, in Davies, T. A. and B. P. Luyendyk et al., Initial Reports of the Deep Sea Drilling Project, vol. 26, U. S. Government Printing Office, Washington, D.C., 1974.

Luyendyk, B. P. and W. Rennick, Tectonic history of aseismic ridges in the eastern Indian Ocean, Bull. Geol. Soc. Amer., 88, 1347-1356, 1977.

Minster, J. B., T. H. Jordan, P. Molnar, and E. Haines, Numerical modeling of instantaneous plate tectonics, Geophys. J. R. Astr. Soc., 36, 541-576, 1974.

Minster, J. B. and T. H. Jordan, Present-day plate motions, J. Geophys. Res., in press, 1978.

Morgan, W. J., Deep mantle convection plumes and plate motions, Amer. Assoc. Pet. Geol. Bull., 56, 203-213, 1972.

Okal, E. A., A surface wave investigation of Gobi-Altai (December 4, 1957) earthquake, Phys. Earth Planet. Int., 12, 319-328, 1976.

Okal, E. A., The July 9 and 23, 1905, Mongolian earthquakes: a surface wave investigation, Earth Planet. Sci. Lett., 34, 326-331, 1977.

Peirce, J. W., The northward motion of India since the Late Cretaceous, Geophys. J. Roy. Astron. Soc., 52, 277-311, 1978.

Richardson, R. M. and S. C. Solomon, Apparent stress and stress for intraplate earthquakes and tectonic stress in the plates, Pageoph., 115, 317-331, 1977.

Richter, C. F., Elementary Seismology, W. H. Freeman, San Francisco, 1958.

Rothé, J. P., Seismicity of the Earth, UNESCO, Paris, 1969.

Sclater, J. G. and R. L. Fisher, The evolution of the east central Indian Ocean, with emphasis of the tectonic setting of the Ninetyeast Ridge, Geol. Soc. Am. Bull., 85, 683-702, 1974.

Stover, C. W., Seismicity of the Indian Ocean, J. Geophys. Res., 71, 2575-2581, 1966.

Sykes, L. R., Seismicity of the Indian Ocean and a possible nascent island arc between Ceylon and Australia, J. Geophys. Res., 75, 5041-5055, 1970.

Tarr, A. C., World Seismicity Map, United States Geological Survey, Washington, D.C., 1974.

Tsai, Y. B. and K. Aki, Precise focal depth determination from amplitude spectra of surface waves, J. Geophys. Res., 75, 5729-5743, 1970.

Veevers, J. J., Seismic profiles made underway on leg 22, in, von der Borch, C. C., J. G. Sclater et al., Initial Reports of the Deep Sea Drilling Project, vol. 22, U. S. Government Printing Office, Washington, D.C., 1974.

Wickens, A. J. and J. H. Hodgson, Computer Reevaluation of Earthquake Mechanism Solutions, 1922-1962, Dominion Observatory, Ottawa, 1967.

Chapter 3

AN EARTHQUAKE SWARM ON THE CHAGOS-LACCADIVE RIDGE AND ITS TECTONIC IMPLICATIONS

ABSTRACT

An unusual, isolated swarm of earthquakes occurred on the Chagos-Laccadive Ridge in the central Indian Ocean. Between 1965 and 1970 sixteen earthquakes were located at approximately 6.0°S, 71.3°E on the steep west-facing scarp of the Chagos Bank. This swarm forms the only major seismic activity in the period 1963-1976 on the otherwise aseismic ridge. The mechanisms of the three largest earthquakes were studied using body and surface wave data. All are extremely similar: shallow normal faulting on an east-west fault plane. Such faulting is difficult to reconcile with that expected from either the trend of the Chagos-Laccadive Ridge or the spreading direction at the nearby Central Indian Ridge. The swarm may have occurred at depth on a cross fracture remaining from the breakup of the Chagos Bank and the Mascarene Plateau and the formation of the present Central Indian Ridge.

INTRODUCTION

The Chagos-Laccadive Ridge, in the central Indian Ocean, is an elevated region trending roughly N-S, formed by the Laccadive, Maldive and Chagos island groups. As a long, linear shallow zone, it is one of the aseismic ridges which characterize the Indian Ocean.

The nature and origin of the ridge are not well understood. McKenzie and Sclater [1971] interpreted magnetic anomalies as showing that in Cretaceous through Eocene time (51 m.y. ago) a large transform fault ran North-South instead of the present Central Indian Ridge. As India moved north, left lateral motion occurred on this transform. Fisher et al. [1971] suggested that during this period the Chagos-Laccadive Ridge and the southern Mascarene Plateau were formed, as a single feature. It is not clear whether the volcanism which presumably formed the ridge occurred along the "leaky" transform fault, at the spreading ridge to the south, or as a result of a migrating hot spot. The one site on the ridge which was drilled falls on the conventional depth-age curve [Detrick et al., 1977]. Thus, over this period of time, the Chagos-Laccadive Ridge may have been rather similar to the Ninetyeast Ridge [Sclater and Fisher, 1974].

Fisher et al. [1971] proposed that the relative motion between the Indian Plate (east of the Chagos Transform Fault) and the Somalian Plate (on the west) then changed, causing the long transform to break up into a series of ridge-ridge transforms, forming the present Central Indian Ridge (Figure 3.1). The bathymetry and epicenters show transform faults striking roughly NE-SW (note the prominent Vema Fracture Zone), connected by ridge segments oriented approximately NW-SE. Figure 3.2

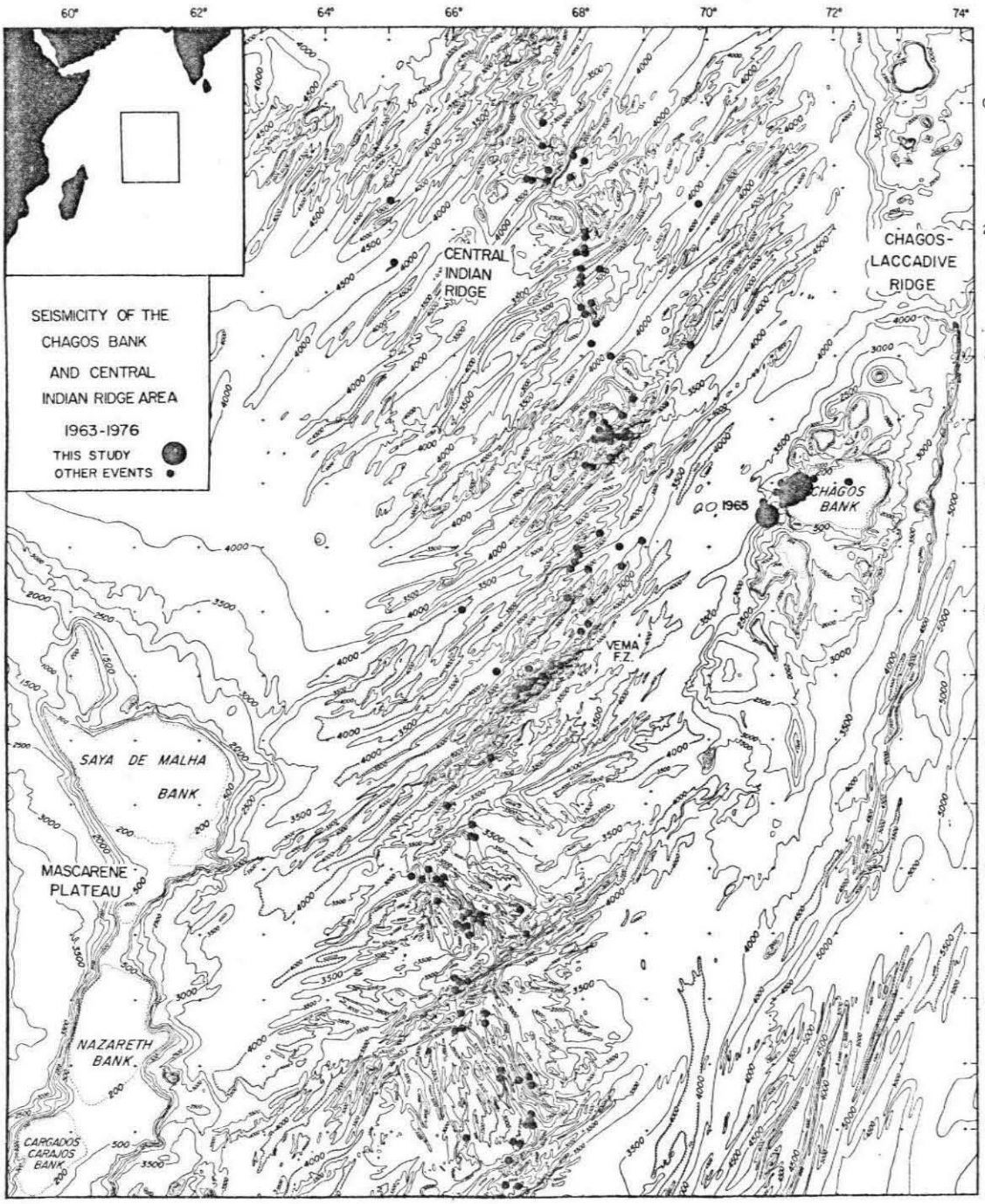

Figure 3.1. Seismicity of the Chagos Bank and Central Indian Ridge, plotted on bathymetry of Fisher et al. [1974]. Large dots indicate events studied in this work. (Not all of the Chagos Bank swarm events are plotted due to clustering.)

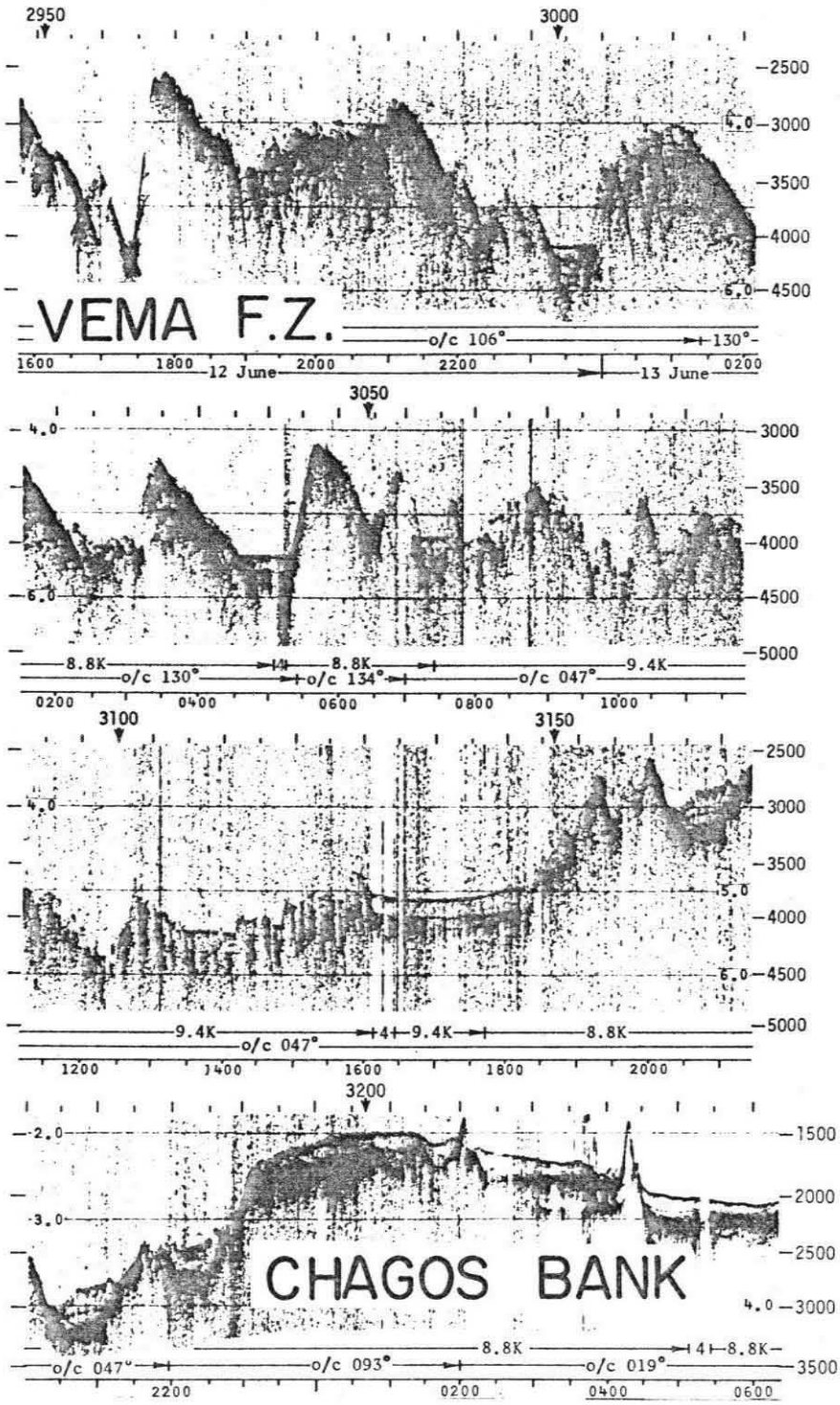

Figure 3.2. Airgun profile from the Vema Fracture Zone onto the Chagos Bank. Distance scale in nautical miles, vertical scale in meters. Note the steep scarp of the Chagos Bank. The swarm occurred on a similar scarp, 200 km to the north.

shows a series of airgun records, along a profile from the Vema Fracture Zone, across the east foothills of the Central Indian Ridge, up to the crest of the Chagos Bank [Fisher et al., 1974].

The Central Indian Ridge now separates the Chagos Bank area from the bathymetric highs to the west: the Saya de Malha, Nazareth, and Cargados Carajos Banks. These features form a portion of the Mascarene Plateau, which extends to the Seychelles Bank, to the northwest. Fisher et al. [1971] suggested that once the Central Indian Ridge formed, spreading tore the Mascarene Plateau and the Chagos Bank apart, leaving steep scarps on either side. The bathymetry shows that if the Mascarene Plateau and Chagos-Laccadive Ridge are rotated back together, the Chagos Bank fits between the Saya de Malha and Nazareth Banks. Fisher et al. [1974] date this separation as lower Oligocene (30 m.y.). This model for the evolution of the Chagos-Laccadive and Central Indian Ridges, as well as the Mascarene Plateau is shown in Figure 3.3.

Little additional data are available on the southern segment of the Chagos-Laccadive Ridge. Seismic refraction measurements [Francis and Shor, 1966] are interpreted as showing typical oceanic crust with a rather shallow Moho. Free air gravity anomalies are almost zero [Kahle and Talwani, 1975] suggesting that the ridge is in isostatic equilibrium. The available data on the entire Chagos-Laccadive Ridge are summarized by Ben Avraham and Bunce [1977].

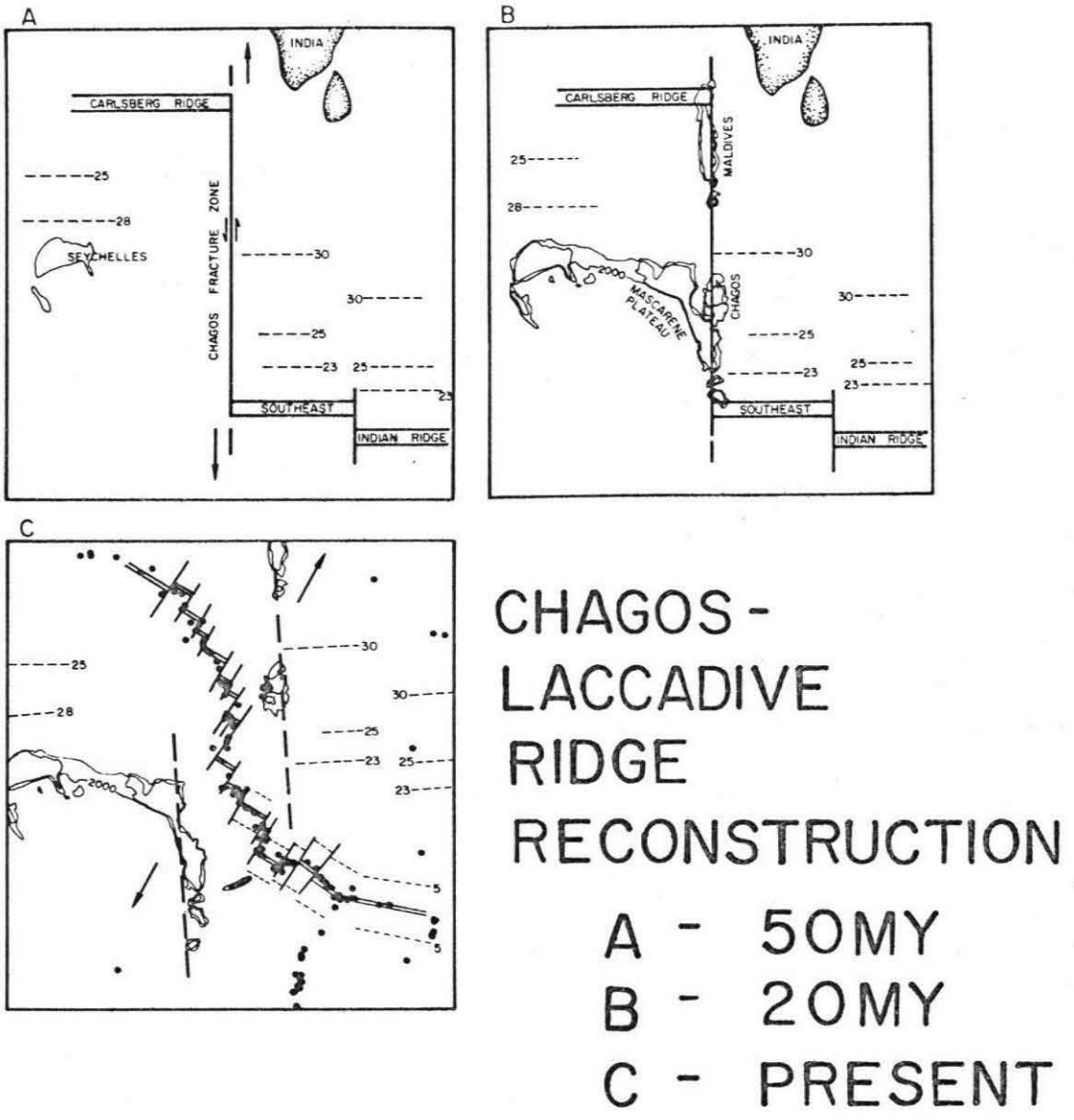

Figure 3.3. Evolution of the Chagos Bank area [Fisher et al., 1971].
A. Central Indian Ocean in Eocene time (anomaly 21, 50.m.y.b.p.). Left lateral motion is occurring on the Chagos transform fault.
B. Central Indian Ocean in Miocene time (anomaly 6, 20 m.y.b.p.). The Chagos-Laccadive Ridge and Mascarene Plateau have been formed as a single feature, and are beginning to separate as the transform fault breaks up.
C. Central Indian Ocean at present. The Central Indian Ridge separates the Chagos Bank and Mascarene Plateau.

SEISMICITY

The sequence of earthquakes discussed in this paper occurred between 1965 and 1970, and are listed in Table 3.1. The locations are from the International Seismological Center, the body wave magnitudes are from the Preliminary Determination of Epicenters, and surface wave magnitudes were measured for this study using a set of ten azimuthally distributed stations: WIN, SHL, NAI, PRE, MUN, AAE, IST, QUE, NDI, SHI. These events, together with those located on the Central Indian Ridge are plotted in Figure 3.1. The time covered in Figure 3.1 (1963 - 1976) is that for which WWSSN data are available, and were included in the locations.

Location of earthquakes in the Indian Ocean has historically been a problem [Gutenberg and Richter, 1965], due to poor azimuthal coverage and a lack of close-in stations. Figure 3.1 provides an estimate for the location accuracy, in that most earthquakes locate on the ridge and transforms. It is clear that the sixteen events in the Chagos Bank swarm form a distinct group and can be resolved from those related to the Central Indian Ridge. The stated locations within this group may not be accurate enough to yield relative positions, but they are adequate to show that these are on the western scarp of the Chagos Bank. No other earthquakes were reported during this time period anywhere else on the Chagos-Laccadive Ridge.

Examination of Table 1 suggests that these earthquakes collectively form a type of swarm, rather than a main shock-aftershock sequence. Although the first (September 1965) event was the largest, it had no reported aftershocks within a two day period. Then, in November 1967,

Table 3.1

CHAGOS BANK EARTHQUAKE SWARM

Date	Origin Time	Location	m_b	Ms
September 12, 1965	22:02:37	6.5°S 70.8°E	6.2	6.0
November 10, 1967	18:38:37	6.0°S 71.3°E	5.4	
November 11, 1967	11:55:56	6.0°S 71.3°E	5.6	5.2
November 11, 1967	12:14:57	6.0°S 71.3°E	5.7	
November 11, 1967	15:05:10	6.1°S 71.3°E	5.3	
November 11, 1967	17:42:17	6.1°S 71.4°E	5.4	
November 11, 1967	17:59:57	6.1°S 71.3°E	5.7	
November 11, 1967	19:07:32	6.2°S 71.3°E	4.9	
November 11, 1967	20:18:11	6.0°S 71.3°E	5.4	
November 28, 1967	2:21:57	6.2°S 71.3°E	5.1	
March 2, 1968	22:02:24	6.1°S 71.4°E	5.6	5.4
March 15, 1968	12:51:57	6.2°S 71.4°E	5.3	
March 20, 1968	22:00:04	6.1°S 71.2°E	5.3	
December 3, 1968	10:40:30	6.1°S 71.3°E	4.9	
July 12, 1969	5:57:11	6.0°S 71.3°E	5.3	
January 11, 1970	3:14:24	6.2°S 71.3°E	4.9	

eight events occurred within a two day period. Some of these are shown in Figure 3.4, a seismogram from Quetta, Pakistan, a comparatively nearby high gain station. The largest shock on the record is the smallest of the three whose mechanisms were determined in this study. The smaller events on the record were too small for mechanism determination: the largest of these (at 17:59) appears very similar in mechanism to the earlier event, though not enough first motions could be read to permit a definite conclusion.

The earthquake sequence appears to have tapered off and ended by 1970. No events in this area are reported in the six year period 1970 - 1976. Thus, the Chagos Bank swarm is isolated both in time and space, forming an extremely unusual earthquake sequence.

FOCAL MECHANISMS

Figure 3.5 shows fault plane solutions for the three largest events of the Chago Bank swarm. First motions from long period vertical components of WWSSN stations are plotted on the lower focal hemisphere. All three mechanisms are generally similar: an east-west plane dipping about 65° to the north is well constrained by the first motions. Station coverage is good for the largest event, and poorer for the two smaller events.

The first motions are not adequate to constrain any of the mechanisms completely. The second planes were constrained from the radiation pattern of surface waves. Love and Rayleigh wave trains were isolated, tapered and filtered between 25 and 100 seconds. They were then equalized to a propagation distance of 90°, using the method

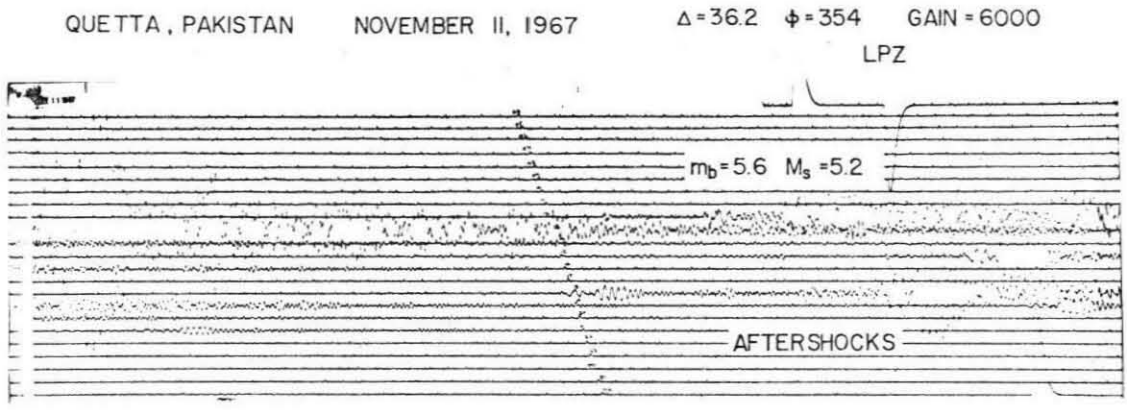

Figure 3.4. Long period vertical seismogram at QUE, showing earthquakes of November 11, 1967. Note that events with similar reported m_b, for example, the largest shock that day (at about 12 hours) and the aftershock at about 18 hours, differ greatly in surface wave magnitude. QUE is near a body wave node, and on a Rayleigh wave loop.

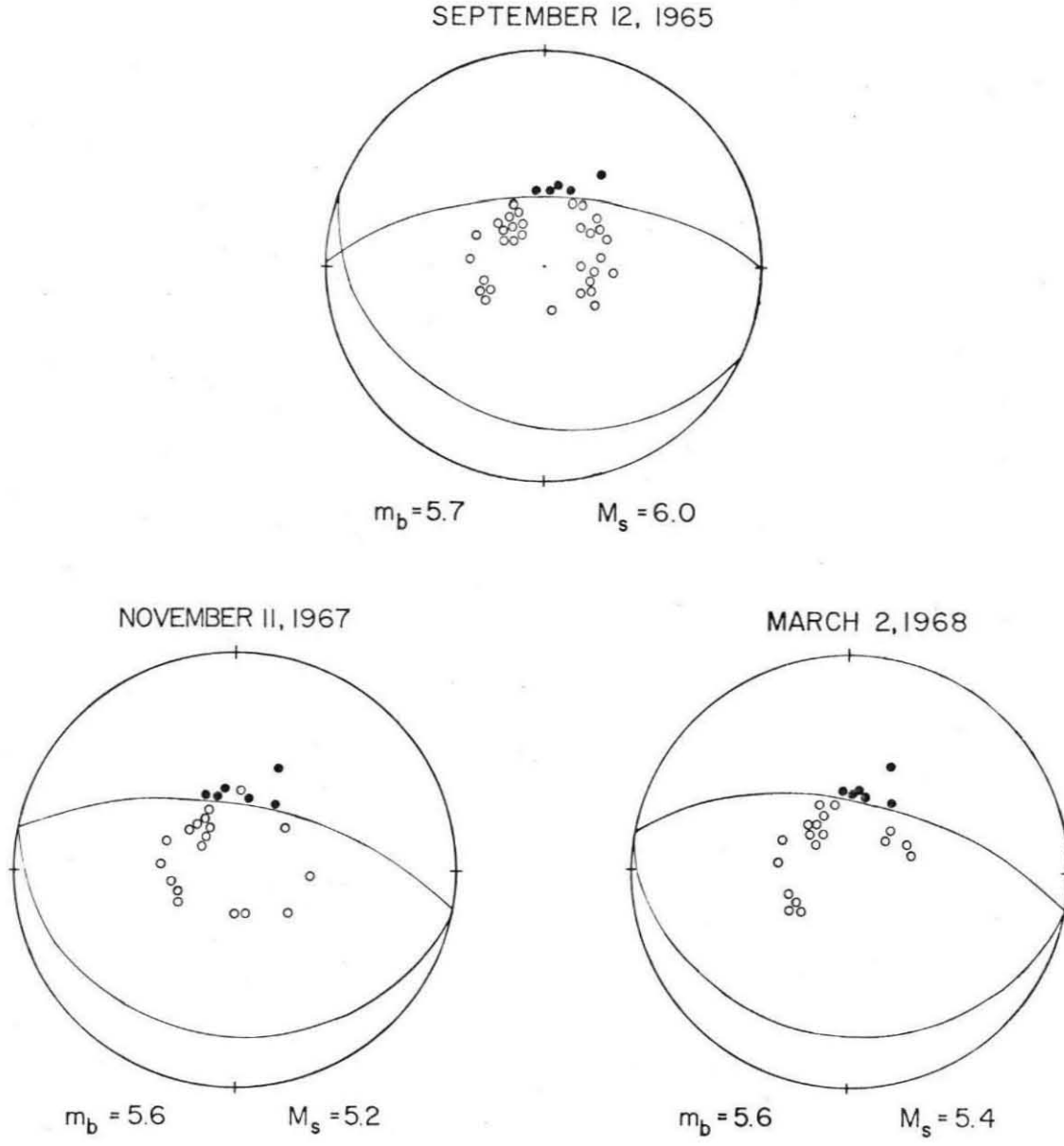

Figure 3.5. First motions for the three earthquakes studied, plotted on the lower focal hemisphere. The second nodal planes are constrained using surface waves. All events are almost pure normal faults.

of Kanamori [1970a,b]. The amplitude spectral densities are shown as a function of azimuth in Figure 3.6. The spectral density averaged over the 30-40 second period band is plotted for the two smaller events, while the larger event, with longer period energy, is averaged over the 45-55 second band.

This type of analysis was developed for great earthquakes and has usually been applied to large events with much longer period energy (thus reducing effects due to lateral structure along the propagation path). It has, however, also been applied to smaller events [Hart et al., 1977; Ebel et al., 1978] in the California area. Additional difficulties are introduced for the Chagos Bank events due to poor station coverage. Still, the radiation patterns, though jagged, are clearly recognizable.

The two lobed Rayleigh wave and four lobed Love wave radiation patterns, with coincident nodal directions, immediately suggest dip-slip faulting. The precise fault slip angle can be found by matching the maximum (loop) and minimum (node) directions. The best fitting theoretical radiation patterns, and the data, are shown in Figure 3.6.

All three events represent normal faulting on an essentially east-west plane, as summarized in Table 3.2. Banghar and Sykes [1969], using first motions and S-wave angles, suggested a solution for the 1965 event with a much greater component of strike-slip motion. Such a solution is not compatible with the surface waves. Sykes and Sbar [1974] suggested mechanisms for the other two events which are in accord with these solutions.

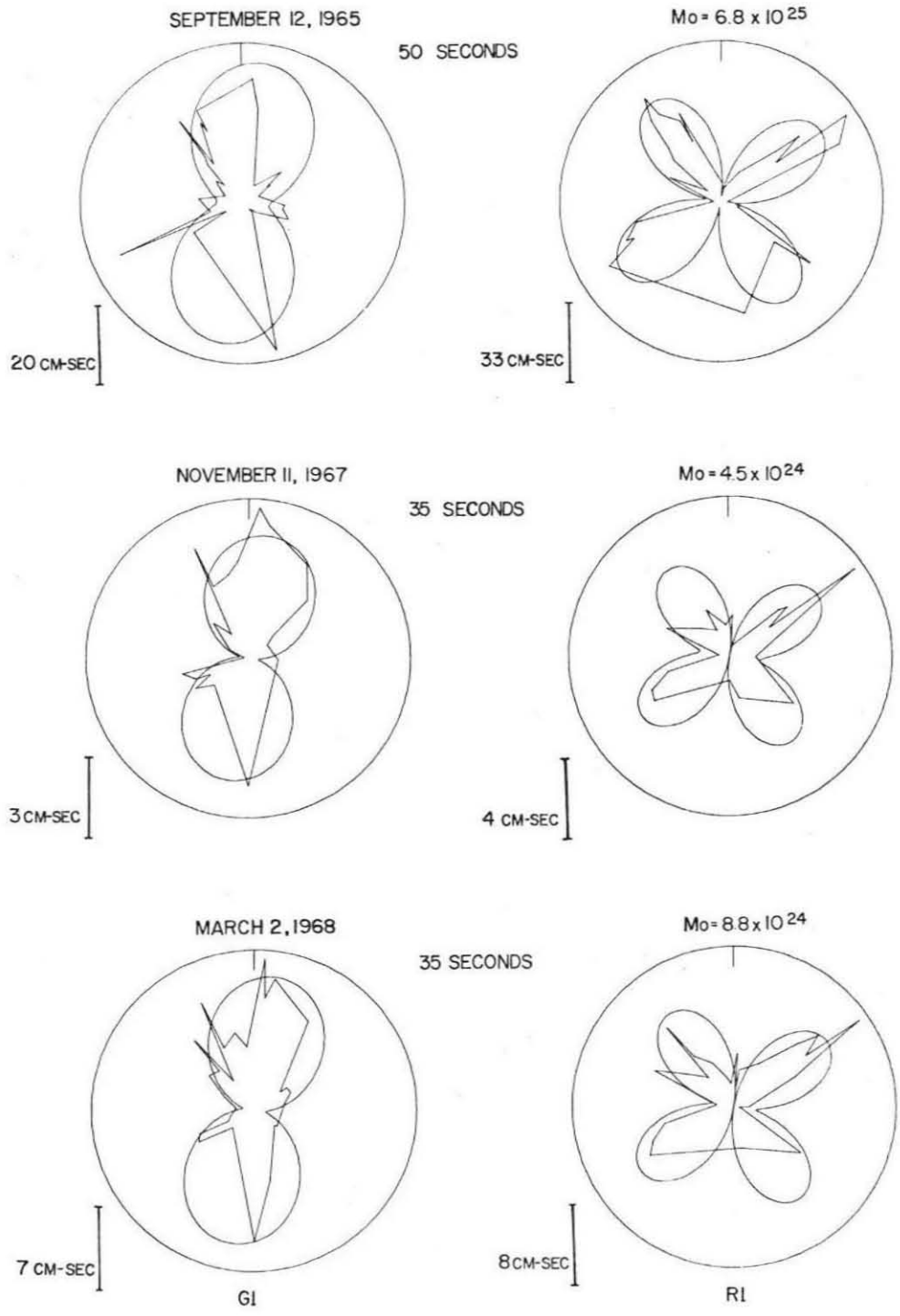

Figure 3.6. Theoretical and observed surface wave spectral amplitudes as a function of azimuth. Seismic moments were determined using the Rayleigh waves at the periods indicated.

Table 3.2

FAULT PARAMETERS

Date	ϕ	δ	λ	Mo
September 12, 1965	270°	60°	260°	6.8×10^{25} dyne-cm
November 11, 1967	280°	65°	270°	4.5×10^{24} dyne-cm
March 2, 1968	280°	60°	270°	8.8×10^{24} dyne-cm

Conventions follow Kanamori and Stewart [1976].

The seismic moment of each event can be found from the spectral densities in Figure 3.6. (The spectral density is given for the WWSSN 15-100 long period instrument at a gain of 1500.) Theoretical spectral densities, including the effects of attenuation and instrument response, were computed for the known mechanisms [Kanamori and Stewart, 1976], yielding the moment shown. These are averaged from the eight stations with the largest spectral densities. The earth model used is 5.08 M [Kanamori, 1970c], with a source at 16 km, and Q values are taken from Tsai and Aki [1969].

The moments are obtained only from the Rayleigh waves. Moments computed using Love waves are a factor of 2-3 higher, as the theoretical spectral densities were computed uisng only fundamental mode Love and Rayleigh waves. Fukao and Abe [1971] noted that the first three Love wave (torsional) overtones (higher modes) have group velocities similar to that of the fundamental mode. This situation is shown in Figure 3.7, for the first three overtones for earth model 1066A [Gilbert and Dziewonski, 1975]. The plot covers a range of frequencies (45-100 seconds) and group velocities (4.3-4.6 km/sec) suitable for standard surface wave analyses for earthquakes of the size studied here. Thus, at a period of 50 seconds, all four branches can contribute energy to the seismogram. Arrival times at a distance of 90° are also marked. Thus, the higher modes, especially the first overtone, can overlap with the fundamental mode and produce interference effects [Thatcher and Brune, 1969].

The higher mode Love waves are quite efficiently excited, even by shallow sources. This is shown by Table 3.3 where the excitation

coefficients, computed for model 1066A for a source at a depth of 15 km, are listed. $P_L^{(1)}$ and $Q_L^{(1)}$ [Kanamori and Stewart, 1976] are coefficients, which, when weighted by source geometry factors of order one and combined, give the theoretical amplitude spectral density. To estimate the maximum possible moment misdetermination, note that the overtones may have a combined amplitude comparable to or greater than the fundamental model. Thus a moment calculated using only the fundamental mode may yield a serious overestimate.

The higher mode dispersion curves are quite sensitive to near surface structure, and thus differ substantially for oceanic and continental regions [Thatcher and Brune, 1969]. (Figure 3.7 was calculated for an average (gross) earth model, 1066A.) The higher modes overlap much less with the fundamental for an oceanic structure. Thus, multiple surface waves (e.g., G3) with longer and more complex propagation paths will tend to separate the higher modes more from the fundamental. This effect, as well as the fact that at longer periods of several hundred seconds (at which larger earthquakes are studied) higher mode contamination is reduced, allowed other studies to obtain consistent Love and Rayleigh wave moments [Abe, 1972].

For smaller earthquakes, in which G1 is used for analysis at periods less than about 60 seconds this effect can be quite important. The moment overestimate can be reduced somewhat by measuring amplitudes in the time (rather than spectral) domain, thus exploiting the group velocity differences between overtone branches, but it is extremely difficult to separate the first higher mode from the fundamental. Fortunately, Rayleight waves are not affected by this problem, since the group velocities of the higher modes differ substantially from

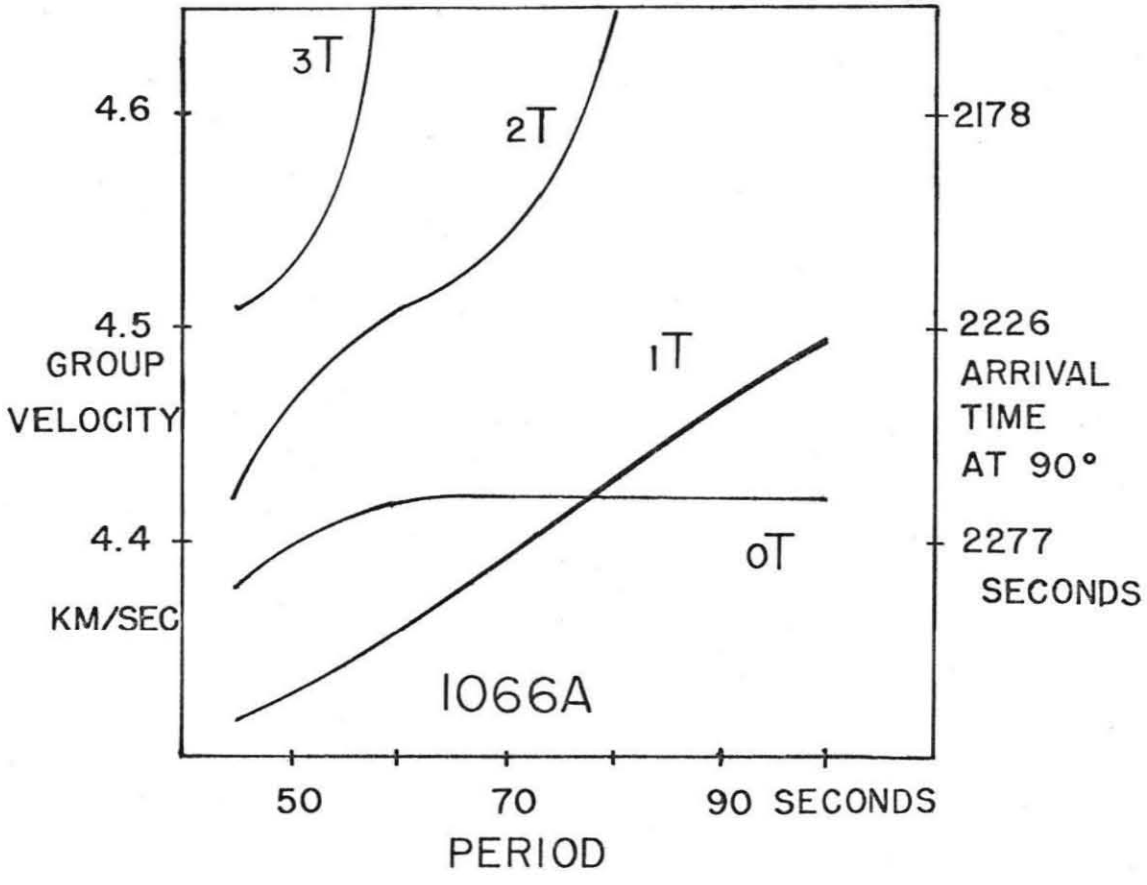

Figure 3.7. Dispersion curves for the fundamental and first three higher Love wave (torsional) branches for earth model 1066A. At 50 seconds, all four branches fall within the period-group velocity window plotted. At 100 seconds the fundamental and first overtone are still close in arrival time, but the second and third overtones are no longer in this window.

Table 3.3

EXCITATION COEFFICIENTS FOR TORSIONAL BRANCHES

(Model 1066A, source depth 15 km)

	$P_L^{(1)}$	$Q_L^{(1)}$
Fundamental ($_0T$)	-4.4	- .61
First overtone ($_1T$)	-1.94	- .38
Second overtone ($_2T$)	- .992	- .248
Third overtone ($_3T$)	- .657	- .209
First three overtone branches combined	-4.24	- .83

those of the fundamental mode for both continental and oceanic structures.

The moments of these earthquakes are quite high, given the surface wave magnitudes. The scaling relations of Geller [1976] suggest that an earthquake of M_S 6.0 would have a moment of 8×10^{24} dyne-cm, almost an order of magnitude less than that determined from the surface waves. (Such an anomalously high moment was also noted for the Oroville earthquake by Hart et al. [1977].) Such high moments allow surface wave analysis to succeed for such low magnitude events.

Given the known mechanism the focal depth can be estimated using body waves. The simplest possible model of farfield body wave radiation is one in which the pulse is made up of the direct ray and the rays reflected off the free surface. Thus, the farfield P wave is modeled as the sum of direct P, pP and sP (the shear wave converted at the free surface). Following Fukao [1971] and Kanamori and Stewart [1976], the problem can be simplified by replacing all near source structure by a homogeneous layer. A further simplification is to replace the full solution of the wave equation [Helmberger, 1974] with the essentially geometric optics first-motion-approximation [Langston and Helmberger, 1975].

These simplifications are valid only for the first few seconds of the body wave seismogram. Later portions of the record are influenced both by near source and receiver structure.

Figure 3.8 shows P waves on the long period vertical components at six stations for the 1965 earthquake, and synthetic seismograms computed for various focal depths, including the effects of attenuation and the instrument response. (A crustal velocity of 6.8 km/sec

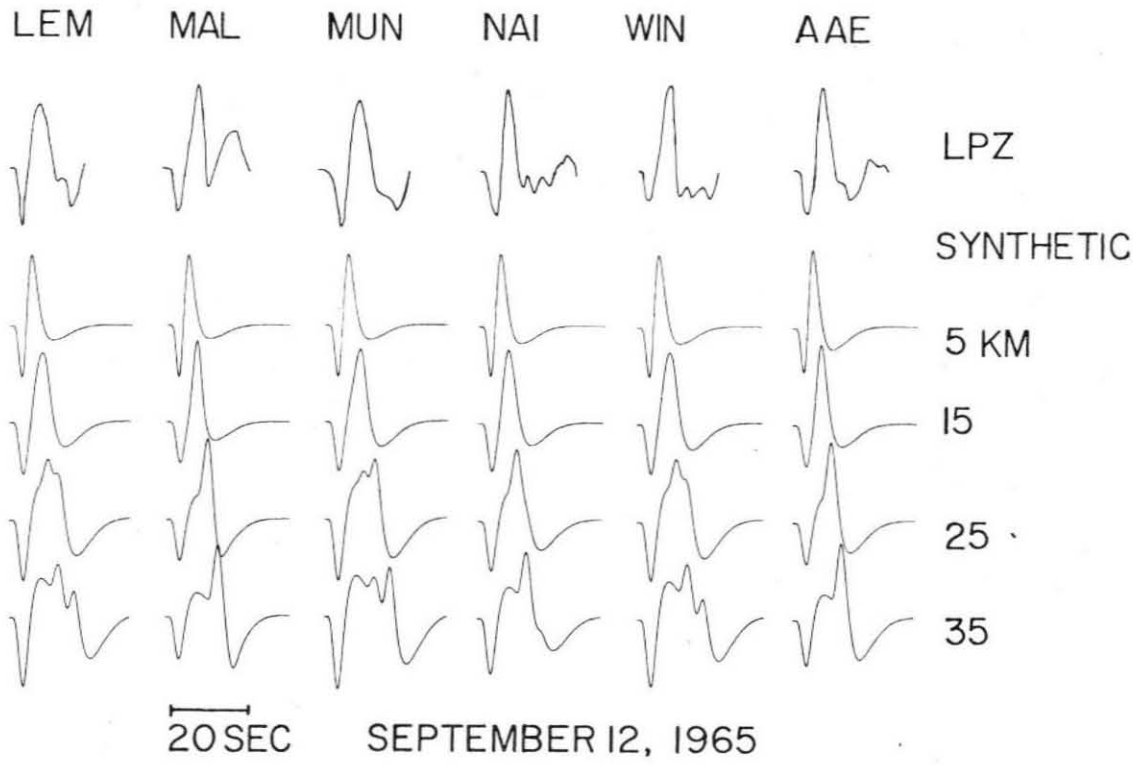

Figure 3.8. Long period vertical records at six stations, for the September 12, 1965 earthquake. Synthetic seismograms, computed for different focal depths, suggest that the source is at a depth of 15 km or shallower. The synthetics for the 15 km depth agree quite well with the initial body wave pulse.

[Francis and Shor, 1966] was used for the calculations.) The focal mechanism (Figure 3.5) shows that all but a few near-nodal Indian stations will be in the dilational quadrants, in which the waveforms vary only slightly with azimuth.

For a focal depth of 15 km, the data and synthetics agree well for 10-12 seconds, until additional body wave arrivals appear on the record. Deeper focal depths produce waveforms which are clearly inappropriate; a shallow depth yields too short a pulse duration. The source-time function, a three second symmetric trapezoid with a one second rise time, yielded the best fits of a variety tested. The source appears, then, to be at a depth of 15 km or shallower.

This procedure yields a body wave moment of 3.5×10^{25} dyne-cm, approximately half that obtained from the 50-second surface waves. Such a discrepancy, suggesting that the source had a substantial long period component, has been reported for other events, including the Oroville earthquake [Hart et al., 1977].

Only the 1965 event showed body waves large enough to justify waveform modeling. The two smaller earthquakes body waves have trace amplitudes less than a few millimeters; only the first pulse is resolvable. In general the pulses for both earthquakes are quite simple and resemble the larger event closely, suggesting similar focal depths.

An additional test for the focal depth is shown in Figure 3.9. The short period vertical components, six of which are shown, show a later phase approximately six seconds after the direct P wave. The consistency of the phase at different, azimuthally distributed stations, suggests that it is not due to local receiver structure. As ten

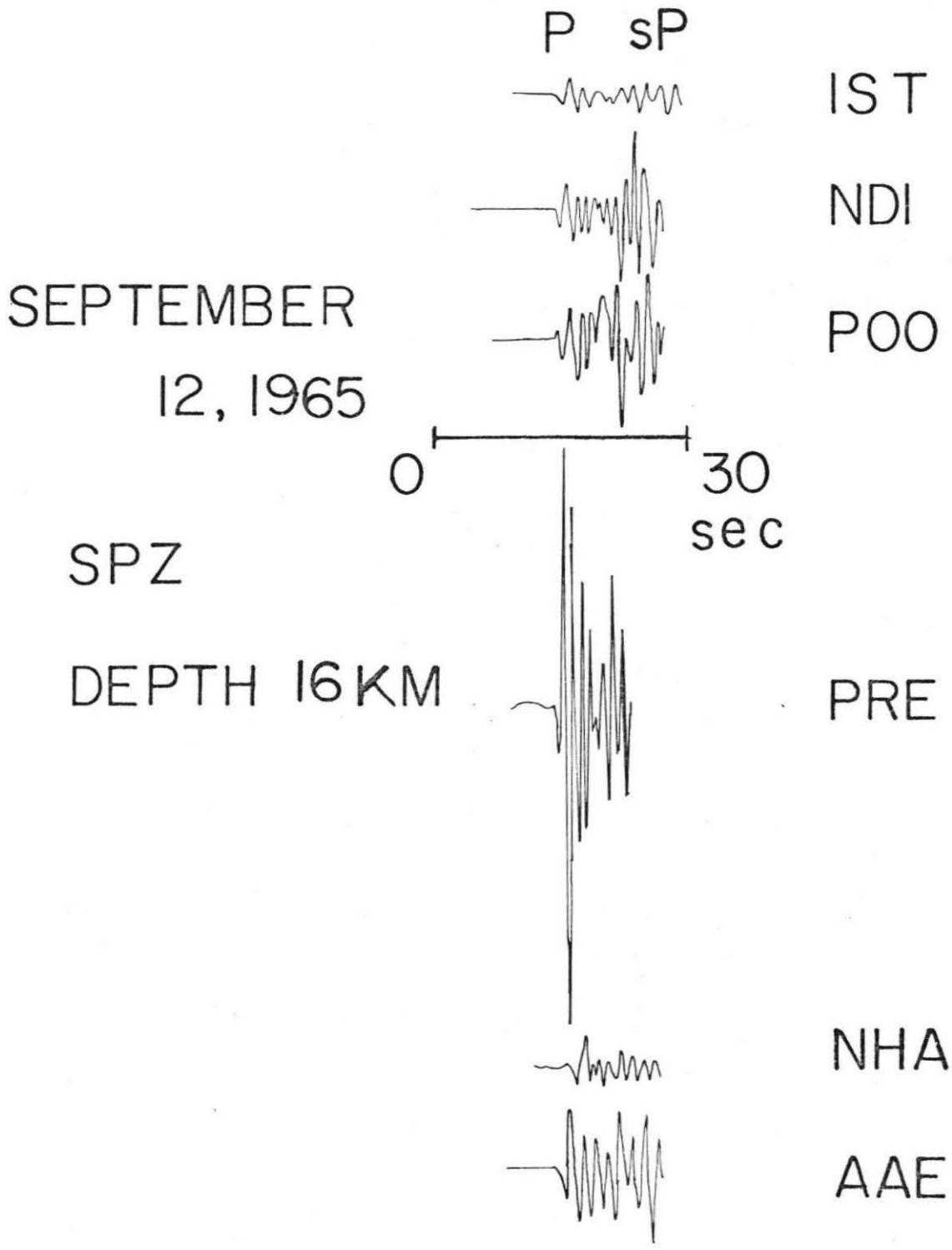

Figure 3.9. Short period vertical records at six WWSSN stations, for the September 12, 1965 earthquake. If the second arrival is sP, the focal depth is about 16 kilometers. (A minute mark occurs during the POO record.)

seconds of the long period component could be matched by the simple three rays model, this phase is unlikely to be due to near source effects. It should then be one of the free surface reflections, and its delay time should yield the focal depth. pP, the obvious candidate, implies a focal depth of about 24 km. The synthetic long period seismograms for this depth did not match well. On the other hand, if the later phase is sP, then the focal depth would be approximately 16 km, in general accord with that obtained from the synthetics. If so, then pP is presumably buried in the signal associated with the first arrival. This is not purely a radiation pattern effect, as pP should be sizable at several of these stations. This later phase appears with the same time delay on short period records of the two smaller earthquakes; again suggesting similar focal depths for all events.

TECTONIC IMPLICATIONS

The Chagos Bank swarm represents an extremely unusual phenomenon. Its location on the steep scarp face of the Chagos Bank is not easily explained by conventional tectonic models.

One possibility is that the Chagos Bank swarm is related to the Vema Fracture Zone, as the swarm's location is directly along the trend of the fracture zone. This would be difficult to reconcile with the earthquake mechanisms, as strike-slip faulting would be the logical result. Moreover, the fault planes, rather than paralleling the fracture zone trend, cut across it.

An alternate hypothesis would suggest that the earthquakes are related to the steep scarp on the Chagos Bank. Fisher et al.'s [1971]

model, in which the Chagos Bank and Mascarene Plateau were torn apart, implies that the ocean floor at the base of the scarp is much younger than the elevated area. Such a situation could lead to differential subsidence and dip slip faulting along a plane roughly parallel to the Chagos Bank. All three mechanisms show faulting almost perpendicular to the Chagos Bank.

Thus the swarm cannot be easily related to any of the bathymetric features in the area. On the other hand, it should probably not be considered an "intraplate" event, generated by the forces applied to the plate as a whole. In such a case, so close to the spreading ridge, the intraplate stress axes would presumably be controlled by the spreading direction [Forsyth and Uyeda, 1975; Richardson et al., 1976; Fujita and Sleep, 1978]. This does not seem the case, which is hardly surprising for earthquakes on an anomalous structure like the Chagos-Laccadive Ridge.

As these earthquakes seem inexplicable in terms of standard tectonic models, an unusual model may be tenable. Perhaps, at depths within the lithosphere, an east-west tending fracture remaining from the separation of the Chagos Bank and Mascarene Plateau is still active. Although this is not the current spreading direction, such a fracture could have formed in the early stages of the breakup. The existence of normal faulting, and swarm-type seismicity may even suggest material being intruded into such a fracture. In the absence of any surficial expression, of course, such a feature must remain hypothetical.

The seismicity and mechanisms on the Chagos-Laccadive Ridge seem quite different from those on the morphologically similar Ninetyeast

Ridge [Stein and Okal, 1978]. This may be an artifact of the sampling period, since historical (from 1918 on) earthquakes are known on the Ninetyeast Ridge, while this study considered only recent (1963-1976) events to avoid mislocated Central Indian Ridge earthquakes. Barring this effect, it appears that the Chagos-Laccadive Ridge is generally aseismic, except for the knot of earthquakes on the Chagos Bank; the Ninetyeast Ridge has a continuous seismic zone along a large fraction of its length. The Ninetyeast Ridge is probably still an active tectonic feature; the Chagos-Laccadive Ridge seems dormant except for this one region on the Chagos Bank.

CONCLUSION

The earthquake swarm that occurred on the Chagos-Laccadive Ridge between 1965 and 1970 represents the only seismicity from 1962 to 1976 on an otherwise aseismic ridge. These earthquakes represent almost pure normal faulting on an east-west trending plane, which cannot be easily reconciled with the present day tectonics of the area. A still-active fracture at depth, remaining from the breakup of the Chagos Bank and Mascarene Plateau, offers a possible explanation of this unusual swarm.

REFERENCES

Abe, K, Focal process of the South Sandwich Islands earthquake of May 26, 1964, Phys. Earth Planet. Interiors, 5, 110-122, 1972.

Bangar, A. R. and Sykes, L. R., Focal mechanisms of earthquakes in the Indian Ocean and adjacent regions, J. Geophys. Res., 74, 632-649, 1969.

Ben Avraham, Z. and Bunce, E. T., Geophysical study of the Chagos-Laccadive Ridge, Indian Ocean, J. Geophys. Res., 82, 1295-1305.

Detrick, R. S., J. G. Sclater and J. Thiede, The subsidence of aseismic ridges, Earth Planet. Sci. Lett., 34, 185-196, 1977.

Ebel, J. E., L. J. Burdick and G. S. Stewart, The source mechanism of the August 7, 1966 Baja California earthquake, Bull. Seism. Soc. Amer., in press, 1978.

Fisher, R. L., J. G. Sclater and D. P. McKenzie, Evolution of the Central Indian Ridge, Western Indian Ocean, Bull. Geol. Soc. Amer., 82, 553-562, 1971.

Fisher, R. L. et al., Site 23, in, Fisher, R. L. et al., Initial Reports of the Deep Sea Drilling Project, vol. 24, U. S. Government Printing Office, Washington, D.C., 1974.

Forsyth, D. and S. Uyeda, On the relative importance of the driving forces of plate motion, Geophys. J., 43, 163-200, 1975.

Francis, T. J. G. and G. G. Shor, Jr., Seismic refraction measurements in the northwest Indian Ocean, J. Geophys. Res., 71, 427-449, 1966.

Fujita, K. and N. Sleep, Membrane stresses near midocean ridge-transform intersections, Tectonophysics, in press, 1978.

Fukao, Y., Seismic body waves from surface faults, J. Phys. Earth, 19, 271-281, 1971.

Fukao, Y. and K. Abe, Multimode Love waves excited by shallow and deep earthquakes, Bull. Earthquake Res. Inst. Tokyo Univ., 49, 1-12, 1971.

Geller, R. J., Scaling relations for earthquake source parameters and magnitudes, Bull. Seism. Soc. Am., 66, 1501-1523, 1976.

Gilbert, F. and A. M. Dziewonski, An application of normal mode theory to the retrieval of structural parameters and source mechanisms from seismic spectra, Phil. Trans. R. Soc., A278, 187-269, 1975.

Gutenberg, B. and C. F. Richter, Seismicity of the Earth and Associated Phenomena, Hafner, New York, 1965.

Hart, R. S., R. Butler and H. Kanamori, Surface-wave constraints on the August 1, 1975 Oroville earthquake, Bull. Seism. Soc. Am., 67, 1-8, 1977.

Helmberger, D. V., Generalized ray theory for shear dislocations, Bull. Seism. Soc. Am., 64, 45-64, 1974.

Kahle, H. G. and M. Talwani, Gravimetric Indian Ocean Geoid, Z. Geophys., 39, 167-187, 1975.

Kanamori, H., Synthe is of long period surface waves and its application to earthquake source studies -- Kurile Island earthquake of October 13, 1963, J. Geophys. Res., 75, 5011-5027, 1970a.

Kanamori, H., The Alaska earthquake of 1964: radiation of long-period surface waves and source mechanism, J. Geophys. Res., 75, 5029-5040, 1970b.

Kanamori, H., Velocity and Q of mantle waves, Phys. Earth Planet. Interiors, 2, 259-275, 1970c.

Kanamori, H. and G. Stewart, Mode of strain release along the Gibbs Fracture Zone, Mid-Atlantic Ridge, Phys. Earth Planet. Interiors, 11, 312-332, 1976.

Langston, C. A. and D. V. Helmberger, A procedure for modeling shallow dislocation sources, Geophys. J., 42, 117-130, 1975.

McKenzie, D. and J. G. Sclater, The evolution of the Indian Ocean since the late Cretaceous, Geophys. J. Roy. Astr. Soc., 25, 437-528, 1971.

Richardson, R. M., S. C. Solomon, and N. H. Sleep, Intraplate stress as an indicator of plate tectonic driving forces, J. Geophys. Res., 81, 1847-1856, 1976.

Sclater, J. G. and R. L. Fisher, The evolution of the east central Indian Ocean, with emphasis on the tectonic setting of the Ninetyeast Ridge, Geol. Soc. Amer. Bull., 85, 683-702, 1974.

Stein, S. and E. A. Okal, Seismicity and tectonics of the Ninetyeast Ridge area: evidence for internal deformation of the Indian plate, J. Geophys. Res., in press, 1978.

Sykes, L. R. and M. L. Sbar, Focal mechanism solutions of intraplate earthquakes and stresses in the lithosphere, in Geodynamics of Iceland and the North Atlantic Area, ed. Kristjansson, D. Reidel and Co., Dordrecht, Holland, 207-224, 1974.

Thatcher, W. and J. N. Brune, Higher mode interference and observed anomalous apparent Love wave phase velocities, J. Geophys. Res., 74, 6603-6611, 1969.

Tsai, Y. B. and K. Aki, Simultaneous determination of the seismic moment and attenuation of seismic surface waves, Bull. Seism. Soc. Amer., 59, 275-287, 1969.

PART II

MODELS FOR ASYMMETRIC AND OBLIQUE SPREADING AT MIDOCEAN RIDGES

Chapter 1

INTRODUCTION

The midocean ridge system, the largest of the suboceanic topographic features, is distinguishable both by its elevation and its seismic activity. In this zone of high heat flow, rugged topography and active seismicity the oceanic plates are generated and begin to spread apart. The morphology of this zone gives crucial insight into the seafloor spreading process.

Ewing and Heezen [1956] were the first to note that the midoceanic ridge system was truly worldwide, and predict the existence of ridges in unsurveyed areas from seismicity alone. In 1947 the first cores were obtained from the Mid-Atlantic Ridge by R/V Atlantis, showing the presence of fresh igneous rock (including pillow basalts) and establishing the volcanic activity of the ridges. With the introduction of precision depth recorders the morphology of the ridge system became clearer. Heezen et al. [1959] reported the prominent axial rift which extends the length of the Mid-Atlantic ridge, while Menard [1960] showed that the East Pacific Rise, instead, had an axial high. Von Herzen and Uyeda [1963] showed that heat flow at the ridges was much higher than in the ocean basins, and decayed with distance from the ridge crest.

In his [1962] classic "essay in geopoetry" Hess suggested that the ocean floors were generated at the ridges and destroyed at trenches. This was proved by the work of Vine and Matthews [1963] (as well as Morley in a paper rejected by the Journal of Geophysical Research). The analysis of seafloor magnetic anomalies became a crucial tool

in understanding the seafloor spreading process. Excellent general accounts of the early developments in understanding midocean ridges are given by Wertenbaker [1974] and Uyeda [1978].

After the spreading of the seafloor was proved, the mechanics of the process became a major subject of study. Hess' simple idea, that the ridges represented upwelling limbs of convection cells, was no longer tenable. Simple geometric considerations (for example, the fact that Antarctica is surrounded by ridges) showed that ridges migrate with time. Tectonic history (for example, the west coast of North America) [Atwater, 1970] showed that ridges could encounter trenches and then cease to spread. Such behavior is difficult to explain in terms of a convection cell. In addition, one would expect such cells to have characteristic dimensions, while, in fact, trench-ridge distances vary by orders of magnitude. Thus ridges are now generally considered "passive" features, at which mantle material upwells, whose location is determined by plate motions [Sleep, 1969; Lachenbruch, 1973, 1976; Sleep and Rosendahl, 1978].

As the plates spread away from the ridge, the lithosphere thickens and cools. This effect can be seen both in heat flow measurements, and from the increase in ocean depth with the square root of age [Sclater and Francheteau, 1970]. Thus an extremely simple thermal plate cooling model can explain the morphology and heat flow at some distance from the ridge.

The situation is more complicated very near the ridge. The topography is rougher, and the mechanics are more complicated. This is clear from examination of the magnetic anomaly data. In

particular, as discussed in the following two chapters, the plates sometimes spread both asymmetrically (one flank faster than the other) and obliquely (spreading direction not perpendicular to the ridge). This can frequently be seen from surface ship data, and is quite clear from deep tow data. Figure 1.1 [Macdonald, 1977] shows bathymetry and magnetics in the FAMOUS area, Mid Atlantic Ridge. The ridge is spreading asymmetrically and obliquely. The following two chapters explore the mechanics of such processes.

Chapter 2 appears in Earth and Planetary Science Letters as Stein et al. [1977]. Chapter 3 is in press in the same journal [Stein, 1978].

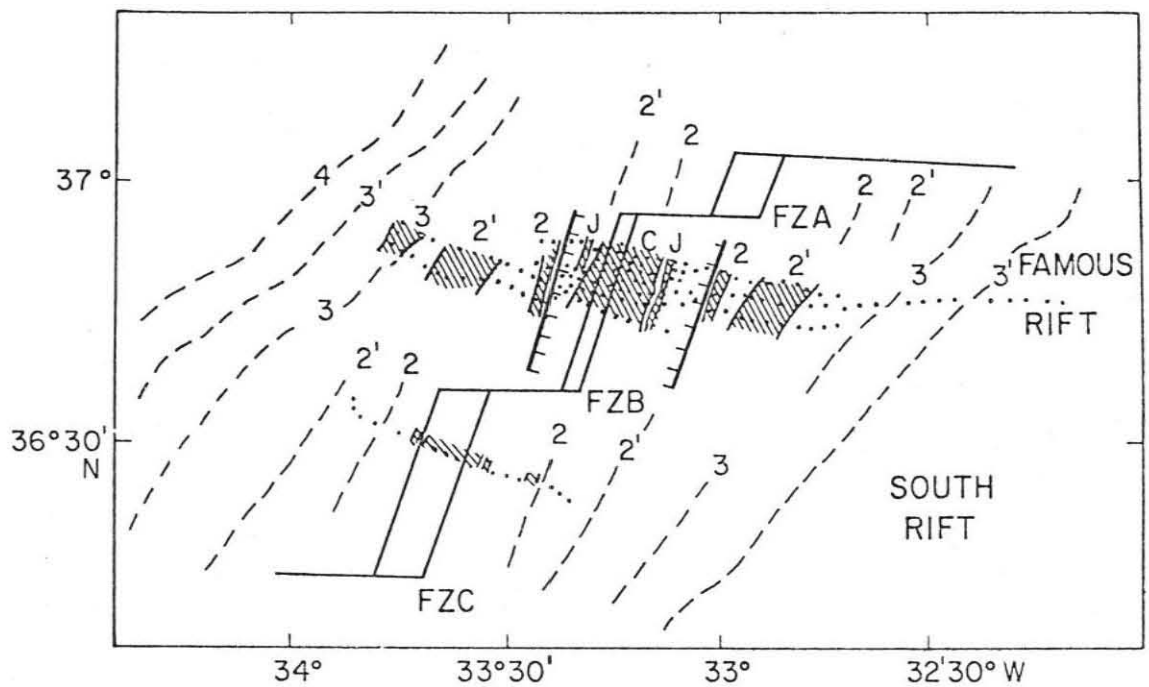

Figure 1.1. The FAMOUS (French American Mid-Ocean Undersea Study) area on the Mid-Atlantic Ridge (36°N, 33°W). Magnetic anomalies identified from deep tow data are shaded, those determined from surface ship data are dashed. Lines with tick marks indicate the rift valley walls. Spreading is asymmetric, with the east side fast (also see Figure 2.5). The spreading direction, as defined by fracture zones FZA, FZB and FZC, is 17° oblique to the spreading axis (double solid lines).

REFERENCES

Atwater, T., Implications of plate tectonics for the Cenozoic tectonic evolution of North America, Bull. Geol. Soc. Amer., 81, 3513-3536, 1970.

Ewing, M. and B. C. Heezen, Some problems of Antarctic submarine geology, in Amer. Geophys. Union Geophys. Monograph, 1, ed.,A. Cray et al., 75-81, 1956.

Heezen, B. C., M. Tharp and M. Ewing, The floors of the oceans. I. The North Atlantic, Geol. Soc. Amer., Special Paper 65, 1959.

Hess, H. H., History of the ocean basins, in Petrological Studies: A Volume in Honor of A. F. Buddington, ed. A. F. J. Engel, H. I. James and B. F. Leonard, 599-620, 1962.

Lachenbruch, A. H., A simple mechanical model for oceanic spreading centers, J. Geophys. Res., 78, 3395-3417, 1973.

Lachenbruch, A. H., Dynamics of a passive spreading center, J. Geophys. Res., 81, 1883-1902, 1976.

Macdonald, K. C., Near bottom magnetic anomalies, asymmetric spreading, oblique spreading and tectonics of the accreting plate boundary on the Mid Atlantic Ridge, near 37°N, Bull. Geol. Soc. Amer., 88, 541-565, 1977.

Menard, H. W., The East Pacific Rise, Science, 132, 1737-1746, 1960.

Sclater, J. G. and J. Francheteau, The implications of terrestrial heat flow observations on current tectonic and geochemical models of the crust and upper mantle of the earth, Geophys. J. Roy. Astr. Soc., 20, 509-542, 1970.

Sleep, N. H., Sensitivity of heat flow and gravity to the mechanism of seafloor spreading, J. Geophys. Res., 74, 542-549, 1969.

Sleep, N. H. and B. Rosendahl, Topography and tectonics of midocean ridge axes, Rev. Geophys., submitted, 1978.

Stein, S., A model for the relation between spreading rate and oblique spreading, Earth Planet. Sci. Lett., in press, 1978.

Stein, S., H. J. Melosh and J. B. Minster, Ridge migration and asymmetric seafloor spreading, Earth Planet. Sci. Lett., 36, 51-62, 1977.

Uyeda, S., The New View of the Earth, Freeman, San Francisco, 1978.

Vine, F. J. and D. H. Matthews, Magnetic anomalies over ocean ridges, Nature, 199, 947-949, 1963.

Von Herzen, R. P. and S. Uyeda, Heat flow through the eastern Pacific floor, J. Geophys. Res., 68, 4219-4250, 1963.

Wertenbaker, W., The Floor of the Sea, Little, Brown and Co., Boston, 1974.

Chapter 2

RIDGE MIGRATION AND ASYMMETRIC SEAFLOOR SPREADING

ABSTRACT

This chapter proposes that asymmetric seafloor spreading occurs as a consequence of the relative motion between ridges and slow moving mantle material below. A mechanical model of asymmetric spreading predicts that the trailing flank of a ridge migrating with respect to the mantle spreads fastest. Thus absolute motions can be used to predict a direction of asymmetry both of magnetic anomalies and bathymetry. These predictions are tested against published data and found to be in good agreement in most places. The magnitude of the asymmetry, however, seems to vary dramatically over short distances along a ridge. These details of the asymmetric spreading process are too complicated for this simple mechanical model to describe. The predictions of the ridge migration model are compared to those of asymmetric cooling models and models in which the ridge spreads asymmetrically so as to remain above a source fixed in the mantle, and appear acceptable.

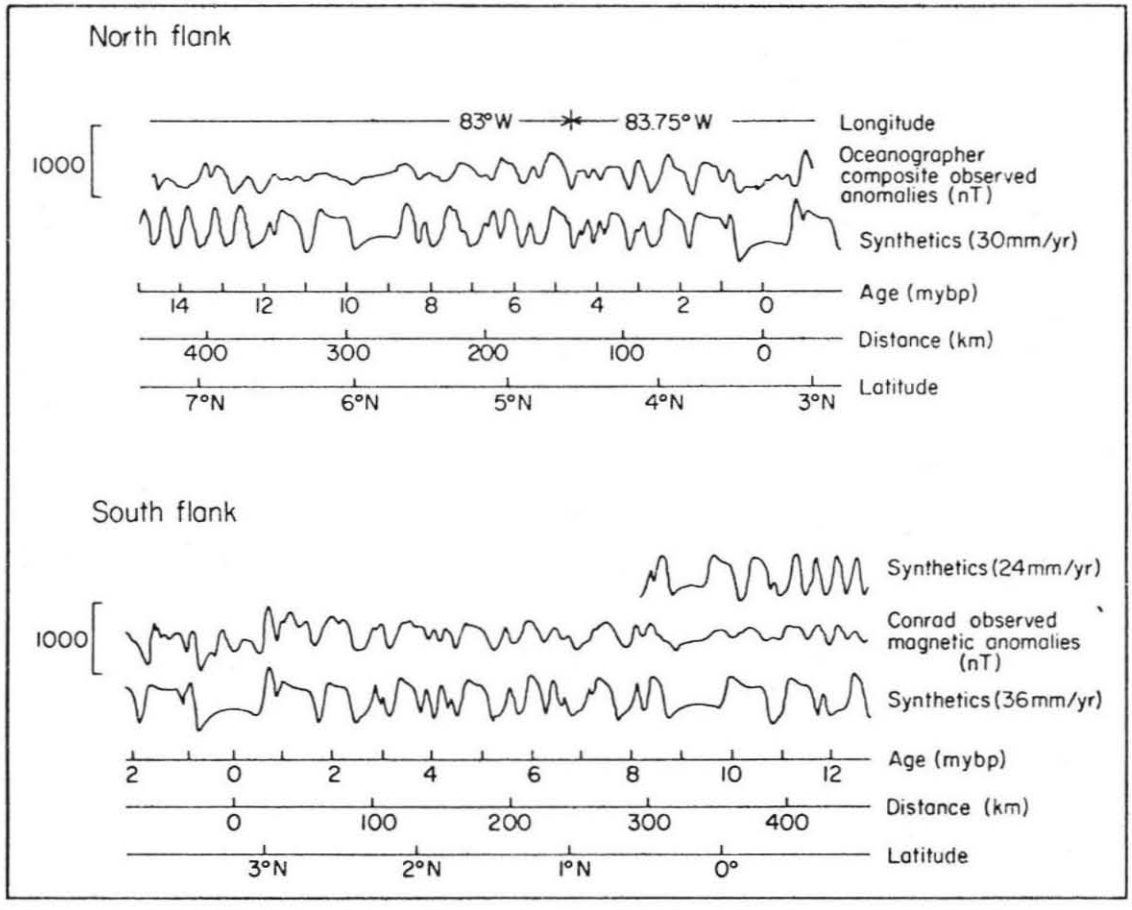

Figure 2.1. Magnetic anomalies on the eastern (Costa Rica) segment of the Cocos-Nazca rise [Hey, 1977]. The spreading rate is determined by generating synthetic anomalies and matching the data. The north flank is best fit with a half rate of 3 cm/yr; while the south flank is best fit by 3.6 cm/yr. Both fits are excellent for at least five million years.

INTRODUCTION

The first analyses of seafloor magnetic anomalies laid heavy emphasis on the striking symmetry of the profiles about the ridge. In general, both flanks were fit at any given time with the same spreading rates. For several years it was commonly believed that this was always the case, and a requirement of the spreading process.

The first possible case of asymmetric spreading was reported by Dickson, Pitman and Heirtzler [1968] who showed systematic differences in the distance from the ridge axis to anomaly 5 on the two flanks. They interpreted this, however, as due to possible misidentification of the ridge axis. It was not until several years later that the possibility of asymmetric spreading was explicitly stated. Weissel and Hayes [1971] suggested asymmetric spreading south of Australia and Herron [1971] noted it on the East Pacific Rise. In recent years it is becoming increasingly common to analyze spreading rate data without the preconception of symmetry. An especially striking example is shown by Hey [1977], Figure 2.1.

It is important to recognize that symmetric spreading is in no way a geometrical or mechanical requirement of the spreading process. The total spreading rate at a ridge is controlled by the separation of the rigid plates on either side, but this total spreading may be divided differently between the two ridge flanks. Thus the position of the ridge axis controls the difference of the two half spreading rates although their sum is fixed.

In this chapter we will explore a simple mechanical model of asymmetric spreading. The model suggests that the absolute motion of

the ridge with respect to a slowly moving mantle below influences the direction of asymmetric spreading. The data are limited and of varying quality, but, in general, they appear consistent with this hypothesis.

GEOMETRY OF RIDGE MIGRATION

Expressions are first derived to describe the relative motion between the lithosphere and mantle at a ridge. Using absolute plate velocity vectors it is possible to construct a vector which measures the migration of the ridge in the chosen absolute reference frame. This frame may be viewed as one fixed with respect to a slowly moving mantle [Morgan, 1972]. Using this migration vector, the mechanics of a ridge can be modeled to predict the eventual occurrence and direction of asymmetric spreading.

Consider two plates, i and j, with instantaneous rotation vectors $\vec{\Omega}_i$ and $\vec{\Omega}_j$ in a chosen absolute reference frame. At a point on the ridge $\vec{r}$, velocities on either side of the ridge are

$$\vec{V}_i = \vec{\Omega}_i \times \vec{r}$$

$$\vec{V}_j = \vec{\Omega}_j \times \vec{r}.$$

At some time later, the ridge has migrated to a new point. As shown in Figure 2.2, the velocity of the ridge is given by

$$\vec{a} = (\vec{V}_j + \vec{V}_i - 2\vec{V}_a)/2$$

where $\vec{V}_a$ is the correction vector due to any asymmetry of spreading. It is defined as

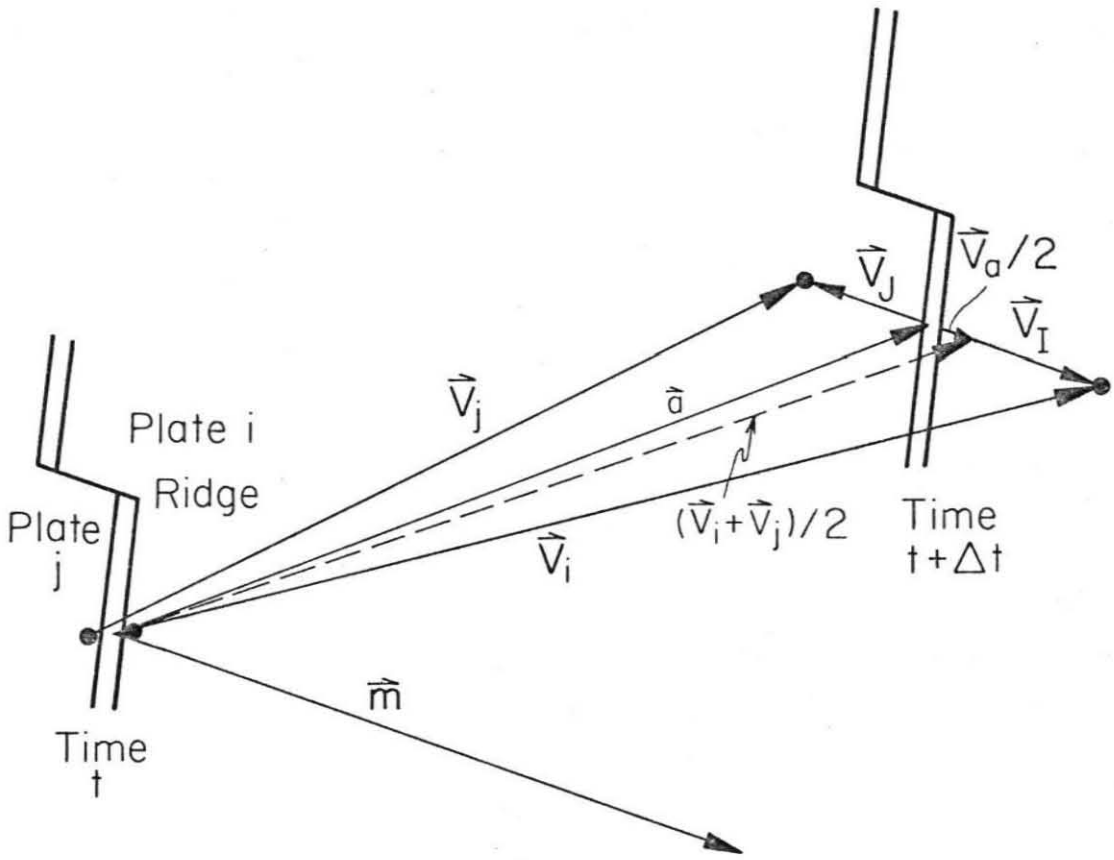

Figure 2.2. Geometry of ridge migration. $\vec{V}_i$, $\vec{V}_j$ are absolute motion vectors, $\vec{V}_I$, $\vec{V}_J$ are spreading vectors and $\vec{V}_a$ is the asymmetry vector, $\vec{m}$, is the migration vector, giving the component of the ridge's motion in the spreading direction with respect to the mantle.

$$\vec{V}_a = \frac{\vec{V}_I + \vec{V}_J}{2}$$

where $\vec{V}_I$ and $\vec{V}_J$ are vectors in the spreading directions whose magnitudes are equal to the half spreading rates on their respective plates.

These vectors are defined using a unit vector $\hat{i}$ which points away from the ridge toward the direction of spreading on plate i. In terms of the absolute velocity vectors $\vec{V}_i$ and $\vec{V}_j$ this vector is defined as $\hat{i} = (\vec{V}_i - \vec{V}_j)/|\vec{V}_i - \vec{V}_j|$ The spreading velocities of the plates relative to the ridge are thus $\vec{V}_I = V_I\hat{i}$ and $\vec{V}_J = -V_J\hat{i}$. This convention has been chosen to ensure that $\vec{V}_I$ and $\vec{V}_J$ are both positive.

The projection of $\vec{a}$ on the spreading direction $\hat{i}$ is

$$\vec{m} = (a \cdot \hat{i})\hat{i} = \frac{(\vec{V}_j + \vec{V}_i - 2\vec{V}_a) \cdot (\vec{V}_i - \vec{V}_j)}{2|\vec{V}_i - \vec{V}_j|^2} (\vec{V}_i - \vec{V}_j).$$

The migration vector, $\vec{m}$, is the component of the ridge's migration in the spreading direction. It can be used to identify the trailing flank of the ridge and predict the direction of asymmetric spreading.

A SIMPLE MECHANICAL MODEL FOR ASYMMETRIC SPREADING

Figure 2.3 shows a simple two dimensional model of an asymmetrically spreading ridge. Consider a frame of reference attached to the ridge, and a region of the crust and upper mantle enclosing it. The left hand plate moves away from the ridge with velocity $\vec{V}_I$ while the right hand plate moves with $\vec{V}_J$. At a depth h in the mantle (which may coincide with the base of the asthenosphere) there is a general flow of mantle material to the right with velocity $\vec{V}_m$. In general it is

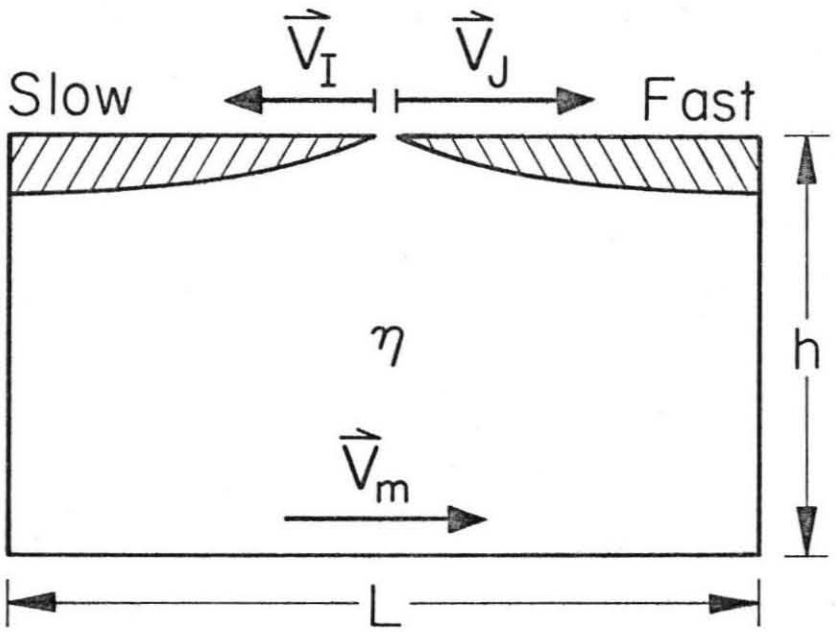

Figure 2.3. Geometry of the ridge dynamics model. The ridge is fixed in this frame of reference. Plate j is predicted to accrete faster, as it trails the migrating ridge. $\vec{V}_m$, the negative of the migration vector, gives the direction of mantle material flow in the ridge fixed frame.

assumed that this relative motion is produced by the migration of the ridge, rather than by motion within the stationary or slowly moving mantle. The mantle motion $\vec{V}_m$ is then the negative of the migration vector $\vec{m}$, $\vec{V}_m = -\vec{m}$.

The general framework of this model is that of a passively spreading ridge whose total spreading rate

$$V = |\vec{V}_J - \vec{V}_I|$$

is controlled by external forces. Note that V is the relative velocity of the two plates: it is independent of the velocity of either the plates or the ridge with respect to the deep mantle. The ridge may spread either symmetrically or asymmetrically, without altering the absolute velocities of either plate, as long as the total spreading rate is fixed. The asymmetry of spreading is described by the parameter A, (note that $\vec{V}_I$ and $\vec{V}_J$ are colinear)

$$(\vec{V}_J - \vec{V}_I)A = (\vec{V}_J + \vec{V}_I)$$

Thus, for symmetric spreading $\vec{V}_J = -\vec{V}_I$ and A = 0. If plate j does not accrete new seafloor material ($V_J = 0$), while plate i accretes at the total spreading rate V ($V_I = -V$), then A = -1. Conversely, if plate i does not accrete ($\vec{V}_I = 0$) while j spreads ($V_J = V$), A = +1. A positive asymmetry A indicates that the trailing flank of the ridge spreads fastest, as illustrated in Figure 2.1.

It is relatively easy to produce models in which this situation gives rise to asymmetric spreading. This can be done either by considering the upwelling mantle material as a fluid,

and determining the spreading geometry that will yield a minimum energy dissipation solution, or by considering the stresses on the rigid plates themselves.

The fluid mechanical argument is given in detail by Stein et al. [1977]. This result is easy to demonstrate qualitatively. Figure 2.2 shows that the total shear beneath plate i is of order $(|V_I| + |V_m|)/h$, while the shear beneath plate j is of order $(|V_J| - |V_m|)/h$. The total shear beneath plate i is always larger than that beneath plate j.

Each plate accretes new material from the mantle at a rate dependent upon the total spreading rate and the degree of symmetry. As a plate spreads away from the ridge the flow field induced by its accretion interacts with the shear flow beneath it. Since the energy dissipated is the square of the total strain rate, the total dissipation is largest where the shear flow is largest. Thus, plate i should accrete more slowly than plate j, since the shear (hence the energy dissipation rate) beneath it is larger than the shear (energy dissipation rate) beneath plate j.

Alternately, the same result can be seen by considering the stresses on the two plates. As the stresses are proportional to the strains, the leading plate (plate i) will be under higher shear stress and fracture. It seems reasonable that the ridge axis will then shift in that direction, resulting in plate j spreading faster. In this view we are considering asymmetric spreading to be the result of infinitesimal ridge jumps.

Thus it seems plausible that the motion of a ridge with respect to the mantle favors asymmetric spreading with the trailing ridge flank spreading faster. The detailed mechanism of this process, and the possible significance of the different stresses in either flank of the ridge merit more investigation than can be given here. Models of great complexity can be made to describe the process, but it is difficult to believe that such models represent the essential physics of the complex ridge system. It seems most useful to use this simple, intuitive model and attempt to determine if the predicted effect in fact occurs. As discussed later, this effect appears to be only a tendency that biases asymmetric spreading toward one direction. The actual magnitude of the asymmetry seems to be controlled by local effects, so that asymmetries can be predicted, at best, only qualitatively.

Finally, note that the asymmetric accretion of material which we have described does not involve any thermal perturbations on either flank of the ridge. The temperatures of the two flanks will be affected only by the different spreading rates. Thus this model predicts no deviation from the general relation between ocean depths and the square root of age shown by Sclater and Francheteau [1970]. This is important in considering different models of asymmetric spreading.

COMPUTATION OF MIGRATION VECTORS

The model described in the preceding section predicts a relation between ridge migration vectors and asymmetric spreading. To compute

migration vectors an absolute motion model must be chosen. Such models are determined by finding relative plate motions and then imposing a rigid body rotation of the entire lithosphere.

A variety of different approaches have yielded generally similar absolute motion models, so the migration vectors differ only slightly for different models. The model chosen is Model AM2 of Jordan [1975] which requires zero absolute motion for Africa. (The idea that Africa is stationary with respect to the mantle has also been proposed on geologic grounds by Burke and Wilson [1972].) A wide variety of absolute motion models are all generally consistent with the hot spot trace data [Jordan, 1975]. Selection of any one of these produces only minor changes in the direction of ridge migration vectors, except along the South Atlantic ridge and south of Africa. The asymmetric spreading model yields best results when the South Atlantic ridge is migrating west, which occurs if Africa is fixed.

The migration velocities computed from AM2 are shown on Figure 2.4. The arrows point in the direction of the ridge migration with respect to the deep mantle (assumed fixed in the hot spot frame) and have lengths proportional to the migration velocity. For convenience, the migration vectors are computed neglecting the small correction factor V_a, which is always much smaller than the total spreading rate. Also plotted is a small data set of asymmetries taken from published results discussed below. The shaded side of the rectangle shows the fast spreading side. Unshaded rectangles indicate symmetric spreading. The percentage of asymmetry is also

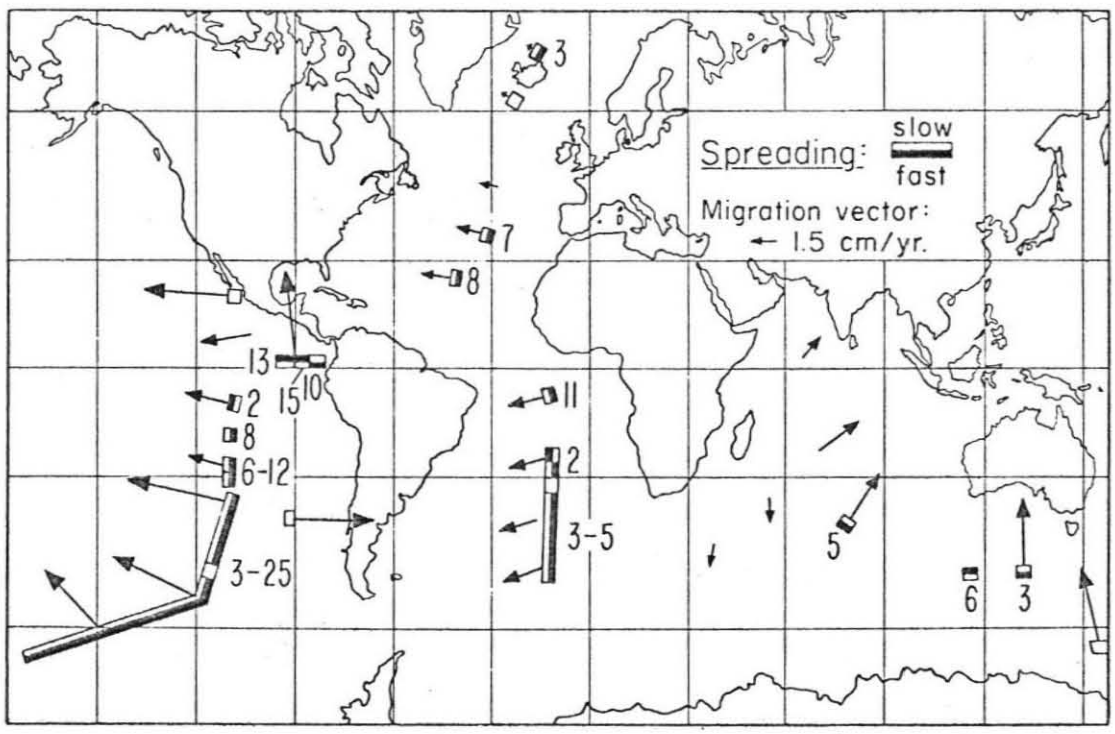

Figure 2.4. Computed migration vectors and observed asymmetries. Asymmetries are quoted as percentages: differences in spreading rates divided by the sum. Asymmetries are given over the longest period available at each location, but never beyond anomaly 5. (In areas of recent asymmetries and longer term gross symmetry, e.g., FAMOUS, the recent asymmetry is plotted.) In general the plate trailing the migrating ridge seems to spread faster.

indicated. (In areas of dense measurements the range is shown.)

DATA

Since the absolute motion model is based on instantaneous motions, only relatively recent data are used. Nothing beyond anomaly 5 (nine million years) is included in this data set. Possible consequences of this choice are explored below.

The literature was searched for published spreading rates, determined independently for both limbs. Only those compiled from profiles, rather than from processed contour maps, are used. In measuring and quoting asymmetries an attempt was made to exclude major shifts of the spreading axis, as a result of which entire anomalies are either repeated or lacking on one flank. On the other hand, smaller ridge jumps are difficult to separate from continuous asymmetric spreading, especially as one may be the limit of the other [Hey, 1977]. As this chapter attempts to predict asymmetric accretion with a simple model, rather than explore the precise mechanisms involved, such a distinction is not crucial for this purpose.

Spreading rates are available for several sites in the North Atlantic. Johnson et al. [1972] report asymmetry on the Kolbeinsey Ridge, north of Iceland: the east flank spreads at 8.2 mm/yr and the west at 7.7 mm/yr out to anomaly 5. (This interpretation has been questioned by Palmason [1973].) South of Iceland, on the Reykjanes Ridge, Talwani et al. [1971] show symmetric spreading.

The FAMOUS area (36°N, 33°E) has been extensively studied using both surface and deep tow instruments [Needham and Francheteau, 1974; Macdonald, 1977; Macdonald and Luyendyk, 1977]. Both rifts show evidence of asymmetric spreading. The north FAMOUS rift spread at a half rate of 7.0 mm/yr to the west, and 13.4 mm/yr to the east, until anomaly 2 (1.7 m.y.). Prior to this the direction of asymmetry reversed: 13.3 mm/yr to the west and 10.8 mm/yr to the east (Figure 2.5). These average to a smaller asymmetry over the last four million years, still with the east flank fast. The south FAMOUS rift spreads at 9.8 mm/yr to the west, and 10.6 mm/yr to the east (complete data are only available over Brunhes time. Despite these asymmetries surface magnetic data [Phillips and Fleming, 1975] for the FAMOUS area show gross symmetry over a much longer time period (ten million years).

At 26°N, Lattimore et al. [1974] report half-rates of 13 mm/yr to the east, and 11 mm/yr to the west out to anomaly 5. (Prior to this the direction of asymmetry appears to have oscillated.)

In the South Atlantic at 6-8°S, Van Andel and Heath [1970] show the east flank spreading faster with different rates out to anomalies 3 or 5. Further south, of seven measurements to anomaly 5 by Dickson et al. [1968], five show spreading faster to the east, one shows symmetric spreading, and one shows spreading faster to the west. These are over a ridge length of 22° (28°S-50°S). Similar results are given by Loomis and Morgan [1973] for Project Magnet flights in the same area.

Thus along the Mid-Atlantic ridge there seems to be a strong

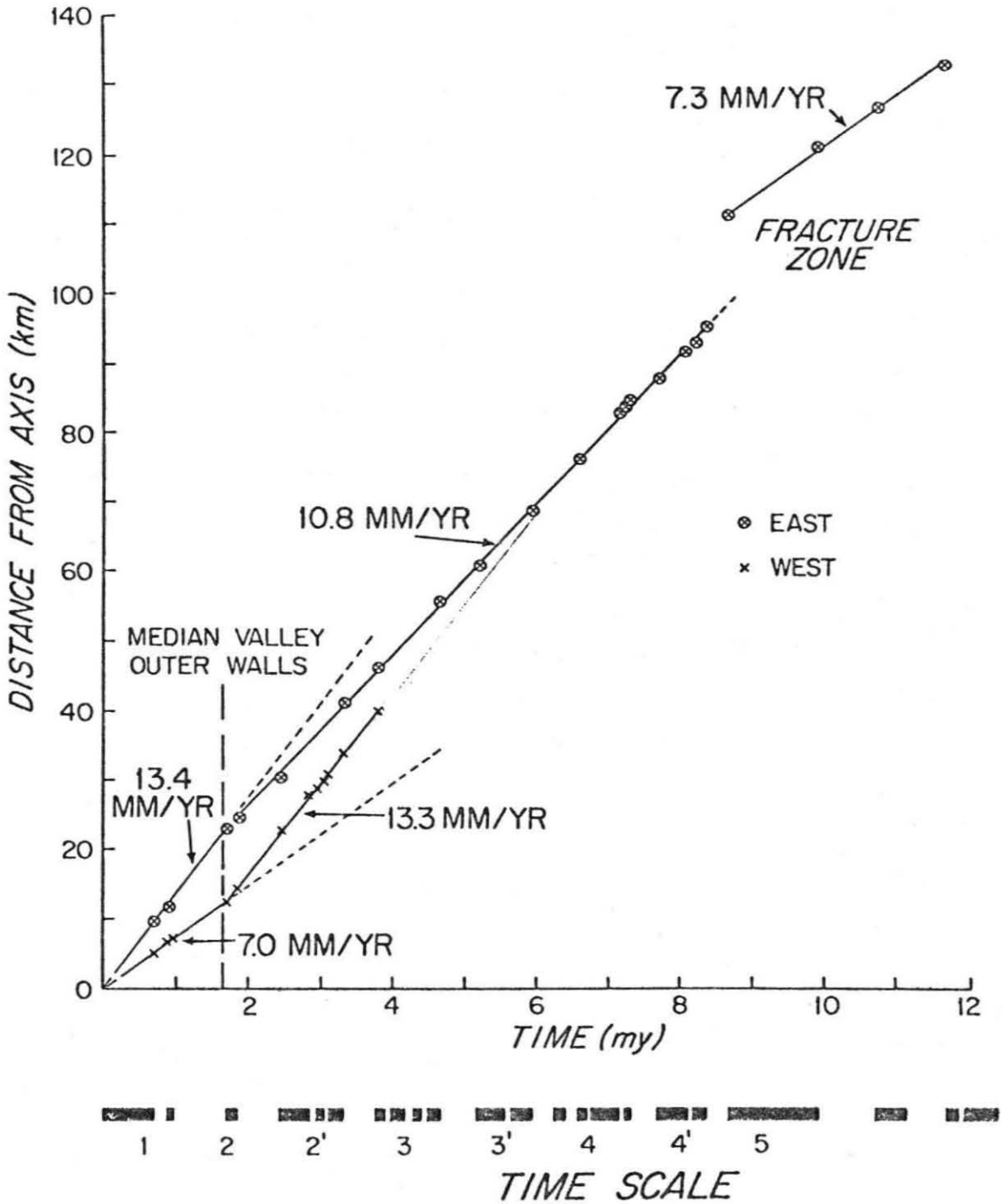

Figure 2.5. Magnetic anomalies as a function of distance from the ridge crest, FAMOUS area (see Figure 1.1) after Macdonald [1977]. This is a composite of all the deep tow data.

tendency for the east flank to spread faster than the west during the last several million years. This effect appears real, despite the difficulties involved in measuring spreading rates to the necessary accuracy over a slow spreading ridge. It also appears that over longer periods, tens of millions of years, the asymmetry has averaged out to produce a general symmetry.

Asymmetric spreading occurs at many locations in the Pacific. Klitgord et al. [1975] describe symmetric spreading on the Cocos-Pacific boundary at 21°N. Rea [1977] shows slight asymmetry at 9-12°S, on the East Pacific rise: 80 mm/yr to the west and 77 mm/yr to the east. Herron's [1971] two profiles further south (19°S, 28°S) show the Nazca plate to be spreading faster than the Pacific plate over the past five million years. At 31°S Rea [1977] finds average east and west flank rates of 86 and 77 mm/yr, respectively, since 2.41 m.y. ago. The Costa Rican rift at 83°W spreads faster to the south (Nazca) side than to the north [Klitgord et al., 1975]. Further west (86°W) the Galapagos ridge shows the reverse direction out to Jaramillo time [Klitgord et al., 1975]. Hey [1977] and Hey et al. [1977] also find the north flank spreading faster near the Galapagos (99°W-93°W), and the south flank faster at 83°W-84°W on the Costa Rican rift. The Chile ridge shows symmetric spreading [Klitgord et al., 1973].

The profiles of Molnar et al. [1975] in the South Pacific show the Antarctic side (out to anomaly 2 or 2') to be spreading faster in almost all cases over a range from 110°W to 180°W and 35°S to 65°S. Some of these profiles are shown in Figure 2.6. (Measuring only out to 2 or 2' avoids confusion with ridge jumps which appear on the

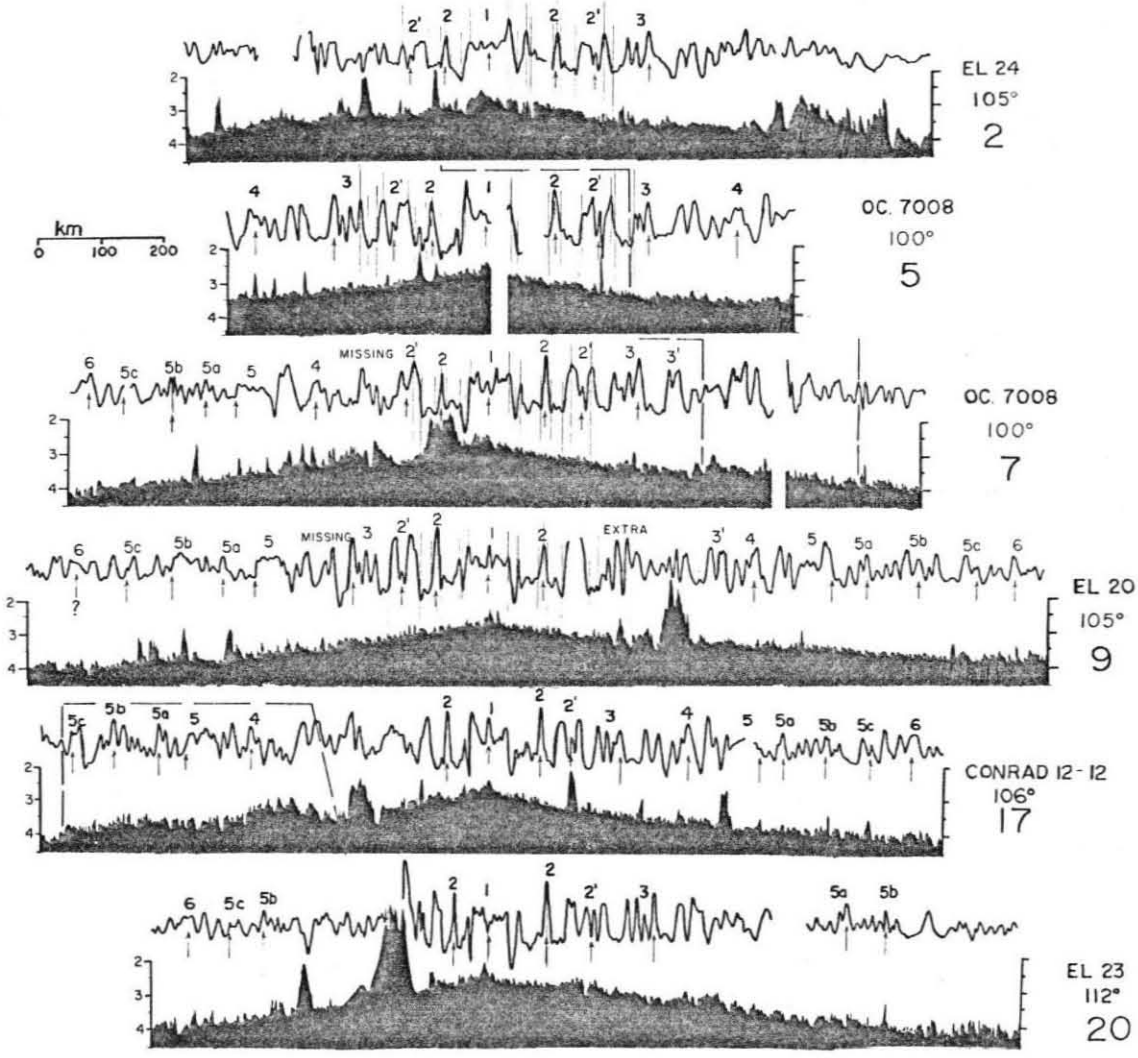

Figure 2.6. Magnetic anomalies and bathymetry across the East Pacific Rise, showing asymmetric spreading with the east (right) side fast. Ridge jumps appear as "missing" and "extra" anomalies, fracture zones as dashed lines.

same profiles.) This asymmetry was noted by Herron [1971]. Falconer [1972] reports symmetric spreading at 61°S, 161°E on the India-Antarctica boundary. South of Australia, Weissel and Hayes [1971] show one profile with the Indian side fast, and another with the reverse out to seventeen million years. (Prior to seventeen million years both profiles had the north side fast.) Further west, at 40°S, 80°W Schlich and Patriat [1971] (profile GA1-6, anomaly 1-2) shows Antarctic spreading faster than India.

It appears, then, that asymmetric spreading is a common worldwide phenomenon. Frequently the direction of asymmetry over the last several million years is the same for substantial distances along the ridge (for example, the mid-Atlantic and Pacific-Antarctic ridges).

ANALYSIS

The majority of these measurements are consistent with the prediction of this model: the flank trailing the migrating ridge spreads faster. Only a small fraction of the data show asymmetries opposite those predicted. Frequently the spreading is symmetric, but this model predicts a preferred direction of asymmetric spreading rather than its certain occurrence.

The most convincing evidence for a fundamental process of asymmetric spreading is the data [Dickson et al., 1968; Van Andel and Heath, 1970; Loomis and Morgan, 1973] in the South Atlantic and in the South Pacific [Molnar et al., 1975; Herron, 1971]. The consistency of the direction of asymmetry over thousands of kilometers argues against its being a purely local phenomenon.

On the other hand, the magnitude of the asymmetry varies considerably. Measurements (central anomaly to 2 or 2', or any more sophisticated scheme) on the South Pacific profiles yield asymmetries varying between 5 and 25 percent. Some of this variation may be due to noise in the data, but it still appears that the magnitude of the asymmetry is being controlled by local effects. Many processes at the ridge, unrelated to ridge migration, can influence the pattern of spreading. These include structural control of intrusion patterns, the shape and cooling history of magma chambers, and local irregularities in mantle flow.

The full complexity of the process of asymmetric spreading can be seen in detailed studies of the FAMOUS area [Macdonald, 1977; Macdonald and Luyendyk, 1977]. Two adjacent ridge segments approximately fifty kilometers apart have very different asymmetries. The direction and magnitude of asymmetry changes quite rapidly (in less than .15 m.y.). The spreading is quite oblique (17°). At least in this area, asymmetric spreading occurs on a very fine scale, with no evidence of discrete ridge jumps of more than several hundred meters.

Clearly no simple model of the dynamics of a ridge can adequately describe these local effects. Thus it would be surprising to find a simple relation between migration velocity and asymmetry. It would not be surprising to find occasional sites where local effects counteract or even reverse the effects of ridge migration.

Another possible problem is the assumption that the ridge is migrating much faster than any motion in the underlying mantle. If this assumption is violated then the migration vector will not predict

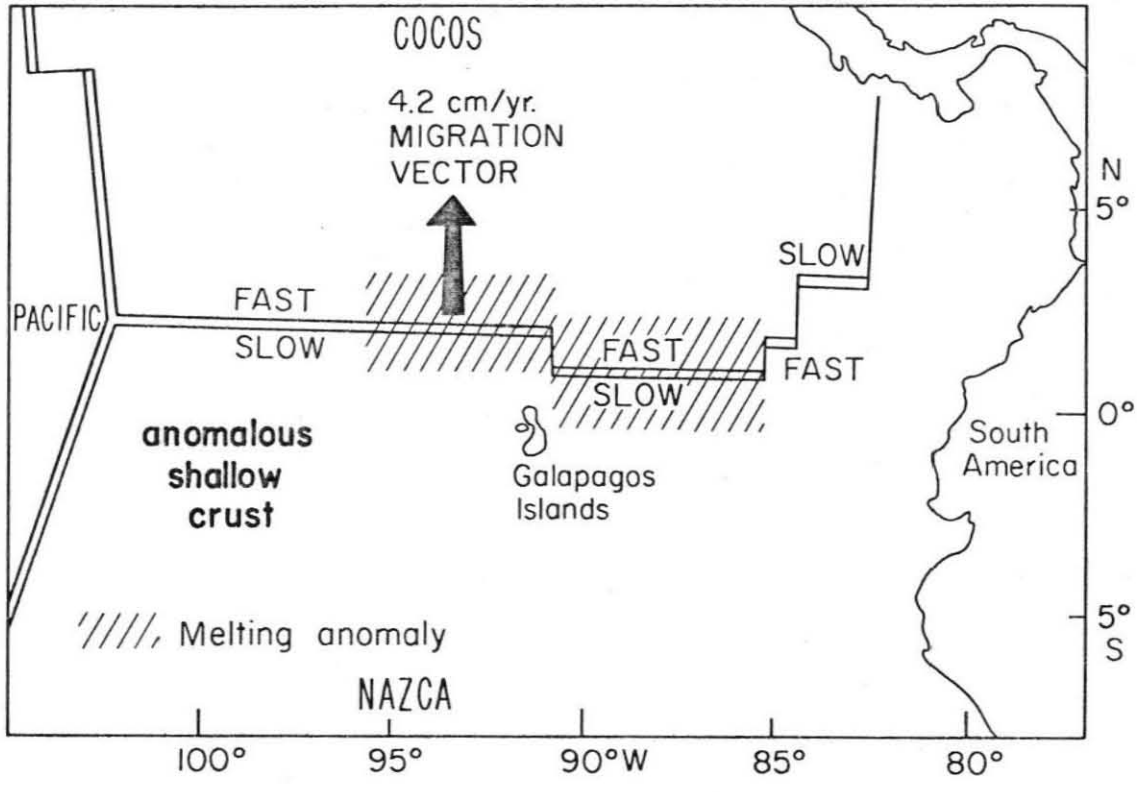

Figure 2.7. An interpretation of the Cocos-Nazca ridge data. The ridge migration model predicts that the south flank would spread faster, unless an outflow of material from the hot spot near the Galapagos Islands is reversing the direction of net mantle flow. The region affected by the possible hot spot outflow overlaps with the region of the Galapagos melting anomaly, and a region of anomalously shallow crust.

the asymmetry. This may be the case near the Galapagos hot spot. Hey [1977] and Hey et al. [1977] suggest that asymmetric spreading on the Galapagos Ridge is related to the hot spot to the south. If there is substantial outflow of material from the hot spot then the direction of net motion between the ridge and asthenosphere would be the reverse of that predicted by the migration vector. In such a case the north side, as observed, would be the fast spreading side. This area generally coincides with the anomalous petrology of the Galapagos melting anomaly [Anderson et al., 1975] often attributed to the hot spot. It is interesting to note that of two profiles shown by Klitgord et al. [1975] the one on the Galapagos Ridge (86°W) shows the north side fast, while further away (83°W) the south side is fast. Hey's [1977] and Hey et al.'s [1977] profiles at 99-93°W show the north side fast, and at 83-84°W also have the south side fast. Thus the Costa Rican rift may be far enough away that it is not affected by any outflow from the hot spot. This situation is shown in Figure 2.7. It is also interesting to note that the area south of the Cocos-Nazca Rise, and east of the East Pacific Rise, is one of anomalously shallow crust [Lonsdale, 1977a; 1977b]. This has been interpreted [Trehu, 1975] as a possible consequence of thermal effects due to upwelling at the Galapagos hot spot.

An alternative theory of asymmetric spreading has been advanced by Weissel and Hayes [1974] and Hayes [1976]. This model is based on their observation that bathymetric data south of Australia show depths on the south (Antarctic) flank of the ridge consistently shallower than to the north. The conventional depth-age relation would then imply

that the south flank is spreading faster. This is the direction of asymmetry predicted by our migration vector. Yet before seventeen million years their analysis of magnetic anomalies shows the reverse -- the north flank fast (both in "zone A" and "zone C").

To explain this discrepancy Hayes invokes a thermal model of asymmetric cooling in which the Antarctic plate is "hotter" and spreads more slowly. This model has been criticized in some detail by Fujita and Sleep [1978]. Using Sleep's [1975] thermal model of an asymmetrically spreading ridge, they show that higher temperatures persist at greater distances from the axis on the fast side, as shown in Figure 2.8. This causes preferential intrusions which reposition the ridge axis and thus oppose the asymmetric spreading. They also show that if a thermal perturbation related to a "hot spot" causes asymmetric cooling, thermal conduction would prevent the process from continuing for any appreciable length of time.

A second difficulty with this asymmetric cooling model is the prediction that in areas of asymmetric spreading the usual depth-age relation would be violated. Trehu's [1975] study of the South Pacific and Galapagos ridges shows that on both ridges the bathymetric asymmetries are in complete accord with magnetic asymmetries. This contradicts an asymmetric cooling model but agrees with a ridge migration model which predicts no anomalous thermal effects.

The final problem with the asymmetric cooling model is that it would require a symmetric and relatively uniform distribution of "hot spots" on the slower side in order to account for the apparent consistency of the direction of asymmetry over large segments of ridges. Thus

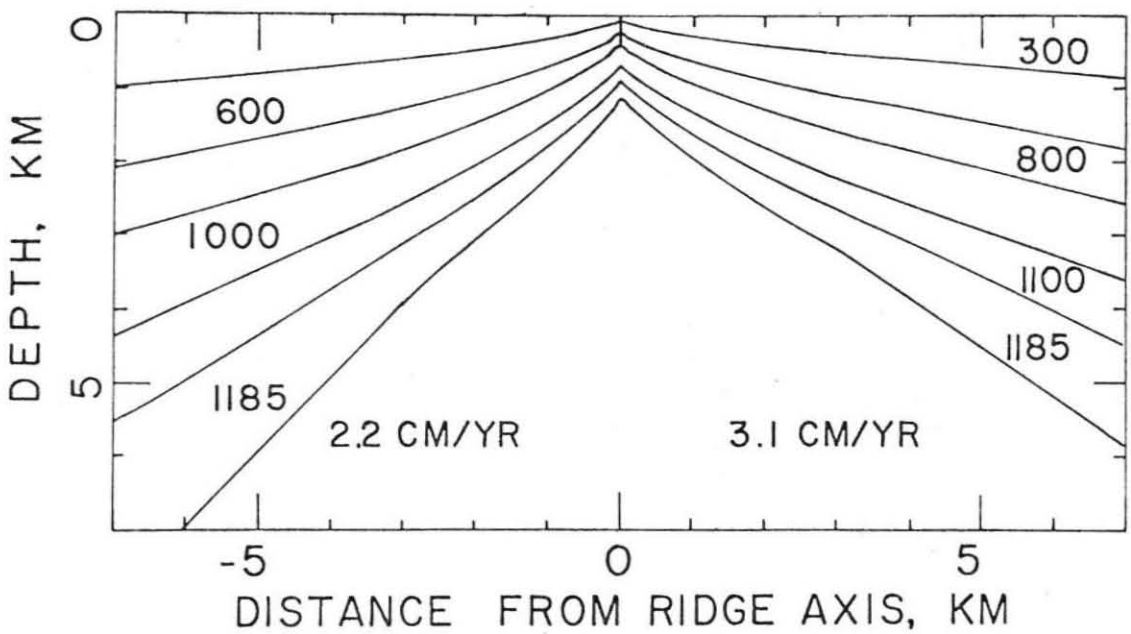

Figure 2.8. Thermal model of an asymmetrically spreading ridge [Sleep, 1975]. Temperatures are given in degrees Celsius. The fast spreading side is hotter at any distance from the ridge. If bathymetry is controlled by thermal contraction [Sclater and Francheteau, 1970], the fast spreading side would be shallower, as observed on the East Pacific Rise and Galapagos Ridge.

it seems unlikely that the phenomena observed south of Australia are representative of the general process of asymmetric spreading. Furthermore, the structural and bathymetric complexities of this area may indeed be due to some local effects, but asymmetric cooling is probably not an adequate explanation.

It is also worth noting that the direction of asymmetry predicted by any model in which the ridge attempts to remain above a source fixed in the mantle is the opposite of what a migration model predicts. Essentially, in such a model the leading flank of the migrating ridge would spread faster so as to prevent the ridge from moving away from its previous location. Most of the data seem to show the reverse -- the trailing flank spreads fastest.

This model does not allow for any prediction of asymmetries beyond about nine million years. Many authors [Van Andel and Heath, 1970; Loomis and Morgan, 1973; Klitgord et al., 1975] have shown spreading rate changes between the present and that time. Presumably, by the time of anomaly 5, plate rates were different enough to make the calculation of absolute motion models difficult. There is also the related difficulty that prior to that time hot spots may have had substantial relative motion [Molnar and Atwater, 1973]. It is thus difficult to determine the relation between older asymmetries and ridge migration.

Despite these difficulties, on a regional or global scale, the directions of the recent asymmetries seem well correlated with the direction of ridge migration. Further tests of this theory can be made by examining larger and more homogeneous data sets of magnetic

anomalies. The present data are not adequate to demonstrate conclusively that the effect proposed is real, though it is generally consistent with the model. Additional data would also allow increased resolution of the local details of the process of asymmetric spreading.

CONCLUSION

Ridge migration with respect to the mantle and asymmetric spreading appear related. The direction of the observed asymmetry seems to be that predicted by considerations of ridge mechanics and "absolute" motion models. Although this simple model does not completely describe the dynamics of the spreading process, it appears reasonable to expect that more complex and accurate models will also yield asymmetric spreading with a preferred direction resulting from ridge migration. Despite the noise in the data and random local effects, observations show a definite tendency for the plate trailing the migrating ridge to spread faster.

REFERENCES

Anderson, R. N., D. A. Clague, K. D. Klitgord, M. Marshall, and R. K. Nishimori, Magnetic and petrologic variations along the Galapagos spreading center and their relation to the Galapagos melting anomaly, Geol. Soc. Am. Bull., 86, 683, 1975.

Burke, K. and J. T. Wilson, Is the African plate stationary?, Nature, 239, 387-390, 1972.

Dickson, G. L., W. C. Pitmann, III, and J. R. Heirtzler, Magnetic anomalies in the South Atlantic and ocean floor spreading, J. Geophys. Res., 73, 2087-2100, 1968.

Hayes, D. E., Nature and implications of asymmetric seafloor spreading, Geol. Soc. Am. Bull., 87, 994-999, 1976.

Herron, E. M., Crustal plates and seafloor spreading in the Southeastern Pacific, Antarctic Oceanology I, Antarctic Research Series 15, 229-237, 1971.

Hey, R. N., Tectonic evolution of the Cocos-Nazca "spreading center", Geol. Soc. Am. Bull., 88, 1404-1420, 1977.

Hey, R. N., G. L. Johnson and A. Lowrie, Recent plate motions in the Galapagos area, Geol. Soc. Am. Bull., 88, 1385-1403, 1977.

Falconer, R. K. H., The Indian-Antarctic-Pacific triple junction, Earth Planetary Sci. Lett., 17, 151-158, 1972.

Fujita, K. and N. H. Sleep, Membrane stresses near midocean ridge-transform intersections, Tectonophysics, in press, 1978.

Johnson, G. L., J. R. Southall, P. W. Young, and P. R. Vogt, Origin and structure of the Iceland Plateau and Kolbeinsey Ridge, J. Geophys. Res., 77, 5688-5696, 1972.

Jordan, T. H., The present day motions of the Caribbean plate, J. Geophys. Res., 80, 4433-4440, 1975.

Klitgord, K. D., J. D. Mudie, P. A. Larson, and J. A. Grow, Fast seafloor spreading on the Chile ridge, Earth Planet. Sci. Lett., 20, 93-99 , 1973.

Klitgord, K. D., S. P. Huestis, J. D. Mudie and R. L. Parker, An analysis of near bottom magnetic anomalies: seafloor spreading and the magnetized layer, Geophys. J. R. Astr. Soc., 43, 387-424, 1975.

Lattimore, R. K., P. A. Rona, and O. E. DeWald, Magnetic anomaly sequence in the central North Atlantic, J. Geophys. Res., 79, 1207-1209, 1974.

Lonsdale, P., Structural geomorphology of a fast-spreading rise crest: the East Pacific Rise, near 3°25'S, Mar. Geophys. Res., 3, 251-294, 1977a.

Lonsdale, P., Regional shape and tectonics of the equatorial East Pacific Rise, Mar. Geophys. Res., 3, 295-316, 1970b.

Loomis, T. P. and W. J. Morgan, Seafloor spreading rate changes in the South Atlantic, Mar. Geophys. Res., 2, 3-9, 1973.

Macdonald, K. C., Near bottom magnetic anomalies, asymmetric spreading, oblique spreading, and tectonics of the accreting plate boundary on the Mid-Atlantic ridge near 37°N, Geol. Soc. Am. Bull., 88, 541-555, 1977.

Macdonald, K. C. and B. P. Luyendyk, Deep-tow studies of the structure of the Mid-Atlantic ridge crest hear 37°N (FAMOUS), Geol. Soc. Am. Bull., 88, 621-636, 1977.

Molnar, P. and T. Atwater, Relative motion of hot spots in the mantle, Nature, 246, 288, 1973.

Molnar, P., T. Atwater, J. Mammerickx and S. M. Smith, Magnetic anomalies, bathymetry and the tectonic evolution of the South Pacific since the Cretaceous, Geophys. J. R. Astr. Soc., 40, 383-420, 1975.

Morgan, W. J., Deep mantle convection plumes and plate motions, Bull. Am. Assoc. Pet. Geol., 56, 203-213, 1972.

Needham, H. D., and J. Francheteau, Some characteristics of the rift valley in the Atlantic Ocean near 36°48'N, Earth Planet. Sci. Lett., 22, 29-43, 1974.

Palmason, G., Comments on "origin and structure of the Iceland Plateau and Kolbeinsey Ridge" by G. L. Johnson, J. R. Southall, P. W. Young and P. R. Vogt, J. Geophys. Res., 78, 7019, 1973.

Phillips, J. D. and H. S. Fleming, The Mid-Atlantic ridge west of the Azores 35-39°N, Trans. Am. Geophys. Union (abstract), 56, 374, 1975.

Rea, D. K., Analysis of a fast spreading rise crest: the East Pacific Rise, 9-12°S, Mar. Geophys. Res., 2, 291-313, 1976.

Rea, D. K., Local axial migration and spreading rate variations, East Pacific Rise, 31°S, Earth Planet. Sci. Lett., 34, 78-84, 1977.

Rona, P. A., Asymmetric fracture zones and seafloor spreading, Earth Planet. Sci. Lett., 30, 109-116, 1976.

Sclater, J. G. and J. Francheteau, The implications of terrestrial heat flow observations on current tectonic and geochemical models of the crust and upper mantle of the earth, Geophys. J. R. Astr. Soc., 20, 509-542, 1970.

Schlich, R. and P. Patriat, Anomalies magnetiques de la branche Est de la dorsale medio-Indienne entre les iles Amsterdam et Kerguelen, C. R. Acad. Sci. Paris (B), 272, 773, 1971.

Sleep, N. H., Formation of oceanic crust: some thermal constraints, J. Geophys. Res., 80, 4037, 1975.

Solomon, S. C., N. H. Sleep and R. M. Richardson, On the forces driving plate tectonics: inferences from absolute plate velocities and intraplate stress, Geophys. J. R. astr. Soc., 42, 769-801, 1975.

Stein, S., H. J. Melosh and J. B. Minster, Ridge migration and asymmetric seafloor spreading, Earth Planet. Sci. Lett., 36, 51-62, 1977.

Talwani, M., C. C. Windisch, and M. G. Langseth, Jr., Reykjanes ridge crest: a detailed geophysical study, J. Geophys. Res., 76, 473-517, 1971.

Trehu, A. M., Depth versus $(age)^{1/2}$: a perspective on mid-ocean rises, Earth Planet. Sci. Lett., 27, 287-304, 1975.

Van Andel, T. H. and G. R. Heath, Tectonics of the Mid-Atlantic ridge, 6-8° south latitude, Mar. Geophys. Res., 1, 5-36, 1970.

Weissel, J. K. and D. E. Hayes, Asymmetric spreading south of Australia, Nature, 213, 518-521, 1971.

Weissel, J. K. and D. E. Hayes, The Australian-Antarctic discordance: New results and implications, J. Geophys. Res., 79, 2579-2587, 1974.

Chapter 3

A MODEL FOR THE RELATION BETWEEN SPREADING RATE AND OBLIQUE SPREADING

ABSTRACT

Atwater and Macdonald [1977] have suggested that oblique spreading occurs at midocean ridges which spread slowly (half rate less than 3 cm/yr), while the spreading is perpendicular at faster spreading ridges. This chapter explores this relation using the ratio of the power dissipated at ridges to that on transform faults to determine the most energetically favorable ridge-transform geometry. Simple models of a ridge and a transform show that the minimum energy dissipation configuration is a function of the spreading rate. The angle of oblique spreading (θ) is related to the spreading rate approximately by $\sin \theta \sim V^{-1}$. Thus oblique spreading is a natural result of ridge mechanics and need not be produced by external forces applied to the ridge.

INTRODUCTION

It is becoming increasingly clear that midocean ridges often spread such that ridge segments are not exactly perpendicular to their transform faults. A well known example of this is the FAMOUS area -- all three fracture zones are aligned about 17° from the perpendicular to the ridge crest (Figure 1.1) [Macdonald, 1977; Macdonald and Luyendyk, 1977]. Similar effects had previously been noted on many of the large North Atlantic fracture zones. Such features are long enough, and have enough topographic relief, that they can often be well surveyed by surface ship observations. Van Andel et al. [1971], showed that the Vema Fracture Zone (11°N, 43°W -- not to be confused with the Indian Ocean's Vema Fracture Zone discussed in Part I, Chapter 3) forms an angle of about 10° with the ridge segments to the north and south. They suggested that the morphology of the Vema Fracture Zone (a narrow trough with high walls) might be due to secondary spreading, associated with a reorientation of the fracture zone, induced by past changes in the direction of spreading along the ridge. Eittreim and Ewing [1975] reported a detailed seismic survey of the area, showing faulting in the sediments filling the fracture zone consistent with active transform faulting. Fracture zones further to the north [Collette et al., 1974] are also oblique to the spreading axis. Searle and Laughton [1977] conducted a survey using side-looking sonar of the Kurchatov Fracture Zone (40.5°N), and presented a detailed map (Figure 3.1) showing that the fracture zone is quite oblique to the ridge crest. Macdonald [1977] suggested that such oblique spreading was stable on the slow spreading Mid-Atlantic Ridge.

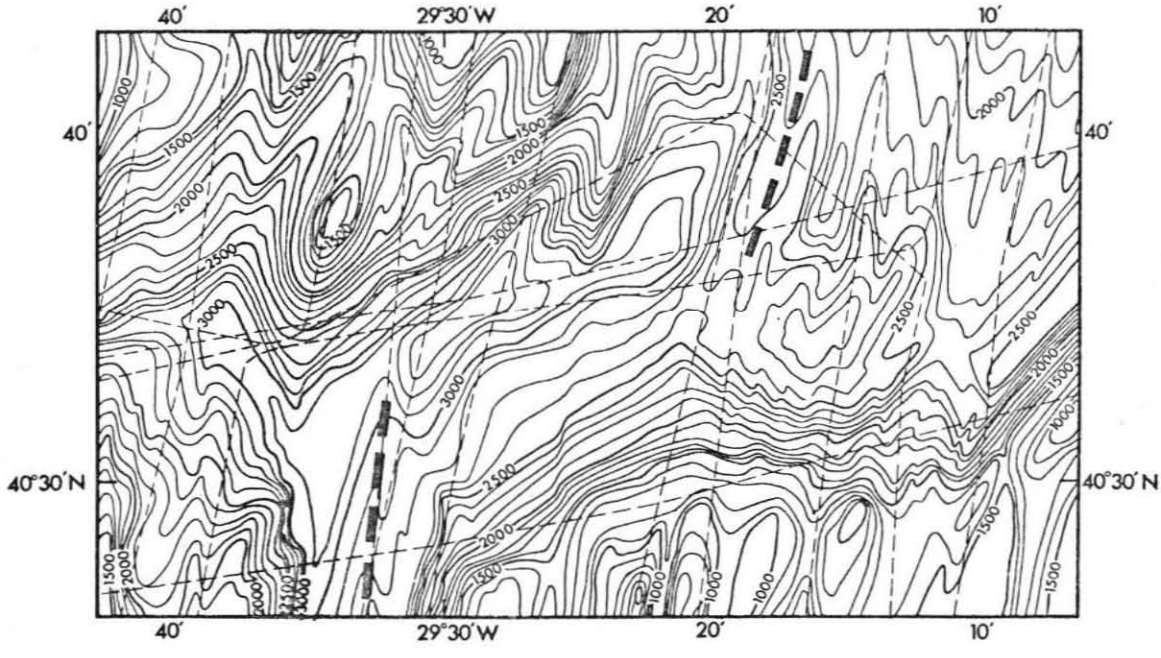

Figure 3.1. Side-looking sonar map of the Kurchatov Fracture Zone area [Searle and Laughton, 1977]. The heavy dashed lines represent the ridge axis. The transform fault is about 30° oblique; the half spreading rate is about 1 cm/year.

In contrast, fracture zones along the East Pacific Rise are almost exactly perpendicular to the ridge crest [Lonsdale, 1977a, 1977b]. Figure 3.2 shows the Quebrada and Gofar transforms in relation to the East Pacific Rise. Both are almost perpendicular to the adjacent ridge segments. Lonsdale [1977b] proposed that this orthogonality was characteristic of the fast spreading East Pacific Rise.

Atwater and Macdonald [1977] compiled data from a variety of spreading centers, and proposed a general relation between spreading rate and oblique spreading. They suggested that oblique spreading, with angles between 6 and 38°, occurs only on ridges with half spreading rate less than 3 cm/yr, while faster spreading ridges spread in a direction perpendicular to the ridge axis.

This chapter will attempt to provide a simple physical model for this phenomenon. This model attempts to have oblique spreading produced purely by the dynamics of the ridge, without requiring the imposition of external forces on factors such as changes in the direction of plate motions.

Although the problem of a velocity dependence of oblique spreading has not been explicitly studied, a closely related problem has. Lachenbruch and Thompson [1972] explored the issue of why transform faults and ridges were nearly orthogonal. They suggested that the ridge-transform configuration was a minimum energy state. The perpendicular configuration would result from a situation in which the rate of energy dissipation per unit ridge length was far greater than that per transform length. This stable configuration would be one which

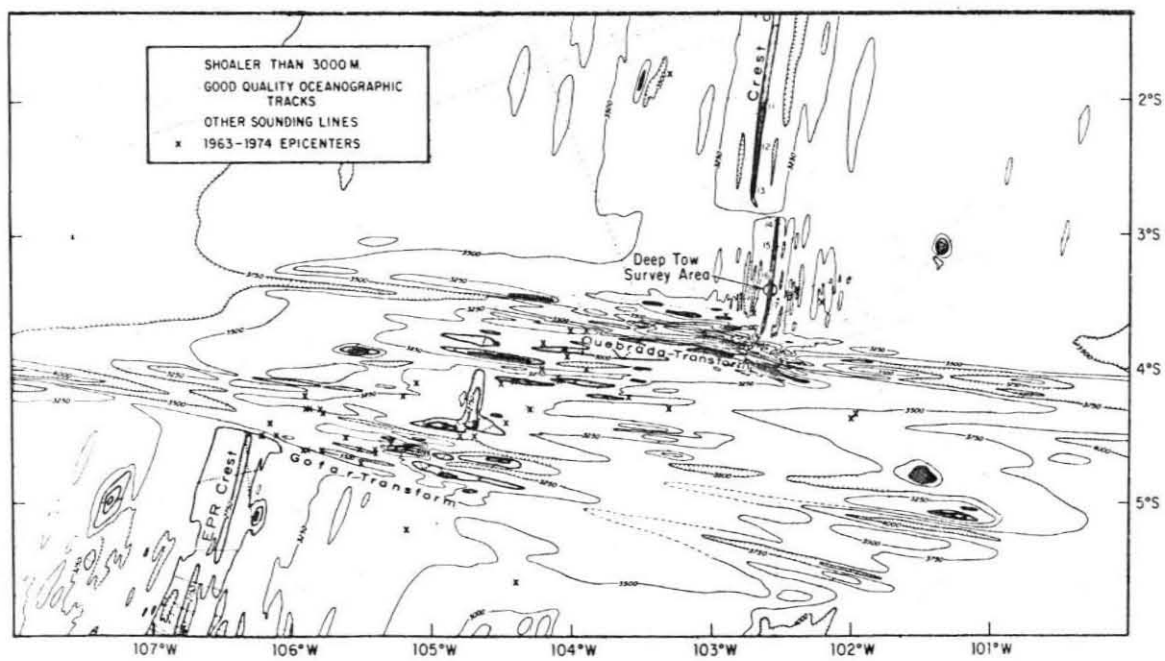

Figure 3.2. Bathymetry of the East Pacific Rise south of the triple junction, from Lonsdale [1977b]. The Quebrada and Gofar transforms are approximately perpendicular to the spreading axis. The half spreading rate is 7.7 cm/year. (Note that the ridge crest is changing strike across the survey area.)

minimized the length of ridge segments. Lachenbruch [1973] and Froidevaux [1973] explored the energetics of such a process.

To study the velocity dependence of such a process the spreading rate is explicitly included in models of both ridges and transforms. The ridge model is the conduit upwelling model introduced by Sleep [1969] and expanded by Lachenbruch [1973]. Transforms are modeled either as stable sliding faults or as viscous slip zones. The combination of conduit ridge and shearing fault gives a relation between oblique spreading angle Θ and half spreading rate V of $\sin \Theta \sim V^{-1}$. This crude model shows the general trend noted by Atwater and Macdonald [1977].

RIDGE-TRANSFORM GEOMETRY

The essential argument used by Lachenbruch and Thompson [1972] was that the ridge-transform system would adjust to a minimum energy state. If the power expended per unit ridge length is R_R and that per unit transform length is R_T, the stable configuration (Figure 3.3) is one which minimizes the total power dissipated. This can be found by considering the line from A to B, which trends at an angle β to the normal to the spreading direction. If A and B are separated by a distance L along the spreading direction, and a distance h perpendicular to it, the energy dissipated per unit time is

$$E = R_R \left(\frac{h}{\cos\Theta} \right) + R_T(L - h \tan\Theta).$$

The minimum dissipation solution is exactly correct for the slow steady motion of a viscous, isothermal, incompressible fluid, an approximation used for slow flow with velocity boundary conditions and conservative body forces [Batchelor, 1971]. In this case minimum dissipation can be derived either by uniqueness or from stability considerations using perturbations of the total kinetic energy [Glansdorff and Prigogine, 1971].

A more general form of the stability analysis can be derived using thermodynamic effects as well as the energy dissipation. This stability analysis gives the correct results for more complicated fluid problems, such as the onset of convection in the Rayleigh-Bénard problem [Glansdorff and Prigogine, 1971].

The limiting assumption of the stability analysis is that small perturbations of the flow from equilibrium are being considered. In our model we are perturbing the geometry of the problem (the ridge-transform configuration) and looking for the minimum dissipation configuration. We assume, as did Lachenbruch and Thompson [1972], that this proceedure, while not formally justified, will allow us to estimate the correct solution.

Thus, setting the derivative with respect to the oblique angle to zero, we find that

$$\sin \theta = R_T/R_R$$

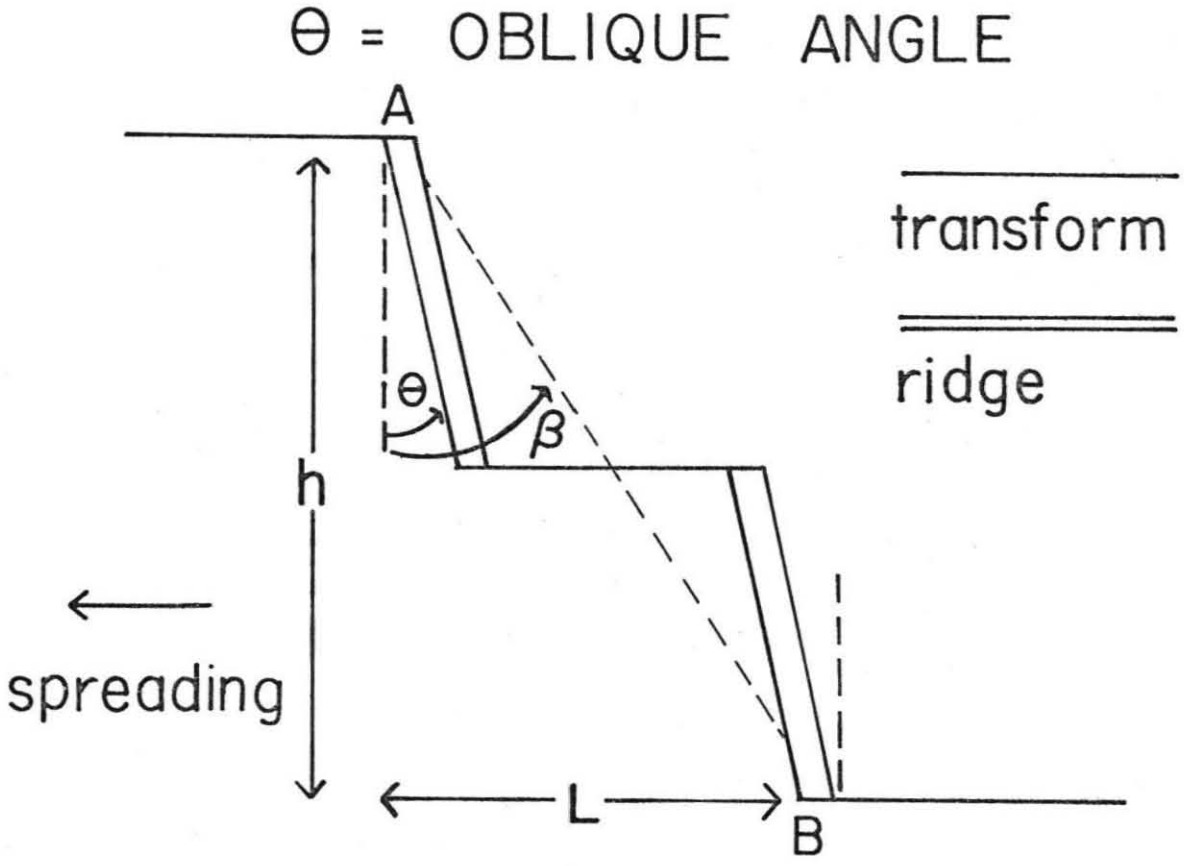

Figure 3.3. Definition of the angle of oblique spreading, Θ, and trend angle, β. The oblique spreading is such that the total transform length decreases and the ridge length increases relative to the perpendicular spreading configuration. The transform defines the spreading direction.

where θ is the angle between the ridge segment and the normal to the transform fault. The usual near orthogonality of ridges and transforms was cited as evidence that R_R is generally much greater than R_T. It is assumed that θ cannot exceed β, as this is clearly unfavorable energetically. Thus, the trend of the ridge-transform system imposes an upper bound on oblique spreading. The present system of ridges and transforms apparently often has enough trend locally to allow for some oblique spreading.

Atwater and Macdonald [1977] noted that when oblique spreading occurs, it acts to reduce the length of transform and increase the length of ridge. This is consistent with the minimum energy idea and suggests that for low spreading rates the ratio of transform energy dissipation to ridge energy dissipation rises somewhat. Thus oblique spreading occurs only on slow spreading ridges.

This phenomenon can be crudely described using simple models of a ridge and transform, which include the effects of spreading rate. The idea is to find the ratio

$$\frac{R_T}{R_R} = \frac{aV^m}{bV^n} = \sin \theta$$

such that m-n is less than zero, so that the slow ridges spread obliquely and the fast ones spread perpendicularly. Figure 3.4 shows the data of Atwater and Macdonald [1977] (also listed in Table 3.1) and a number of possible models. These curves are drawn with the FAMOUS data as a fixed point, since these are probably the best data.

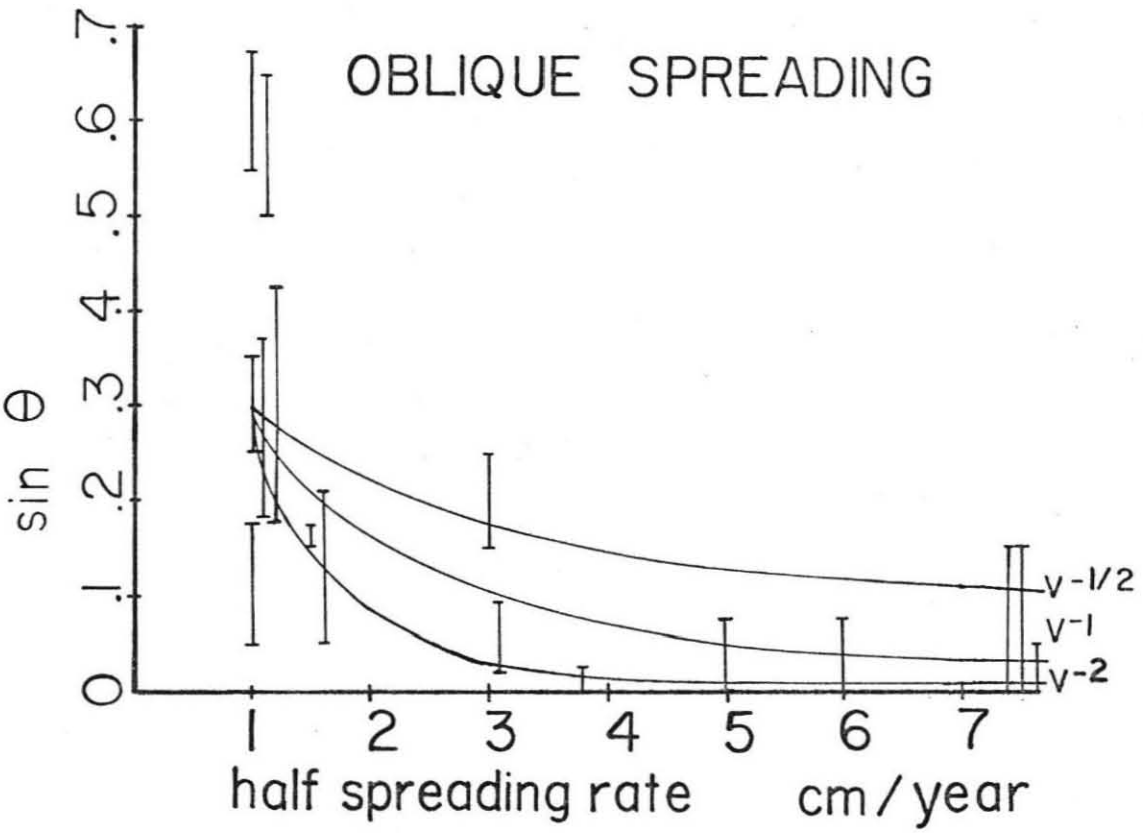

Figure 3.4. Data of Atwater and Macdonald, showing the angle of oblique spreading as a function of half spreading rate. Also plotted are curves for three power law dependences of sin Θ on V. All curves are normalized to the FAMOUS data.

Table 3.1

OBLIQUE SPREADING AND SPREADING RATE

[Atwater and Macdonald, 1977]

Location	Angle of Obliqueness	Half spreading rate (cm/yr^{-1})
Mid-Atlantic Ridge:		
11°N (Vema Fracture Zone)	9° ± 1°	1.5
15°N	7° ± 5°	1.5
30°N (Atlantis Fracture Zone)	6° ± 4°	1
37°N (FAMOUS Area)	17° ± 3°	1
40°N (Kurchatov Fracture Zone)	38° ± 5°	1
52°N (Charlie-Gibbs Fracture Zone)	35° ± 5°	1
Gulf of Aden:		
48°E	16° ± 6°	1
51°E (Alula-Fartak Fracture Zone)	18° ± 7°	1
Juan de Fuca Ridge:		
44°N (Blanco Fracture Zone)	11° ± 3°	3
Gulf of California:		
23°N (Tamayo Fracture Zone)	1° ± 3°	3
Galapagos Spreading Centre		
(Panama Fracture Zone)	2° ± 3°	3
East Pacific Rise:		
9°N (Siqueiros Fracture Zone)	0° ± 4°	6
3°S (Quebrada Fracture Zone)	0° ± 3°	7.5
6°S northern	4° ± 4°	7.5
southern	4° ± 4°	7.5
North East Pacific:		
40°N (Mendocino Fracture Zone)	0° ± 2°	3.7
34°N (Murray Fracture Zone)	-1° ± 3°	5.0

It is also worth noting (Figure 3.4) the large scatter in the data at slow spreading rates. This may be due, in part, to local variations in the angle β which controls the maximum oblique spreading allowed. We shall not attempt to explicitly include this effect, due to the small data set.

Ridge models are far too crude, and the data are too fragmentary to make it reasonable to derive exact values for the R_T/R_R ratio. It is probably worthwhile, though, to seek a model with an appropriate power law dependence on velocity. In this approximate sense any model with a/b of order one and m-m less than zero is acceptable. Clearly no such model is unique -- in a sense, it is sufficient rather than necessary.

TRANSFORM FAULT MODELS

This section presents two simple models of a transform fault, which show a dependence on the power dissipated on the spreading rate. The spreading rate dependence differs between the two models, and their effects can be contrasted.

First, consider the transform as a fault shearing in a stable sliding mode. In this case the sliding stress is assumed to be independent of velocity. Still, Figure 3.5 shows that the rate of work done on the transform depends on the spreading rate. This is because the lithosphere thickens as the square root of age

$$h(x) = C\sqrt{x/V}$$

and thus the transform area between two ridge segments a distance ℓ

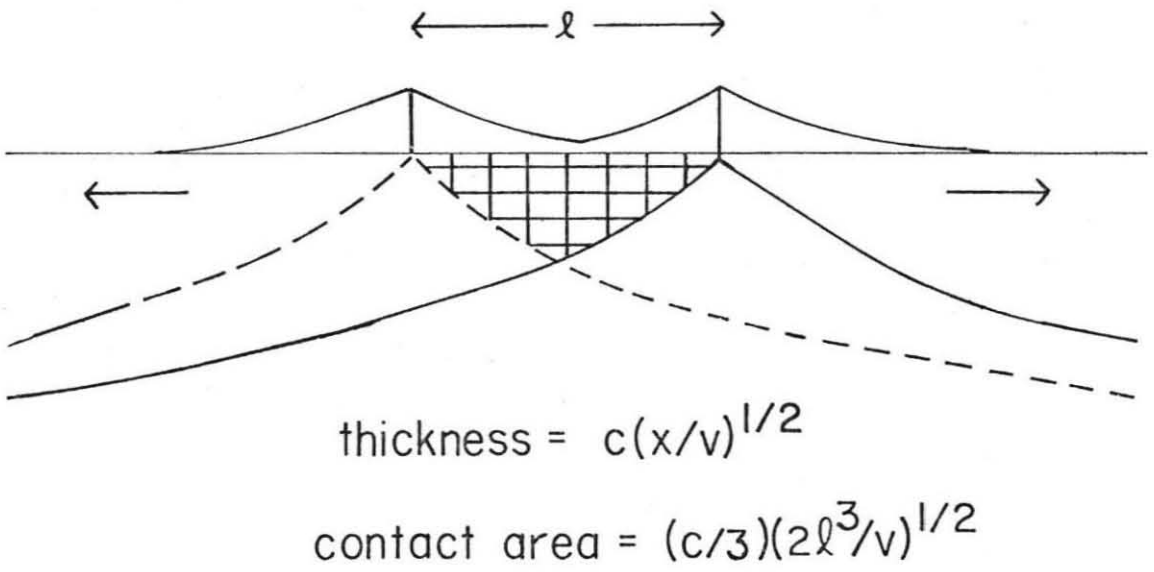

Figure 3.5. Schematic geometry of a ridge-transform fault system. The hatched area is the zone of relative motion, where energy is dissipated. This area increases as V decreases.

apart is

$$A = \frac{\sqrt{2}}{3} C \sqrt{\frac{\ell^3}{V}}$$

Thus, for a sliding stress σ_f, the power dissipated per unit length on the fault is

$$R_T = \frac{2A\sigma_f V}{\ell} = \frac{2\sqrt{2}\ \sigma_f C}{3} \sqrt{\ell\ V}$$

The power dissipated increases with spreading rate.

An alternate model [Froidevaux, 1973] is one in which the transform is a viscous shear zone. In this case, for a shear zone of width b,

$$R_T = \frac{2A\sigma V}{\ell} = \frac{4A\eta\dot{\varepsilon}V}{\ell} = \frac{8\sqrt{2}}{3b}\ \eta C\sqrt{\ell}\ V^{3/2}$$

The power has an additional factor of the spreading rate because the viscous stress depends on the strain rate.

We shall see later that it is difficult to reconcile such a high power law dependence with the observation that oblique spreading occurs on slow spreading ridges. The lower the exponent, the easier it will be to obtain this result. In addition, the stable sliding model is generally more consistent with heat flow measurements on faults [Brune et al., 1969] and seismic data [Kanamori and Anderson, 1975; Burr and Solomon, 1978] which show stress drops for transform fault earthquakes which do not appear to depend on the spreading rate.

RIDGE MODEL

To balance the power dissipated on the transform, we must estimate the power dissipated per unit ridge length in the spreading process. The model we use is one of the simplest available, that of fluid rising through a conduit. This type of model is extremely powerful, as it correctly predicts ridge topography: central rifts at low spreading rates, and central peaks at high spreading rates [Lachenbruch, 1973; Sleep and Rosendahl, 1978].

The model we will use here is derived for the case of two plates separating at constant velocity V, resulting in a suction which causes fluid to upwell between them. The conduit has width 2a and height H, and is filled with an incompressible Newtonian fluid of viscosity η and density ρ. Jaeger [1962] shows that the vertical and horizontal components of velocity are

$$W(x,z) = 3V(H-z)\ (a^2-x^2)/2a^3$$

$$U(x,z) = Vx(3a^2-x^2)/2a^3$$

The two dimensional flow is symmetric about the center axis and the horizontal velocity does not depend on z.

The energy dissipation rate of the system can be found directly

$$R_R = \int \sigma_{ij}\dot{\varepsilon}_{ij}\,dV = 2\eta \int \dot{\varepsilon}_{ij}\dot{\varepsilon}_{ij}\,dV$$

Since the fluid is incompressible, $\dot{\varepsilon}_{xx} = -\dot{\varepsilon}_{zz}$ and

$$R_R = 4\eta \int_{-a}^{a}\int_{o}^{H} (\dot{\varepsilon}_{zz}^2 + \dot{\varepsilon}_{zx}^2)\,dz\,dx$$

where

$$\dot{\varepsilon}_{xx} = \frac{3V}{2a^3}(x^2-a^2)$$

and

$$\dot{\varepsilon}_{xz} = \frac{3V}{2a^3}(z-H)x$$

The dissipation rate is then

$$R_R = 2\eta V^2\left(\frac{H}{a}\frac{24}{5} + \frac{H^3}{a^3}\right)$$

To use this result, it is necessary to estimate the dependence of the conduit width, 2a, on spreading rate. Lachenbruch found that the topography was best fit with $a \sim V^{1/3}$. Higher power dependences, such as V^1 yielded too deep central rifts, while V^0 yields rifts for high spreading rate and peaks for low rates, the opposite of which is observed. For $a \sim V^{1/3}$, the highest power term in R_R is $R_R \sim V^{5/3}$, while $V^{1/2}$ yields a leading term $R_R \sim V^{3/2}$. The precise value of this exponent is not crucial, as the model is quite crude. Inclusion of any one of a number of effects, any of which could justifiably be included, would change the exact value, as discussed later. The approximation $R_R \sim V^{3/2}$ will be used in the remainder of this discussion.

DISCUSSION

Using the stably sliding transform and ridge model defined previously, we find that

$$\sin\Theta \sim \frac{R_T}{R_R} \sim \frac{V^{1/2}}{V^{3/2}} \sim V^{-1}$$

This is the general trend sought earlier -- oblique spreading is favored on slow spreading ridges, while fast ridges are pendicular.

Certainly neither model nor data can resolve, for example, V^{-1} from $V^{-1/2}$ or V^{-2}, but it is satisfying to have a simple model for the velocity dependence of oblique spreading. Note that the viscous shear zone transform ($R_T \sim V^{3/2}$) makes it difficult to obtain such a relation.

An additional item to check is that R_T and R_R are of the same order of magnitude, or else it would not be possible to attribute any significance to the velocity dependence in the exponent. Very roughly, using the estimates

$$\eta = 10^{20} \text{ poise}$$

$$V = 1 \text{ cm/yr}$$

$$\sigma_f = 100 \text{ bars}$$

$$C = 8 \text{ km/(m.y.)}^{1/2}$$

$$\rho = 3 \text{ g/cm}^3$$

$$a = 1 \text{ km}$$

$$H = 3 \text{ km}$$

$$\ell = 10 \text{ km}$$

the power dissipated per unit length becomes $R_R \sim R_T \sim 10^6$ dynes/sec per cm ridge (or transform) length.

It is worth noting that the simple transform fault models given previously predict a dependence of transform fault resistance on fault length. This will occur for any model in which resistance is proportional to fault area. Thus, at constant spreading rate, the obliquity would be proportional to the square root of transform length. This phenomenon does not in fact seem to occur, as was noted by Atwater and Macdonald [1977] in their discussion of minimum energy arguments. For example, on the North Atlantic ridge the 330 km

Vema Fracture Zone is about 9° oblique, while the short (20 km) fracture zones in the FAMOUS area are about 17° oblique, and the 280 km Gibbs Fracture Zone is about 35° oblique. Thus, in Figure 3.2, transforms of different lengths are on the same graph.

One possible explanation for this discrepancy may be that the thickness of the zone of shearing never exceeds a certain maximum thickness. Thus the power dissipated per unit transform length would not increase with transform length above a critical length. This effect could be easily included in these calculations. If the general relation between spreading rate and oblique spreading is borne out by additional data it may be possible to resolve such effects.

The detailed mechanics of the ridge are extremely complicated, including temperature, viscosity and mechanical effects, and are not amenable to this type of simple model. Only sophisticated numerical models can attempt to include these effects [Sleep and Rosendahl, 1978]. The simple analytic model presented here, though, does indicate the general behavior to expect. It is also worth noting that the other common analytic ridge model, that of flow in a wedge [Batchelor, 1970; Skilbeck, 1975] would predict similar effects. The dissipation would go approximately as V^2a^2 (see equations A-4 of Stein et al., [1977]), and thus the ratio $R_T/R_R \sim V^{-5/2}$. Neither analytic model is really suitable for obtaining detailed resolution. The wedge solution predicts the wrong topography (deep rifts) at high spreading rates unless the viscosity of the upwelling material at fast ridges

is much lower than at slow ridges [Skilbeck, 1975]. The conduit solution encounters difficulties at rates greater than about 3 cm/yr, as the region of upwelling broadens rapidly and cannot be well modeled as a conduit [Sleep and Rosendahl, 1978].

Models like this one, which are based on minimum energy principles, are often used in studying slow viscous flow systems [Batchelor, 1970]. They are useful in identifying the state to which a system will evolve, but provide no information on the actual mechanics. For such a problem, again, numerical methods are required. Fujita and Sleep [1978] (Figure 3.5) have examined the stress field of a ridge-transform system and shown that the stress system near the ridge-transform corners is significantly distorted. This is especially true in the presence of an oblique external stress field. Such considerations may control the geometry of intrusion at the ridge, and presumably control the mechanical evolution of an oblique spreading system and other similar nonorthogonal ridge-transform geometries [Hey, 1977; Menard, 1978; Menard and Atwater, 1968; Shih and Molnar, 1975].

CONCLUSION

Using simple mechanical models of a ridge and transform fault, the ratio of power dissipated per unit length can be shown to depend on spreading rate. This ratio is approximately proportional to V^{-1}. Oblique spreading on slow spreading ridges is then favored on energy grounds, with $\sin \theta \sim V^{-1}$. This is in general accord with observations of oblique spreading.

REFERENCES

Atwater, T. and K. C. Macdonald, Are spreading centers perpendicular to their transform faults?, Nature, 270, 715-719, 1977.

Batchelor, G., An Introduction to Fluid Dynamics, Cambridge Univ. Press, Cambridge, 1970.

Brune, J. N., T. L. Henyey and R. F. Roy, Heat flow, stress, and rate slip along the San Andreas fault, California, J. Geophys. Res., 74, 3821-3827, 1969.

Burr, N. C. and S. C. Solomon, The relationship of source parameters of oceanic transform earthquakes to plate velocity and transform length, J. Geophys. Res., 83, 1193-1205, 1978.

Collette, B. J., K. Rutten, H. Schouten and A. P. Slootweg, Continuous seismic and magnetic profiles over the Mid-Atlantic Ridge between 12°N and 18°N, Mar. Geophys. Res., 2, 133-141, 1974.

Eittreim, S. and J. Ewing, Vema Fracture Zone transform fault, Geology, 3, 555-558, 1975.

Froidevaux, C., Energy dissipation and geometric structure at spreading plate boundaries, Earth Planet. Sci. Lett., 20, 419-424, 1973.

Fujita, K. and N. H. Sleep, Finite element models of the stress field of midocean ridges near transform faults (abstract), EOS Trans., AGU, 58, 494, 1977.

Fujita, K. and N. H. Sleep, Membrane stresses near midocean ridge-transform intersections, Tectonophysics, in press, 1978.

Glansdorff, P. and I. Prigogine, Thermodynamic Theory of Structure, Stability, and Fluctuations, Wiley, London, 1971.

Hey, R. N., A new class of pseudofaults and their bearing on plate tectonics, Earth Planet. Sci. Lett., 37, 321-325, 1977.

Jaeger, J. C., Elasticity, Fracture and Flow, Wiley and Sons, New York, 140, 1962.

Kanamori, H. and D. L. Anderson, Theoretical basis of some empirical relations in seismology, Bull. Seismol. Soc. Am., 65, 1073-1095, 1975.

Lachenbruch, A. H., A simple mechanical model for oceanic spreading centers, J. Geophys. Res., 78, 3395-3417, 1973.

Lachenbruch, A. H. and G. A. Thompson, Oceanic ridges and transform faults: their intersection angles and resistance to plate motion, Earth Planet. Sci. Lett., 15, 116-122, 1972.

Lonsdale, P., Structural geomorphology of a fast-spreading rise crest: the East Pacific Rise, near 3°25'S, Mar. Geophys. Res., 3, 251-294, 1977a.

Lonsdale, P., Regional shape and tectonics of the equatorial East Pacific Rise, Mar. Geophys. Res., 3, 295-316, 1977b

Macdonald, K. C., Near bottom magnetic anomalies, asymmetric spreading, oblique spreading and tectonics of the accreting plate boundary on Mid-Atlantic ridge near 37°N, Geol. Soc. Am. Bull., 88, 541-565, 1977.

Macdonald, K. C. and B. P. Luyendyk, Deep-tow studies of the structure of the Mid-Atlantic ridge crest near 37°N (FAMOUS), Geol. Soc. Am. Bull., 88, 621-636, 1977.

Menard, H. W., Breakup of the Farallon plate by pivoting subduction, J. Geol. Res., 86, 99-110, 1978.

Menard, H. W. and T. Atwater, Changes in the direction of seafloor spreading, Nature, 219, 463-467, 1968.

Searle, R. C. and A. S. Laughton, Sonar studies of the Mid-Atlantic Ridge and the Kurchatov Fracture Zone, J. Geophys. Res., 82, 5313-5328, 1977.

Shih, J. and P. Molnar, Analysis and implications of the series of ridge jumps that eliminated the Surveyor transform fault, J. Geophys. Res., 80, 4815-4822, 1975.

Skilbeck, J. N., On the fluid dynamics of ridge crests, Woods Hole Summer Program in Geophysical Fluid Dynamics Notes, 2, 113-122, 1975.

Sleep, N. H., Sensitivity of heat flow and gravity to the mechanism of seafloor spreading, J. Geophys. Res., 74, 542-549, 1969.

Sleep, N. H. and B. Rosendahl, Topography and tectonics of midocean ridge axes, Rev. Geophys., submitted, 1978.

Stein, S., H. J. Melosh and J. B. Minster, Ridge migration and asymmetric seafloor spreading, Earth Planet. Sci. Lett., 36, 51-62, 1977.

Van Andel, T. H., R. P. von Herzen and J. D. Phillips, The Vema Fracture Zone and the tectonics of transverse shear zones in oceanic crustal plates, Mar. Geophys. Res., 1, 261-283, 1971.

PART III

ATTENUATION STUDIES USING SPLIT NORMAL MODES

Chapter 1

INTRODUCTION

Following the observation of split peaks with varying amplitudes in the free oscillation spectra of the 1960 Chilean earthquake [by Ness et al., 1961 and Benioff et al., 1961], Pekeris et al. [1961] and Backus and Gilbert [1961] showed that the splitting could be explained by the earth's rotation. The $2\ell+1$ singlets in the multiplet of angular order ℓ are split such that each one has a distinct eigenfrequency, amplitude and phase. The individual singlets are also broadened by attenuation. Thus the splitting is observable only for low angular order (long period) multiplets for which the frequency separation due to splitting of the singlets is greater than the spectral line broadening due to attenuation. The combined effects of splitting and peak broadening due to attenuation pose substantial difficulty for Q measurements.

Conventional attenuation measurement techniques consider a single damped harmonic oscillator. In this case attenuation can be easily measured in either the time or the frequency domain. In the time domain the amplitude is given by

$$A(t) = e^{-\omega t/2Q} e^{i\omega t}$$

and Q can be found directly form the ratio of the amplitudes at two different times. Equivalently, Q can be determined from the shape of the spectral peak. This Lorentzian, or resonance curve, for a lightly damped system has a width $\Delta\omega$ when its amplitude reaches half of the maximum value. Q can then be found using

$$Q = \omega/\Delta\omega.$$

Unfortunately, the situation becomes more complicated when two oscillators with similar frequencies interfere. Their spectral peaks overlap, making it difficult to measure Q from the peak width. In the time domain, the two oscillators beat, producing a complicated interference pattern whose amplitude rises and falls with time. Attenuation, if present, is superimposed on the beat pattern. It is thus not possible to measure Q using the amplitude of the beat pattern as a function of time, without knowing the amplitude and phase of the individual oscillators.

To see this, consider the beating of two oscillators with the same Q

$$A(t) = \cos(\omega_1 t + \phi_1)e^{-\omega_1 t/2Q} + \cos(\omega_2 t + \phi_2)e^{-\omega_2 t/2Q}$$

This is approximately equal to

$$A(t) = 2 \cos\left[\frac{(\omega_1 + \omega_2)t + (\phi_1 + \phi_2)}{2}\right]$$
$$\times \cos\left[\frac{(\omega_1 - \omega_2)t + (\phi_1 - \phi_2)}{2}\right] e^{-\bar{\omega}t/2Q}$$

provided that ω_1 and ω_2 are close enough that their average ($\bar{\omega}$) can be used in the exponential. Q cannot be measured directly from the time series, as the amplitude is controlled by the beating. The net amplitude sometimes <u>increases</u> with time, in contrast to the pure decaying oscillator.

The real situation is far more complicated. Rather than two oscillators, we have $2\ell+1$ (five for ${}_0S_2$), each with their own eigenfrequency, phase and <u>amplitude</u>. It is not possible to derive a simple expression for this interference, either in the time or frequency domains which will isolate the terms involving Q. Thus, to measure Q,

it is necessary to know the amplitude and phase of each singlet, and to combine them to form a time series including the interference effects.

The following chapter demonstrates such a method. It is based on the results of Stein and Geller [1977] for the theoretical amplitude and phase of the singlets excited by an earthquake source of known fault geometry. These results are illustrated in Figure 1.1, from Geller and Stein [1977]. The figure shows the spectra of the spheroidal multiplets ${}_0S_2$ and ${}_0S_3$ excited by the Chilean earthquake, as observed on a strainmeter (striking 38.4°W of N) at Isabella, California. Dahlen's [1968] splitting parameters are used to identify the azimuthal order numbers of the peaks in Figure 1.1 and the center frequency is adjusted to give the best fit. The singlet pair with $m = \pm 1$ has much larger amplitudes than the rest of the ${}_0S_2$ multiplet and, similarly, ${}_0S_3^{\pm 2}$ stands out from its multiplet. (The results of a later analysis by Smith [1961] of the spectrum differed somewhat but did not alter the basic conclusion that ${}_0S_2^{\pm 1}$ and ${}_0S_3^{\pm 2}$ had much larger amplitudes than the other singlets of their multiplets.)

As well as the observed spectra, synthetic relative spectral amplitudes computed for the finite fault geometry determined by Kanamori and Cipar [1974] from long period surface wave studies ($\rho = 350°$, $\lambda = 90°$, $\delta = 10°$, $\theta_s = 128°$, $\phi_s = 286.5°$, $L = 800$ km, $V_R = 3.5$ km/sec) and including a precursory slip $t_p = 900$ sec and $\tau_0 = 300$ sec) inferred from a time domain observation [Kanamori and Cipar, 1974] are shown. Relative spectra for an isotropic point source, a model which was used by Pekeris et al. [1961] for the Chilean earthquake, are also shown. For both sources the spectral amplitudes do not depend on the precise frequency

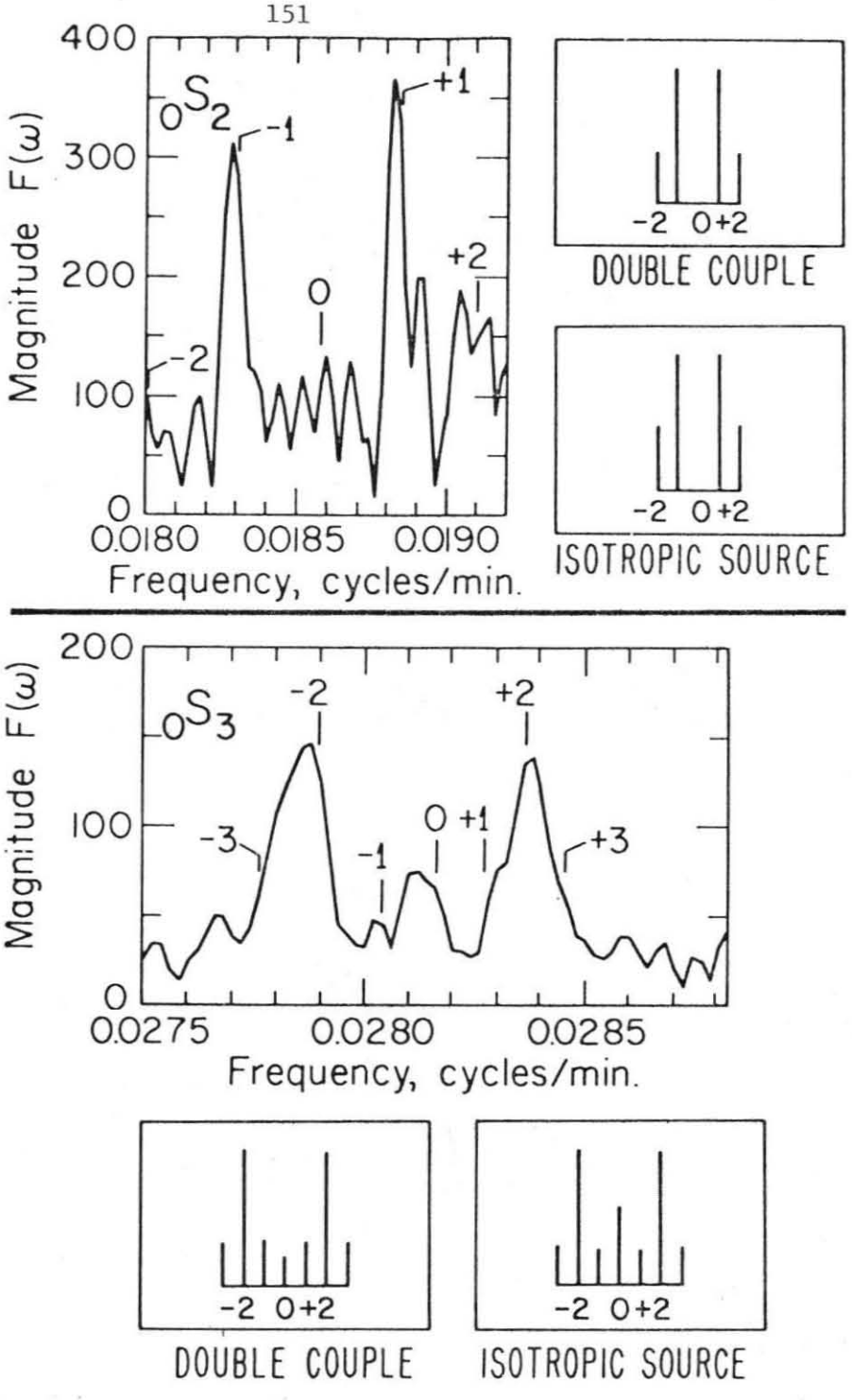

Figure 1.1. Split spheroidal mode spectra for $_0S_2$ (top) and $_0S_3$ (bottom) excited by the Chilean earthquake, as observed on a strainmeter at Isabella, California. The vertical scale of the observed eigenfrequency separation is taken from Dahlen [1968], but the central frequency has been chosen to yield a best fit with the observed peaks. Synthetic relative spectra for an isotropic source and for the finite fault geometry of Kanamori and Cipar [1974] are given for each mode. The amplitudes are normalized and plotted with regular spacing.

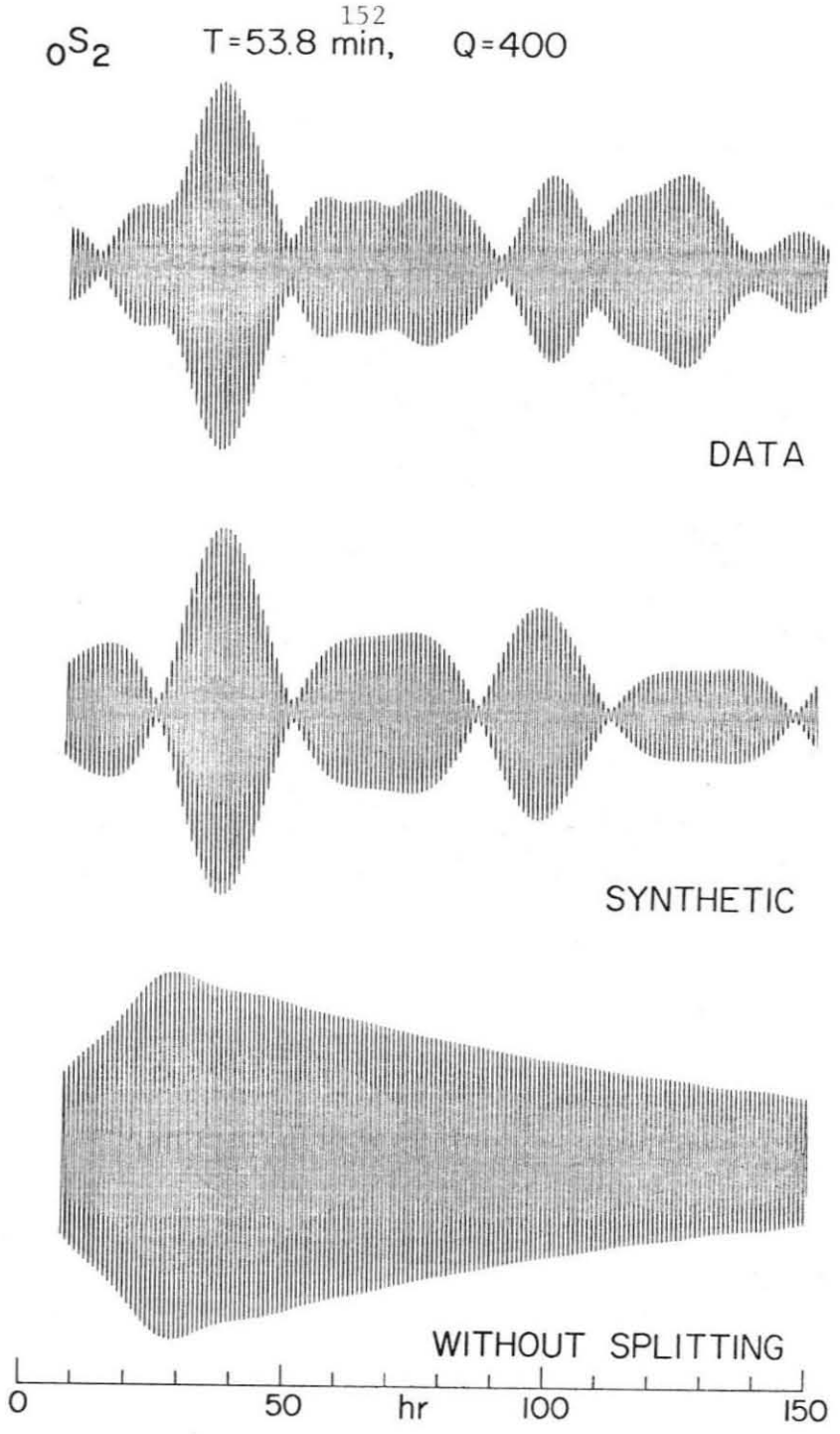

Figure 1.2. Data and synthetics for $_0S_2$. The top trace is filtered data from the high-passed Isabella strain record of the Chilean earthquake. The middle trace is the synthetic seismogram, including the effects of splitting, and the bottom trace is the synthetic without splitting. Both synthetics are computed using the same Q. The synthetics were tapered and filtered in the same way as the data.

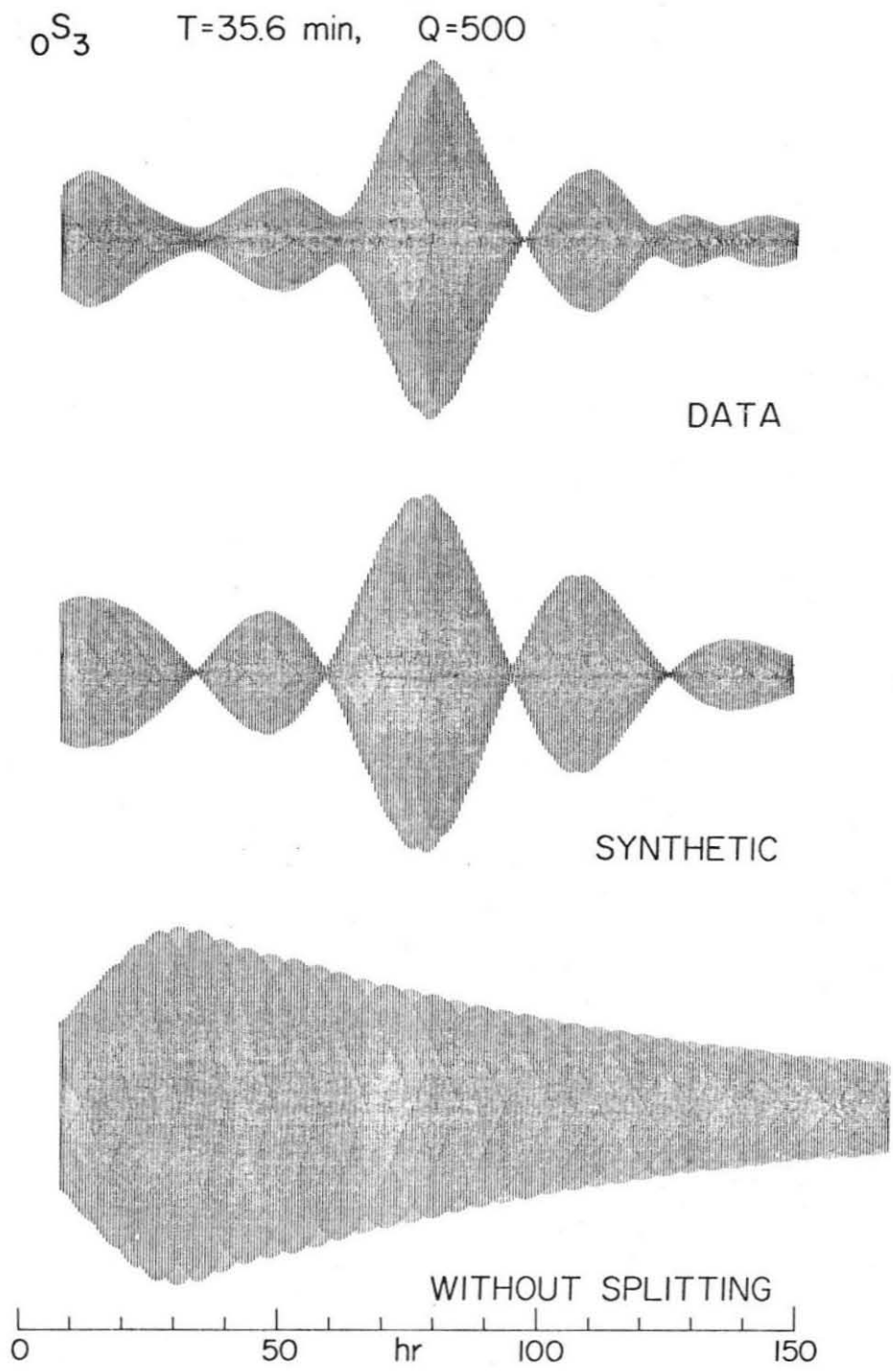

Figure 1.3. Data and synthetics for $_0S_3$. Details are as in Figure 1.2. Note that the maximum trace amplitude occurs eighty hours into the record.

separation, so for convenience the theoretical amplitudes are plotted with regular spacing, although the actual spacing is somewhat asymmetric. The amplitudes of the split modes are symmetric for a point source; interference effects may cause a slight asymmetry for a finite source. However, in this case the finiteness has only a negligible effect on the relative spectral amplitudes.

This makes it possible to describe the complex time series resulting from the interference of the singlets. Figure 1.2 shows the observed time series for the ${}_0S_2$ multiplet, and the synthetic time series predicted from the spectral amplitudes shown in Figure 2.1. The general envelope shape of these modes match the data quite well. Note the large peak at 35 hours for ${}_0S_2$ (Figure 1.2) and the peak at 80 hours for ${}_0S_3$ (Figure 1.3). The nodal times of the data and synthetics also agree quite well. It is therefore possible to estimate Q despite the interference. Similar results for ${}_0S_3$ are shown in Figure 1.3.

The following chapter applies this technique to the two best available data sets -- the Isabella strain meter record of the 1960 Chilean earthquake and the UCLA gravity meter record of the 1964 Alaskan earthquake. The Q_s of the lowest order spheroidal (${}_0S_2$, ${}_0S_3$, ${}_0S_4$, ${}_0S_5$) and torsional (${}_0T_3$, ${}_0T_4$) are estimated. In addition, the long (500 hour) UCLA gravity meter record is used to estimate the Q of the longest period radial mode (${}_0S_0$). These measurements are compared to previously obtained values.

REFERENCES

Backus, G. and F. Gilbert, The rotational splitting of the free oscillations of the earth, Proc. Nat. Acad. Sci. U.S., 47, 362-371, 1961.

Benioff, H., F. Press and S. Smith, Excitation of the free oscillations of the earth, J. Geophys. Res., 66, 605-619, 1961.

Dahlen, F. A., The normal modes of a rotating elliptical earth, Geophys. J. R. astr. Soc., 16, 329-367, 1968.

Geller, R. J. and S. Stein, Split free oscillation amplitudes for the 1960 Chilean and 1964 Alaskan earthquakes, Bull. Seism. Soc. Am., 67, 651-660, 1977.

Kanamori, H. and J. J. Cipar, Focal process of the great Chilean earthquake May 22, 1960, Phys. Earth Planet. Int., 9, 128-136, 1974.

Ness, N., J. Harrison and L. Slichter, Observations of the free oscillations of the earth, J. Geophys. Res., 66, 621-629, 1961.

Pekeris, C. L., Z. Alterman, and H. Jarosch, Rotational multiplets in the spectrum of the earth, Phys. Rev., 122, 1692-1700, 1961.

Smith, S. W., An investigation of the earth's free oscillations, Ph.D. Thesis, California Institute of Technology, 1961.

Stein, S. and R. J. Geller, Amplitudes of the split normal modes of a rotating, elliptical earth excited by a double couple, J. Phys. Earth, 25, 117-142, 1977.

Stein, S. and R. J. Geller, Time domain observations and synthesis of split spheroidal and torsional free oscillations of the 1960 Chilean earthquake: preliminary results, Bull. Seism. Soc. Am., 68, 325-332, 1978.

Chapter 2

ATTENUATION STUDIES USING SPLIT NORMAL MODES FOR THE 1960 CHILEAN AND 1964 ALASKAN EARTHQUAKES

INTRODUCTION

Measurements of attenuation were among the earliest analyses conducted on the normal mode data for the 1960 Chilean earthquake. The primary focus of interest was on the longest period modes with periods of greater than twenty minutes. Benioff et al. [1961] used spectral widths to measure the Q of ${}_0S_3$ from the Isabella record. Alsop et al. [1961b] used a time decay method to find the Qs of the low order spheroidal modes, and Ness et al. [1961] estimated the Q of ${}_0S_0$. Similar analyses were conducted on the data from the 1964 Alaskan earthquake. Smith [1972] summarized all long period Q results to that data, including those of Slichter [1967].

Additional studies of long period Q have recently been conducted [Sailor and Dziewonski, 1978; Buland and Gilbert, 1978]. This renewed interest is motivated by the need to correct earth models for the effects of physical dispersion caused by anelasticity [Akopyan et al., 1975, 1976; Liu et al., 1976], and a desire to derive models of the Q structure of the earth.

Difficulties introduced in measuring the Q of split modes were noted by Alsop et al. [1961a], who found that spectral peaks in two time intervals failed to decrease with time according to any simple law. In a later paper [Alsop et al., 1961b] they proposed conditions under which Q might successfully be measured, despite the splitting. The time domain Q measurement technique used in this chapter is valid without any such limiting assumptions.

This chapter reviews the method used to synthesize split normal modes for Q estimation. This method is then applied to the Isabella

strain meter record of the 1960 Chilean earthquake, and the UCLA gravity meter record of the 1964 Alaskan earthquake. The Q values obtained for the split spheroidal (${}_0S_2$ - ${}_0S_5$) and torsional (${}_0T_3$, ${}_0T_4$) modes are compared to previously published values. In addition, the Q of the unsplit fundamental radial mode (${}_0S_0$) is measured and compared to previous results.

THEORETICAL SPLIT MODE AMPLITUDES

This section summarizes the theoretical results [Stein and Geller, 1977] which allow us to synthesize the split normal mode amplitudes excited by a realistic model of an earthquake source: a double couple of arbitrary orientation resulting from slip on a fault plane. The full derivations are given by Stein and Geller [1977] and will not be repeated here.

The solution for the amplitudes of split modes is obtained by transforming the spherical harmonic expansion of the excitation from the frame of reference of the source into geographic coordinates. The singlet amplitudes are written so that there are separate factors for source location (latitude and longitude), source depth, fault geometry (strike, dip and slip direction), receiver location and the normalized energy of each mode.

For the spheroidal modes and for a step function dislocation with unit moment, the displacement, summing over modes with angular order ℓ and azimuthal order m, is given to zeroeth order by

$$\vec{U}^S(\vec{r},t) = \sum_{\ell=0}^{\infty} \sum_{m=-\ell}^{\ell} \left[\vec{E}_{\ell m}(\vec{r}) e^{i\omega_{\ell m} t} + \vec{E}^*_{\ell m}(\vec{r}) e^{-i\omega_{\ell m} t} \right] e^{-\omega_{\ell m} t/2Q_\ell}$$

where $\omega_{\ell m}$ is the eigenfrequency of the mode. The overtone number, n, will be suppressed for convenience throughout this section. Q is assumed constant for the entire multiplet.

The displacement spectral density of the ℓm-th mode is

$$\vec{E}_{\ell m}(\vec{r}) = D_{\ell m} \left\{ y_1^S(r)\ \vec{S}^1_{\ell m}\ (\theta,\phi) + y_3^S(r)\ \vec{S}^2_{\ell m}\ (\theta,\phi) \right\}$$

where $y_1^S(r)$ and $y_3^S(r)$ are the vertical and radial displacement eigenfunctions defined by Alterman et al. [1959] and implicitly depend on ℓ. θ and ϕ are the colatitude and longitude in geographic coordinates. Dahlen [1968] shows that when rotation and ellipticity are the only perturbations, the surficial eigenfunctions are, correct to zeroeth order, the vector spherical harmonics in geographic coordinates, $\vec{S}^1_{\ell m}$ and $\vec{S}^2_{\ell m}$:

$$\vec{S}^1_{\ell m}(\theta,\phi) = \left(Y_{\ell m}(\theta,\phi)\ ,\ 0\ ,\ 0 \right)$$

$$\vec{S}^2_{\ell m}(\theta,\phi) = \left(0\ ,\ \frac{\partial Y_{\ell m}(\theta,\phi)}{\partial \theta}\ ,\ \frac{1}{\sin\theta}\ \frac{\partial Y_{\ell m}(\theta,\phi)}{\partial \phi} \right)$$

where

$$Y_{\ell m}(\theta,\phi) = (-1)^m \left[\frac{(\ell-m)!}{(\ell+m)!} \right]^{1/2} P_\ell^m(\cos\theta)\ e^{im\phi} \quad (m \geq 0)$$

and

$$Y_{\ell m}(\theta,\phi) = (-1)^m\ Y^*_{\ell -m}(\theta,\phi). \quad (m < 0).$$

Here the associated Legendre polynomials are defined as

$$P_\ell^m(x) = (1-x^2)^{m/2}\ \frac{d^m}{dx^m}\ P_\ell(x)$$

and

$$P_\ell(x) = \frac{1}{2^\ell \ell!} \frac{d^\ell}{dx^\ell} (x^2 - 1)^\ell \quad .$$

The eigenfunctions are the vector spherical harmonics in the geographic coordinates (about the north pole), since we model the earth as being spherically symmetric. The only perturbations in the problem, rotation and ellipticity, are both symmetric about the rotation axis. To find the displacements, we need the excitation coefficients $D_{\ell m}$ for these vector spherical harmonics. These can be obtained from the excitation coefficients used for a nonrotating earth, which are computed in a frame of reference centered on the earthquake source (Figure 2.1). This has been done by Saito [1967].

To transform the excitation coefficients from the source coordinates to the geographic coordinates we make use of the rotation matrix elements [Brink and Satchler, 1968] which transform spherical harmonics from one coordinate frame to another. Since the excitation coefficients can be regarded as the components of a vector whose bases are the vector spherical harmonics, they, too, can be transformed from one frame to the other.

The rotation matrix elements are defined as

$$D^\ell_{mk}(R) = e^{-i(\alpha m + \gamma k)} \, d^\ell_{mk}(\beta)$$

where (summing over all values of t for which the factorials are non-negative),

$$d^\ell_{mk}(\beta) = \sum_t (-1)^t \frac{[(\ell+m)!\ (\ell-m)!\ (\ell+k)!\ (\ell-k)!]^{1/2}}{t!(\ell+m-t)!\ (\ell-k-t)!\ (t+k-m)!}$$

$$\times \ [\sin(\beta/2)]^{2t+k-m} \ [\cos(\beta/2)]^{2\ell+m-k-2t}$$

The argument of these functions is the set of Euler angles $R = (\alpha, \beta, \gamma)$

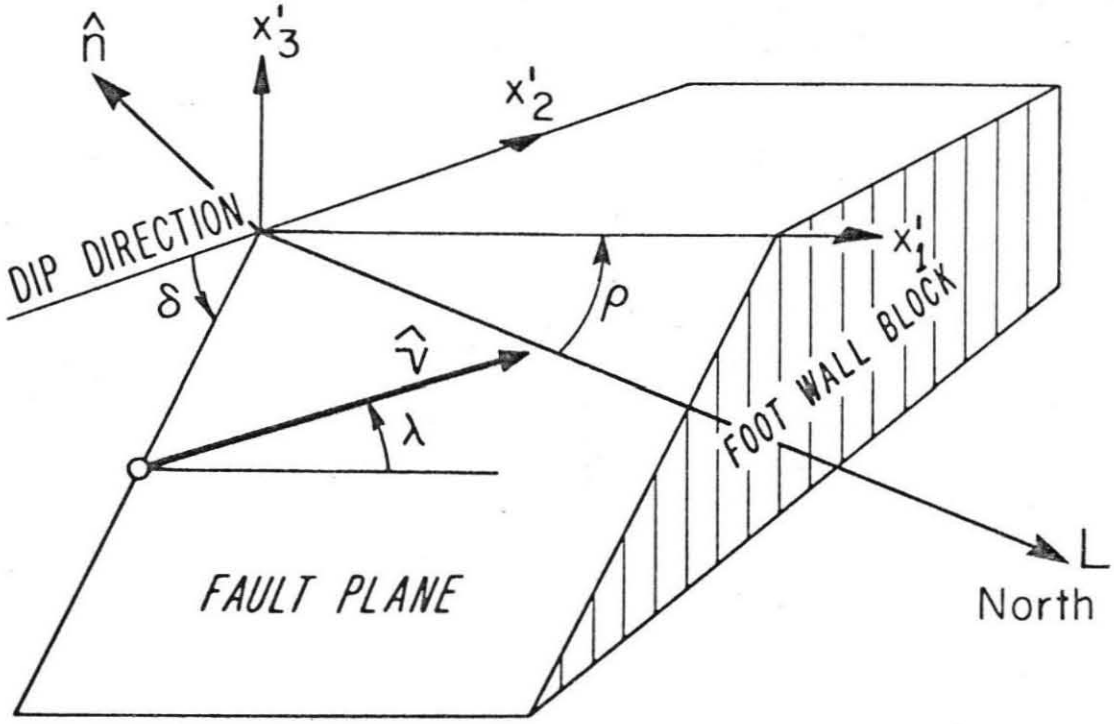

Figure 2.1. Fault representation of Kanamori and Cipar (slightly modified). $\hat{\nu}$ is the slip vector, and gives the displacement of the hanging wall block. $\hat{n}$ is the normal to the fault plane, and L points north. The strike ρ is measured counterclockwise from L. The dip angle δ is measured from the negative X_2' axis, and the slip angle λ is measured in the fault plane counterclockwise from X_1'.

that rotate the geographic coordinate system into the source coordinates. As shown in Figure 2.2, these angles are

$$\alpha = \phi_s$$

$$\beta = \theta_s$$

$$\gamma = \pi + \rho$$

where θ_s and ϕ_s are the epicentral coordinates and ρ is the fault strike, measured counterclockwise from north. We describe all quantities in the source coordinates by primes (X'_i, $D'_{\ell m}$) and their counterparts in the geographic coordinates without primes (X_i, $D_{\ell m}$).

The excitation coefficients transform from the source frame to the geographic frame as

$$D_{\ell m} = \sum_{k=-2}^{2} D^{\ell}_{mk}(R) D'_{\ell k}.$$

The summation ranges over -2 to 2, since for a point double couple only terms $D'_{\ell m}$ with $|m| \leq 2$ are excited. Once the excitation is transformed to the geographic coordinates, all the terms from $-\ell$ to ℓ are excited. For such a source, with unit moment and a step function time history, the source frame excitation coefficients can be expressed as

$$D'_{\ell 2} = K_2 q_2 \; C_{\ell 2}$$

$$D'_{\ell 1} = K_1 q_1 \; C_{\ell 1}$$

$$D'_{\ell 0} = K_0 q_0 \; C_{\ell 0}$$

$$D'_{\ell -1} = K_1 q_1^* \; C_{\ell -1}$$

$$D'_{\ell -2} = K_2 q_2^* \; C_{\ell -2}$$

The $C_{\ell m}$ are normalization constants

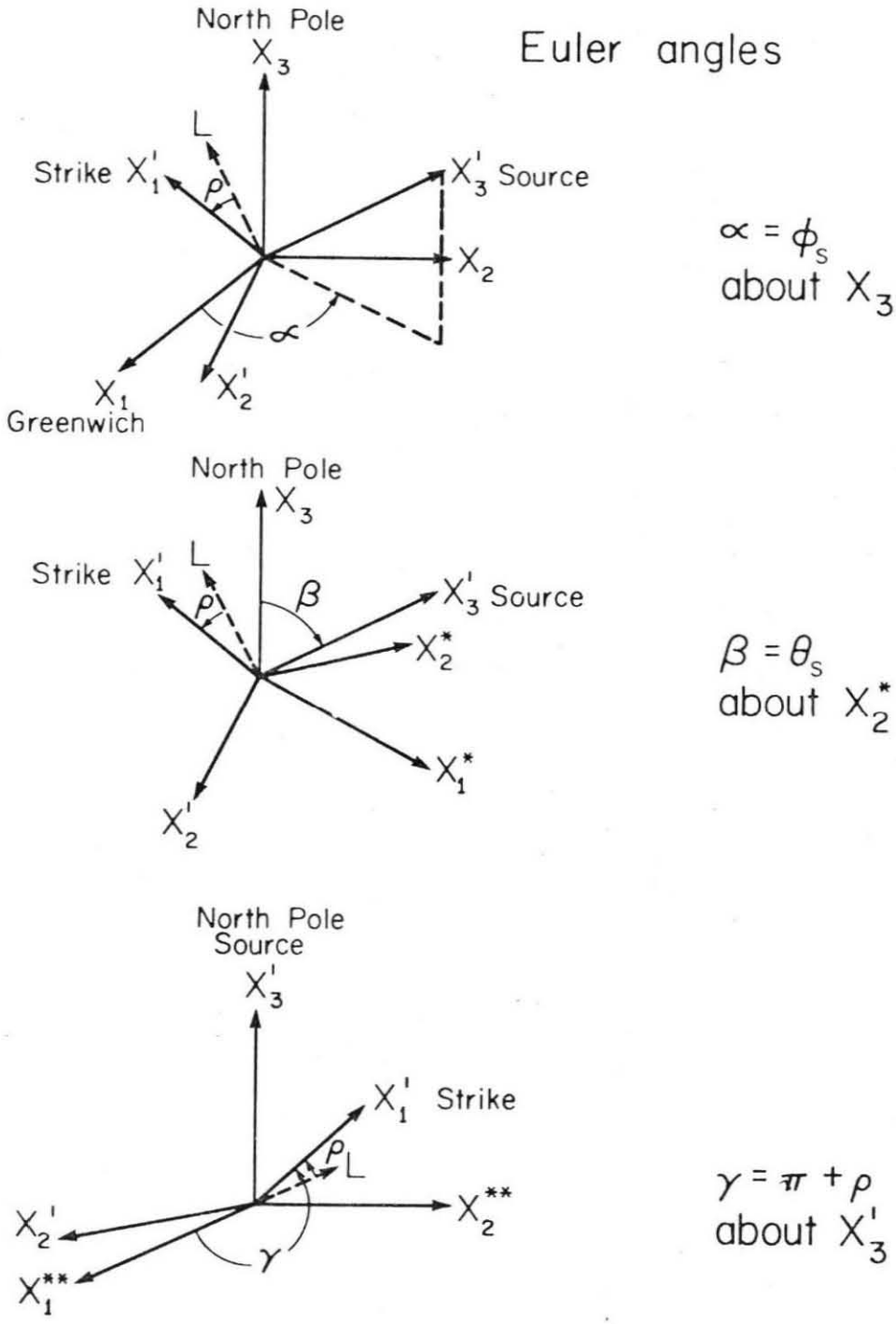

igure 2.2. Euler angles which rotate geographic (X_1, X_2, X_3) axes into source (X_1', X_2', X_3') axes. All rotations are right handed. The line L points north in the X_1' - X_2' plane.

$$C_{\ell m} = \left[\frac{(\ell+m)!}{(\ell-m)!} \right]^{1/2} (-1)^m \qquad \text{for } m \geq 0$$

and

$$C_{\ell m} = C_{\ell -m} (-1)^m \qquad \text{for } m < 0.$$

The fault geometry defines the factors q_m, the radiation pattern coefficients,

$$q_0 = 1/2 \sin \lambda \sin \delta \cos \delta$$

$$q_1 = 1/4 \, (-\cos \lambda \cos \delta + i \sin \lambda \cos 2\delta)$$

$$q_2 = 1/4 \, (-\sin \lambda \cos \delta \sin \delta - i \cos \lambda \sin \delta).$$

Here δ is the fault dip angle and λ is the slip angle, measured counterclockwise from the strike as shown in Figure 2.1.

The source amplitude factors, K_0, K_1 and K_2 were defined by Kanamori and Cipar [1974] to simplify the results of Saito [1967].

$$K_0 = \left(\frac{2\ell + 1}{4\pi \, \omega_\ell^2 (I_1^S + L^2 I_2^S) r_s} \right) \left(\frac{2(3\lambda_s + 2\mu_s)}{\lambda_s + 2\mu_s} \right)$$

$$\times \left(y_1^S(r_s) - \frac{r_s}{3\lambda_s + 2\mu_s} y_2^S(r_s) - \frac{L^2}{2} y_3^S(r_s) \right)$$

$$K_1 = \frac{2\ell + 1}{4\pi \, \omega_\ell^2 (I_1^S + L^2 I_2^S} \frac{y_4^S(r_s)}{\mu_s}$$

$$K_2 = \frac{2\ell + 1}{4\pi \, \omega_\ell^2 (I_1^S + L^2 I_2^S)} \frac{y_3^S(r_s)}{r_s} .$$

λ_s and μ_s are the values of the elastic moduli at the source depth, r_s, and $y_i(r_s)$ are the values of the eigenfunctions. I_1^S and I_2^S are energy

integrals defined by Saito, ω_ℓ is the unperturbed eigenfrequency, and

$$L^2 = \ell(\ell+1).$$

A similar analysis may be performed for an isotropic (purely explosive or compressional) source. For such a source, with step function time history and a unit moment (for each of the three dipoles), the only nonzero source frame excitation coefficient is the m = 0 term (which yields an isotropic radiation pattern). Thus

$$D'_{\ell 0} = K'_0 \, C_{\ell 0}$$

where the source amplitude factor K'_0 is adapted from Takeuchi and Saito [1972]

$$K'_0 = \frac{2\ell + 1}{4\pi \, \omega_\ell^2 (I_1 + L^2 I_2)} \times \left[- \frac{4\mu_s}{(\lambda_s + 2\mu_s)} \frac{y_1(r_s)}{r_s} \right.$$

$$\left. - \frac{y_2(r_s)}{(\lambda_s + 2\mu_s)} + \frac{2L^2 \mu_s y_3(r_s)}{(\lambda_s + 2\mu_s) \, r_s} \right] .$$

Similarly, the torsional mode displacements resulting from a double couple point source with step function source time history are given by

$$U^T(r,t) = \sum_{\ell=0}^{\infty} \sum_{m=-\ell}^{\ell} \left\{ \vec{B}_{\ell m}(r) \, e^{i\omega_{\ell m} t} + \vec{B}^*_{\ell m}(r) \, e^{-i\omega_{\ell m} t} \right\} e^{-\omega_{\ell m} t / 2Q_\ell}$$

Here

$$\vec{B}_{\ell m}(r) = y_1^T(r) \, A_{\ell m} \, \vec{T}_{\ell m}(\theta,\phi),$$

and $\vec{T}_{\ell m}(\theta,\phi)$ is the complex vector spherical harmonic

$$\vec{T}_{\ell m}(\theta,\phi) = \left(0 \, , \, \frac{1}{\sin\theta} \frac{\partial Y_{\ell m}(\theta,\phi)}{\partial \phi} \, , \, - \frac{\partial Y_{\ell m}(\theta,\phi)}{\partial \theta} \right).$$

For the torsional modes the geographical frame amplitudes are

$$A_{\ell m} = \sum_{k=-2}^{2} D^{\ell}_{mk}(R)\ A'_{\ell k}$$

where $A'_{\ell 2} = L_2 p_2 C_{\ell 2}$

$$A'_{\ell 1} = L_1 p_1 C_{\ell 1}$$

$$A'_{\ell 0} = 0$$

$$A'_{\ell -1} = L_1 p^*_1 C_{\ell -1}$$

$$A'_{\ell -2} = L_2 p^*_2 C_{\ell -2}.$$

The radiation pattern terms are

$$p_1 = 1/4\ (-\sin\lambda \cos 2\delta - i \cos\lambda \cos\delta)$$

and

$$p_2 = 1/4\ (-\cos\lambda \sin\delta + i \sin\lambda \sin\delta \cos\delta)$$

and the source amplitude factors defined by Kanamori and Cipar for the degenerate excitation problem are

$$L_1 = \left(\frac{2\ell+1}{4\pi\ \omega_\ell^2\ L^2 I_1^T}\right)\left(\frac{1}{\mu_s}\right)\ y_2^T(r_s)$$

$$L_2 = \left(\frac{2\ell+1}{4\pi\ \omega_\ell^2\ L^2 I_1^T}\right)\left(\frac{1}{r_s}\right)\ y_1^T(r_s).$$

Since the Chilean earthquake spectrum was observed on a strain meter, we compute the horizontal strain components

$$e_{\theta\theta} = \frac{1}{r}\frac{\partial U_\theta}{\partial\theta} + \frac{U_r}{r}$$

$$e_{\phi\phi} = \frac{1}{r \sin\theta} \frac{\partial U_\phi}{\partial \phi} + \frac{U_\theta}{r} \cot\theta + \frac{U_r}{r}$$

$$e_{\theta\phi} = \frac{1}{2} \left[\frac{1}{r} \frac{\partial U_\phi}{\partial \theta} - \frac{U_\phi \cot\theta}{r} + \frac{1}{r \sin\theta} \frac{\partial U_\theta}{\partial \phi} \right]$$

The strains are given in geographic coordinates, so the strain in a strain rod of arbitrary orientation is

$$e_{rod} = e_{\theta\theta} \cos^2\gamma + 2e_{\theta\phi} \cos\gamma \sin\gamma + e_{\phi\phi} \sin^2\gamma$$

where γ is the strain rod orientation measured counterclockwise from north.

DATA

The two data sets most suitable for measuring the attenuation of the longest period modes are the Isabella strain meter record of the 1960 Chilean earthquake, and the UCLA gravity meter record of the 1964 Alaskan earthquake. Although neither instrument was ideal for these purposes, the two earthquakes were large enough to generate acceptable records for long enough time periods (several hundred hours). Even so, the signal-to-noise ratios for the low order modes are low, and limit the possible data analysis substantially. Here, then, techniques are demonstrated which will be far more effective when data from the new long period IDA network become available for large earthquakes.

The Caltech strainmeter at Lake Isabella, California [Benioff, 1959, 1960] provides the longest ultra long period record of the Chilean earthquake. This record was used by Benioff *et al.* [1961] and Smith [1961] in their classic studies which yielded the first spectra showing the longest period modes. Figure 2.3 shows five hundred hours of the strain record,

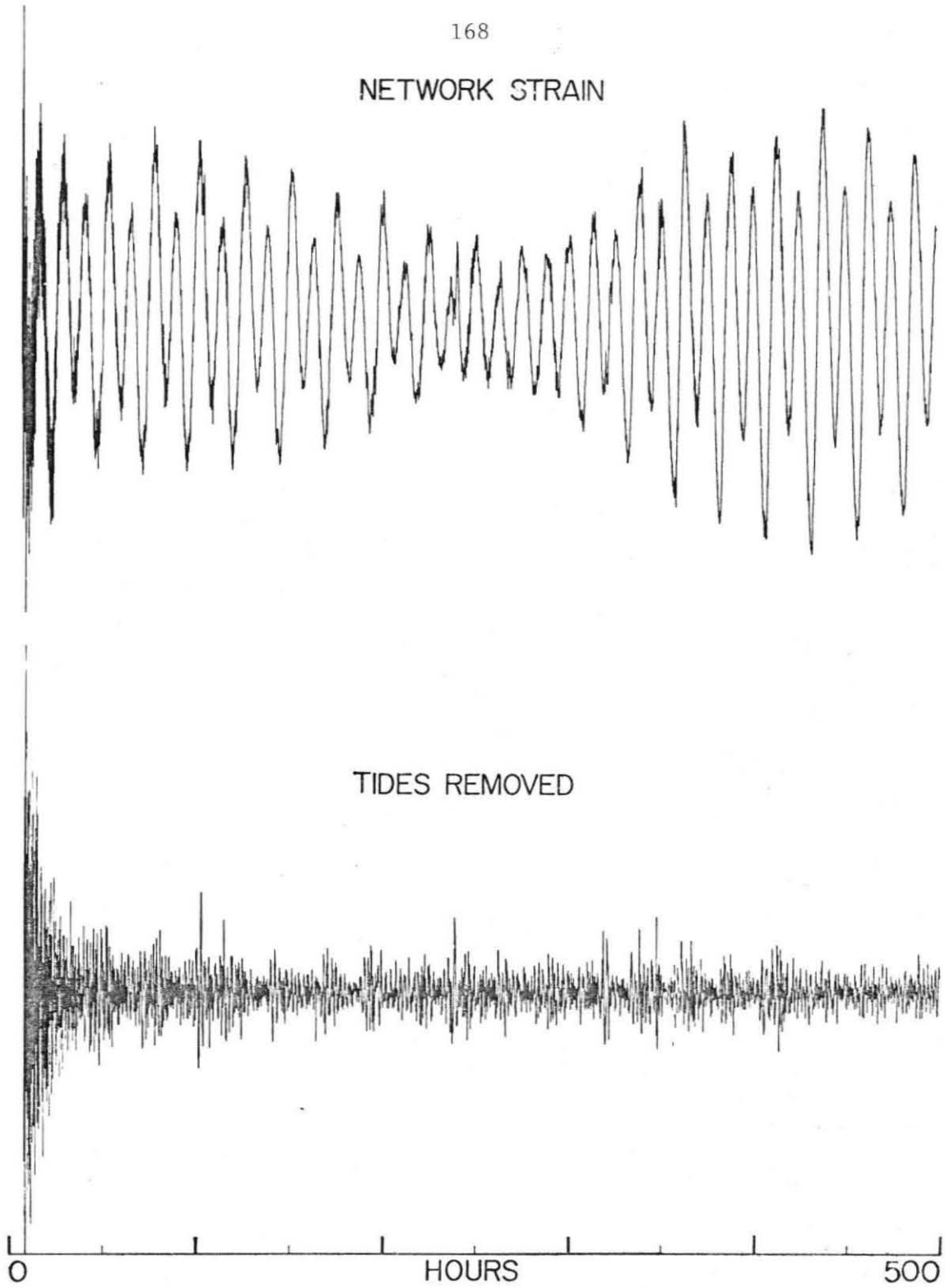

Figure 2.3. Isabella strain record of the Chilean earthquake (top trace) and the high-passed record with tides removed (bottom trace). The origin time of this figure and all Chile others, is 1911 hours, 22 May 1960, the origin time of the main shock. The digitized record (top) begins 289 min later, and 0000 hours, 23 May. The high-passed record (bottom) starts another six hours later.

which was filtered electronically prior to recording to reduce the tidal amplitudes. The record (top) was processed to remove tides by twice subtracting three hour running averages. The resulting record (bottom) was then tapered at both ends for spectral analysis.

The amplitude and phase spectra are shown in Figure 2.4. Frequencies are given in cycles per minutes, and some of the modes are identified. Modes appear as peaks in the amplitude spectra, and as "white" areas in the phase spectrum. (This is because of the π phase shift across a resonance peak [Marion, 1970]. The phase is incoherent except near a well developed peak, yielding the dark areas on the plot, and coherent across a well developed peak.) This can be seen best for "clean" peaks, for example ${}_0S_{12}$ (.12 cpm). Noisier and more jagged peaks, for example ${}_0S_2$, do not stand out as well in the phase spectrum. (Each singlet should ideally have its own resonance curve, which interferes unless the singlets are well separated.) The poor quality of the longest period peaks proved a limiting factor in the later analysis. Some modes (e.g., ${}_0S_0$) are barely resolvable on this record, but can be resolved on the UCLA gravity record. Torsional modes are generally indistinct.

The tapered spectrum was filtered to isolate individual multiplets, as shown in the following set of figures. The filter windows used in the analysis are listed in Table 2.1. The filtered data show the characteristic beating patterns resulting from singlet interference.

The vertical scale on each figure gives the trace amplitude in digital units. The one unit level can usually be regarded as a nominal noise level. As discussed later, in some cases the true noise level

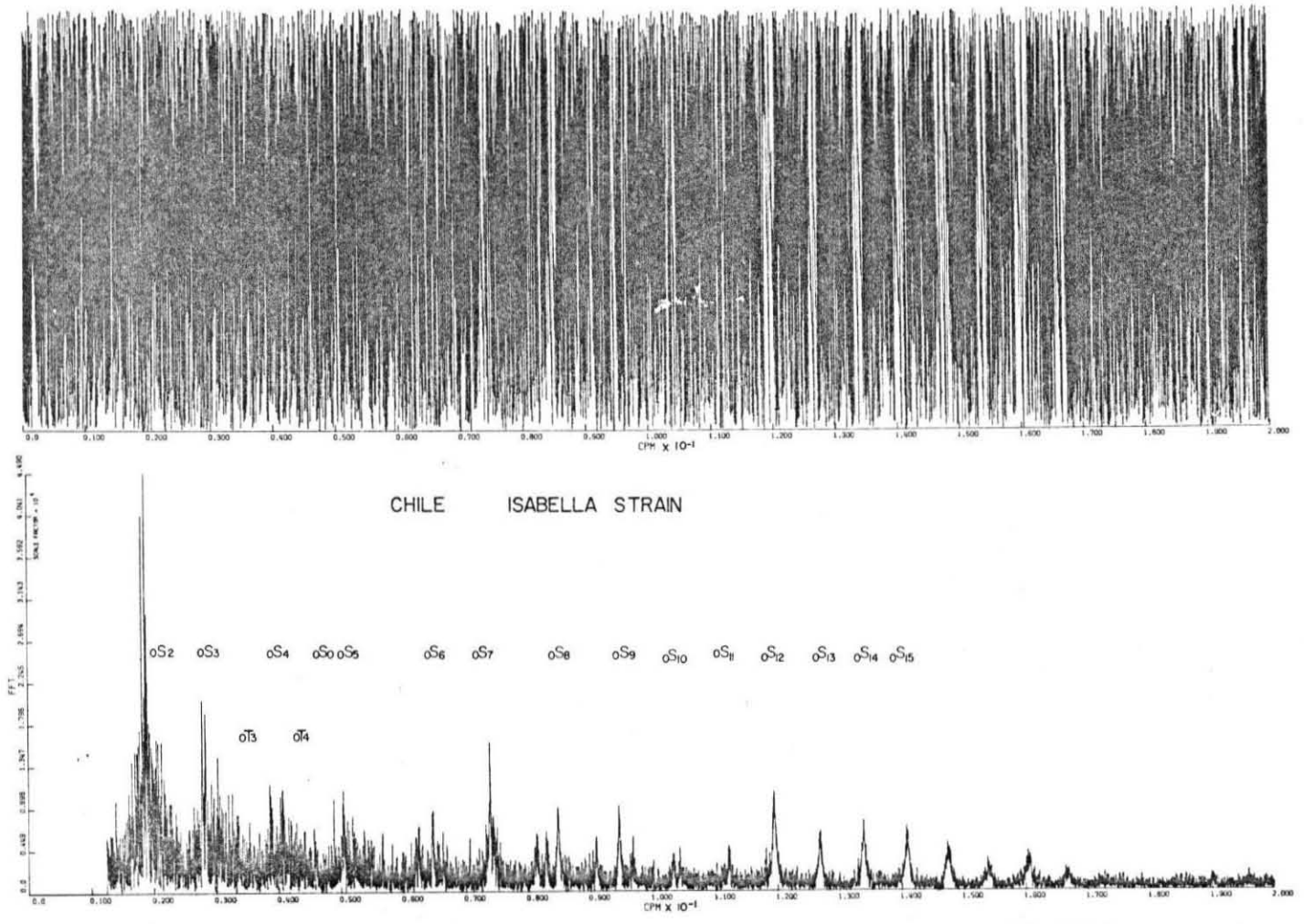

Figure 2.4. Amplitude and phase spectra of the Isabella strain record. Frequencies are in cycles per minute. The short period cutoff is 300 seconds.

Table 2.1

FILTER PASSBANDS

Mode	Min. Frequency (cpm)	Max. Frequency (cpm)
$_0S_2$	0.01750	0.01950
$_0S_3$	0.02726	0.02882
$_0S_4$	0.03821	0.03935
$_0S_5$	0.04986	0.05070
$_0T_3$	0.03481	0.03566
$_0T_4$	0.04565	0.04640
$_0S_0$	0.04830	0.04950

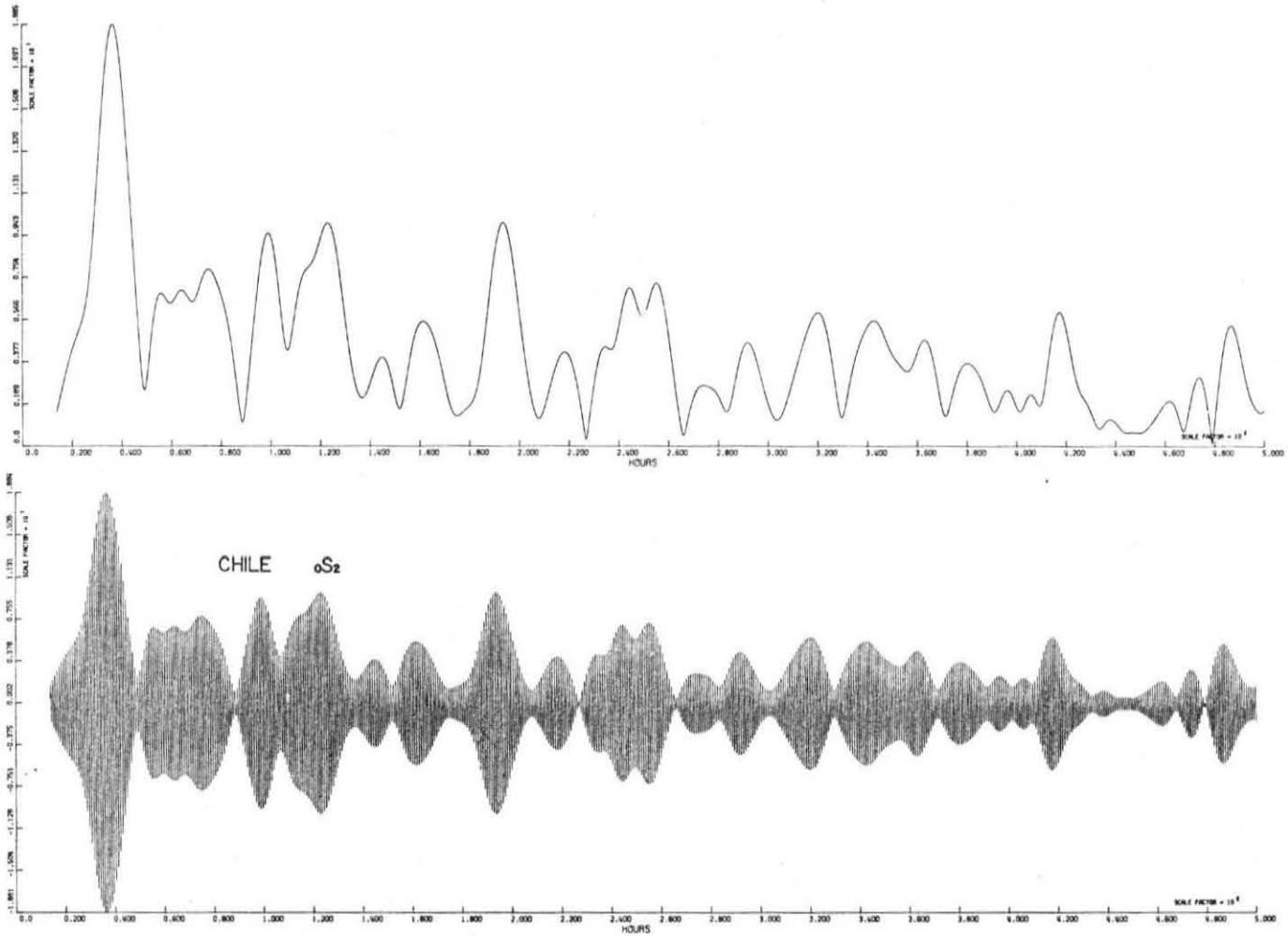

Figure 2.5. Bandpass filtered data and Hilbert transform envelope for $_0S_2$. Time is in hours, amplitude in digital units.

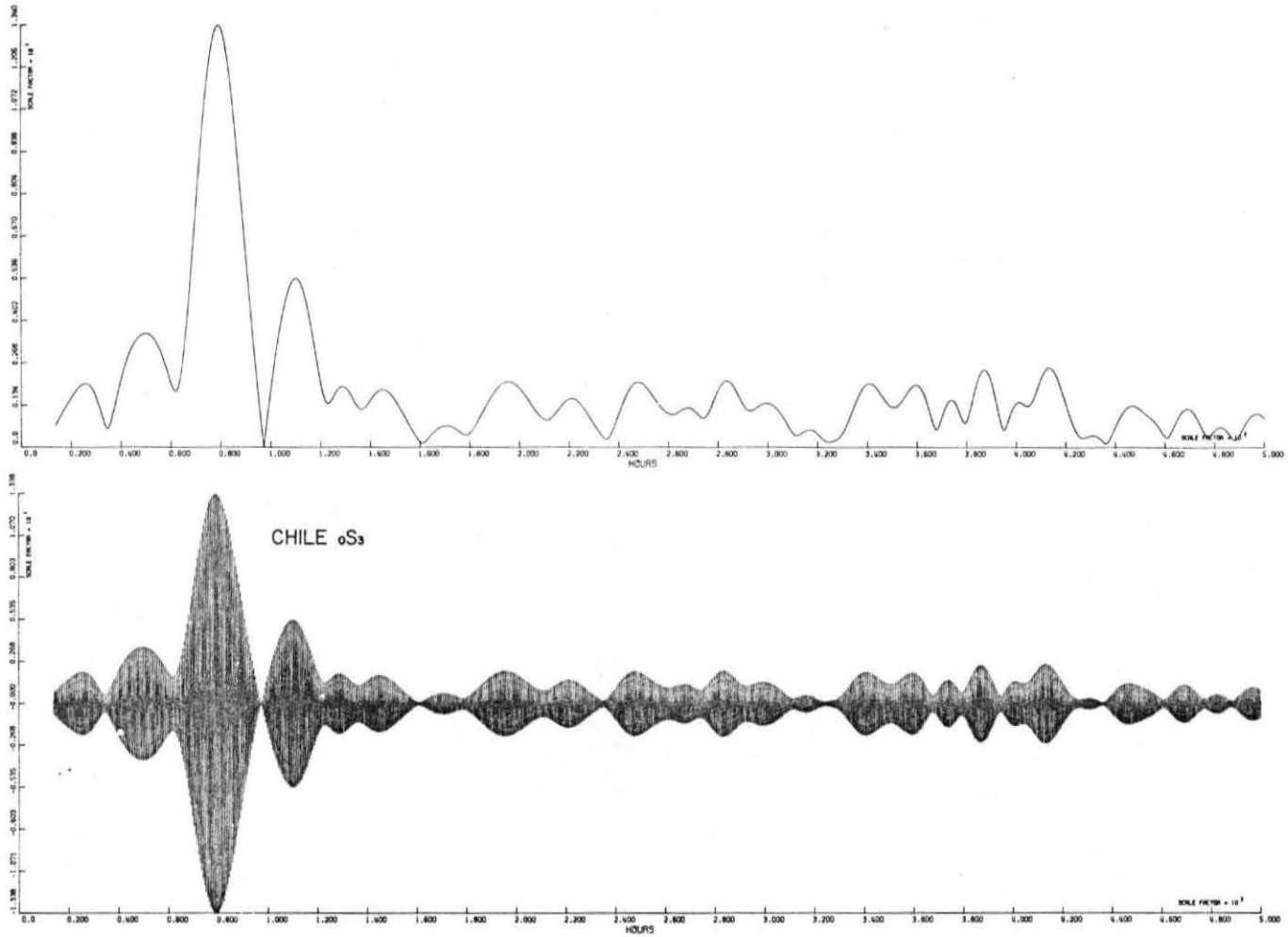

Figure 2.6. Bandpass filtered data and Hilbert transform envelope for $_0S_3$. Time is in hours, amplitude in digital units.

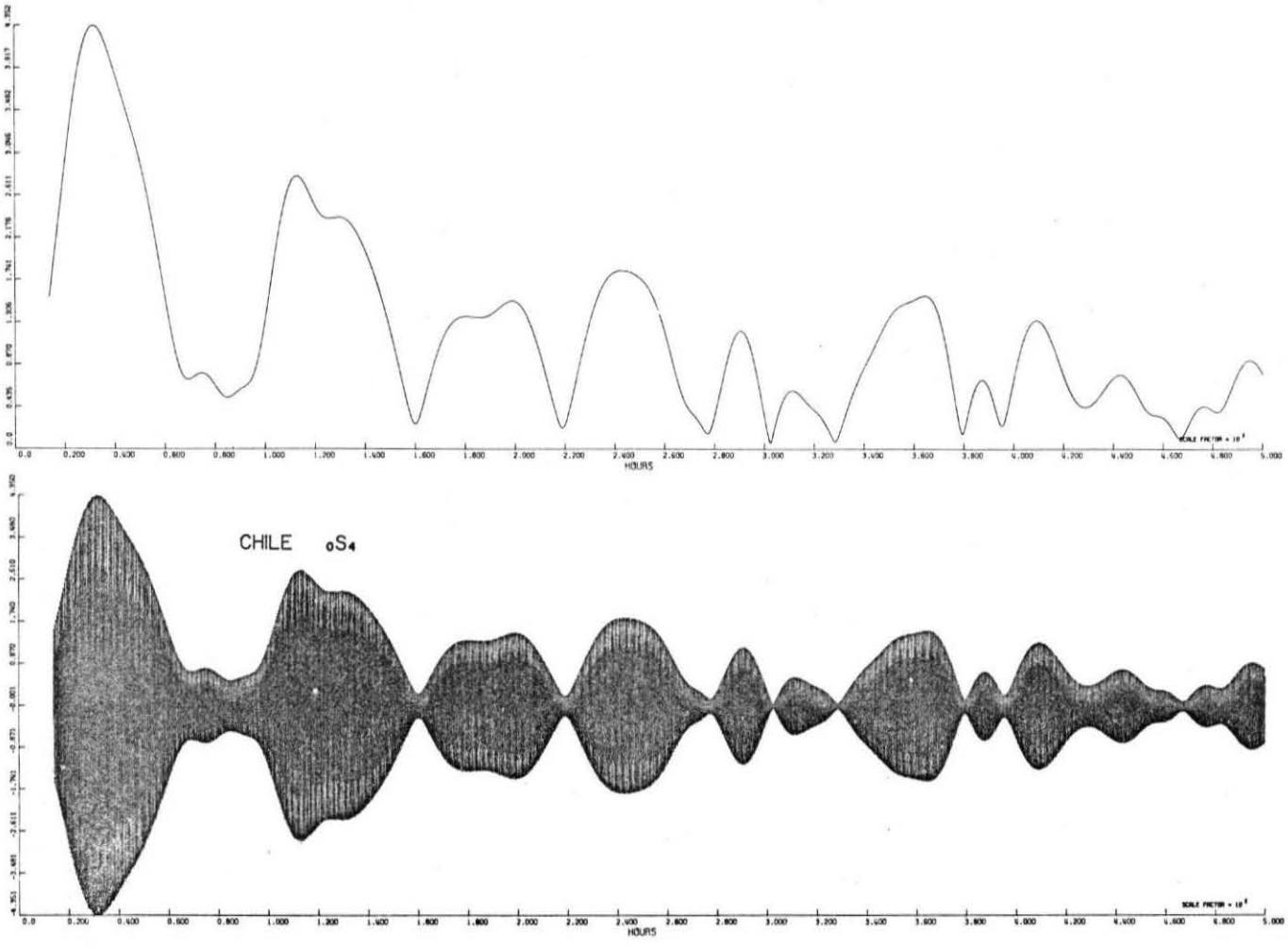

Figure 2.7. Bandpass filtered data and Hilbert transform envelope for ${}_0S_4$. Time is in hours, amplitude in digital units.

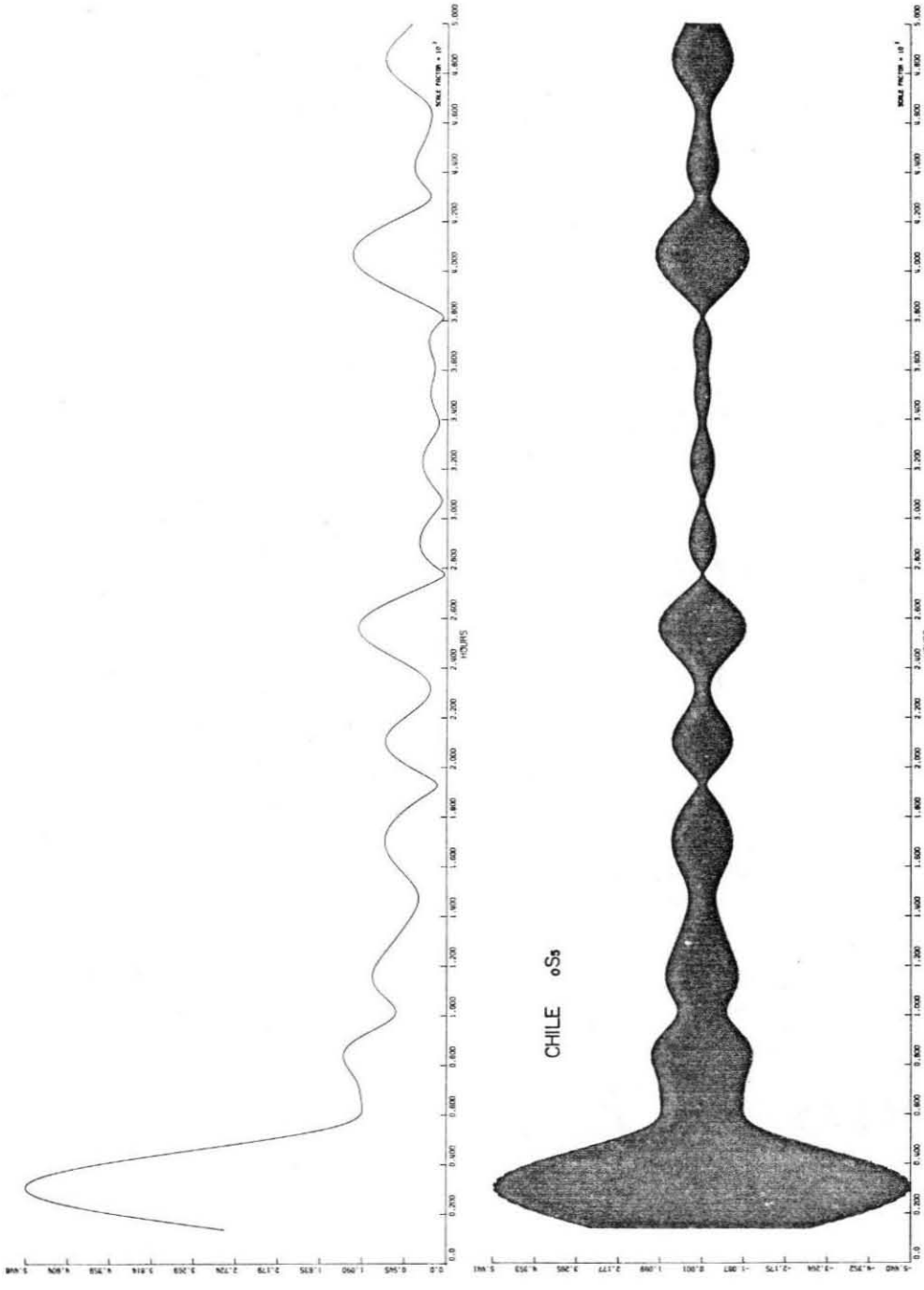

Figure 2.8. Bandpass filtered data and Hilbert transform envelope for $_0S_5$. Time is in hours, amplitude in digital units.

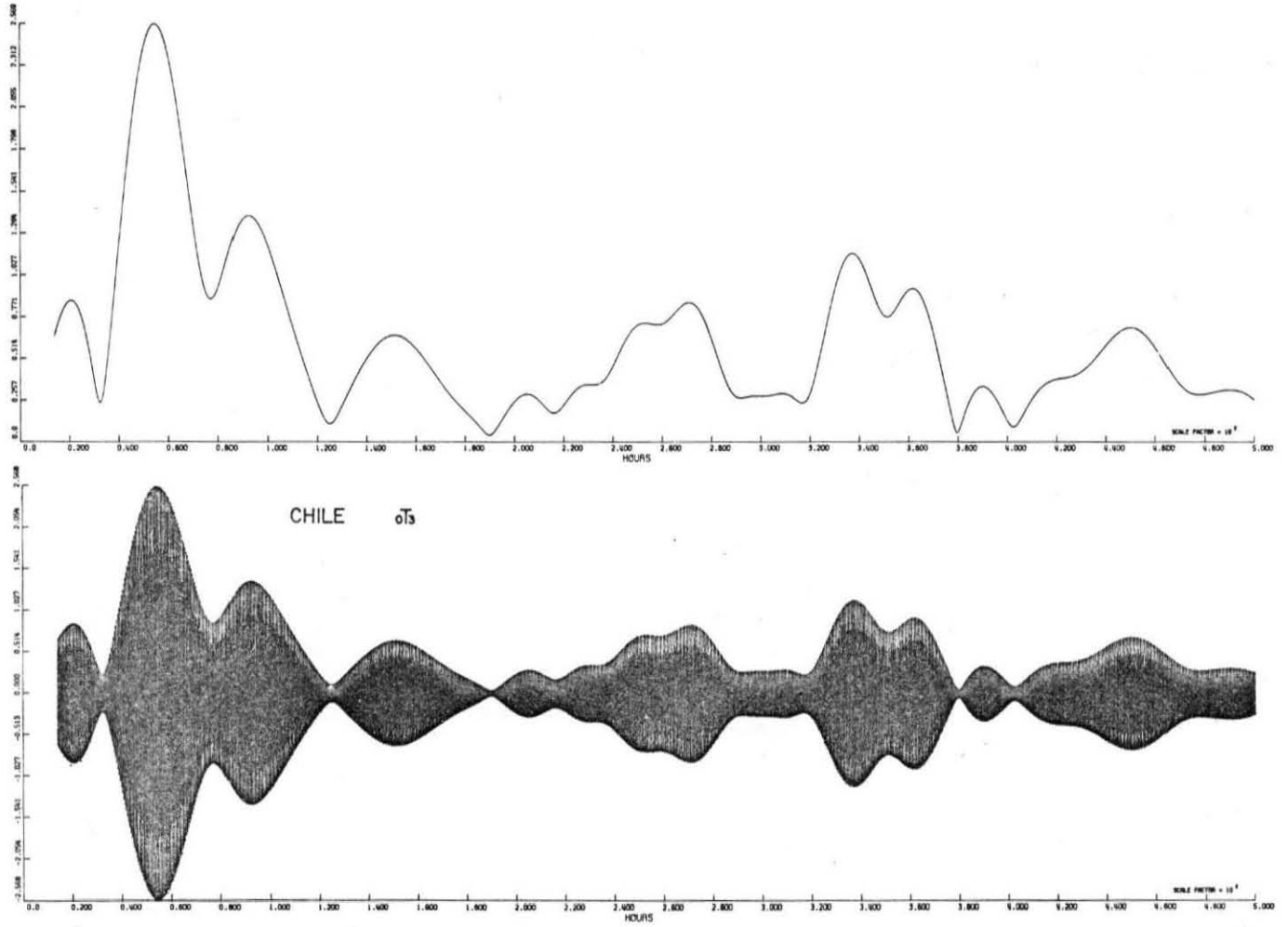

Figure 2.9 Bandpass filtered data and Hilbert transform envelope for $_0T_3$. Time is in hours, amplitude in digital units.

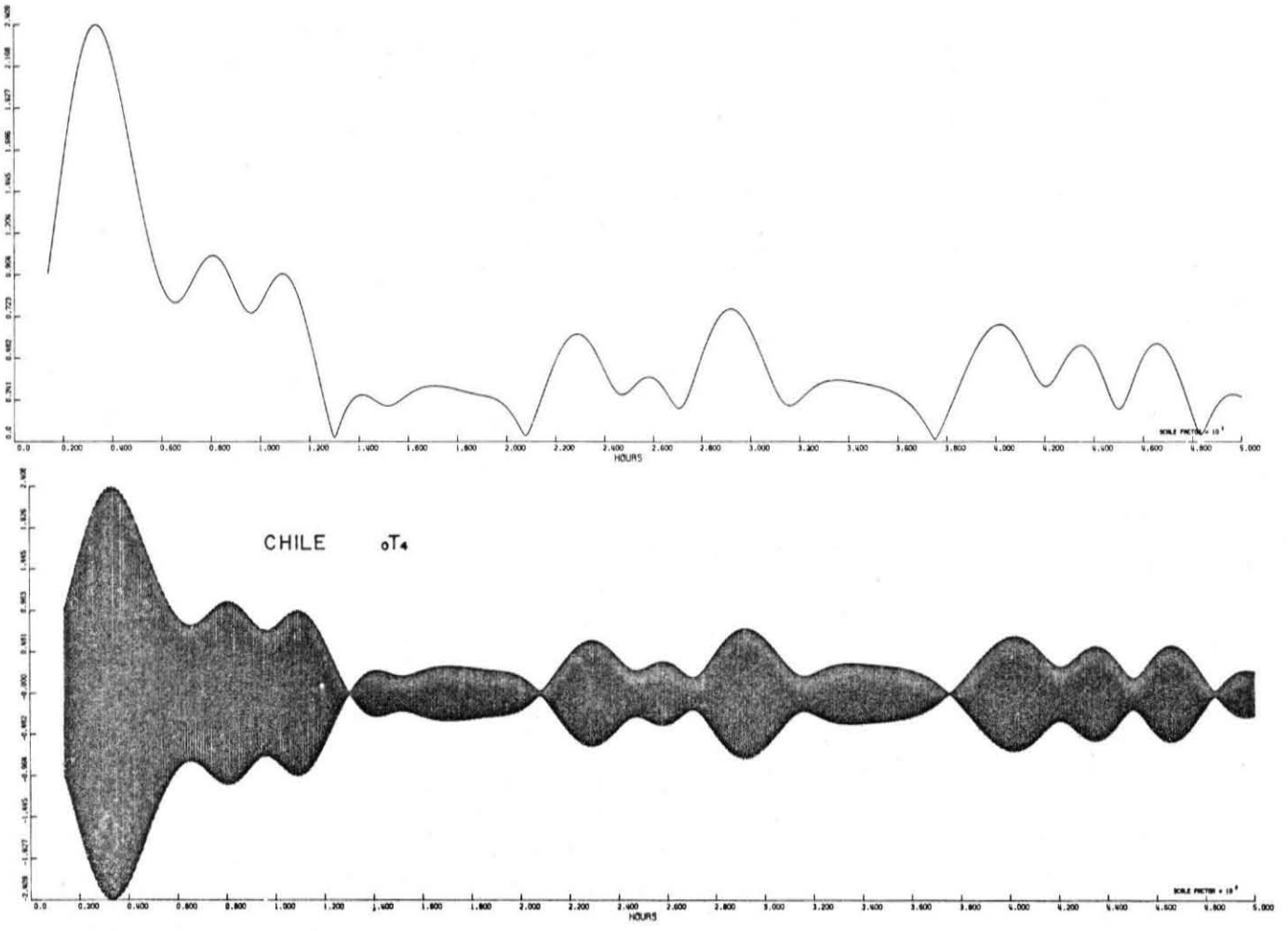

Figure 2.10. Bandpass filtered data and Hilbert transform envelope for ${}_{0}T_{4}$. Time is in hours, amplitude in digital units.

appears to be higher. Some modes remain above the noise level for extended periods of time. In contrast, some modes, such as ${}_0T_3$ (Figure 2.9) and ${}_0T_4$ (Figure 2.10) are barely above the noise level initially and soon decay below it.

The lower portions of each figure show the Hilbert transform envelopes of the time series. These have the information needed for studying the beat patterns and their time decay, and are much easier to store and manipulate than the entire time series. We use these in the later analysis.

The second data set used here is the UCLA gravity meter record of the 1964 Alaskan earthquake [Slichter, 1967]. This is a La Coste-Romberg tidal gravimeter, whose output was punched directly onto cards [Ness et al., 1961]. Two such meters were operating in 1964, one of which (meter 7) yielded data far inferior to the other (meter 4). Only the meter 4 record is used in the later analysis.

The raw record (Figure 2.11) contains a number of large amplitude glitches which have periods of tens of minutes. As this could significantly bias the long period modes, these glitches were removed. Wiggins and Miller [1972] used a prediction error operator to isolate and remove glitches. We fit a straight line across the affected areas (Figure 2.11, bottom), which yielded acceptable results.

The effects of deglitching are shown in Figure 2.12, which shows the amplitude and phase spectra before deglitching. The amplitude and phase spectra after deglitching are given in Figure 2.13.

Filtered time series and envelopes (Figures 2.14-2.17) were obtained for the four spheroidal modes, using the same filter windows as for

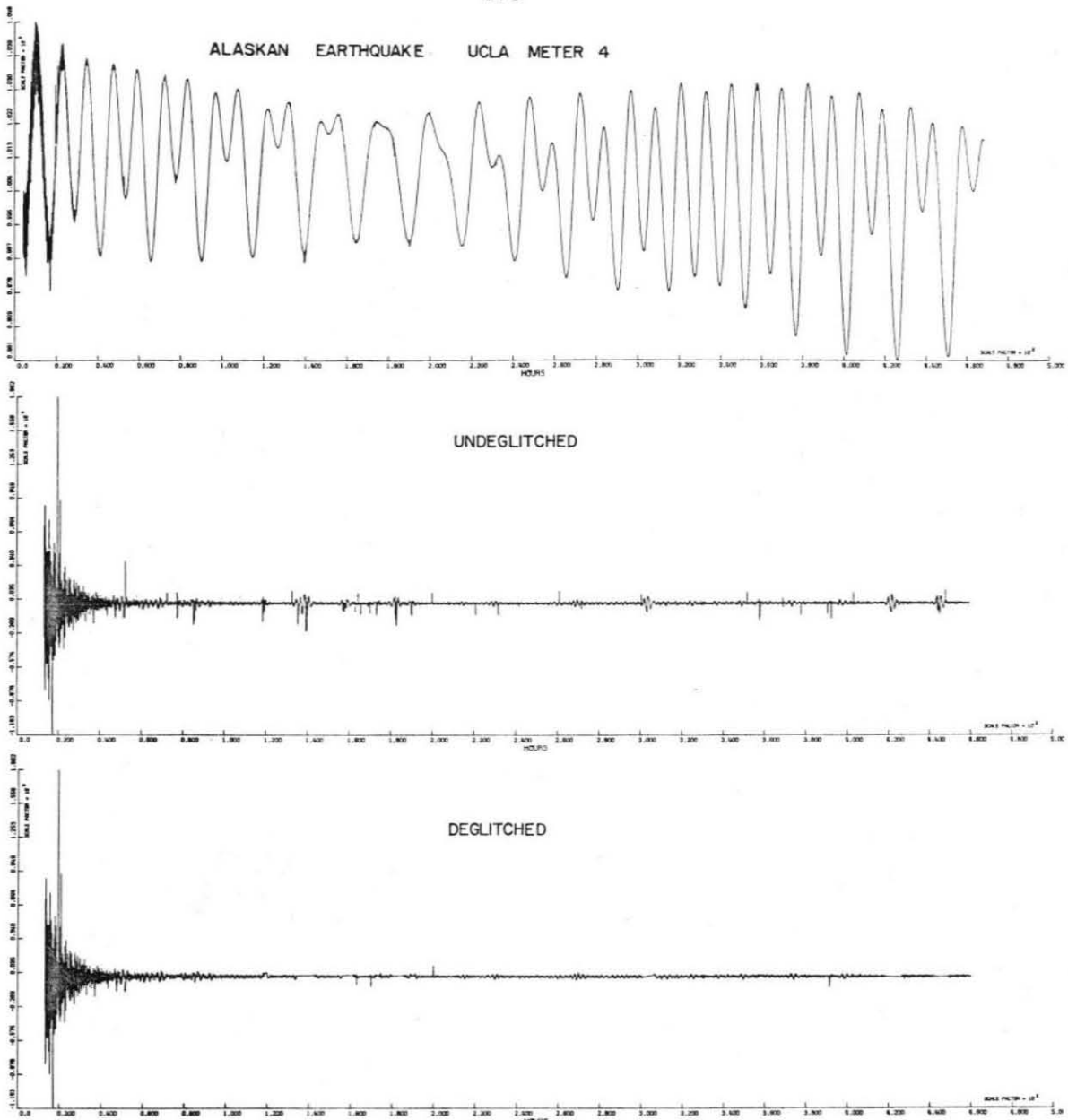

Figure 2.11. UCLA gravity (meter 4) record of the Alaskan earthquake (top). The origin time of this figure, and all other Alaska ones, is 0336 hours, 28 March 1964, the origin time of the main shock. The digitized record begins 256 minutes later. The middle trace shows the large glitches present after tide removal, the lower trace shows the final deglitched record.

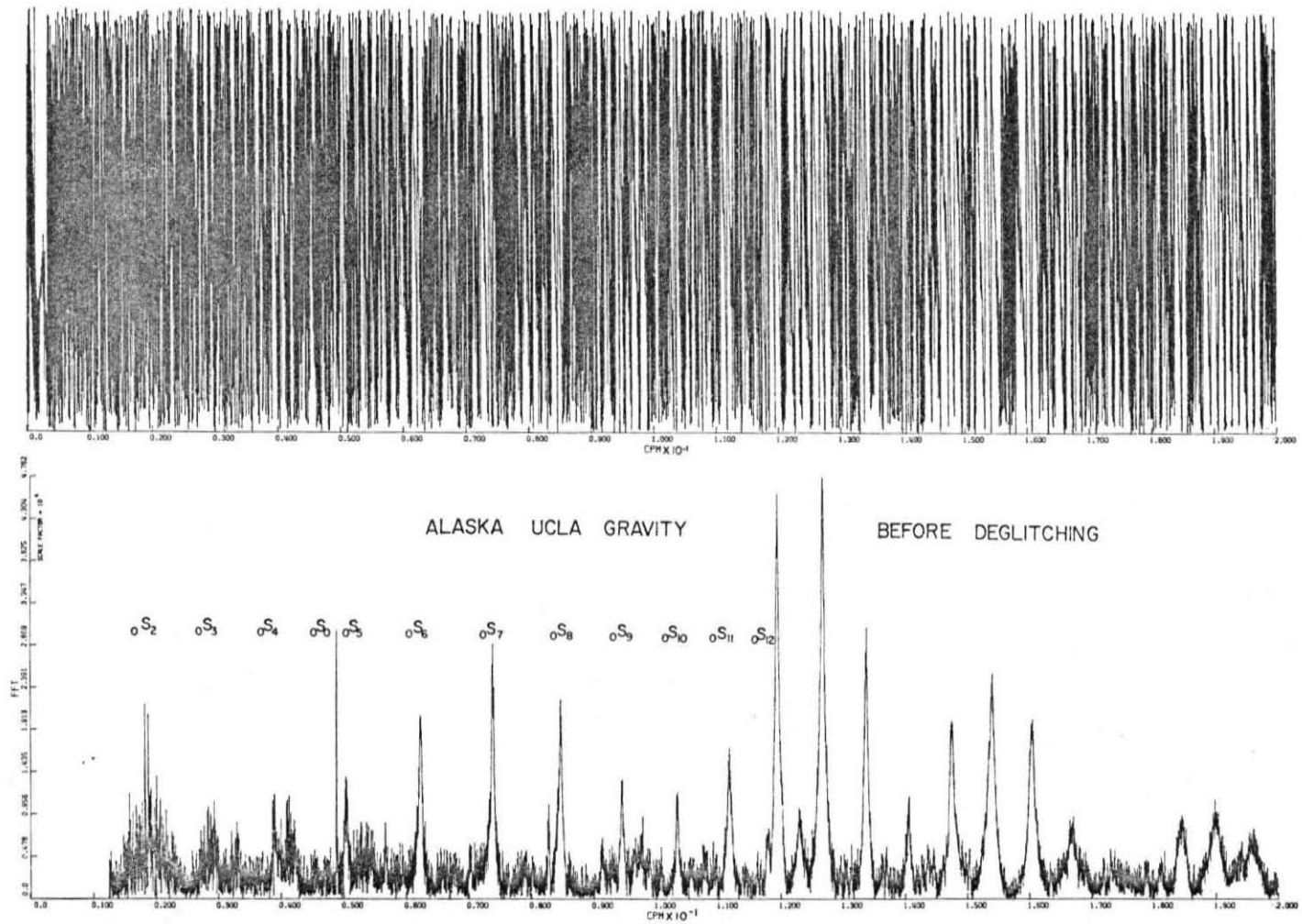

Figure 2.12. Amplitude and phase spectra of the undeglitched gravity meter record. Frequencies are given in cycles per minute. Several long period modes are identified. The short period cutoff is 300 seconds.

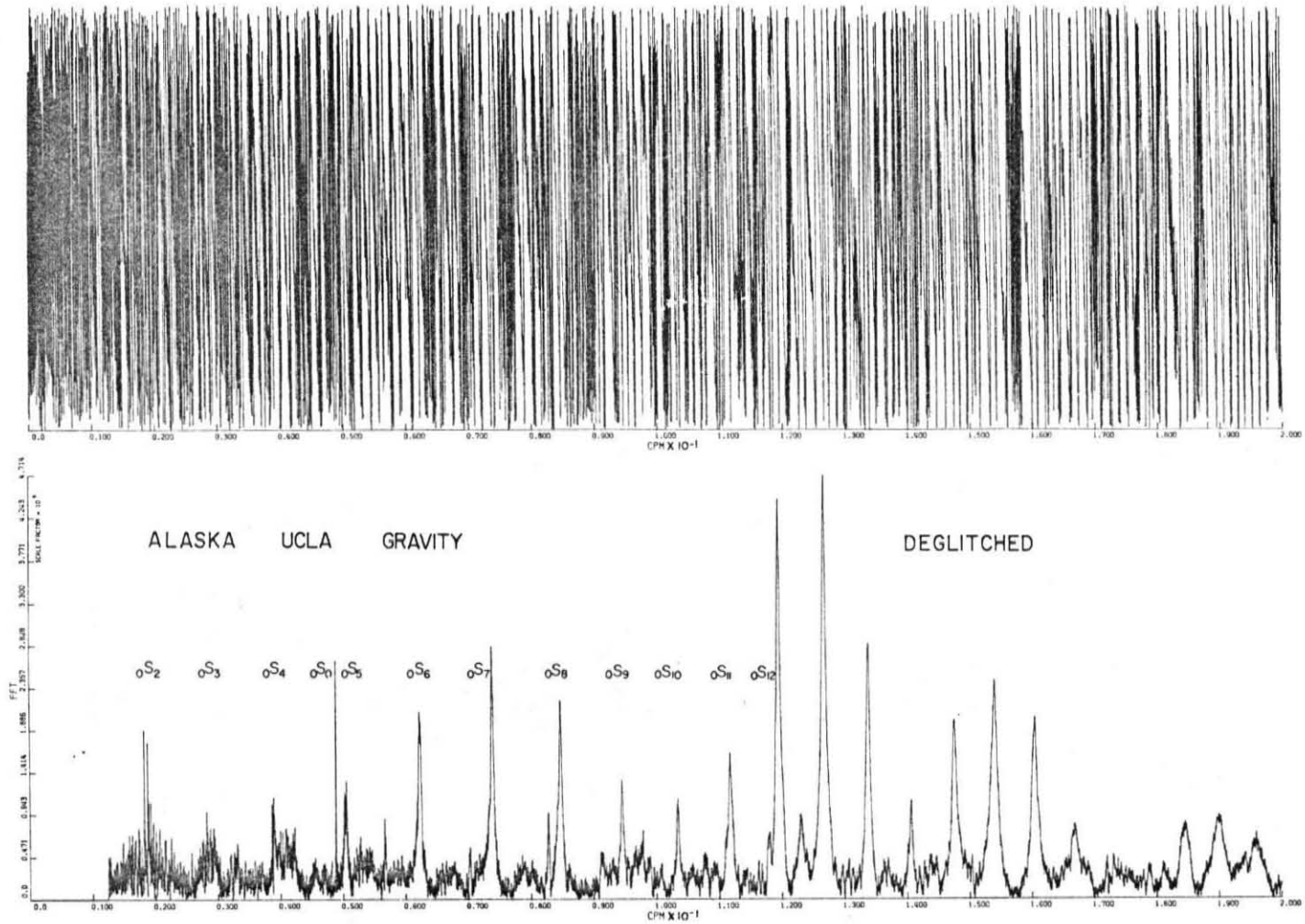

Figure 2.13. Amplitude and phase spectra of the gravity meter record after deglitching. The noise level is reduced substantially. Frequencies are in cycles per minute, with a short period cutoff of 300 seconds.

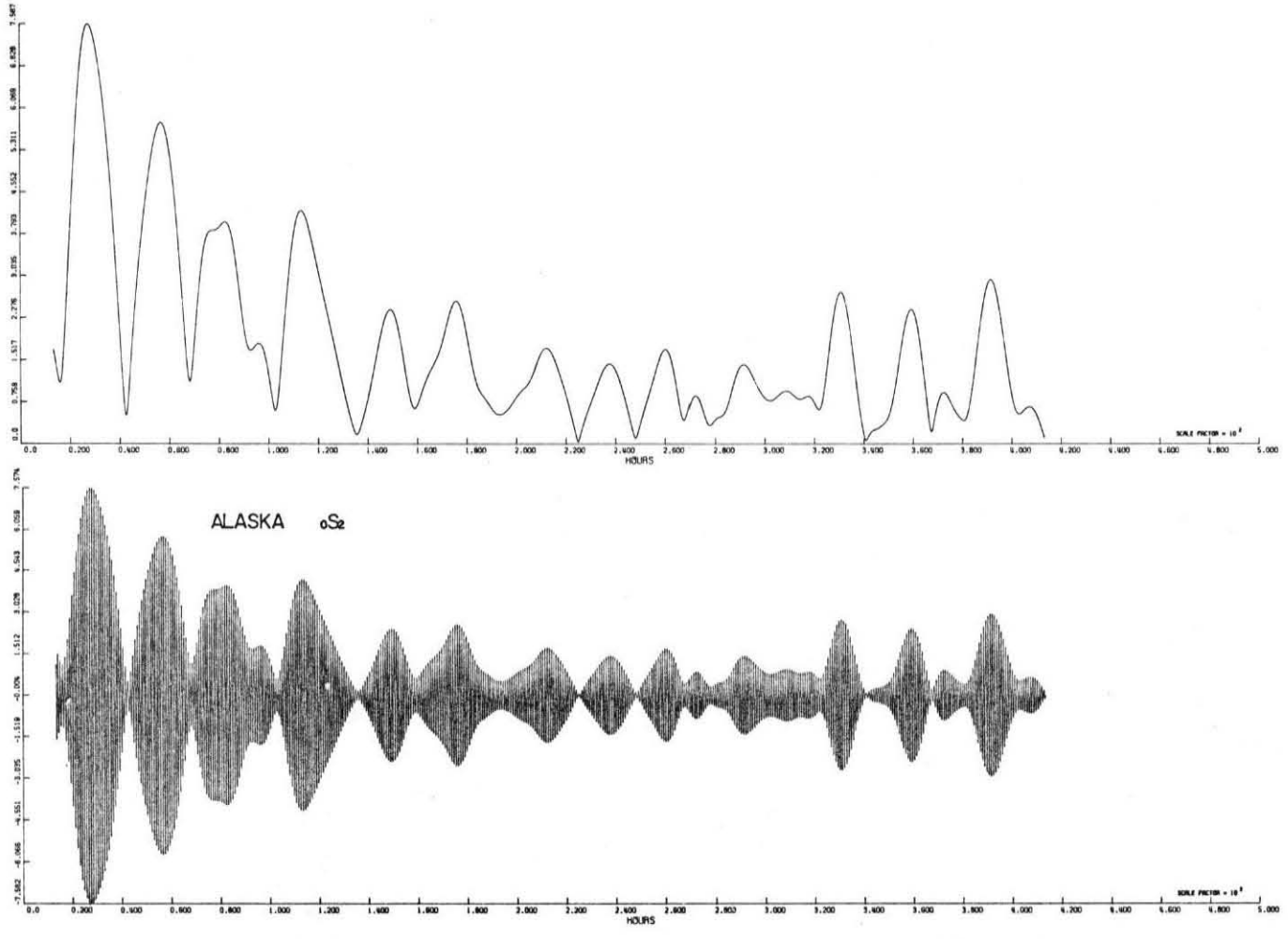

Figure 2.14. Bandpass filtered data and Hilbert transform envelope for $_0S_2$. Time is in hours, amplitude in digital units.

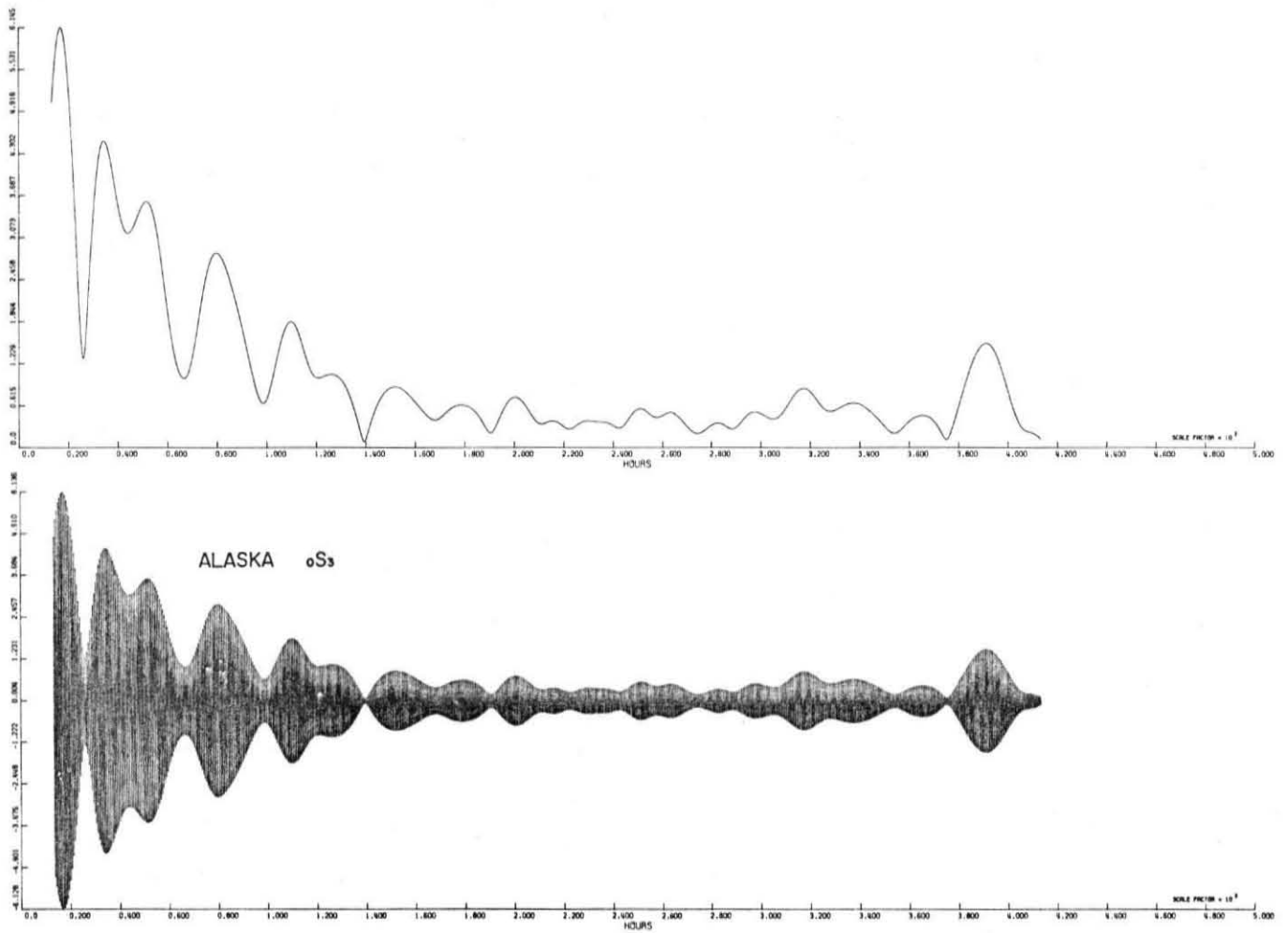

Figure 2.15. Bandpass filtered data and Hilbert transform envelope for ${}_0S_3$. Time is in hours, amplitude in digital units.

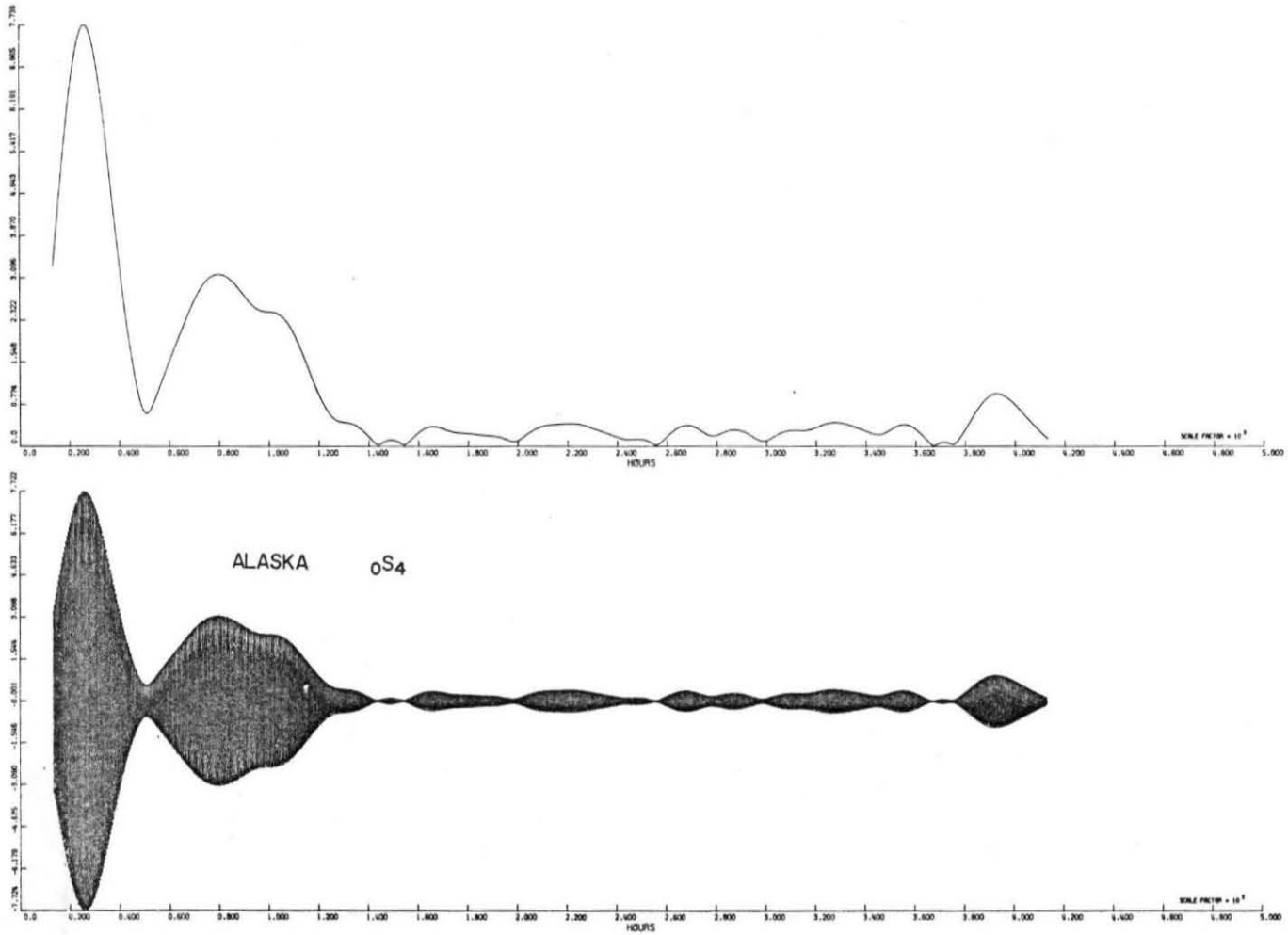

Figure 2.16. Bandpass filtered data and Hilbert transform envelope for $_0S_4$. Time is in hours, amplitude in digital units.

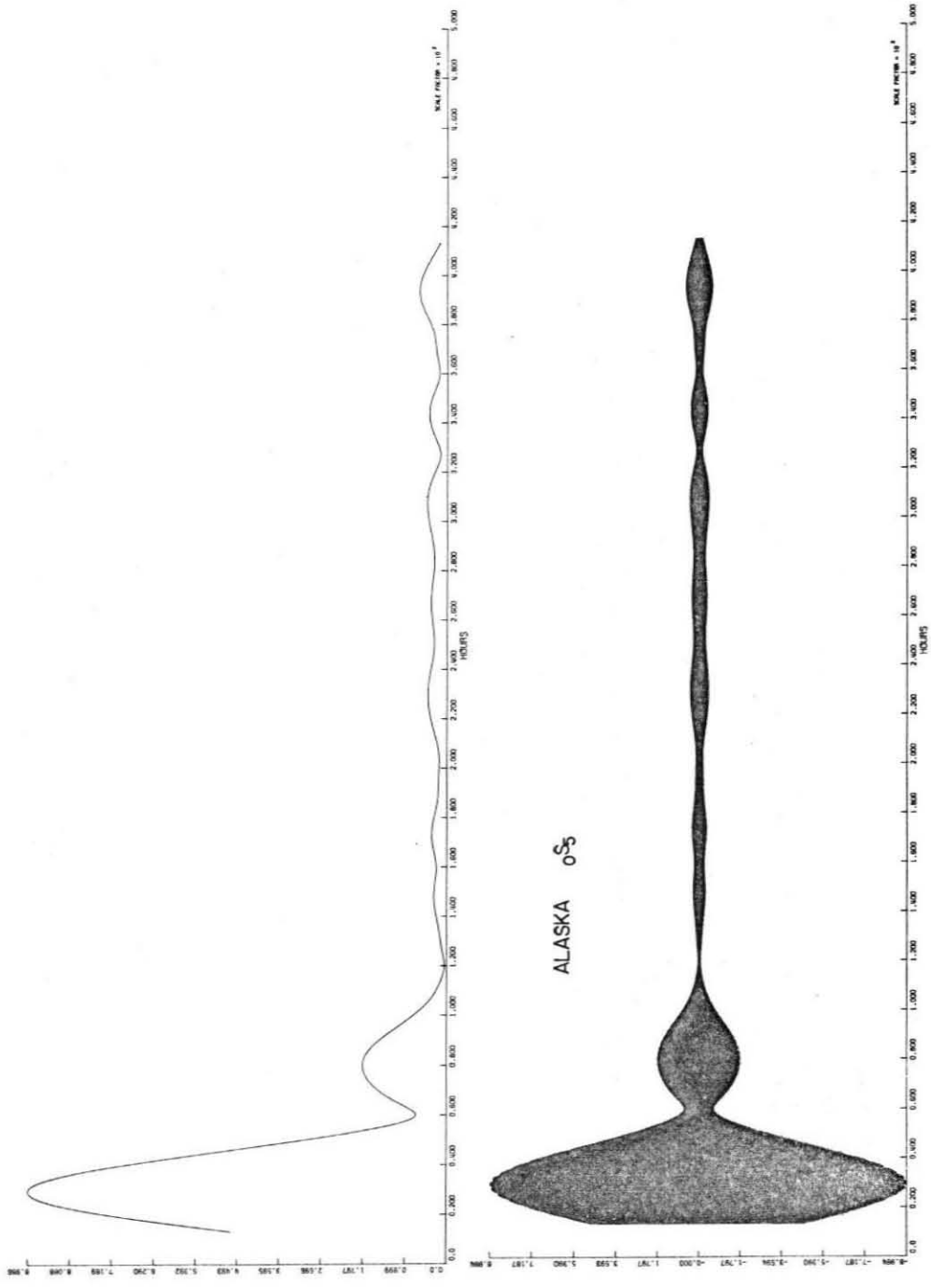

Figure 2.17. Bandpass filtered data and Hilbert transform envelope for $_0S_5$. Time is in hours, amplitude in digital units.

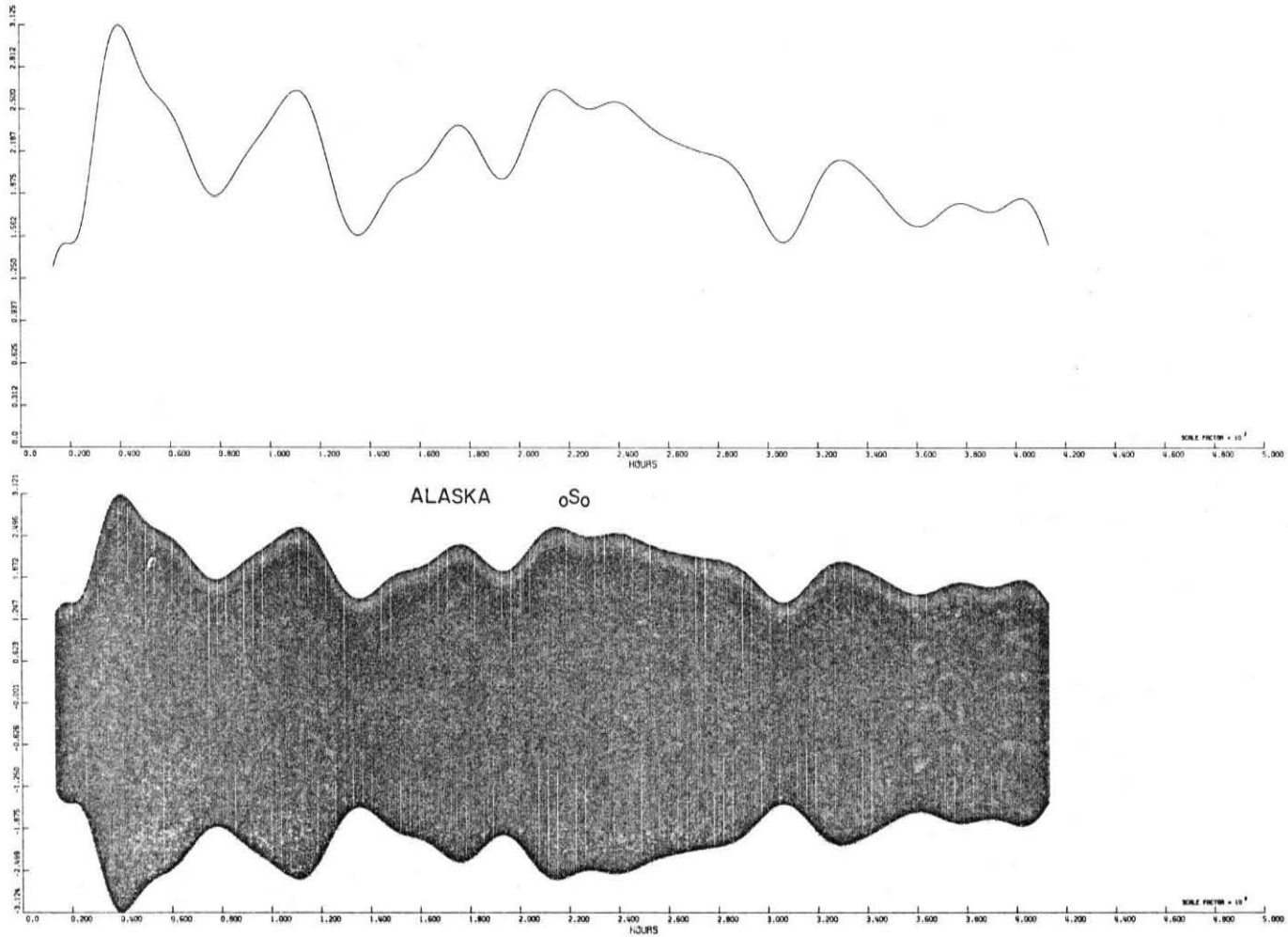

Figure 2.18. Bandpass filtered data and Hilbert transform envelope for $_0S_0$. Time is in hours, amplitude in digital units.

the Chile data (Table 2.1). In addition, the fundamental radial mode, ${}_0S_0$, which was well recorded here (in contrast to the Chile record) is shown in Figure 2.18.

ANALYSIS

To analyze these data, synthetic seismograms for each multiplet were generated using the method previously described. These were then compared to the data to provide an estimate of Q.

The synthetics were calculated, for the appropriate source mechanism, without including the effects of attenuation. A range of different Q values were then applied to the "Q-less" synthetics, and the resulting time series were then tapered and filtered in the same way as the data.

The eigenfrequency of each singlet is computed using Anderson and Hart's [1976] values for the unperturbed eigenfrequencies and Dahlen's [1968] rotational splitting parameters. The elliptical splitting parameters are not used, due to the difficulties involved in previous calculations of these parameters [Woodhouse, 1976]. Dahlen [personal communication] states that more accurate recent computations show that the spheroidal mode elliptical splitting parameters may be neglected for our purposes. Accurate values have not yet been published for the elliptical splitting or torsional modes, or for splitting due to lateral heterogeneities.

The Hilbert transform envelopes of both data and synthetics were smoothed with running averages, for ease of comparison. This is necessary since as time progresses the general decay of data and synthetics are similar but individual beats are not well in phase.

For the Chilean synthetics, we use the source mechanism determined by Kanamori and Cipar [1974] from long period surface waves. The rupture was initiated at 38°S, 286.5°E and propagated at 3.5 km/sec to 46°S, 286.5°E, on a fault plane dipping 10° east and striking N 10°E. (We approximate the finite source by five point sources at a depth of 55 km.) The slip angle is 90°, a pure thrust motion. We are also including a precursory slip [Kanamori and Cipar, 1974; Kanamori and Anderson, 1975] at 41.5°S, 285.7°E with a rise time of 5 min starting 15 min before the main shock, and with a moment equal to that of the main shock.

For the Alaskan synthetics, the fault parameters used are those (ρ = 114°, λ = 90°, δ = 20°, θ_s = 29.9, ϕ_s = 212.4°, L = 500 km, V_R = 3.5 km/sec) determined by Kanamori [1970].

All the figures show the smoothed Hilbert transforms of the data and synthetics, for six values of Q: 300, 400, 500, 600, 750, 1000. When necessary, Qs of 1250 and 1500 were added. The Chilean results for ${}_0S_2$ - ${}_0S_5$, ${}_0T_3$ and ${}_0T_4$ are presented first (Figures 2.19-2.24).

The noise levels marked on each plot are assigned somewhat subjectively. The highest noise level, four digital units for ${}_0S_2$, seems appropriate in that the signal amplitude stabilizes at about this level. This is consistent with the fact that the noise level for the ${}_0S_2$ multiplet (see the spectrum, Figure 2.4) seems higher than for the other modes. For the other Isabella records, the noise level is assumed to be the nominal one digital unit noise level. The smoothing intervals were also chosen empirically, to smooth out major irregularities and noise bursts in the data.

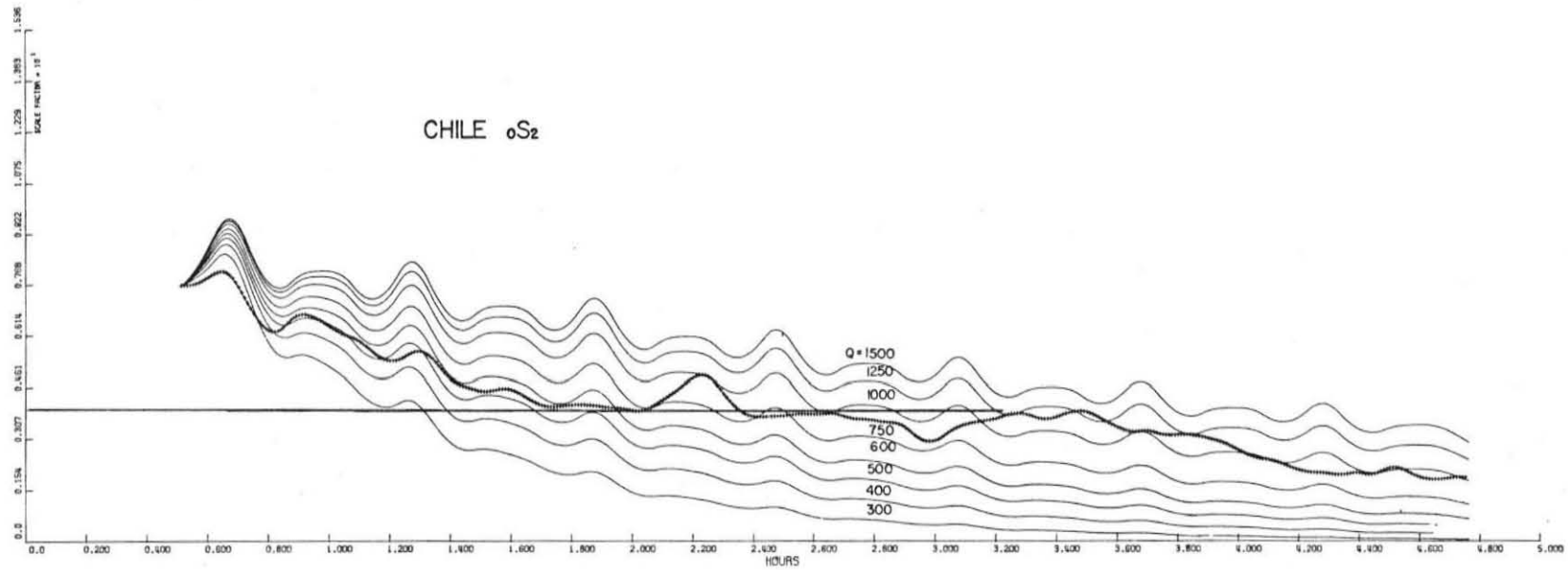

Figure 2.19. Data and synthetics for eight different Q values, for $_0S_2$. The noise level is four digital units, and the smoothing window is 75 hours. Time is in hours since the origin time (1911 hours, 22 May 1960). All curves are normalized to begin at the same point. The time and normalization conventions are the same for all the Chile records.

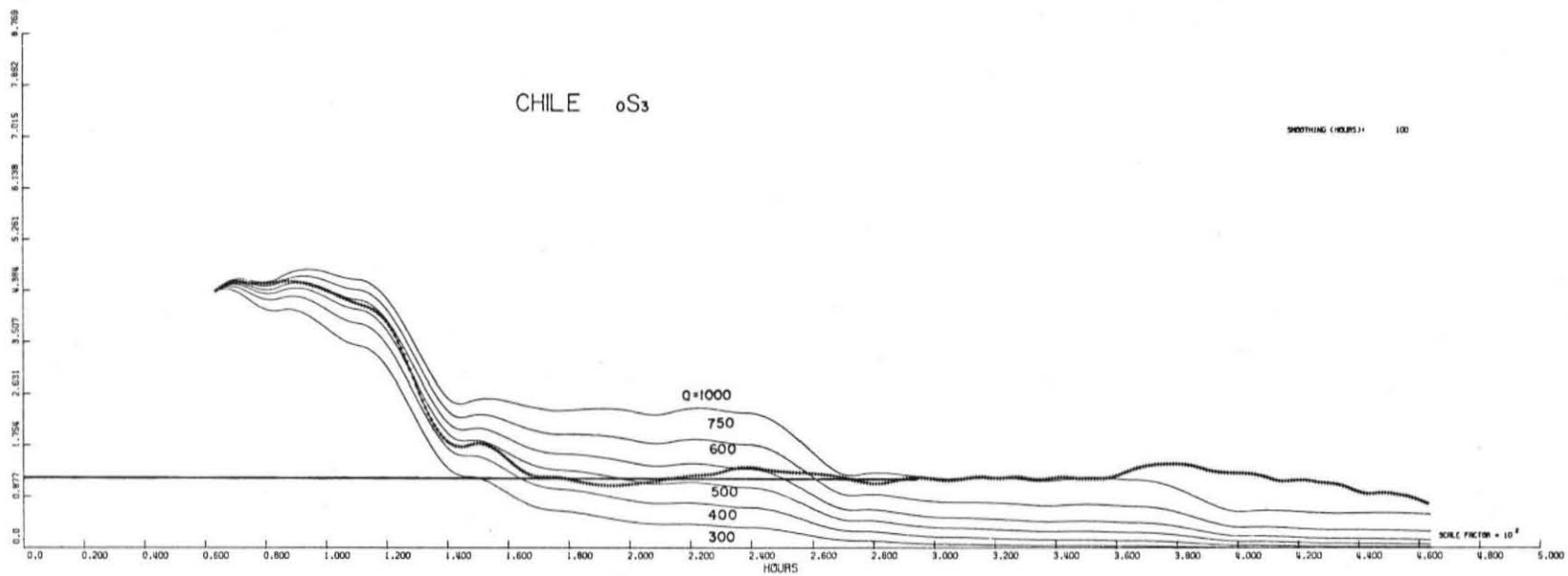

Figure 2.20. Data and synthetics for ${}_0S_3$. The noise level is one digital unit, and the smoothing window is 100 hours long.

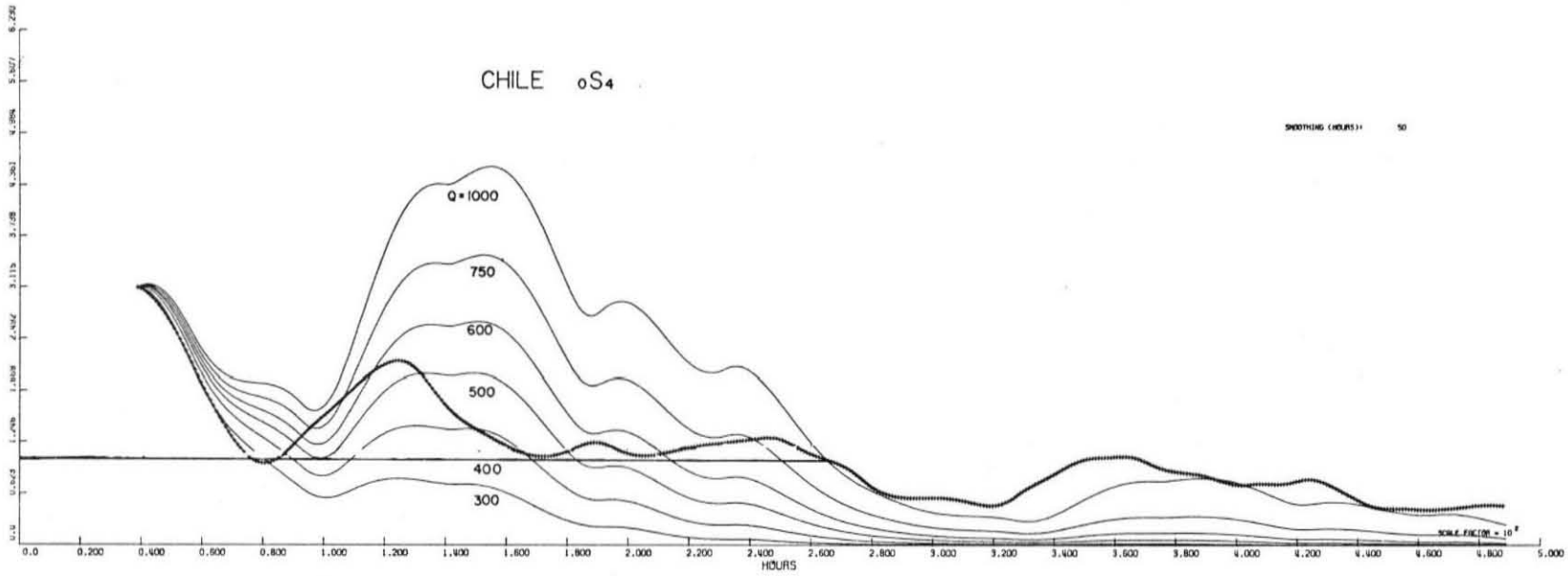

Figure 2.21. Data and synthetics for $_0S_4$. The noise level is one digital unit, and the smoothing window is 50 hours long.

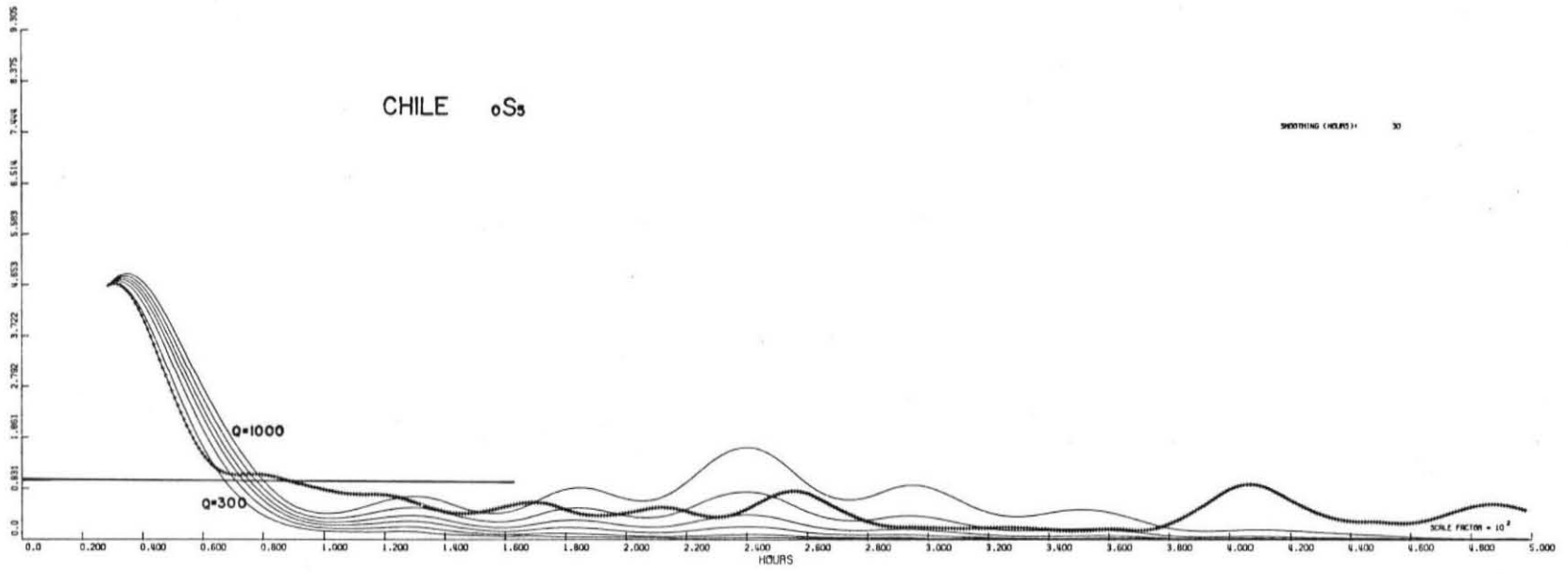

Figure 2.22. Data and synthetics for $_0S_5$. The noise level is one digital unit, and the smoothing window is 30 hours long.

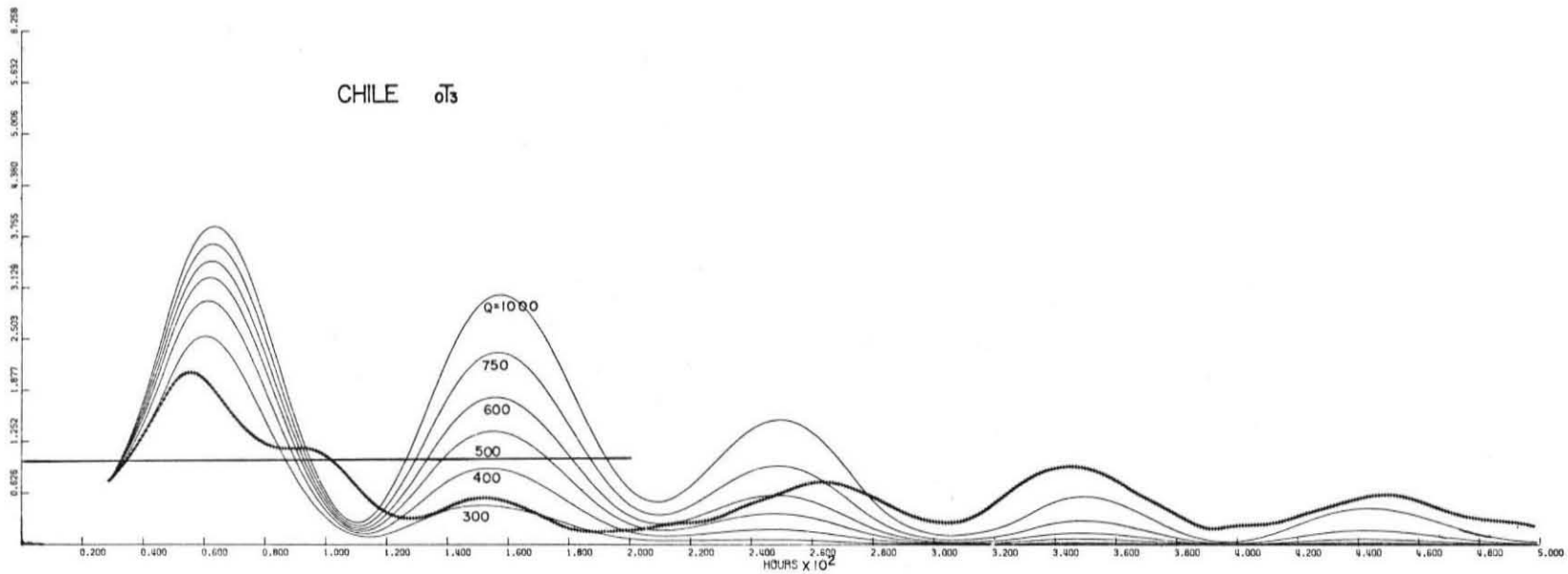

Figure 2.23. Data and synthetics for $_0T_3$. The noise level is one digital unit, and the smoothing window is 30 hours long.

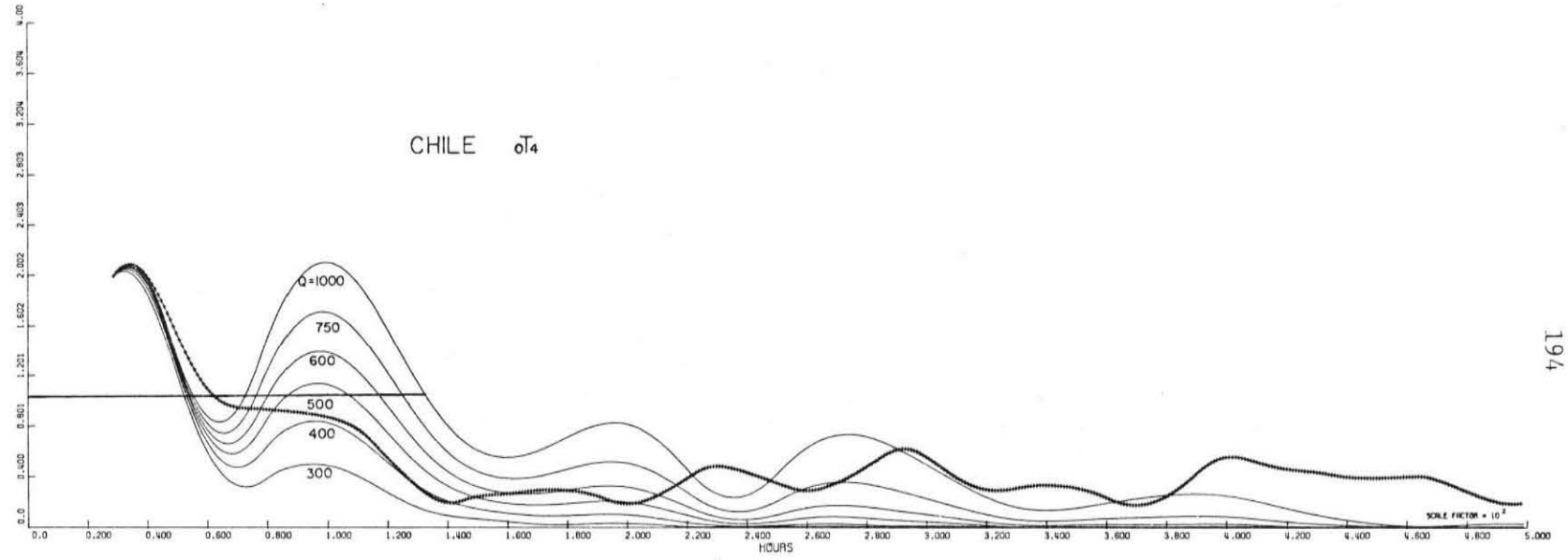

Figure 2.24. Data and synthetics for $_0T_4$. The noise level is one digital unit, and the smoothing window is 30 hours long.

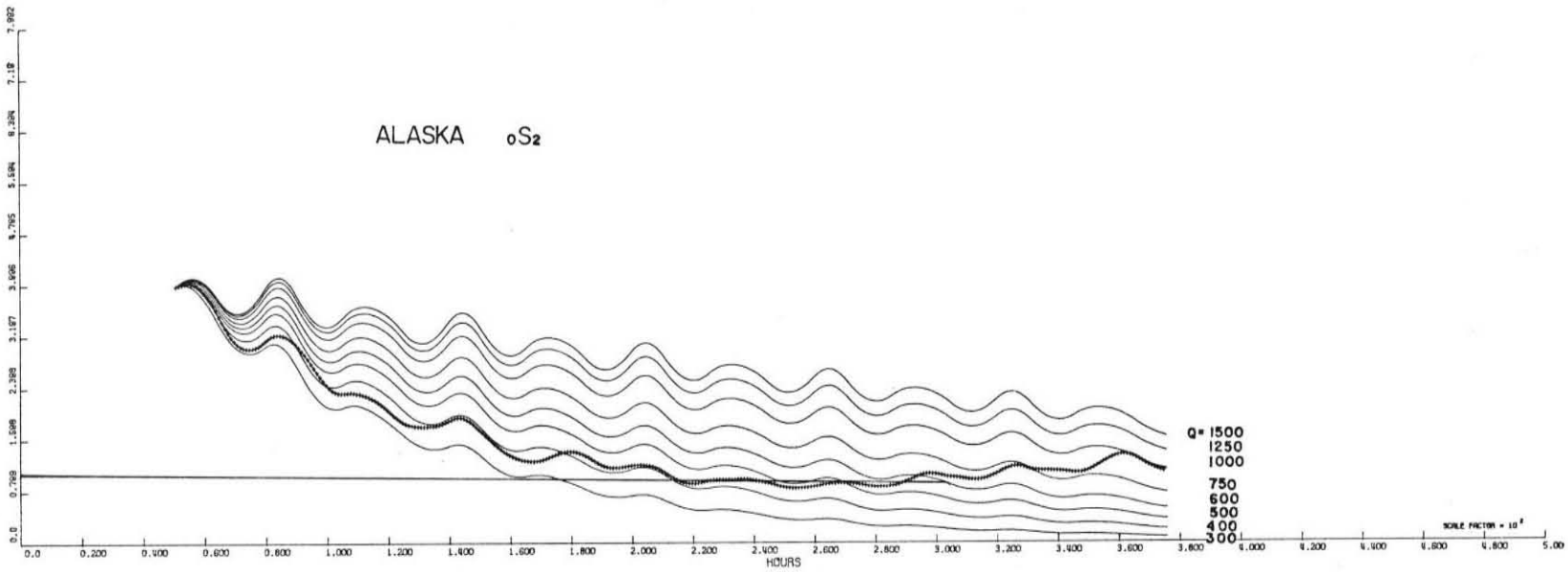

Figure 2.25. Data and synthetics for ${}_0S_2$ on the UCLA gravity record of the Alaskan earthquake. Time is in hours since the origin time (0336 hours, 28 March 1964) on the next five figures. The noise level is one unit, and the smoothing window is 75 hours long.

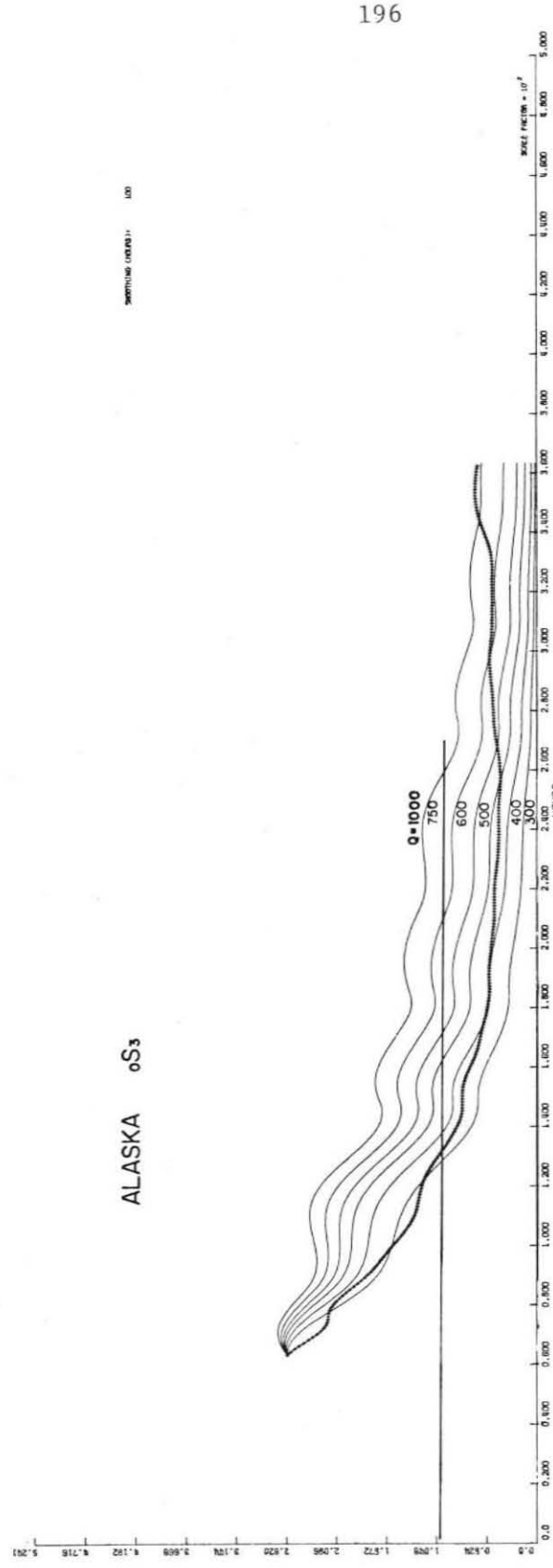

Figure 2.26. Data and synthetics for $_0S_3$. The noise level is one unit, and the smoothing window is 100 hours.

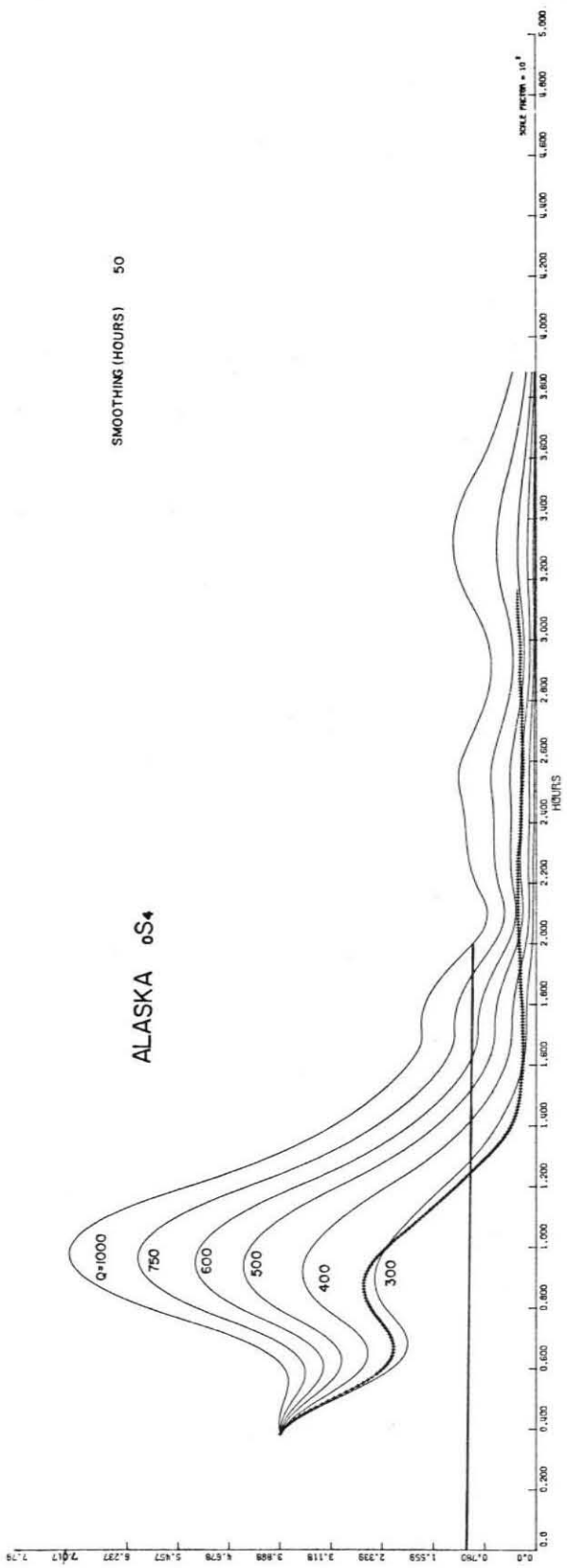

Figure 2.27. Data and synthetics for $_0S_4$. The noise level is one unit and the smoothing window is 50 hours.

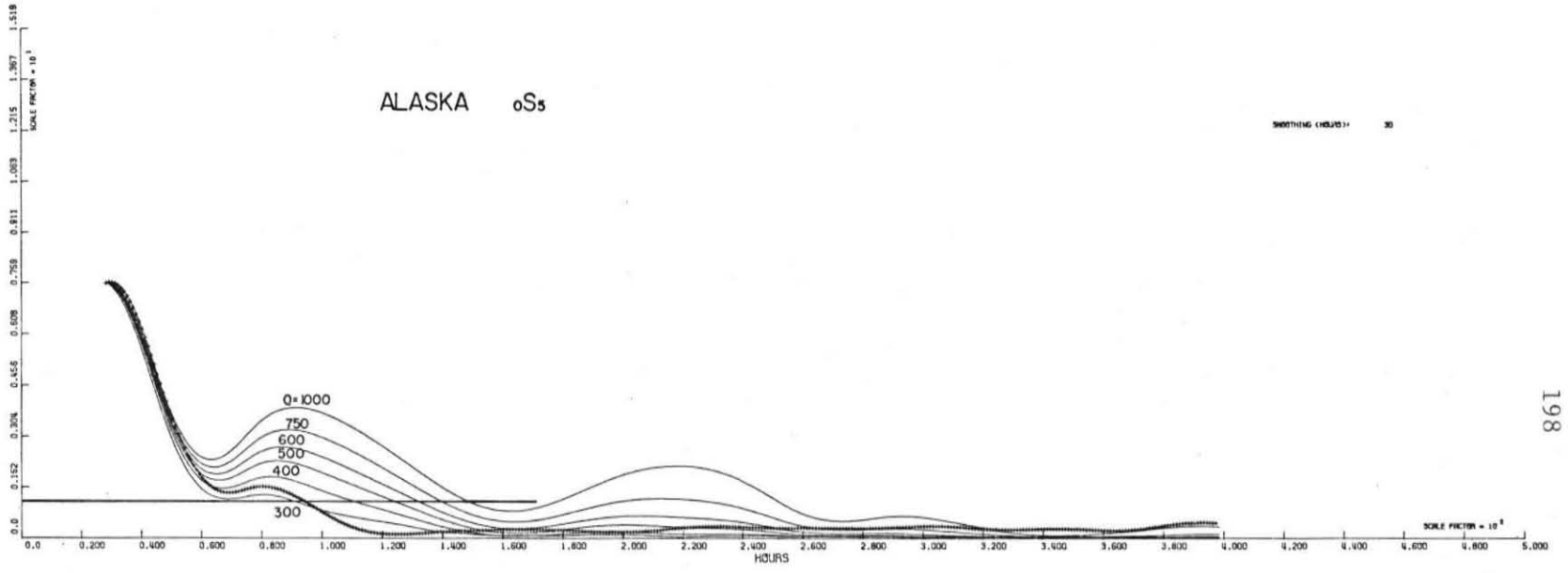

Figure 2.28. Data and synthetics for $_0S_5$. The noise level is one unit and the smoothing window is 30 hours.

Q is measured (estimated) by comparing the smoothed data to the smoothed synthetic curves, which bracket the data. The best-fitting Q is that obtained by using the maximum record length before the noise level is reached. These best fitting Qs are tabulated in Table 2.3, along with those obtained by previous investigations.

This procedure works well for modes with adequate signal levels; in this case, the four Chile spheroidal mode records. The results are much less satisfactory for the torsional modes (Figures 2.23 and 2.24). This is hardly surprising as the torsional mode peaks in the spectrum (Figure 2.4) are almost undetectable.

Figures 2.25-2.28 show the four corresponding spheroidal modes from the UCLA gravity record for the Alaskan earthquake. In general, the signal level is adequate and the noise level is considered to be one digital unit. The resulting Qs are also listed in Table 2.3.

The fundamental radial mode, ${}_0S_0$ was well recorded on the UCLA gravity meter (see the spectrum, Figures 2.5 and 2.6). Radial modes which have uniform displacement at any place on the earth's surface, are not subject to splitting. In this case the mode should decay as a pure damped harmonic oscillator. In such case, Q can be estimated by fitting a straight least-squares line to the logarithm of the amplitude.

The UCLA Alaskan earthquake record has been the only record suitable for analysis of ${}_0S_0$. (The Chilean record, Figure 2.4, shows a much poorer peak for this mode, and yields unacceptable results.) Surprisingly a variety of authors have analyzed this record and obtained widely divergent Q values. Slichter [1967] reported a Q of 13000 ± 2000. Sailor and Dziewonski [1978] found a much lower value, 5663, by taking

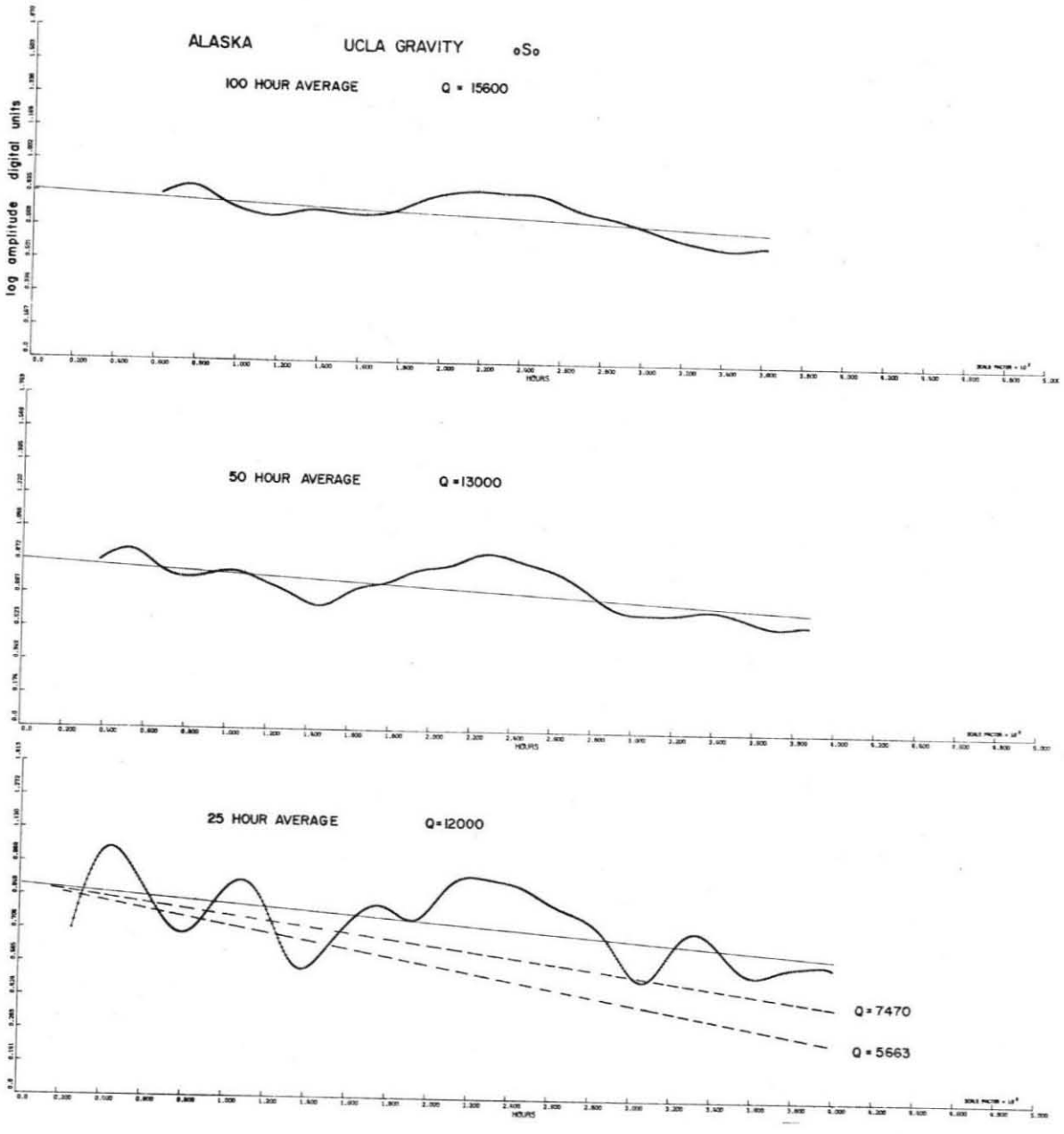

Figure 2.29. Least squares line fit to the logarithm of the amplitude of $_0S_0$, for three different running average windows. The exact values of Q for each fit are given in Table 2.2. The Q values of Buland and Gilbert (7470) and Sailor and Dziewonski (5650) are also indicated.

Table 2.2

Q OF $_0S_0$ FROM LEAST SQUARES AS A FUNCTION OF SMOOTHING WINDOW LENGTH

Window length (hours)	Q
100	15642 ± 152
50	13009 ± 108
25	12047 ± 112
10	13808 ± 175
5	14767 ± 208

the spectral energy in 13 six-day windows (each offset by one day) and fitting a least squares line to the spectral values. Buland and Gilbert [1978] used a method involving the spectral peak width and found a Q of 7470.

In this study Q was estimated by applying running averages to the band passed data, and then fitting a least squares line to all (in excess of 20,000) points. Figure 2.29 shows the results for 100, 50 and 25 hours running average. The precise values of Q obtained are tabulated in Table 2.2, along with the standard deviations obtained from standard least squares theory. Although the data scatter more as shorter smoothing windows are applied, the value of Q is quite stable. Given the noise level and scatter, this procedure yields a Q of about 13000 ± 2000, in accord with Slichter's [1967] value. Least squares lines corresponding to the Buland and Gilbert [1978] and Sailor and Dziewonski [1978] data are also plotted on Figure 2.29 for comparison.

DISCUSSION

Q values estimated from the data in the previous section are tabulated in Table 2.3. These were obtained from the portions of the record above the noise level. All these values have error bounds approximately ±100, except for the value for $_0S_0$, which is about ±2000, and the torsional modes, which have an error bound of approximately ±200.

Table 2.2 also lists the results obtained by previous studies. In general, the results of this study do not differ substantially from the other values. The major differences are for $_0S_2$ and $_0S_0$. Both

Table 2.3

Q VALUES FROM VARIOUS STUDIES

$_0S_2$	
425	This study, Alaska/UCLA
550	This study, Chile/Isabella
775	Buland and Gilbert [1978], Alaska/UCLA
815	Buland and Gilbert [1978], Alaska/UCLA
556	Sailor and Dziewonski [1978], Alaska/UCLA
500	Slichter [1967]
420	Smith [1972], Alaska and Chile/Isabella
370	Alsop *et al*. [1961b], Chile/Ogdensburg
$_0S_3$	
450	This study, Alaska/UCLA
325	This study, Chile/Isabella
460	Sailor and Dziewonski [1978], Alaska/UCLA
500	Slichter [1967], UCLA/Alaska
450	Smith [1972], Alaska and Chile/Isabella
380	Benioff *et al*. [1961], Chile/Isabella
$_0S_4$	
275	This study, Alaska/UCLA
400	This study, Chile/Isabella
411	Sailor and Dziewonski [1978], Alaska/UCLA
400	Slichter [1967], Alaska/UCLA
330	Smith [1972], Alaska and Chile/Isabella
$_0S_5$	
325	This study, Alaska/UCLA
300	This study, Chile/Isabella
352	Sailor and Dziewonski, Alaska/UCLA
300	Smith [1972], Alaska and Chile/Isabella
$_0T_2$	
325	This study, Chile/Isabella
370	Smith [1972], Alaska and Chile/Isabella
400	Smith [1961], Chile/Isabella

Table 2.3 - continued

$_0T_4$	
425	This study, Chile/Isabella
290	Smith [1972], Alaska and Chile/Isabella

$_0S_0$	
13000	This study, Alaska/UCLA
7470	Buland and Gilbert [1978], Alaska/UCLA
5663	Sailor and Dziewonski [1978], Alaska/UCLA
5096	Sailor and Dziewonski [1978], Alaska/UCLA
4229	Sailor and Dziewonski [1978], Alaska/UCLA
3996	Sailor and Dziewonski [1978], Alaska/UCLA
13000	Slichter [1967], Alaska/UCLA
900	Smith [1967], Chile/Isabella
>7500	Ness et al. [1961], Chile/UCLA

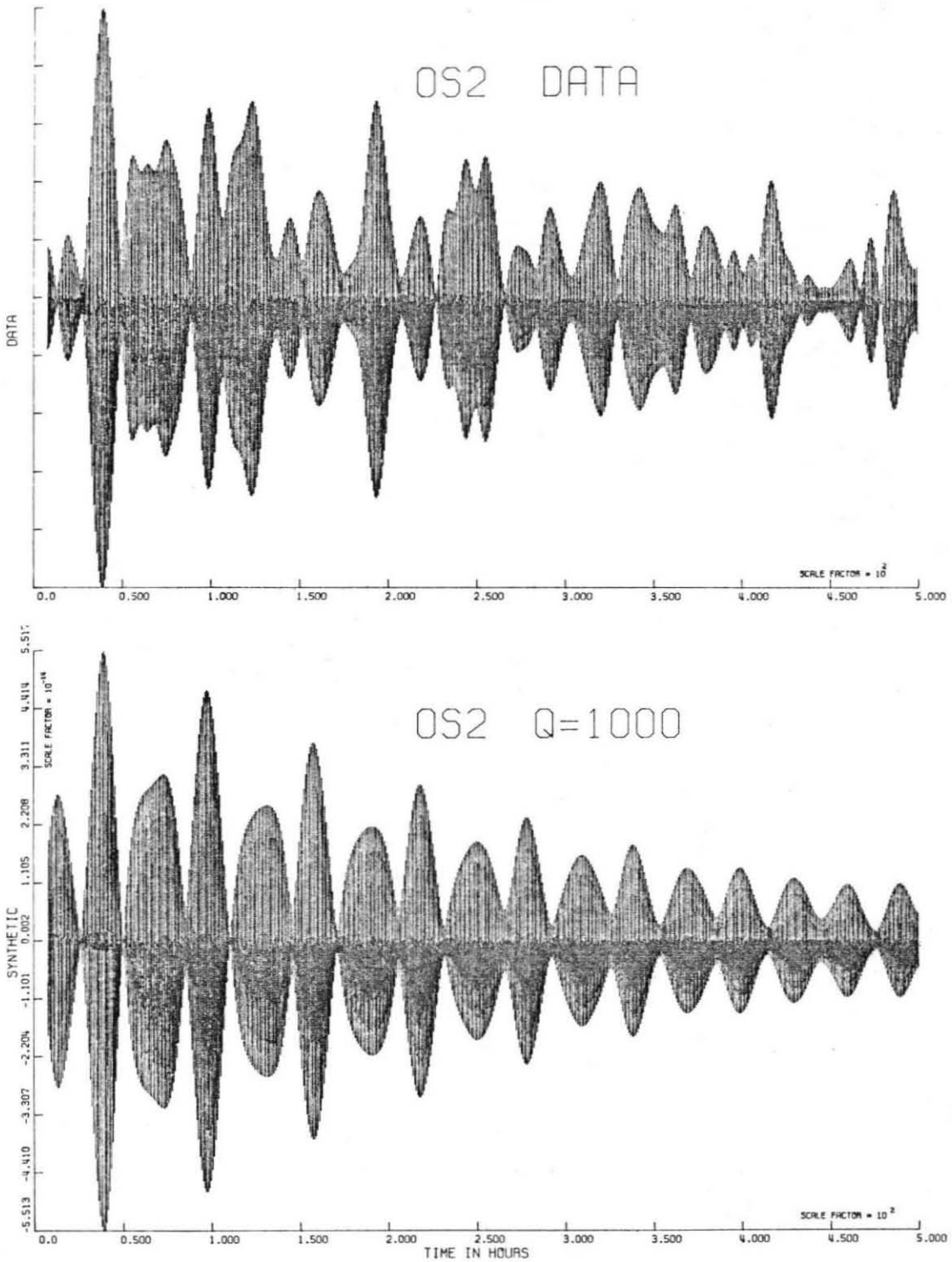

Figure 2.30 500 hour data and synthetics for the Isabella Chile record. The synthetic and data do not agree well after about 200 hours.

of these modes have substantial significance for gross earth models.

Our value for the Q of ${}_0S_0$ (13000 ± 2000) is in accord with that of Slichter [1967], somewhat higher than that of Buland and Gilbert [1978] (7470) and much higher than those of Sailor and Dziewonski [1978] (5662-3996). Sailor and Dziewonski interpreted their low value as requiring bulk dissipation in the earth, either in the inner core or the upper mantle. Such bulk dissipation is not required by the results of this study. This is in accord with model MM8 [Anderson et al., 1965] which predicts a Q for ${}_0S_0$ of 10068 with no bulk dissipation.

Buland and Gilbert [1978] argued against the existence of a low Q zone at the base of the mantle, from the high value (775-815) of the Q of ${}_0S_2$. Our results (425-550) are in general accord with Slichter [1967] and Sailor and Dziewonski [1978], and are much lower. Such data may be consistent with the presence of a low Q zone.

The scatter in Q values reported by various investigators is clearly due to the poor quality of the limited body of data available for such ultra long period studies. This limitation is illustrated in Figure 2.30. Here all 500 hours of the Chilean strain record at Isabella are plotted. A synthetic was generated, using the same methods as Figure 1.2, for all 500 hours of record. Even if an extremely high Q (1000) is used, the data have a higher amplitude than the synthetic after several hundred hours. Moreover, for the first hundred and fifty hours, there is a general correspondence between the data and synthetics (see the expanded playout in Figure 1.2). This correspondence is almost gone three hundred hours after the earthquake. The data appear to be now composed of almost pure noise bursts, but it is difficult to impose any

formal criterion to delineate the transition from signal to noise. Any Q measurement technique will thus face substantial difficulties. Although our choice of noise level (Figure 2.19) probably minimizes this problem, the essential limitation is still the low signal quality.

CONCLUSION

Comparison of narrow-band filtered data and synthetic seismograms generated using theoretical results for the excitation of split modes is a valuable technique for Q estimation. Such methods are necessary when it is not possible to isolate individual singlets, and the combined beat pattern must be used. The limitations on this method resulting from the quality of the data from the early 1960s can be removed once long period data from the IDA network [Agnew et al., 1976] for large earthquakes become available.

REFERENCES

Agnew, D., J. Berger, R. Buland, W. Farrell and F. Gilbert, International deployment of accelerometers: a network for very long period seismology, EOS Trans., Am. Geophys. Un., 57, 180-188.

Akopyan, S., V. Zharkov and V. Lyubimov, The dynamic shear modulus in the interior of the earth, (in Russian), Doklady Akademii Nauk SSR, 223, 1-3, 1975.

Akopyan, S., V. Zharkov and V. Lyubimov, Corrections to the eigenfrequencies of the earth due to the dynamic shear modulus, (in Russian), Fizika Zemli, 12, 625-630, 1976.

Alsop, L. E., G. Sutton and M. Ewing, Free oscillations of the earth observed on strain and pendulum seismographs, J. Geophys. Res., 66, 621-629, 1961a.

Alsop, L. E., G. H. Sutton and M. Ewing, Measurement of Q for very long period free oscillations, J. Geophys. Res., 66, 2911-2915, 1961b.

Alterman, Z., H. Jarosch and C. L. Pekeris, Oscillations of the earth, Proc. R. Soc. London, A252, 80-95, 1959.

Anderson, D. L., A. Ben-Menahem and C. B. Archambeau, Attenuation of seismic energy in the upper mantle, J. Geophys. Res., 70, 1441-1448, 1965.

Anderson, D. L. and R. S. Hart, An earth model based on free oscillations and body waves, J. Geophys. Res., 81, 1461-1475, 1976.

Benioff, H., Fused-quartz extensometer for secular, tidal and seismic strains, Bull. Geol. Soc. Am., 70, 1019-1032, 1959.

Benioff, H., Long period seismographs, Bull. Seism. Soc. Am., 50, 1-13, 1960.

Benioff, H., F. Press and S. Smith, Excitation of the free oscillations of the earth, J. Geophys. Res., 66, 605-619, 1961.

Brink, D. M. and G. R. Satchler, Angular Momentum, Clarendon Press, Oxford, 1968.

Buland, R. and F. Gilbert, Improved resolution of complex eigenfrequencies in analytically continued spectra, Geophys. J. Roy. astr. Soc., 52, 457-470, 1978.

Dahlen, F. A., The normal modes of a rotating elliptical earth, Geophys. J. R. astr. Soc., 16, 329-367, 1968.

Liu, H. P., D. L. Anderson and H. Kanamori, Velocity dispersion due to anelasticity: implications for seismology and mantle composition, Geophys. J. Roy. astr. Soc., 47, 41-58, 1976.

Kanamori, H., The Alaska earthquake of 1964: radiation of long-period surface waves and source mechanism, J. Geophys. Res., 75, 5029-5040, 1970 .

Kanamori, H. and D. L. Anderson, Amplitude of the earth's free oscillations and long-period characteristics of the earthquake source, J. Geophys. Res., 80, 1075-1078, 1975.

Kanamori, H. and J. J. Cipar, Focal process of the great Chilean earthquake May 22, 1960, Phys. Earth Planet. Int., 9, 128-136, 1974.

Marion, J. B., Classical Dynamics of Particles and Systems, Academic Press, New York, 1970.

Ness, N., J. Harrison and L. Slichter, Observations of the free oscillations of the earth, J. Geophys. Res., 66, 621-629, 1961.

Sailor, R. V. and A. M. Dziewonski, Measurements and interpretation of normal mode attenuation, Geophys. J. Roy. astr. Soc., in press, 1978.

Saito, M., Excitation of free oscillations and surface waves by a point source in a vertically heterogeneous earth, J. Geophys. Res., 72, 3689-3699, 1967.

Slichter, L. B., Spherical oscillations of the earth, Geophys. J., 14, 171-177, 1967.

Smith, S. W., An investigation of the earth's free oscillations, Ph.D. Thesis, California Institute of Technology, 1961.

Smith, S. W., The anelasticity of the mantle, Tectonophysics, 13, 601-622, 1972.

Stein, S. and R. J. Geller, Amplitudes of the split normal modes of a rotating, elliptical earth excited by a double couple, J. Phys. Earth, 25, 117-142, 1977.

Takeuchi, H. and M. Saito, Seismic surface waves, Methods Comp. Phys., 11, 217-295, 1972.

Wiggins, R. A. and S. P. Miller, New noise-reduction technique applied to long-period oscillations from the Alaskan earthquake, Bull. Seism. Soc. Am., 62, 471-479, 1972.

Woodhouse, J. H., On Rayleigh's principle, Geophys. J., 46, 11-22, 1976.